DISS. ETH NO. 29029

Load-deformation behaviour of reinforced concrete structures affected by local corrosion

A thesis submitted to attain the degree of

DOCTOR OF SCIENCES

(Dr. sc. ETH Zurich)

presented by

SEVERIN SEBASTIAN HÄFLIGER

MSc ETH Civil Eng, ETH Zurich

born on 25.07.1989

accepted on the recommendation of

Prof. Dr. Walter Kaufmann (ETH Zurich, examiner)

Prof. Dr. Beatrice Belletti (Università di Parma, co-examiner)

Prof. Dr. Terje Kanstad (NTNU, co-examiner)

2023

Preface

A recent study[1] concluded that 56% of the maintenance costs for the Swiss civil engineering infrastructure are directly related to corrosion damage, summing up to 411 Mio. Swiss Francs spent annually on average. The financial impact of corrosion is thus in the same range as that caused by natural hazards (about CHF 300 Mio./yr.[2]) or fire incidents (about CHF 310 Mio./yr.[3]). Moreover, the effective related costs may even be much higher since the economic and environmental costs (for traffic jams, CO_2 emissions, etc.) are not included in the figures above.

One of the main reasons for the high costs is the lack of knowledge regarding the assessment of reinforced concrete structures affected by corrosion: Whereas the prevention and detection of corrosion, as well as possible repair strategies, are an integral part of engineering education and practice, little is known about the effects of corrosion damage on the structural behaviour. Consequently, no strategies exist today to assess structural safety in case of corrosion, and structures are retrofitted or even replaced as soon as corrosion damage is detected. This preventive repair and replacement – often much earlier than initially planned in the structure's life cycle – without clarifying its necessity and benefits by a previous structural analysis is neither sustainable nor cost-effective.

The results of the present research project indicate that existing models tend to significantly underestimate the load-carrying and deformation capacity of locally corroded structures: Beneficial effects caused by the triaxial stress state at the corrosion pits and the corrosion damage distribution among the reinforcing bars were found to partly compensate for the negative influence of the reinforcing bars' cross-section loss. Although these effects are not yet fully understood today, they imply that reinforced concrete structures affected by local corrosion can be kept in service (without retrofitting) longer than it is currently assumed. This finding is a milestone since maximising the service life of our infrastructure is the most effective strategy to reduce its costs and carbon footprint.

This thesis aims to take a first step towards this goal by exploring the identified beneficial effects and describing the underlying mechanisms on a sound mechanical basis. However, despite the promising results of the experimental campaigns and theoretical investigations, more research is needed to fully understand the load-bearing behaviour of locally corroded structures, and to elaborate corresponding assessment guidelines. Nevertheless, the tremendous impact of prolonging the service life of affected structures on their sustainability and maintenance costs compensates multifold for the effort spent on additional research.

Zurich, January 2023 Severin Haefliger

[1] Yilmaz, D. and Angst, U., 'Korrosionsbedingte Kosten an Ingenieurbauwerken im Schweizer Strassennetz,' *Beton- und Stahlbetonbau*, vol. 115, no. 6, pp. 448-458, 2020. DOI: 10.1002/best.202000004.

[2] Swiss Federal Office for the Environment, `https://www.bafu.admin.ch/bafu/en/home/topics/natural-hazards/in-brief.html` (31.1.2023)

[3] Swiss Fire Prevention Advisory Service, `https://www.bfb-cipi.ch/ueber-bfb/statistiken` (31.1.2023)

Summary

A growing number of ageing structures is affected by pitting corrosion due to the ingress of chlorides or structural defects such as honeycombs. The resulting local damage reduces their load-carrying capacity and – even more pronouncedly – their deformation capacity due to the corresponding strain localisation. The latter is particularly critical for statically indeterminate structures whose structural safety relies on plastic load redistributions or for structures whose main loading is deformation-dependent, such as the earth pressure in the case of retaining walls. In fact, many design rules in current codes are based on the lower bound theorem of the plasticity theory (though often implicitly, e. g. by neglecting initial internal or external restraint stresses), which requires a sufficient deformation capacity as commonly available in uncorroded elements. These rules are, however, no longer applicable to locally corroded structures unless their deformation capacity is carefully assessed. Unfortunately, and despite much research conducted over the past decades, no mechanically consistent, generally applicable assessment strategies in case of local corrosion exist. This thesis addresses this knowledge gap by investigating the influence of local corrosion on the load-deformation behaviour of reinforced concrete structures, focusing on the practical case of corroding cantilever retaining walls.

A comprehensive series of tensile tests on artificially damaged bare reinforcing bars revealed the influences of (i) strain rate, (ii) varying microstructural layers over cross-section, and (iii) the pit geometry on their load-deformation behaviour. Whereas the varying strain rate (i) along the bar axis tends to increase the tensile strength at the corrosion pit, it is potentially reduced for increasing cross-section loss in modern reinforcing bars exhibiting a varying microstructure (ii) over the cross-section, as it is characteristic for quenched and self-tempered ("Tempcore") reinforcing bars. Depending on the pit geometry (iii), the apparent uniaxial tensile strength and the deformation capacity in the pit and in its vicinity increase due to a triaxial stress state. This effect counteracts strain localisation and leads to a significantly higher deformation capacity of affected bars than assumed by common strain localisation models.

A series of large-scale tests on cantilever retaining wall segments with artificially damaged reinforcing bars confirmed a pronounced influence of the effective corrosion distribution among the reinforcing bars, as anticipated based on a preliminary theoretical analysis: the load-carrying and deformation capacity of structures containing many slightly corroded bars differs significantly from that of structures with only a few but severely corroded bars, even if the total cross-section loss is equal in both cases. Hence, merely indicating the mean cross-section loss is inappropriate to conclude on the load-deformation behaviour of a structure. Two hybrid tests, where the corrosion damage was increased at simultaneously decreasing load simulating the earth pressure, revealed that the deformation increase caused by an increasing cross-section loss is very limited even for considerable damage (approximately 1 mrad rotation for 40% cross-section loss). Deformations might notably increase only very close to failure, which challenges the successful application of monitoring systems relying on deformation measurements.

Finally, a mechanically consistent model enabling the reliable assessment of the structural safety and the load-deformation behaviour of locally corroded reinforced concrete structures was developed: the Corroded Tension Chord Model. In its basic version, this model combines the effects of tension stiffening and strain localisation. Based on the experimental observations, it was enhanced to account for the effects of a triaxial stress state at the corrosion pit, considering axisymmetric damage. The model predictions of the experimental results are very promising, with the comparison indicating an additional softening effect – exceeding that of the triaxial axisymmetric stress state – at the corrosion pit, probably caused by superimposed bending stresses due to unilateral corrosion. The deformation capacity of the specimens was thus clearly less impaired than predicted by established strain localisation models.

Zusammenfassung

Eine zunehmende Anzahl älterer Bauwerke ist von Lochfrasskorrosion betroffen, sei es durch Chloridverseuchung oder infolge einer schadhaften Bewehrungsüberdeckung. Diese lokale Schädigung reduziert den Tragwiderstands und insbesondere das Verformungsvermögens infolge einer Verformungslokalisierung. Letzteres ist primär relevant bei statisch unbestimmten Tragwerken, deren Tragwiderstand plastische Lastumlagerungen voraussetzt, wie auch bei Tragwerken, deren Einwirkung von ihrer Verfomung abhängt. Tatsächlich beruhen viele Bemessungs- und Überprüfungsmethoden auf dem unteren Grenzwertsatz der Plastizitätstheorie, was ein ausreichendes Verformungsvermögen voraussetzt (wie es bei intakten Tragwerken in der Regel auch vorhanden ist). Diese Methoden können daher nicht unbesehen auf lokal korrodierte Tragwerke angewendet werden, vielmehr ist ein ausreichendes Verformungsvermögen explizit nachzuweisen. Trotz intensiver Forschung existieren jedoch heute keine mechanisch konstenten, allgemein anwendbaren Methoden für die Tragsicherheitsüberprüfung der von Lochfrasskorrosion betroffenen Bauwerke. Die vorliegende Arbeit zielt darauf ab, diese Wissenslücke zu schliessen. Sie untersucht dazu den Einfluss lokaler Korrosion auf das Last-Verformungsverhalten betroffener Tragwerke, mit Schwerpunkt auf dem praktischen Anwendungsfall lokal korrodierender Winkelstützmauern.

Die Resultate einer umfassenden Serie von Zugversuchen an künstlich geschädigten Bewehrungsstäben zeigten den Einfluss (i) der Dehungsgeschwindigkeit, (ii) der unterschiedlichen Mikrostruktur über den Stabquerschnitt und (iii) der Schädigungsgeometrie auf. Die über die Stablänge variierende Dehnungsgeschwindigkeit (i) führt zu einer leichten Erhöhung der Zugfestigkeit im geschädigten Bereich, wohingegen moderne Bewehrungsstäbe mit unterschiedlicher Mikrostruktur über den Querschnitt (ii) mit zunehmendem Querschnittsverlust überproportional an Zugfestigkeit einbüssen. Je nach Schädigungsgeometrie (iii) erhöht ein dreiachsiger Spannungszustand die einachsige Zugfestigkeit und das Verformungsvermögen im Bereich der Schädigungsstelle. Diese Effekte wirken einer Verformungslokalisierung entgegen, weshalb Modelle, welche alleinig auf der Verformungslokalisierung aufbauen, das Verformungsvermögen lokal korrodierender Stäbe typischerweise stark unterschätzen.

Grossmassstäbliche Versuche an Winkelstützmauersegmenten bestätigten den deutlichen Einfluss der Verteilung des Korrosionsschadens über die verschiedenen Bewehrungsstäbe, wie er aufgrund einer theoretischen Vorstudie vermutet wurde. So unterscheidet sich das Last-Verformungsverhalten von Versuchskörpern mit vielen leicht korrodierten Stäben stark von denjenigen mit wenigen, stark korrodierten Stäben, selbst bei identischem Gesamtquerschnittsverlust. Die alleinige Angabe eines mittleren Querschnittsverlusts reicht somit nicht aus, um die Tragsicherheit eines Bauwerks zu beurteilen. Zwei Hybridversuche, bei denen der Querschnittsverlust während des Versuchs gesteigert und gleichzeitig die Einwirkung analog dem Erddruck reduziert wurde, zeigten, dass eine Verformungszunahme infolge zunehmenden Querschnittsverlusts selbst bei beachtlichen Verlusten sehr gering ist (ca. 1 mrad bei 40% Querschnittsverlust). Die Verformungen würden voraussichtlich erst kurz vor Erreichen des Bruchzustands markant zunehmen, was eine grosse Herausforderung für eine erfolgreiche Bauwerksüberwachung auf Grundlage von Verfomungsmessungen darstellt.

Schliesslich wurde mit dem korrodierten Zuggurtmodell ein mechanisch konsistentes Modell entwickelt, mit dem das Last-Verformungsverhalten von lokal korrodierenden Tragwerken zuverlässig beurteilt werden kann. In seiner ursprünglichen Version kombiniert das Modell den Einfluss der Zugversteifung mit jenem der Verformungslokalisierung. Es wurde aufgrund des in den Versuchen beobachteten Verhaltens weiterentwickelt, um den Einfluss dreidimensionaler Spannungen an der Korrosionsstelle zu berücksichtigen. Die Resultate der Versuchsnachrechnungen sind sehr vielversprechend und weisen auf die Existenz eines zusätzlichen Effekts hin, der die Dehnsteifigkeit des Stabs im Bereich der Korrosionsstelle weiter verringert. Dieser Effekt ist wahrscheinlich auf Biegespannungen bei einseitig angreifender Korrosion zurückzuführen. Insgesamt war die Abnahme des Verformungsvermögens damit deutlich geringer als von bisherigen, rein auf Verformungslokalisierung basierenden Modellen vorausgesagt.

Acknowledgements

At the time I joined the Chair of Concrete Structures and Bridge Design of Professor Walter Kaufmann in March 2015, the freshly formed research group had existed for about one year, which allowed my colleagues and me to contribute to various very interesting projects like the planning, construction, and commissioning of the Large Universal Shell Element Tester LUSET and the procurement and testing of innovative measurement technologies in fibre optic strain sensing and digital image correlation. Their application to structural concrete elements has been challenging and exciting at the same time, giving unprecedented and valuable insights into the elements' structural behaviour. Profiting from these experiences, I had the great opportunity to start my own research on the load-deformation behaviour of locally corroded reinforced concrete structures, which culminated in conducting a series of large-scale and hybrid tests in LUSET, being doubtlessly one of the highlights of my time working at the chair. Investigating these structures, which reveal so many interesting – and sometimes unanticipated – effects on different structural levels, has been incredibly fascinating.

First and foremost, I want to express my sincere gratitude to Prof. Dr. Walter Kaufmann for welcoming me in his research group, offering me the great chance to be involved in these interesting projects, and providing me with this exciting research topic. Throughout my time as a doctoral student, I profited a lot from his broad and deep expertise in structural concrete and the inspiring discussions on new ideas and obtained results. I highly appreciated his encouragement and trust, and I am very grateful for the freedom he provided to find my own way in research and to try out new (and sometimes unconventional) approaches, still offering support whenever needed.

While working on the topics of lap splices, triaxial stress states, and the modelling of retaining walls, I enjoyed the many discussions with Dr. Karel Thoma, my second advisor, on the nature of the Tension Chord Model and the challenges, opportunities and also drawbacks of Nonlinear Finite Element Analyses. Karel joined our chair when this research project was in its last phase but contributed to it significantly and wholeheartedly, for which I am very thankful.

Furthermore, I want to thank Prof. Dr. Beatrice Belletti from the University of Parma and Prof. Dr. Terje Kanstad from the NTNU in Trondheim for being part of my doctoral committee. I am very grateful for their time and energy spent reviewing my thesis and the very interesting and fruitful discussion at my doctoral defence.

Work would only have been half the fun without my great colleagues in our "Betonaffa"-group. I would like to thank Dr. Jaime Mata-Falcón for his excellent advice in scientific and personal life, his great ideas, the encouraging discussions, and for showing me how to make presentations more catchy; Patrick Bischof, my office mate, for the numerous vivid discussions, his incredible creativity, his expertise, support, and his constantly positive mindset; Alex Beck and Demis Karagiannis for the creative discussions, for teaching me "How to LUSET", and making exam corrections more fun; Tena Galkovski, Yasmin Lemcherreq, Tomislav Markic, Minu Lee, and Nicola Gehri for the many discussions on how to measure bond and crack kinematics, how to glue glass fibres, getting the fibre optics device to measure, choosing the right speckle size and the best digital image correlation settings; Nathalie Reckinger, for the very interesting discussions on ductility, for co-supervising many student projects, and for her support in several projects when time was once again running short – I really appreciated this; Lucia Licciardello and Andreas Näsbom, for the great fun we had when speckling inside the box-girder of Europabrücke; and of course Rebecca Ammann, Vera Balmer, Lukas Gebhard, Alejandro Giraldo-Soto, Renate Hilfiker, George Klonaris, Fabian Morger, Marius Weber, and Karin Yu, with whom it was a pleasure to work with, to laugh and share ideas – especially in our refurnished coffee room. All of you contributed

to this thesis in one way or another, and I am extremely thankful for your help in the lab and the great time we had in the office and on our various group events.

The experiments in the laboratory could not have been carried out and completed successfully without the contribution and expertise of our institute's lab team. I am very grateful to Dominik Werne, Christoph Gisler, Pius Herzog, Thomas Jaggi, and Martin Viertel, as well as Thomas Meierhans, Paul Fischlin, and Oliver Zgraggen from the metals and carpenter's workshop for their great support.

I had the chance to work closely together with several very motivated Master's students who were supporting this research project during their Master's theses or as student assistants. I express my gratitude to Rebecca Ammann, Sara Fomasi, Pius Cottier, Manuel Stocker, Moritz Studer, Vanessa Studer, Monica di Vincenzo, and Caroline Wirion. A special thank goes to Sina Fehr for her tireless support in conducting the large-scale experiments in LUSET during the pandemic and always providing me with tasty coffee.

Although this thesis mainly focuses on the structural effects of local corrosion, it also touches other research fields, which provided me the chance to collaborate with and learn from experts in these fields. I would like to thank Prof. Dr. Ueli Angst and Dr. Carolina Boschmann Käthler from the Chair of Durability of Engineering Materials, and Dr. David Perozzi from the Chair of Geomechanics for their sound advice and the fruitful and close collaboration.

Reinforcing steel of specific manufacturing types was needed for the experiments on single reinforcing bars and retaining wall segments. I would like to thank Pirmin Schuler, Gustav Giczi, Laurent Mathez, and Holger Simon of Debrunner Acifer Bewehrungen AG for their openness to my unconventional concerns, their professional consulting, and their support in organising the wished products.

This research project was partially funded by the Swiss Federal Roads Office and the Swiss Federal Office of Transport, whose contribution is gratefully acknowledged.

Finally, I would like to express my deepest gratitude to my family and, in particular, Daliah for their patience, encouragement and everlasting support.

Table of contents

1 Introduction

This thesis presents the results of a research programme [73] on the implications of local reinforcement corrosion on the load-deformation behaviour of reinforced concrete (RC) structures. The programme focused on cantilever retaining walls as case study objects since a considerable number of these ageing structures are affected by local corrosion. Nevertheless, the findings and developed models are applicable to a wide range of structural elements.

The introduction presents the context of the thesis and illustrates the effects of local corrosion damage on the load-carrying and deformation capacity of RC cantilever retaining walls. After an overview of the current state of the art, the open research questions and the research objectives are summarised. Finally, the thesis structure is outlined.

1.1 Context and motivation of the present study

1.1.1 Deterioration processes related to corrosion

Carbonation-induced and chloride-induced corrosion are the two main corrosion types occurring in RC structures, besides atmospheric and stray-current-induced corrosion, and hydrogen-induced stress-corrosion cracking [25]. They differ regarding the depassivation mechanism, the corrosion rate, and the deterioration effects, i. e. the occurrence of uniform or local corrosion.

Carbonation-induced uniform corrosion results from the ingress of carbon dioxide into concrete (mostly dissolved as carbon acid in water), reacting with the calcium hydroxide of the cement paste, which thus reduces the alkalinity and leads to steel depassivation. Since this process occurs extensively, corrosion initiates over a considerable length of the affected reinforcing bars. However, the corrosion rate is usually low due to the randomly located anodes and cathodes along the bar, leading to a diameter loss in the order of merely 0.01 mm/yr. However, the volume expansion of the corrosion products often causes further damage by cracking and spalling of the concrete cover [25].

Chloride-induced local corrosion results from the ingress of chloride ions dissolved in water (originating, e. g. from deicing salt), which locally destroy the protective passive layer on the reinforcing bar in the alkaline concrete. Once the corrosion process is initiated, a local macrocell forms, with the corrosion pit acting as small anode and the neighbouring parts of the still passive reinforcing bar, as well as electrically connected further reinforcement, as large cathode. The electrochemical process is stabilised by the aggressive acidic environment present in the pit and the increasing alkalinity at the cathode, protecting the neighbouring steel. The macrocell causes high corrosion and penetration rates of up to 1 mm/yr. In contrast to carbonation-induced corrosion, the corrosion products are dissolved in the acidic solution in the pit, which prevents cracking and spalling of the concrete cover. Therefore, often no deterioration signs are visible on the concrete surface [25].

1.1.2 Effects of corrosion on structural safety

The structural safety of RC structures affected by *uniform corrosion* is mainly impaired by the spalling of the concrete cover, often occurring excessively, and the accompanying bond reduction, which potentially leads to a loss of reinforcement anchorage and a deterioration of the concrete compression zone. Bond

reduction further compromises structural serviceability by reducing the stiffness of the structure. On the other hand, the loss of the bar cross-sectional area is rather a secondary problem for this corrosion type since it progresses very slowly (see Section 1.1.1).

In contrast, *local corrosion* primarily reduces structural safety by the rapidly increasing bar cross-section loss over a short length, leading to pronounced corrosion pits. The reduced bar cross-sectional area directly impairs the load-carrying capacity of RC structures, and the localised nature of the deterioration reduces their deformation capacity due to strain localisation. Since the plastic deformations of reinforcing steel are an order of magnitude larger than the elastic ones, the bar length over which plastic deformations occur is decisive for the deformation capacity. The latter thus significantly decreases if the bar cross-sectional area is reduced over a short length, particularly if plastic deformations only occur in the damaged part, whereas the remaining bar merely deforms elastically.

1.1.3 Cantilever retaining walls affected by local corrosion

A pilot study conducted by the Swiss Federal Roads Office FEDRO [52] revealed that many RC cantilever retaining walls, built in the 1960s and 1970s along the motorways and railroads, are affected by local corrosion damage of the main tensile reinforcement at the backside of the wall. The corrosion occurs just above the construction joint between the footing and the wall and is presumably caused by the presence of honeycombs as a result of poor concrete compaction and segregation at the time of construction. Hence, the reinforcement in this area has not been entirely passivated, but instead, a limited part of its surface has been easily accessible to water and oxygen. This led to atmospheric-induced corrosion and, since only the bars at the honeycomb were active (anode) and the remaining reinforcement in the wall was passivated (cathode), the formation of macrocells. The large difference in the anodic and cathodic surface area caused a very high corrosion rate and a rapid loss of cross-sectional area, resulting in the typical pitting usually observed for chloride-induced corrosion, despite the absence of chlorides. Among all investigated bars in the pilot study, 24% exhibited corrosion damage with a mean cross-section loss of 37%, resulting in an overall cross-section loss of approximately 9% [52]. According to a subsequently conducted study [138] reinvestigating the results of the pilot study, 42% of all assessed retaining walls revealed corrosion damage. Hence, the mean number of affected bars in a corroding wall needed to be adjusted to $0.24/0.42 = 57\%$, and the mean cross-section loss was corrected to $0.09/0.42 = 21\%$.

Retaining walls are mainly loaded by earth pressure, whose value depends on the deformation of the structure. Following the recommendations of the Swiss Code SIA 162 (in vigour between 1956 and 1989) [144], retaining walls in Switzerland were designed to resist the active earth pressure at the ultimate limit state, which implicitly assumes that the deformation capacity of the structure is sufficient for the earth pressure to drop from pressure at rest to active pressure. This assumption needs to be carefully assessed for corroding retaining walls since their deformation capacity is most likely reduced (see Section 1.1.2). In the unfavourable case that the residual deformation capacity is insufficient for the earth pressure to adopt the active pressure, the load acting on the retaining wall will typically exceed the one assumed in design. In combination with the reduced load-carrying capacity due to the cross-section loss and the fact that most retaining walls are segmented in their longitudinal direction, impeding global load redistributions, this increases the risk of affected walls to fail in a brittle manner.

In addition to the considerable uncertainty regarding structural safety, the mentioned pilot study revealed that corrosion detection is highly challenging for retaining walls. The thickness of the wall above the footing, which is usually >0.5 m, impedes detecting the corroding reinforcement at the rear side of the walls with conventional methods applied at the front side, such as half-cell potential mapping or georadar measurements [52]. Therefore, even severe corrosion damage is likely to remain undetected until failure unless much more cost- and time-intense inspection methods (e. g. excavating the backfill) are applied.

1.1.4 Motivation and focus of this thesis

Although the effects of corrosion on the load-deformation behaviour of RC structures have been investigated for several decades, they are still not fully understood, and hence, no general assessment strategy for affected structures exists today. Due to this lack of knowledge and driven by the intention to minimise the risk of a potential failure, structures are usually retrofitted or even replaced soon after corrosion is detected, which may considerably shorten their actual service life compared to the initially planned life span. Given the many kilometres of retaining walls in Switzerland and other countries being potentially affected by local corrosion, this leads to high economic costs and is all but sustainable, thus raising the need for assessment methods potentially prolonging the service life of structures after corrosion initiation. Moreover, alternative approaches are needed to detect the corrosion damage in retaining walls and monitor their behaviour, for whose development the understanding of the load-deformation behaviour is equally relevant.

This thesis focuses on the load-deformation behaviour of RC structures affected by local corrosion. Building on the knowledge of previous studies, it aims to identify and explore the key effects of local corrosion influencing the global structural behaviour and to develop consistent mechanical models for these effects. The focus for the design of the experimental campaigns is kept on retaining walls, whereas their findings and derived models should be applicable to other types of structural elements.

1.2 Overview of the state of the art and open research questions

The following section presents an overview of the recent findings in corrosion research and identifies open research questions. It focuses on the effects of corrosion on bare reinforcing bars, bond between corroded bars and concrete, and the behaviour of structural elements containing corroded reinforcement; other subdomains in corrosion research, such as the corrosion of prestressing tendons and the corrosion-related deterioration of the concrete compression zone as well as reinforcing bars in compression, are neglected. At the end of the section, additional research questions relevant to the structural modelling of corroded RC structures are formulated.

1.2.1 Load-deformation behaviour of corroded reinforcing bars

The effects of corrosion on the load-deformation behaviour of reinforcing bars have been investigated in numerous studies, many of them comprising tension tests on naturally corroded and artificially damaged reinforcing bars. In most studies, the reinforcing bars were cast in concrete and damaged artificially by electrochemically induced corrosion prior to testing [4, 10, 15, 34, 46, 53, 83, 85, 151], and only a few studies conducted experiments on mechanically damaged reinforcing bars [34, 46] and naturally corroded bars extracted from old existing structures and structural elements [62, 122]. The corrosion damage has mostly been characterised by the average cross-section loss determined from the bar mass loss [4, 10, 15, 46, 53, 83, 85], and only a few studies indicated the actual (maximum) cross-section loss [34, 62, 122]. One study [151] referred the measured data to the average and maximum cross-section loss, emphasising a significant difference in the obtained results.

All studies concluded that corrosion impairs the load-carrying and deformation capacity of reinforcing bars, outlining an approximately linear relationship between the cross-section loss and the reduction of load-carrying capacity, and a disproportionate decrease in deformation capacity with respect to the cross-section loss. The apparent material properties were mostly found to be unaltered, but some authors [34, 62, 84, 151] indicated a slight increase in tensile strength (i. e. peak load referred to the minimum cross-sectional area), and one study [62] pointed out an altered steel stress-strain behaviour including a loss of the yield plateau, yet without offering an explanation.

Few researchers investigated the potential influence of the pit geometry on the bar load-deformation behaviour theoretically [54, 80] or experimentally [8, 58, 166]. They varied the pit depth, pit length, pit

shape (e. g. unilateral, bilateral, axisymmetric), and the number of consecutive pits, reporting a significant influence on the load-carrying and deformation capacity despite the equal residual cross-sectional areas of some specimens. It was hypothesised that the effects could be related to the occurrence of a triaxial stress state and local bending moments at the pit. These studies concluded that referring the measured data to the average cross-section loss, e. g. by indicating the steel mass loss, is inadequate to characterise the corrosion damage. A few studies [86, 102] aimed at characterising the pit geometry with three-dimensional surface scans and extracting the effective cross-sectional area, second moment of inertia, and eccentricity of the section centroid to the original bar axis. They pointed out a rather weak correlation between the average cross-section loss (determined from the mass loss) and structural parameters such as the minimum cross-sectional area or the minimum second moment of inertia.

Since the early 1990s [137], a considerable amount of the reinforcement in many countries has been produced as hot-rolled, quenched and self-tempered (QST) reinforcing bars (so-called Tempcore® or Thermex® bars), exhibiting a varying microstructure over the cross-section (highly ductile core of moderate strength, high-strength outer annulus of moderate ductility). Such bars continuously alter their apparent (mean) material characteristics with increasing corrosion-induced cross-section loss due to the change in the relative portion of the respective microstructures to the entire cross-sectional area [11, 12, 55, 139].

In the context of local corrosion damage of bare reinforcing bars, the following research questions remain open:

(i) The damage pattern resulting from electrochemically induced corrosion is rather associated with (severe) uniform corrosion than local pitting corrosion: the reinforcing bars are damaged along their entire length, which hardly represents the single corrosion pits typically observed, e. g. in retaining walls. The quantification of the corrosion damage using the global mass loss is of limited significance for local corrosion since no conclusions can be drawn regarding relevant parameters, such as the residual minimum cross-sectional area. Thus, it is unclear whether the findings of these studies apply to corroding reinforcing bars where pitting is the predominant corrosion type.

(ii) The few studies investigating the influence of the pit geometry pointed out that the load-deformation behaviour of reinforcing bars with different pit shapes may vary considerably, despite equal residual cross-sectional area. Although acknowledged as highly relevant for pitting corrosion, the effects and their potential reasons have scarcely been investigated, and only two studies followed up on the problem theoretically using Finite Element analyses [54, 80].

(iii) The studies reporting an increasing tensile strength (observed for local and uniform corrosion) and describing a different yield behaviour of the reinforcing bars indicate an influence of the corrosion damage on the apparent mechanical properties of the bar. An altered stress-strain behaviour, including a loss of the yield plateau, can also be observed in the published data of other studies (e. g. [8, 34, 51, 58, 83, 166]) but was hardly ever discussed. The mechanical reason for the altered behaviour is unclear but most relevant for a realistic modelling of the strain localisation effect occurring for local corrosion.

(iv) The stresses observed in the plastic strain range from quasi-static tensile tests on reinforcing bars, including the apparent yield stress and tensile strength, depend on the applied (quasi-static) strain rate, as already shown decades ago, e. g. by [95, 98]. The strain rate may vary considerably over the length of a bar with a local cross-section loss due to the differing tensile stiffness. Regarding the observed increased tensile strength (see Point (iii)), the differences in strain rate should be considered. However, no experimental data of tensile tests on modern reinforcing bars applying quasi-static strain rates is available.

(v) Today, a large amount of the reinforcement is produced as QST bars, which are thus also widely used in experimental campaigns on corrosion. However, results from corrosion experiments conducted on such bars without accounting for the effects of the different microstructures are inconclusive. Although their behaviour has been investigated by some studies [11, 12, 55, 139], no simple mechanical model to account for the varying mechanical properties of the different microstructure layers is available.

1.2.2 Implications of corrosion on bond between reinforcement and concrete

The influence of uniform corrosion on bond has previously been investigated mainly with pullout tests on artificially corroded reinforcing bars [16, 104, 115, 149]; the results of the different test campaigns are comprehensively summarised in [56]. The studies reported a moderate bond strength increase for slight cross-section losses up to approximately 10% due to a volume expansion of the corrosion products and the corresponding increase of transverse pressure. However, the bond strength decreases to approximately half its initial value for a further increasing cross-section loss, mainly because of longitudinal cracking and eventual spalling of the concrete cover triggered by the further increasing volume expansion of the corrosion products. A lubricating effect of the corrosion product layer and the decreasing rib height due to the corrosion damage are secondary reasons for the bond strength decrease [24, 26]. Based on the published experimental results, modelling approaches to capture the influence of uniform corrosion on bond have been presented [24, 26, 37, 41].

Many of the tested pullout specimens were damaged by electrochemically-induced corrosion, often by applying very high electric currents leading to high corrosion rates. One study [109] claimed that the applied electric current influences the composition of the resulting corrosion products, which differ in volume expansion. This could lead, e. g. to a more severe concrete spalling behaviour in experiments (with high currents to accelerate corrosion) than observed for naturally corroded structural elements and thus influence the results of the pullout tests.

In the case of local corrosion, bond is much less deteriorated since either no significant corrosion products are formed (for chloride-induced corrosion, see Section 1.1.1) or no significant transverse pressure emerges (for atmospheric corrosion in the case of honeycombs with large voids; additionally, the products are likely to be washed out by water ingress). Hence, this thesis does not further analyse the implications of uniform corrosion on bond.

1.2.3 Load-deformation behaviour of corroded structural concrete members

The residual load-deformation behaviour of structural concrete members containing corroded reinforcement was investigated in numerous studies [5, 17, 35, 36, 103, 110, 131, 135, 150, 157]. Mainly flexural members were tested, which had been damaged by accelerated electrochemically induced corrosion prior to loading, accompanied by the typical longitudinal cracks along the reinforcing bars and partly by spalling of the concrete cover. Two studies [35, 150] tested beams in bending, whose reinforcement was damaged by natural chloride-induced corrosion. All studies reported a reduction in load-carrying and deformation capacity with increasing cross-section loss, similar to the findings for the bare reinforcing bars. One study [135] pointed out a change in failure mode, i. e. from flexural failure in the uncorroded reference specimen to shear failure in the corroded specimen, which was attributed to the corrosion damage of the shear reinforcement. The experiments conducted by Rebhan et al. [131] are of particular interest here since they tested artificially corroded cantilever retaining wall segments. The reinforcing bars were subjected to electrochemically induced corrosion over a short length (recess of 25 mm, approximately 20 cm above the construction joint), applying rather high currents, until a mass loss of 50% was reached. The specimens were subsequently loaded with an out-of-plane shear force at the top.

In most cases, the cross-section loss was estimated by calculating the average mass loss from the applied electric current using Faraday's law and assuming a spatially uniformly distributed cross-section loss. One study [103] underlined that the average mass loss might be inadequate for characterising the corrosion damage and estimating the specimen's load-carrying capacity since the latter is attributed to the minimum residual bar cross-sectional area and its location in the beam. To estimate the cross-section loss among the bar length, the specimens investigated in that study were x-rayed in various positions, and the cross-section loss was determined from the pictures.

In the context of localised corrosion damage on RC structural elements, the following research questions remain open:

(vi) Corrosion was induced electrochemically in most experiments in RC members, leading to a cross-section loss over an extensive length of the bars, longitudinal cracking, and sometimes spalling of the concrete cover. This deterioration is rather associated with uniform corrosion than pitting corrosion, where the cross-section loss occurs pointwise and often without cracking of concrete and bond deterioration (see Section 1.1.1). As for the corroded bare reinforcing bars, the residual minimum cross-sectional areas in the bars and their locations cannot be determined from the global mass loss. It is thus unlikely that the findings obtained in these studies apply to RC members affected by pitting corrosion, where the cross-section loss is spatially limited.

(vii) In the analysed experiments, all bars were affected by corrosion due to the applied deterioration method. This damage pattern is rather unusual for local corrosion, where often only a part of the parallel reinforcing bars is affected by corrosion. Consequently, little is known about the behaviour of members containing parallel reinforcing bars with varying individual corrosion damage.

(viii) It is uncertain if the load-deformation curves obtained in experiments on specimens with constant corrosion damage and monotonically increasing load apply to structures with a constant or decreasing load (e. g. the earth pressure loading on retaining walls) and increasing corrosion damage. Load-path-dependent effects occurring in reinforced concrete may influence the behaviour since either the corroding bars or the entire structure is unloaded.

1.2.4 Further effects influencing corroded RC structures and their modelling

It is challenging to include the findings on the load-deformation behaviour of locally corroded bare reinforcing bars in structural models describing the behaviour of RC members since local phenomena need to be accurately captured on a superordinate structural level. Including the effects of local corrosion in approaches of continuum mechanics (e. g. Finite Element (FE) models) is not straightforward due to the localised nature of the problem, which raises questions regarding the adequate size of a representative volume element (RVE). If the RVE size is chosen very small (e. g. if individual reinforcing bars – with and without corroded sections – are modelled inside a concrete matrix), the computational costs to model the behaviour of an entire structure are excessive. On the other hand, if the RVE is chosen in an adequate size to model an entire structure, the locally different behaviour in the corroded section, especially the strain localisation effect, has to be captured in the element formulation. Hence, the following research question on how to include local effects in continuum mechanical models remains open:

(ix) Today, no model exists at the interface between the different structural levels (superordinate structural level and local reinforcement corrosion). However, such models would have a great potential for analysing the influence of local corrosion on the load-deformation behaviour of structures and structural elements at reasonable computational costs and without neglecting the governing effects.

In retaining walls, a lap splice is typically located above the construction joint enabling an efficient construction process. The double amount of reinforcement stiffens the lowest part of the wall and thus limits its deformation capacity [118, 154, 155]. Furthermore, experimental results indicate that the discontinuous deformation distribution over the splice length favours larger cracks at the lap splice ends [3, 154, 155]. From the literature review, the following research question emerges:

(x) While the load-carrying capacity of lap splices is well examined, their load-deformation behaviour has been investigated very scarcely, and very few – mainly empirical – approaches exist to model the behaviour [155]. In retaining walls, where the lap splice is located in the highest loaded region potentially undergoing plastic deformations, its influence on the load-deformation behaviour of the structure needs to be carefully assessed.

1.3 Research objectives and delimitations

As mentioned in Section 1.1.4, this thesis aims at a better understanding of the load-deformation behaviour of structures affected by local corrosion, exploring the underlying mechanical phenomena, and finding potential modelling approaches with regard to their future application in the assessment of locally corroded retaining walls. Based on the research question (RQ) elaborated in Section 1.2, the following main research objectives are formulated:

- Investigation of the phenomena occurring for bare reinforcing bars containing local corrosion damage and their influences on the bar load-deformation behaviour (RQ (i)). A special focus is put on the effects of the varying strain rate (RQ (iv)), the different microstructure layers for QST bars (RQ (v)), the pit geometry (RQ (ii)), and reasons for a potentially altered yield behaviour (RQ (iii)).
- Development of a mechanical model based on the established Tension Chord Model to describe the load-deformation behaviour of structural elements affected by local reinforcement corrosion (RQ (ix)).
- Development of mechanical models suitable to describe the load-deformation behaviour of subelements located in retaining walls, such as lap splices (RQ (x)).
- Validation of the aforementioned models with large-scale experiments on cantilever retaining wall segments containing locally damaged reinforcement under varying loading conditions (RQ (vi)), especially focussing on the influence of a varying corrosion distribution among the reinforcing bars (RQ (vii)) and the influence of a decreasing load at increasing corrosion damage (RQ (viii)).

The following delimitations are made regarding related research questions and research fields:

- The thesis focuses on local pitting corrosion of reinforcing bars. Uniform corrosion is not analysed.
- Corrosion-related effects reducing the bond stresses are not investigated.
- The investigation is limited to structural elements carrying tensile and moment loads, and the corrosion of the respective tensile and flexural reinforcement. Effects related to corrosion of the shear reinforcement are excluded.
- Corrosion initiation mechanisms and corrosion propagation over time are not analysed.
- Corrosion detection methods and suitable strategies to monitor corroding structures are not treated in detail.
- As an application case, the bending behaviour of cantilever retaining walls is analysed, without considering other types of retaining walls, such as gravity walls and anchored retaining walls. The shear resistance of the cantilever retaining walls is assumed to be sufficient.
- The thesis assumes the simplest possible load-carrying mechanism for cantilever retaining walls. Potential global load redistributions in the longitudinal (horizontal) direction are not analysed since most retaining walls are segmented over short distances.
- The soil-structure interaction is merely investigated from the structure's point of view. Modelling approaches regarding the behaviour of the earth pressure are adopted from [125].

Figure 1.1 shows a schematic load-deformation curve of a retaining wall segment at increasing (mean) cross-section loss ζ_m (bending moment at construction joint vs mean wall rotation, grey) along with potential earth pressure load paths to illustrate their interaction. It is assumed – inspired by the results of this study as well as previous experimental investigations – that the deformation capacity decreases disproportionally with an increasing cross-section loss. On the right side, potential influences on the load-carrying and deformation capacity discussed in Section 1.2 are illustrated, and arrows indicate how these effects are linked. Some effects influence the structural behaviour in multiple ways, which is represented by additional grey dotted arrows. The illustration does not claim to be complete but rather aims to visualise the possible influences discussed in the thesis and serve as a map providing guidance to

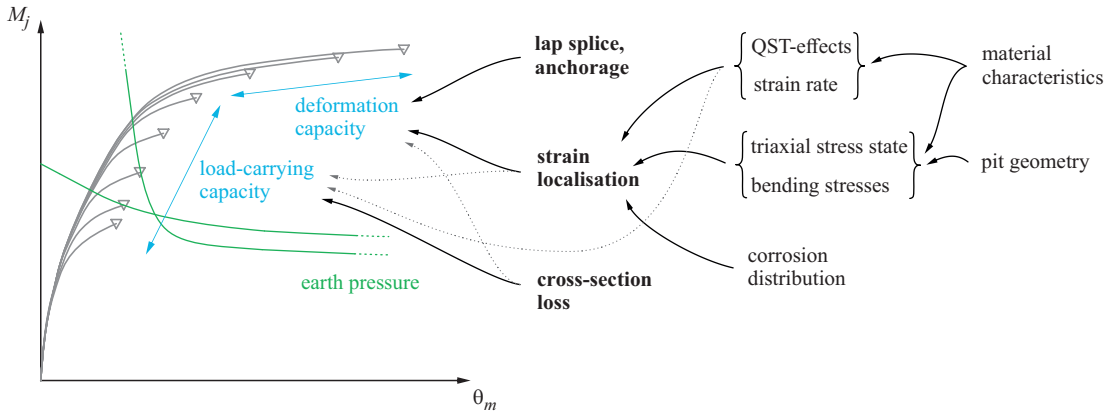

Fig. 1.1 – Schematic load-deformation behaviour of cantilever retaining wall segment for increasing cross-section loss (grey) along with earth pressure load paths and potential effects influencing the behaviour.

the reader: it is included at the beginning of each chapter in a slightly adapted version, highlighting the key aspects covered in the respective chapter.

1.4 Structure of thesis

Chapter 2 presents an enhancement of the established Tension Chord Model (TCM) to capture the effects of a corrosion pit close to a crack on the load-deformation behaviour of a crack element. It forms the basis to include the effects of local corrosion in higher-level structural models (RQ (ix)).

Chapter 3 analyses the effects of strain rate on the apparent mechanical properties of reinforcing bars. It addresses the question of whether the varying strain rates in the corroded and uncorroded bar sections occurring in experiments need to be considered (RQ (iv)).

Chapter 4 investigates the mechanical properties of the different microstructure layers over the cross-section of a QST reinforcing bar and how they contribute to the composite bar. It presents a simple modelling approach to estimate the residual mechanical properties for unilateral and axisymmetric cross-section loss (RQ (v)).

Chapter 5 explores the occurrence of a triaxial stress state for different geometries of axisymmetric corrosion pits. It addresses the altered yield behaviour of the bar at the pit and in its vicinity, studies the influence regarding the peak load, and proposes a simplified modelling approach based on an in-depth FE analysis (RQ (i)-(iii)).

Chapter 6 presents the results of large-scale experiments on cantilever retaining wall segments investigating the influence of local corrosion on the load-deformation behaviour. It comprises the findings of hybrid tests, where the corrosion damage was increased during the tests and the load was adapted depending on the wall deflections to simulate a decreasing earth pressure (RQ (vi)-(viii)).

Chapter 7 applies the concept of the TCM to lap splices to examine their load-deformation behaviour. It provides new insights into the load transfer between two reinforcing bars and its implications on the deformation capacity (RQ (x)).

Chapter 8 combines the developed modelling approaches for localised corrosion with existing models based on the TCM to analyse the results obtained in the experimental campaign presented in Chapter 6. It explores the load-carrying mechanisms of the specimens exhibiting different corrosion damage and examines the influence of local phenomena on the global structural behaviour (RQ (i)-(iii), (vi)-(x)).

Finally, **Chapter 9** summarises the main findings, draws final conclusions, and gives an outlook on future research.

Note that Chapters 2-7 correspond to scientific publications, as indicated at the beginning of each chapter along with the information on the contributions of the authors.

2 Corroded Tension Chord Model: Load-deformation behaviour of structures with locally corroded reinforcement

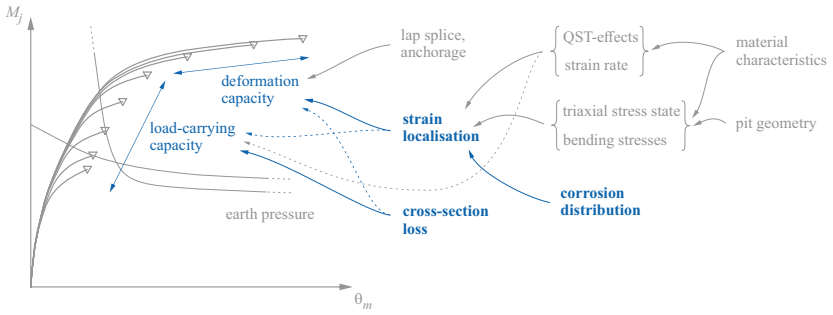

This chapter presents an enhancement of the established Tension Chord Model (TCM) to account for a local cross-section loss of the reinforcing bar near the crack. The emerging Corroded Tension Chord Model (CTCM) forms the starting point to analyse the load-deformation behaviour of locally corroded reinforced concrete members and reveals the basic effects of cross-section loss and strain localisation, with the latter depending on the varying distribution of the corrosion damage among the reinforcing bars. The chapter corresponds to the published version of the following article:

> Haefliger, S. & Kaufmann, W. 'Corroded Tension Chord Model: Load-deformation behaviour of structures with locally corroded reinforcement,' *fib Structural Concrete*, vol. 23, no. 1, pp. 104-120, 2022. doi: 10.1002/suco.202100165.

The lead author (Severin Haefliger) built up on the idea and first calculations of the second author (Walter Kaufmann) of modelling the load-deformation behaviour of locally corroding tension chords with an enhancement of the TCM, refined the model in the course of his doctoral studies, and conducted the presented numerical analyses under the supervision of the second author.

Abstract

Localised corrosion may considerably impair the load-bearing and deformation capacity of reinforced concrete structures. The Corroded Tension Chord Model CTCM allows investigating the related effects. The model combines the effects of tension stiffening and strain localisation due to a local cross-section loss to calculate the load-deformation behaviour of tension members and entire structural elements containing locally corroded reinforcing bars on a sound mechanical basis. Based on simple equilibrium considerations, the critical loss of cross-sectional area is introduced, beyond which most of a reinforcing bar's ductility or a structure's deformation capacity, respectively, is lost. For conventional European reinforcing steel, even small cross-section losses may be sufficient to impair ductility drastically. Illustrative calculations on structural elements with various spatial corrosion distributions but identical mean cross-section loss reveal that the load-deformation behaviour strongly depends on the specific corrosion parameters: Structures with few heavily corroded reinforcing bars seem to be less critical regarding strength and deformation capacity than structures with many slightly corroded reinforcing bars.

2.1 Introduction

Local and/or uniform corrosion due to, e. g. chloride ingress or carbonation affects many ageing reinforced concrete structures. Both deterioration mechanisms considerably reduce the load-carrying capacity of structures due to cross-section loss of reinforcement, bond degradation and concrete spalling. Corrosion reduces the cross-sectional area of affected reinforcing bars, whereby the cross-section is lost much faster for pitting than for uniform corrosion due to the formation of macro elements [25]. Various studies have shown that the pit morphology can have a significant influence and, in particular, affect the tensile strength disproportionately to the cross-section loss, i. e. reduce the ultimate stress due to a triaxial stress state and local bending moments in the vicinity of the pit [8, 58, 80, 166]. Uniform corrosion due to, e. g. carbonation causes corrosion products with a larger volume than the original reinforcing bar. This volumetric expansion can lead to excessive cracking and spalling of the surrounding concrete, which may reduce the concrete compression zone and strongly degrade bond, leading to the loss of reinforcement anchorage.

Local pitting corrosion affects the load-carrying capacity of a structure and strongly reduces its deformation capacity, as was experimentally verified by several studies [8, 34, 39, 46]. This effect is mainly caused by strain localisation due to cross-section loss. It is particularly relevant for statically indeterminate structures requiring moment redistributions (e. g. multi-span continuous girders) or in the case of deformation dependent loading (e. g. earth pressure action on cantilever retaining walls). The assumption of a sufficient deformation capacity, which is a prerequisite to applying models based on the lower bound theorem of plasticity theory, is therefore no longer valid, and the residual deformation capacity of such structures needs to be specifically assessed. However, to the authors' knowledge, sound mechanical models to determine the load-deformation behaviour of structures affected by localised corrosion are currently missing.

The present study addresses this knowledge gap by extending the established Tension Chord Model TCM [114], briefly outlined in Section 2.3.1, by considering a crack element containing a reinforcing bar with reduced cross-section, simulating corrosion-induced damage. The resulting Corroded Tension Chord Model (CTCM), Section 2.3.2, enables calculating the load-deformation behaviour of single crack elements with locally corroded reinforcement. By assembling several crack elements – with or without damaged reinforcement – and applying common mechanical concepts, the CTCM allows to predict the elastic and plastic load-deformation behaviour of entire structural elements. Thereby, the model provides a sound mechanical basis to explain several relevant phenomena occurring in locally corroded structural elements, such as, e. g. the substantial decrease in deformation capacity observed in experiments [103]. In contrast to other models as, e. g. finite element analyses, it is based on only a few analytical equations, and can thus easily be extended and combined with various other modelling approaches.

The basic concepts and first results of the CTCM were published in [77]. The present paper examines the effects of localised corrosion on different structural levels and extends the concept of the CTCM to a wider range of problems. Subsequently, the load-deformation behaviour of single and multiple crack elements, assembled to structural elements, is analysed for several illustrative examples. A validation of the proposed model against experimental data, including [77] will be presented in a future paper, currently in preparation.

2.2 Effects of localised corrosion on different structural levels

2.2.1 Single reinforcing bar (microscopic level)

Localised corrosion alters a reinforcing bar's load-deformation behaviour by several mechanisms. These are (i) generally higher stresses in the corroded cross-section to resist equal tensile forces as the non-corroded part, (ii) a varying strain rate due to the different stiffnesses of the corroded and non-corroded

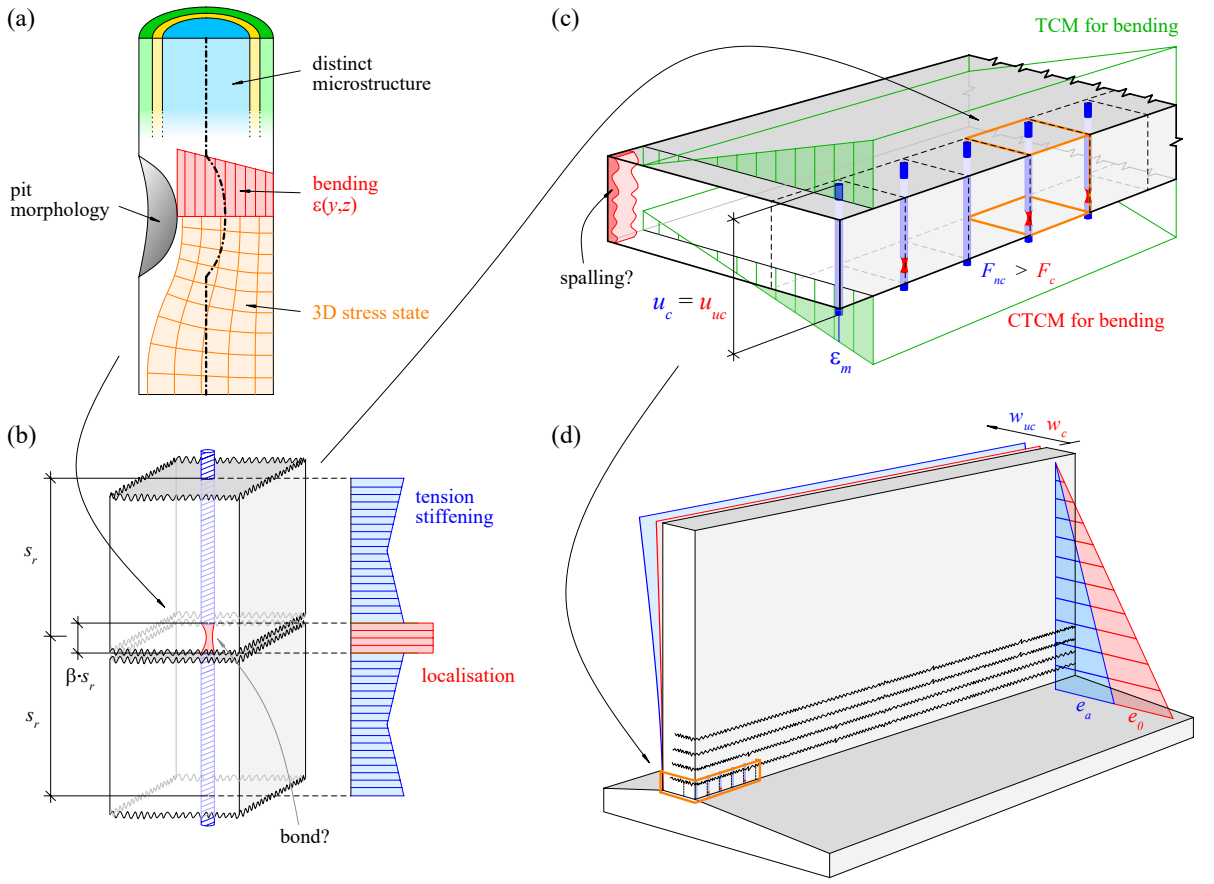

Fig. 2.1 – Effects of localised corrosion on different structural levels: (a) phenomena influencing a reinforcing bar's stress-strain behaviour in case of localised (pitting) corrosion (microscopic level); (b) single crack element with corroding reinforcing bar surrounded by concrete, with indicated tension stiffening effect (mesoscopic level), considering bond degradation and strain localisation due to cross-section loss; (c) part of a structural element in bending delimited by two cracks (mesoscopic level), consisting of a parallel assembly of crack elements and concrete in compression, indicating influences of corrosion on compression and tension side (spalling and redistribution of tension forces); (d) structure in bending (macroscopic level), e. g. cantilever retaining wall, with part analysed in (c), indicated load distribution (active earth pressure, and earth pressure at rest) and maximum deflection with (w_c) and without (w_{uc}) the influence of pitting corrosion.

parts, (iii) a distinct microstructure over cross-section for quenched and self-tempered (QST) reinforcing bars, and (iv) a triaxial stress state and (v) local bending moment near the pit, as illustrated in Figure 2.1(a).

The influence of strain rate, leading to higher exhibited stresses in steel in the plastic range when being increased, has been known for a long time. It is well investigated for various strain rates [30, 31, 95, 98], and has recently been revisited and confirmed for quasi-static strain rates of modern reinforcing bars [69]. In the context of experiments on locally corroded reinforcing bars, this effect should be considered since the various tensile stiffnesses in the corroded and non-corroded part of a bar lead to significantly different strains rates.

QST reinforcing bars, also known as "Tempcore®" reinforcing bars, exhibit distinct microstructure layers with different stress-strain characteristics over the cross-section (Figure 2.1(a)). In particular, they consist of a ductile, lower strength core (ferritic/perlitic), surrounded by a transition zone (bainitic) and a less ductile, higher strength outer annulus (martensitic). This results in a reinforcing bar combining the favourable material characteristics but can lead to a considerable strength reduction in case of uniform corrosion, as was shown by [55, 71, 80]. However, [71] pointed out that the change in stress-strain characteristics is less pronounced for pitting corrosion compared to uniform corrosion.

The load-deformation behaviour of a reinforcing bar containing a corrosion pit is significantly influenced by the pit morphology [8, 39, 80, 166]. The stress trajectories are deviated due to the local cross-section reduction, leading to a triaxial stress state in the pit region (Figure 2.1(a)). In the case of unilateral corrosion damage, local bending moments due to a shift of the neutral axis potentially lead to a lower failure load than expected when applying the nominal tensile strength to the reduced cross-sectional area. These phenomena were encountered in many experimental campaigns [8, 39, 58, 166] and, to date, primarily investigated with a Finite Element Model by [80]. Besides these publications and despite the high relevance of these effects, they have only been scarcely treated in literature. Therefore, the authors are currently extending the CTCM to account for these effects. However, this is work in progress and beyond the scope of this paper.

2.2.2 Strain localisation due to cross-section loss (mesoscopic level)

When experimentally investigating reinforcing bars with single or multiple corrosion pits, a severe reduction of the elongation at ultimate load is often observed in experiments [34, 39, 46]. In some studies on corrosion, this effect is related to corrosion-induced changes in material characteristics [10, 53, 55]. However, in the authors' understanding, it is at most a secondary effect. Indeed, the reduced ductility can perfectly be explained considering strain localisation due to cross-section loss, as also pointed out by [39]. The related effects on the load-deformation behaviour, briefly outlined below, are not limited to corrosion-induced damage but very well known, e. g. in metallurgy or from statically indeterminate structures containing elements of distinct stiffnesses.

Consider a reinforcing bar consisting of an undamaged (uncorroded) part UC and a damaged (corroded) part C, with length l_{uc} and l_c, respectively, loaded by a tensile force F (Figure 2.2). Material properties are uniform (yield stress f_{sy}, tensile strength f_{su}), but the initial cross-sectional area A_s is reduced in part C to

$$\begin{aligned} A_{s,c} &= (1-\zeta)A_s \\ 0 < \zeta &= A_{lost}/A_s \leq 1 \end{aligned} \tag{2.1}$$

over the short length $l_c \ll l_{uc}$, where ζ denotes the relative loss of cross-sectional area. The total elongation of the bar corresponds to the sum of elongations of its undamaged and damaged parts, as indicated in Figure 2.2

$$u_{tot} = u_{s,uc} + u_{s,c} = \varepsilon_{s,uc} \cdot l_{uc} + \varepsilon_{s,c} \cdot l_c \tag{2.2}$$

The stresses in the two parts of the bar differ by a factor $(1-\zeta)$ since by equilibrium

$$\begin{aligned} F &= A_s\sigma_{s,uc} = A_{s,c}\sigma_{s,c} = (1-\zeta)A_s\sigma_{s,uc} \\ \sigma_{s,c}(\zeta) &= \frac{\sigma_{s,uc}}{(1-\zeta)} \end{aligned} \tag{2.3}$$

Under a given load F, reducing the cross-section increases the total elongation slightly due to the resulting higher stresses and strains in the damaged part C. On the other hand, the ultimate load of the bar and the stresses at ultimate in the undamaged part UC are reduced according to Equation (2.3) to

$$\begin{aligned} F_u &= A_{s,c}f_{su} = (1-\zeta)A_s f_{su} \\ \sigma_{s,uc,max} &= (1-\zeta)f_{su} \end{aligned} \tag{2.4}$$

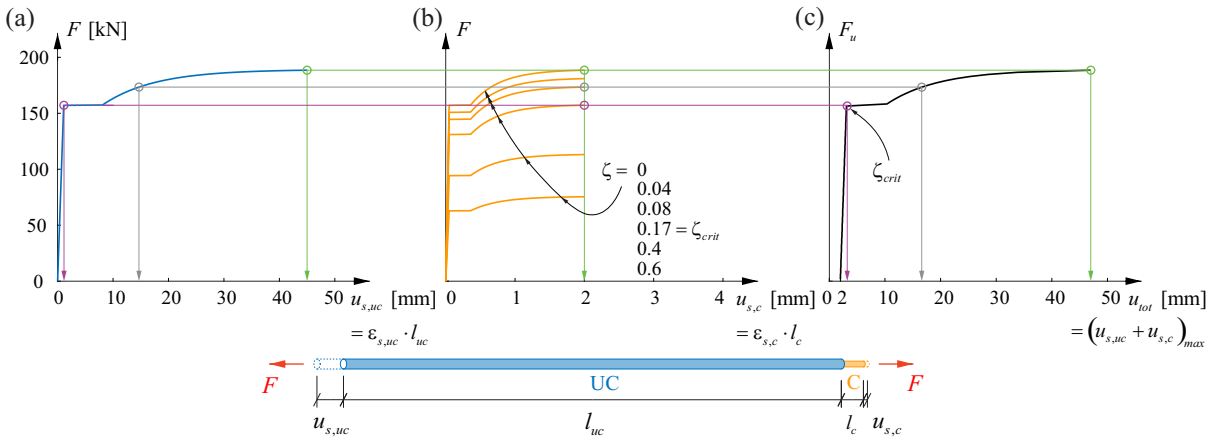

Fig. 2.2 – Example to illustrate the strain localisation effect: (a) load-deformation behaviour of reinforcing bar part UC with length l_{uc} and constant cross-section; (b) load-deformation behaviour of a reinforcing bar part C with length $l_c \ll l_{uc}$ and continuously reduced cross-section; (c) resulting load-bearing capacity F_u vs. deformation capacity u_{tot} of entire bar (serially combining parts UC and C) with length $l_{uc} + l_c = 470\,\text{mm}$, $l_c/l_{uc} = 0.044$, and $f_{sy}/f_{su} = 0.83$.

Consequently, the total elongation of the bar at ultimate is reduced (see Figure 2.2(c)), as

$$\varepsilon_{s,uc,max} = \varepsilon_s\left(\sigma_{s,uc,max}\right) = \varepsilon_s\left((1-\zeta)\, f_{su}\right) < \varepsilon_s\left(f_{su}\right) \tag{2.5}$$

Since $l_c \ll l_{uc}$, the total elongation at ultimate decreases disproportionately with ζ, and is drastically reduced if the bar in the undamaged part UC remains elastic over the length l_{uc}.

Two parameters govern the behaviour of the total reinforcing bar: the cross-section loss ζ and the length ratio l_c/l_{uc}. For steel, the critical cross-section loss ζ_{crit}, as defined in Figure 2.2(c), beyond which the damaged part C ruptures before the undamaged part UC reaches the yield stress, can be found by simply formulating equilibrium (as recently also pointed out by [39])

$$\begin{aligned} A_s f_{sy} &\stackrel{!}{=} (1-\zeta_{crit})\, A_s f_{su} \\ \zeta_{crit} &= 1 - \frac{f_{sy}}{f_{su}} \end{aligned} \tag{2.6}$$

For a cross-section loss smaller than ζ_{crit}, the undamaged part of the reinforcing bar experiences large inelastic strains, whereas for a higher cross-section loss, the remaining tensile strength of the damaged section C is not sufficient to yield the undamaged part. Hence, plastic strains localise in the damaged part C, and since $l_c \ll l_{uc}$, the total elongation at ultimate, essentially corresponding to the plastic deformation capacity, is drastically reduced. As seen from Equation (2.6), ζ_{crit} solely depends on the material characteristics, particularly on the yield stress f_{sy} and tensile strength f_{su}. For the characteristics of modern European reinforcing steel with $f_{sy} \approx 500\,\text{MPa}$ and $f_{su} \approx 590...650\,\text{MPa}$, critical cross-section losses of merely $\zeta_{crit} \approx 0.12...0.2$ result. If the reinforcing steel strictly satisfies the minimum strain hardening ratios required for code compliance according to EN 1992-1-1:2004 [38], values as low as $\zeta_{crit} = 0.05, 0.08$ and 0.15 result for the ductility classes A, B and C, respectively. The residual deformation capacity, i. e. the inelastic elongation of the entire bar at rupture, depends on the ratio l_c/l_{uc}: the shorter the damaged length l_c compared to l_{uc}, the stronger the maximum elongation is reduced, with zero residual deformation capacity for $\zeta > \zeta_{crit}$ in the limiting case $l_c/l_{uc} \to 0$. For typical pit sizes and crack element lengths s_r (= crack spacing, see Figure 2.1(b)), this ratio is in the range of $l_c/l_{uc} \approx 0.01...0.1$, see Section 2.3.2.

Figure 2.3 illustrates the loss of deformation capacity due to strain localisation as the ratio of maximum elongations with and without cross-section loss ζ, respectively, for a hot-rolled (HR) and cold-worked (CW) reinforcing bar. The length ratios were chosen at the boundaries of the estimated range

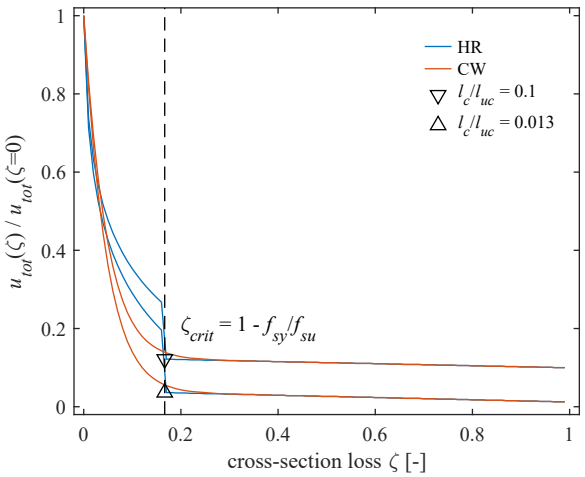

Fig. 2.3 – Loss of deformation capacity shown as ratio of maximum elongation u_{tot} with cross-section loss ζ to maximum elongation without cross-section loss for a hot-rolled (HR) and cold-worked (CW) reinforcing bar with constitutive relationships according to Equations (2.15) and (2.16) and material characteristics given in Table 2.1. The upper curve corresponds to a length ratio $l_c/l_{uc} = 30/300 = 0.1$, the lower curve to $l_c/l_{uc} = 10/800 = 0.013$.

(see Section 2.3.2) as $l_c/l_{uc} = 10/800 = 0.013$ and $l_c/l_{uc} = 30/300 = 0.1$. While this example is merely used to illustrate the general effect of strain localisation, the constitutive relationships and material properties were chosen to correspond to those used in the examples illustrating the CTCM (Sections 2.3.1 and 2.3.2) for comparison. It can be seen that most of the deformation capacity (88% and 96% for the HR and CW steel, respectively) is lost even before reaching the critical cross-section loss ζ_{crit}. For higher cross-section losses $\zeta > \zeta_{crit}$, there is no further notable decrease of the residual deformation capacity, whose value beyond $\zeta = \zeta_{crit}$ mainly depends on the length ratio l_c/l_{uc}. The constitutive relationship (favourable effect of the yield plateau of HR steel) has a visible effect only for $\zeta < \zeta_{crit}$.

2.2.3 Single crack element (mesoscopic level)

The effect of strain localisation has to be superimposed to the other effects mentioned in Section 2.2.1, which influence the stress-strain diagram of the damaged part; this may potentially lead to an even more critical behaviour. Additionally, as indicated in Figure 2.1(b), the deformation behaviour of a reinforcing bar embedded in concrete is influenced by bond, leading to the tension stiffening effect. Steel stresses, and hence strains, are reduced due to the contribution of the concrete over the length s_r of a crack element, i. e. the section between two cracks. This effect, which further reduces the deformation capacity, can be described by the established Tension Chord Model (TCM), outlined in Section 2.3.1. The extended version of this model, the Corroded Tension Chord Model (CTCM), Section 2.3.2, combines the effect of tension stiffening and strain localisation due to cross-section loss. Additionally, bond degradation near the pit caused by e. g. cracking due to a volumetric expansion of the corrosion products is considered.

2.2.4 Assembly of crack elements and combination with compression chord (mesoscopic level)

In real structures, single reinforcing bars are hardly ever provided. Instead, several reinforcing bars carry the applied load jointly. In many cases, these reinforcing bars are closely spaced, and the structural elements have a high in-plane stiffness, such that identical elongations and equal crack spacings may be assumed for reinforcing bars running in parallel ($u_c = u_{uc}$, compare Figure 2.1(c)). This central assumption, commonly applied in structural concrete modelling, leads to a redistribution of forces from damaged, softer elements to undamaged, stiffer elements in the CTCM.

The theory of the classic TCM was enhanced for modelling the load-deformation behaviour of elements in bending [93, 111]. A similar approach can be used to apply the CTCM to such elements, taking into account further aspects of corrosion (Figure 2.1(c)). In addition to the redistribution of forces from the corroded to the non-corroded elements by assuming equal elongations, the model allows considering concrete spalling at the compression side, caused, e. g. by a volumetric expansion of the corrosion products (if the compression reinforcement is corroding). Even though spalling is less likely for pitting corrosion, it may reduce the compression zone depth and consequently the lever arm of internal forces.

2.2.5 Entire structure (macroscopic level)

Based on the CTCM and using the principles of 2.2.4, the load-deformation behaviour of entire structural elements such as cantilever retaining walls or cantilevering bridge decks [162] can be modelled, and the implications of local corrosion and its spatial distribution over the element can be analysed (Figure 2.1(d)). First calculations showed that effects on microscopic and mesoscopic levels, described in the previous sections, affect the behaviour on the structural level (macroscopic level) quite severely. Due to strain localisation, localised corrosion strongly reduces the deformation capacity of structures, as further outlined in Sections 2.4.1 and 2.4.2.

This issue is a major problem for structures whose main loading is deformation dependent, such as the earth pressure acting on retaining walls. Many of these were designed in the ultimate limit state of structural safety for active earth pressure loading only, as e. g. typical walls built in Switzerland in the 1960s and 1970s, but also more recent ones. This presumes that the structure exhibits sufficient ductility to undergo the deformations required to cause the earth pressure to diminish from pressure at rest e_0 to active pressure e_a (Figure 2.1(d)). If this ductility is compromised by localised corrosion, as detected in many retaining walls near the construction joint between footing and wall due to honeycombs [52], the earth pressure does not drop (unless the entire wall overturns as a rigid body at a lower load, which is unlikely due to higher safety margins in geotechnical design). In addition, the load-bearing capacity is reduced due to corrosion. Combining the two effects, there is a major risk of a brittle failure of the structure. Given the large number of possibly affected structures [52], there is an urgent need for models such as the CTCM, allowing to assess the load-deformation behaviour of structures affected by localised corrosion.

2.3 TCM and CTCM model description

2.3.1 Existing Tension Chord Model TCM

The Tension Chord Model [7, 114] was developed in the 1990s at ETH Zurich. It models the tension stiffening effect, i. e. the effect of bond on structural elements loaded in tension, in a mechanically consistent manner, using only the magnitudes of the bond shear stresses as empirical parameters. The bond shear stress-slip behaviour τ_b-δ is assumed to be rigid-perfectly plastic, with a value τ_{b0} for regions where the reinforcing bar remains elastic and τ_{b1} for regions where the reinforcing bar yields

$$\begin{aligned} \tau_{b0}(\delta(x)) &= \tau_{b0} = 2f_{ct} \\ \tau_{b1}(\delta(x)) &= \tau_{b1} = f_{ct} \end{aligned} \tag{2.7}$$

with f_{ct} = concrete tensile strength. Different to the bond-stress slip relationships shown in Figure 2.4(a), which are generally obtained from conventional pullout tests, nominal bond-stresses τ_b are thus independent of the slip δ, but rather a function of the steel stress σ_s, i. e. $\tau_b(\sigma_s)$. This assumption is related to the work of [143] and enables to decouple the kinematic relations of a differential element of a reinfor-

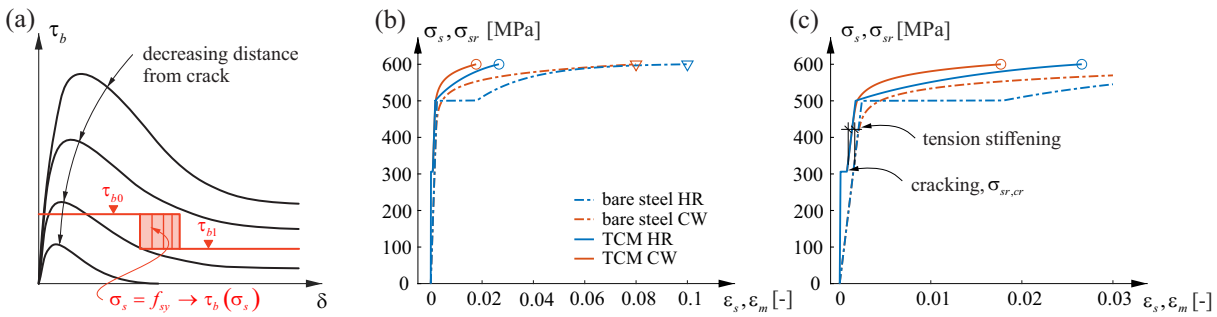

Fig. 2.4 – Constitutive relationships and TCM model response: (a) generic bond stress – slip relationship adapted from conventional pull-out tests (black) and definition of constitutive model used in TCM (red); (b) constitutive stress-strain relationships for hot-rolled and cold-worked steel according to Equations (2.15) and (2.16) and stress-strain diagram of corresponding tension members with properties according to Table 2.1; (c) zoom of stress-strain diagram in (b) at small strains (horizontal shift of the two curves indicates the tension stiffening effect).

cing bar embedded in concrete

$$\frac{d\delta(x)}{dx} = \varepsilon_s(x) - \varepsilon_c(x) \tag{2.8}$$

from the equilibrium conditions of the same element

$$\frac{d\sigma_s(x)}{dx} = \frac{4\tau_b(\delta(x))}{\varnothing} \stackrel{!}{=} \frac{4\tau_b}{\varnothing} \tag{2.9}$$

with $\varepsilon_s(x)$, $\varepsilon_c(x)$ = steel and concrete strains along the reinforcing bar, $\sigma_s(x)$, $\tau_b(x)$ = steel stress and bond shear stress along the reinforcing bar, δ = slip between reinforcing bar and concrete, $\varnothing$ = reinforcing bar diameter. Hence, the differential equation of bond can be solved in closed form for linear elastic behaviour [114]

$$\frac{d^2\delta(x)}{dx^2} = \frac{4\tau_{b0}(1+\rho(n-1))}{E_s\varnothing(1-\rho)} \tag{2.10}$$

with $n = E_s/E_c$ = modular ratio, $\rho = A_s/A_c$ = geometrical reinforcement ratio. Similarly, determining the load-deformation behaviour of tension chords with general stress-strain relationships for the bare reinforcement is greatly simplified, as outlined in the following.

Generally, steel stresses in a reinforcing bar along a crack element, i. e. a tension chord element bounded by two cracks (see Figure 2.5(a)), are obtained by integration of Equation (2.9). Using the TCM, this integration is straightforward since the bond shear stresses are fully determined by the steel stress at a specific location (known by equilibrium) rather than the bond slip (which is unknown a priori, requiring solving the differential equation of bond). Steel stresses are thus defined by

$$\sigma_s(x) = \sigma_{sr} - \frac{4}{\varnothing^2\pi}\tau_b\pi\varnothing x = \frac{F}{A_s} - \frac{4\tau_b x}{\varnothing} \tag{2.11}$$

with $\sigma_{sr} = F/A_s$ = steel stress at the crack, where the reinforcement alone carries the applied tensile force, and F = externally applied force on the tension member. Figure 2.5(a) shows the gradual decrease of the steel stresses from the crack to the middle of the crack element caused by bond shear stresses. Steel strains follow from the steel stresses using an appropriate constitutive relationship $\varepsilon_s = f(\sigma_s)$ (Figure 2.4(b)). Integrating the steel strains over the length of the crack element yields the deformation of

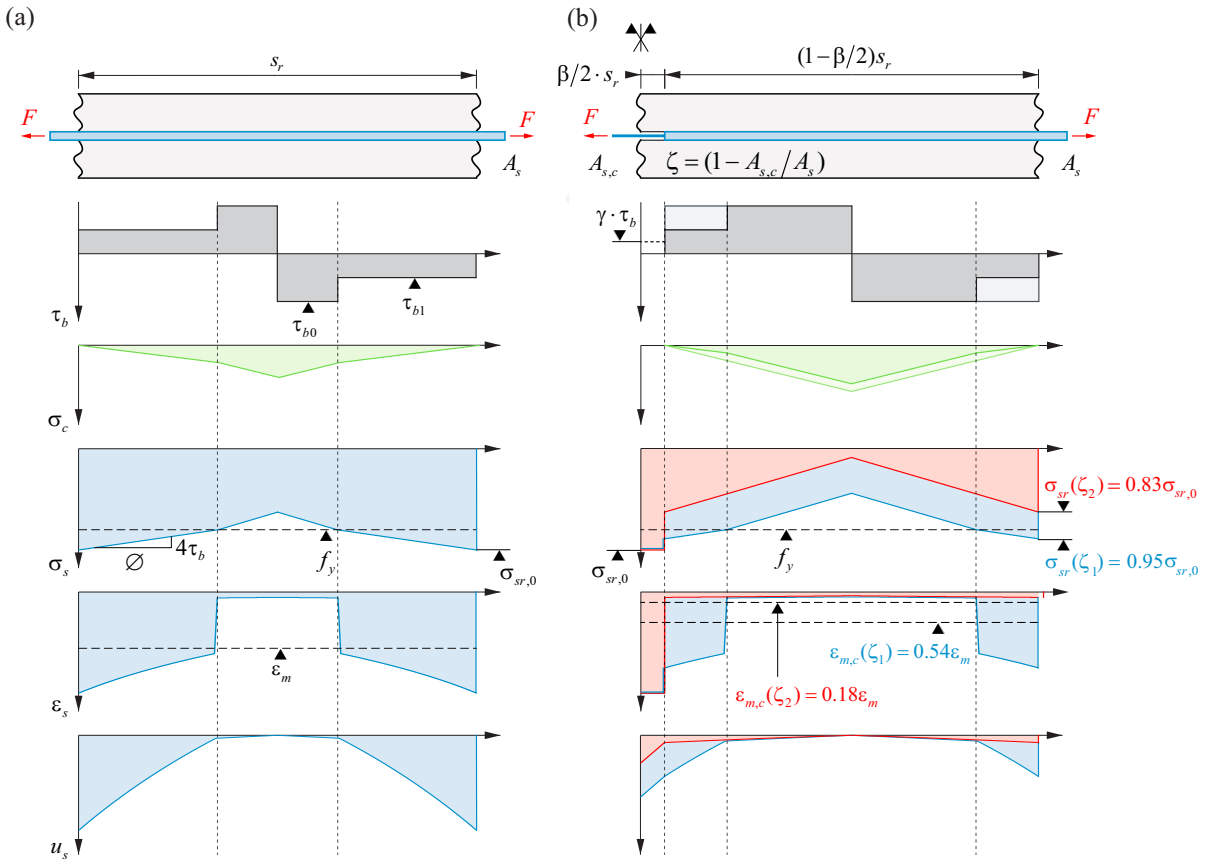

Fig. 2.5 – Modelling concepts of (a) TCM and (b) CTCM illustrated for a crack element of length s_r and a stress at the crack $\sigma_{sr} = 550\,\text{MPa}$. Shown are the distributions of bond stress τ_b, stress in concrete σ_c, steel stress σ_s, steel strain ε_s, and steel deformations u_s. ε_m denotes the mean steel strain over the entire crack element and is equivalent to the mean strain of the crack element. In (b), $\beta/2 \cdot s_r$ denotes half of the length of the corroded section of the reinforcing bar. In blue, the results are given for a cross-section loss $\zeta_1 = 0.05$, in red for $\zeta_2 = \zeta_{crit} = 0.17$. For calculation, an HR reinforcing bar was used. Material parameters are given in Table 2.1.

the reinforcing bar

$$u_s(x) = \int \varepsilon_s(x)dx = \int f(\sigma_s(x))dx \tag{2.12}$$

and by dividing by the original length of the crack element s_r, one gets the mean steel strain over the entire crack element

$$\varepsilon_m = \frac{u_s(x = s_r)}{s_r} \tag{2.13}$$

which is equivalent to the mean strain of the crack element. Using ε_m is particularly useful, as (i) the elongation of any tension member can be directly estimated by multiplying with the member length and (ii) the stress-strain relationships of the tension member – relevant for its global response – and the bare steel can directly be compared, revealing the tension stiffening effect, as shown in Figure 2.4(c).

The slip between concrete and steel at the cracks, obtained by integrating Equation (2.8), can be interpreted as (half) the crack width. Physically, it corresponds to the difference between the deformation of the reinforcing bar u_s (Equation (2.12)) and the surrounding concrete u_c. Practically, concrete deformations are often ignored, as they are magnitudes smaller than steel deformations. Hence, the crack

Tab. 2.1 – Assumed material characteristics and model parameters.

f_{sy}	[MPa]	500	Ø	[mm]	20	ρ	[-]	0.01
f_{su}	[MPa]	600	k_a, k_b	[-]	0.002	τ_{b0}	[MPa]	5.8
ε_{sy} (HR)	[-]	0.00244	k_d	[-]	0.0245	τ_{b1}	[MPa]	2.9
ε_{sh} (HR)	[-]	0.018	f_c	[MPa]	30	s_{r0}	[mm]	495
ε_{su} (HR)	[-]	0.1	f_{ct}	[MPa]	2.9	λ [1)]	[-]	1.0
ε_{su} (CW)	[-]	0.08	E_c	[GPa]	31	$\beta \cdot s_r$ [1)]	[-]	20
E_s	[GPa]	205	n	[-]	6.6			

[1)] except for Figure 2.5: $\lambda = 0.5$, $\beta \cdot s_r = 30\,\text{mm}$

width is

$$w_r = u_s - u_c \approx u_s \tag{2.14}$$

The integral in Equation (2.12) can be solved analytically if an antiderivative to the chosen constitutive model of the steel stress-strain curve exists. The reinforcing bar's mean strain can then be expressed in closed form. Solutions for various constitutive models can be found in [7], notably for hot-rolled and cold-worked steels as well as a bilinear approximation.

The examples in Figures 2.3, 2.4, and 2.5 are calculated using the steel and concrete properties given in Table 2.1 and the constitutive stress-strain relationships according to [7, 129] for cold-worked (CW) steel

$$\begin{aligned} \varepsilon_s &= \frac{\sigma_s}{E_s} + \left(\frac{\sigma_s}{k_c}\right)^a \\ a &= \frac{\ln\left(\left(\varepsilon_{su} - f_{su}/E_s\right)/k_a\right)}{\ln\left(f_{su}/f_{sy}\right)} \\ k_c &= \frac{f_{sy}}{k_b^{1/a}} \\ &\text{normally } k_a = k_b = R_{p02} = 0.2\% \end{aligned} \tag{2.15}$$

and according to [7, 143] for hot-rolled (HR) steel

$$\begin{aligned} &\text{for } 0 \le \varepsilon_s \le \varepsilon_{sy} = f_{sy}/E_s \\ &\qquad \sigma_s = E_s \varepsilon_s \\ &\text{for } \varepsilon_{sy} \le \varepsilon_s \le \varepsilon_{sh} \\ &\qquad \sigma_s = f_{sy} \\ &\text{for } \varepsilon_{sh} \le \varepsilon_s \le \varepsilon_{su} \\ &\qquad \sigma_s = f_{sy} + (f_{su} - f_{sy}) k_d \left(1 - \mathrm{e}^{(\varepsilon_{sh} - \varepsilon_s)/b}\right) \\ &\qquad b = \frac{\varepsilon_{sh} - \varepsilon_{su}}{\ln((k_d - 1)/k_d)} \end{aligned} \tag{2.16}$$

The corresponding equations for the mean strain ε_m determined with the TCM by [7] are shown in the appendix.

Evaluating the TCM for small tensile loads in the linear elastic range allows analysing the cracking behaviour of a tension chord, i. e. the cracking load (see Figures 2.4(c) and 2.5)

$$\sigma_{sr,cr} = \frac{f_{ct}}{\rho}(1+\rho(n-1)) \tag{2.17}$$

and the maximum crack spacing

$$s_{r0} = \frac{f_{ct} \varnothing (1-\rho)}{2\tau_{b0}\rho} \tag{2.18}$$

which is equivalent to the maximum crack element length (see Figure 2.5). Whereas the cracking load is a specific value, theoretical considerations show that the crack spacing can vary by a factor of 2, even in the theoretical case of a constant tensile strength without any scatter, since at the middle between two cracks with maximum spacing s_{r0}, a new crack may form or not [7, 114]. The fact that it is impossible to predict the crack spacing theoretically is very well reflected by the high scatter of crack spacings observed in laboratory tests on tension chords. Therefore, the crack spacing s_r in the TCM is defined as

$$\begin{aligned} &s_{r0}/2 \leq s_r \leq s_{r0} \\ &s_r = \lambda \cdot s_{r0} \\ &0.5 \leq \lambda \leq 1.0 \end{aligned} \tag{2.19}$$

While the simplification of a stepped, rigid-perfectly plastic bond shear stress-slip relationship limits the use of the TCM for analysing local bond behaviour, it is highly useful to assess the behaviour on component and structural levels, e. g. the calculation of crack widths and deformations. As seen from Equations (2.9), (2.12), and (2.14), the steel elongations and crack widths are obtained from the bond stress-slip relationship after two integration steps. Further mechanical concepts (e. g. plane sections hypothesis of Bernoulli-Navier) are then used to determine the deflections of a structure from the strains and curvatures of all sections, typically involving two additional integrations. The averaging related to each integration – along with the observation that idealising the complex phenomenon of bond by considering bond shear stresses uniformly distributed along a nominal perimeter is a drastic idealisation by itself – justifies the simplified stepped, rigid-perfectly plastic bond shear stress-slip relationship. In fact, despite this crude simplification, the TCM reveals excellent agreement with experimental data [7, 94]. Because of its good correlation with experimental data and its simplicity, the TCM is widely applicable and builds part of many complex models such as the Cracked Membrane Model [22, 89, 90] or models investigating the serviceability limit states of structural concrete [29]. It was further enhanced for very small strains [140], bending elements [93, 111] and reversed loading [94].

2.3.2 Corroded Tension Chord Model CTCM

The Corroded Tension Chord Model (CTCM) aims at predicting the load-deformation behaviour of a crack element containing a reinforcing bar with a locally corroded section, induced, e. g. by chloride attack. It assumes that corrosion starts after cracking of the tension chord, i. e. the cracking load was exceeded, and the crack elements are defined at the time of corrosion initiation. A damaged section of total length $\beta \cdot s_r$ is assumed to be present at a crack (left end of crack element in Figure 2.5(b)), extending symmetrically into both adjoining crack elements. In this damaged section, similar to the example in Section 2.2.2, the reinforcing bar has a reduced cross-sectional area $A_{s,c}$ according to Equation (2.1) and hence, steel stresses $\sigma_{s,c}$ and strains increase in this section according to Equation (2.3). Bond is often reduced in the damaged section, due to corrosion-related bond degradation [56] or even missing because

of honeycombs. This can be accounted for with a factor γ, which allows reducing bond proportionally:

$$\begin{aligned} &\tau_{b,c} = \gamma\tau_b \\ &0 \leq \gamma \leq 1 \end{aligned} \tag{2.20}$$

Basically, any model for bond deterioration can be implemented, but often one will set $\gamma = 0$, as bond is almost completely lost – except for very low levels of corrosion – due to lubricating effects of corrosion products and longitudinal cracks. Moreover, the ductility reduction caused by tension stiffening in this zone is negligible compared to the reduction caused by strain localisation due to cross-section loss, particularly for small corrosion lengths $\beta \cdot s_r$.

The concepts and equations of the TCM are extended, accounting for the behaviour in this damaged section. For the case of $\gamma = 0$, the mean strain $\varepsilon_{m,c}$ of the entire crack element, including the damaged section, can be written as

$$\varepsilon_{m,c} = \frac{(1-\beta)\cdot s_r\varepsilon_m + \beta \cdot s_r\varepsilon_s(\sigma_{s,c}(\zeta))}{s_r} = (1-\beta)\cdot\varepsilon_m + \beta\cdot\varepsilon_s(\sigma_{s,c}(\zeta)) \tag{2.21}$$

with s_r in Equations (2.A1) and (2.A2) (in the appendix) being replaced by $(1-\beta)s_r$. As described in Section 2.2.2, the length of the damaged section $\beta \cdot s_r$ is a decisive parameter, which can strongly influence the residual deformation capacity. In a comprehensive study [52], the corrosion parameters (number of corroded reinforcing bars, pit geometry, cross-section loss, etc.) of 56 cantilever retaining walls were assessed. The results revealed that typically, a single corrosion pit per reinforcing bar with a length in the order of 10...30 mm occurred. Thus, $\beta \cdot s_r = 20\,\text{mm}$ is adopted in this study. With typical crack element lengths of 150...400 mm and considering two adjacent crack elements, this corresponds to $\beta = 0.01...0.1$.

Figure 2.5(b) compares the stress distributions within a crack element containing a corroded reinforcing bar with a cross-section loss $\zeta_1 = 0.05$ (blue line) and $\zeta_2 = \zeta_{crit} = 0.17$ (red line) to one containing a non-corroded reinforcing bar in Figure 2.5(a), loaded to the same stress at the crack of $\sigma_{sr} = 550\,\text{MPa}$. For the numerical calculations, the material characteristics given in Table 2.1 and $\lambda = 0.5$ were used. To fulfil equilibrium, in its full cross-section next to the corrosion pit, the reinforcing bar exhibits a stress according to Equation (2.3) of 523 MPa for ζ_1 and 457 MPa for ζ_2, respectively. The relatively moderate drop in stress of 5% and 17% represents the reduction in load-bearing capacity of the damaged crack element and obviously corresponds to the reduction in cross-sectional area of the corroded reinforcing bar. When comparing the resulting mean strain $\varepsilon_{m,c}$ of the corroded crack element, a reduction of 46% and 82% compared to the non-corroded element is observed, exemplarily showing the strong reduction in deformation capacity due to strain localisation.

2.3.3 Assembling corroded and non-corroded crack elements

Crack elements are assembled serially and in parallel to analyse structural elements with several corroded and non-corroded reinforcing bars. The overall load-deformation behaviour of a tension chord consisting of k serially coupled crack elements can be modelled by summing up the deformations of these k elements (at equal force)

$$\begin{aligned} &F_1 \propto F_i \propto F_k \\ &u_{tot} = \sum_{i=1}^{k} u_i \end{aligned} \tag{2.22}$$

The number of corroded and non-corroded crack elements can be varied, applying the CTCM and the TCM to each element accordingly. Whereas this procedure assumes that all crack elements are equally

loaded, varying tension chord forces can be considered by discretising the force distribution, with the crack spacing defining the discretisation length. Each element is then loaded differently, resulting in its specific deformation. Together with further structural mechanical concepts, this approach allows e. g. to predict the deflection of a cantilevering bridge deck with decreasing moment towards the parapet, with tension chords simulating the part around the upper reinforcement layer [162].

The load-deformation behaviour of k crack elements assembled in parallel can be modelled by summing up their forces (at known elongation, compare Figure 2.1(c))

$$\begin{aligned} u_1 &= u_i = u_k \\ F_{tot} &= \sum_{i=1}^{k} F_i \end{aligned} \tag{2.23}$$

Note that in contrast to serial crack elements, where the forces are identical by equilibrium, the elongations of parallel tension chords are not necessarily equal: As the corroded crack elements contain a softer section, they exhibit larger deformations at equal force than non-corroded crack elements. However, the assumption of equal deformations is often justified (similar to the plane sections hypothesis of Bernoulli-Navier, see Section 2.2.4), e. g. in cantilevers or retaining walls with high in-plane stiffness. Hence, corroded and non-corroded crack elements can be assembled in parallel in good approximation by summing up their individual, distinct forces at equal elongation, which leads to a redistribution of forces inside the structural element from (softer) corroding reinforcing bars to (stiffer) non-corroding reinforcing bars.

2.4 Effect of localised corrosion on the load-deformation behaviour

2.4.1 Effect on a single crack element

Figure 2.6(a) shows the load-deformation behaviour F vs. $u_m = \varepsilon_{m,c} \cdot s_r$ of a single crack element of length $s_r = 495\,\text{mm}$ ($\lambda = 1$) containing a reinforcing bar with diameter 20 mm of hot-rolled (HR) steel, which is corroded to various extents. Further material characteristics and model parameters are given in Table 2.1, constitutive steel stress-strain relationships follow Equations (2.15) and (2.16). The response of a bare reinforcing bar is plotted for comparison (dashed line). Obvious is the much stiffer behaviour of the non-corroded crack element (black line) compared to the response of the bare reinforcing bar, which is directly related to the tension stiffening effect.

The response of the crack element to the varying cross-section loss is shown with coloured lines, and a circle indicates the ultimate deformation at failure. Apparent is the disproportional reduction in deformation capacity with only slightly increasing corrosion, followed by a strong reduction in load-bearing capacity for larger cross-section losses.

Figure 2.6(b) shows the ratio of deformation at failure $u_{m,max}$ for a crack element containing a hot-rolled (HR, black line) and a cold-worked (CW, blue line) reinforcing bar, respectively, with increasing cross-section loss, compared to the deformation capacity of a crack element with a non-corroded HR reinforcing bar $u_{HR,m,max}$. Additionally, the ratio of load-bearing capacity F_u of a crack element with a corroded reinforcing bar compared to a crack element without corrosion is plotted (red line). Similar to Figure 2.5(b), the strong decrease in deformation capacity for a comparably low corrosion damage is apparent: The deformation at failure is reduced by 86% at a relative loss of cross-sectional area ζ_{crit} of only 17%, whereas the failure load is reduced proportionally by 17%. For larger cross-section losses, the deformation capacity does not change significantly, whereas the load-bearing capacity further decreases proportionally with the cross-section loss. Note that the deformation capacity of a CW reinforcing bar is generally lower compared to that of an HR reinforcing bar (even without corrosion, $\zeta = 0$) due to (i) the generally lower strain at peak stress ε_{su} and (ii) the different stress-strain curve of the bare reinforcing

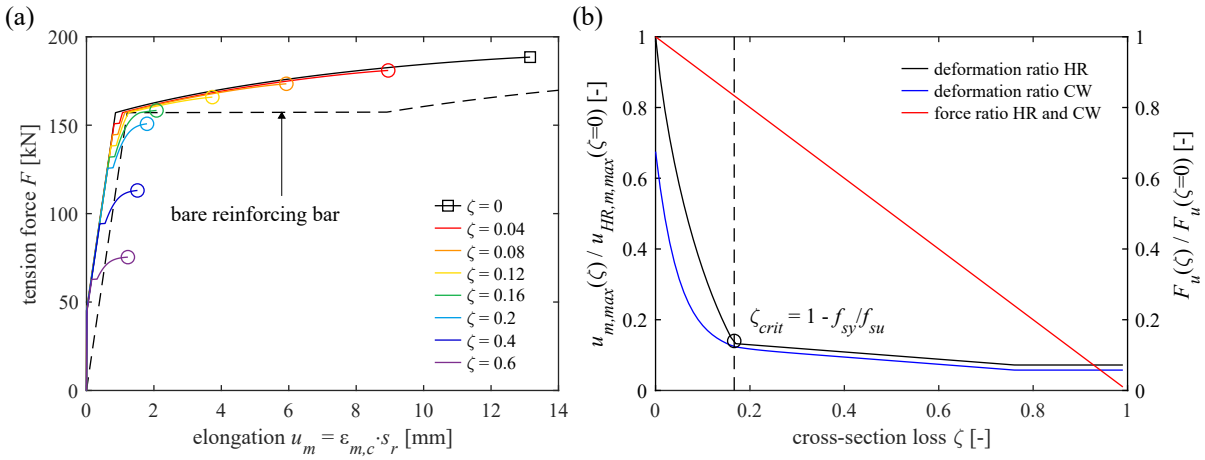

Fig. 2.6 – CTCM model response for a single crack element containing a hot-rolled (HR) reinforcing bar with varying cross-section loss ζ: (a) load-deformation behaviour with circles indicating the failure of the crack element; (b) relative deformation capacity of a crack element with a hot-rolled (HR) and a cold-worked (CW) reinforcing bar $u_{m,max}(\zeta)$, respectively, corroded to various extents, compared to a non-corroded crack element with hot-rolled steel $u_{HR,m,max}(\zeta = 0)$. Additionally, as red line, the relative load-bearing capacity F_u of a corroded crack element, compared to a non-corroded crack element, is shown.

bars, with a steeper gradient (due to the lacking yield plateau) at the beginning of the plastic range for the CW bar (compare Figure 2.4(b)).

The strong initial reduction in deformation capacity, up to a relative cross-section loss $\zeta_{crit} = 17\%$, is a direct consequence of the strain localisation effect related to the short damage length $\beta \cdot s_r$. Remarkably, the relative residual deformation capacity (at $\zeta = \zeta_{crit}$) of 14% in Figure 2.6(b) for $\beta = 0.02$ is much higher than that of the same bare reinforcing bar at equal length ratio β, which amounts to merely about 4% (compare Section 2.2.2 and Figure 2.3). This is not a contradiction, as the ratios of two different elements (one with concrete, the other without) are compared. It shows that the findings on ductility reduction due to strain localisation for bare reinforcing bars cannot be directly transferred to structures containing locally corroded reinforcement, but that the tension stiffening effect has to be appropriately considered and superimposed. However, other effects such as local bending moments in the corroded section (see Section 2.2.1) may further reduce the deformation capacity.

2.4.2 Effect on multiple crack elements

Figure 2.7(a) shows the load-deformation behaviour F vs. u_m of 100 crack elements assembled in parallel, undergoing equal elongation, whereof 50 elements contain a corroded HR reinforcing bar. The cross-section loss of the reinforcing bars varies within 4% and 60%. As dashed lines, the behaviour of 50 and 100 non-corroded crack elements is shown for comparison, and triangles indicate the peak load.

Similar to the observations in Figure 2.6(a), the deformation capacity of the entire structural element decreases up to the critical cross-section loss $\zeta_{crit} = 1 - f_{sy}/f_{su} = 17\%$, followed by a strong reduction of the load-bearing capacity with further increasing corrosion damage. As soon as the corroded reinforcing bars rupture, the load drops to the capacity of the remaining 50 non-corroded crack elements, which still have their full strength and deformation capacity. However, one has to consider that in force-controlled situations, as it applies for the majority of the load cases, the structural elements fail when the maximum load is reached, i. e. the load and deformation indicated with a triangle. Hence, even moderate corrosion may cause a significant loss of deformation capacity.

Figure 2.7(b) shows the load-deformation behaviour of a structural element consisting of 100 crack elements assembled in parallel, whereof n_c elements contain a corroded reinforcing bar with cross-

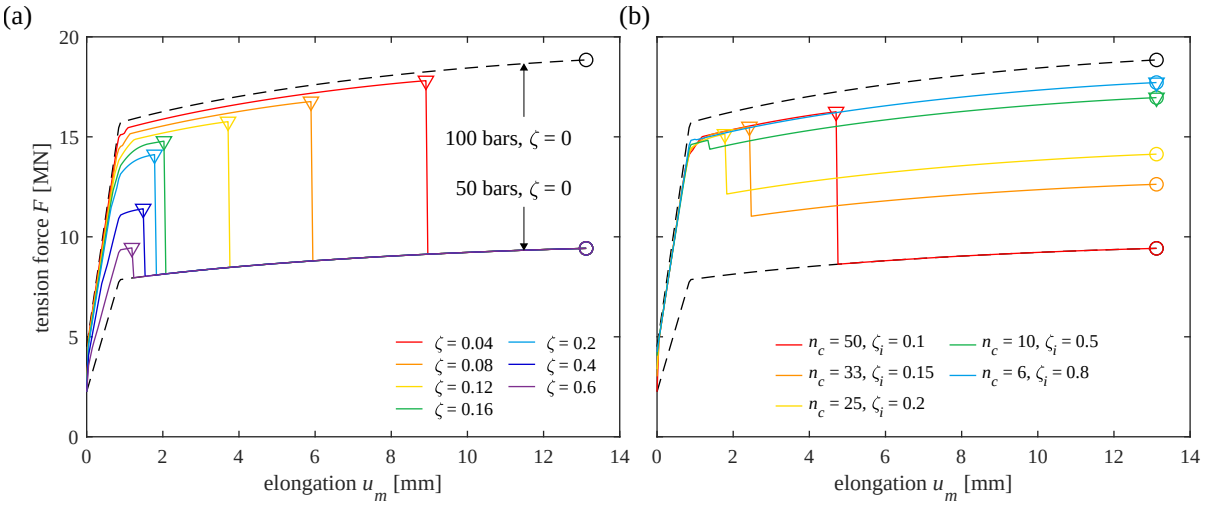

Fig. 2.7 – Load-deformation behaviour of a structural element with 100 crack elements in parallel. (a) $n_c = 50$ crack elements are corroded to an extent ζ; (b) n_c crack elements are corroded to an extent ζ_i, such that the mean cross-section loss $\zeta_m = \zeta_i \cdot n_c/100$ is constant at 5%. Note that an HR reinforcing bar was used for calculation.

section loss of ζ_i. The mean cross-section loss $\zeta_m = \zeta_i \cdot n_c/100$ is kept constant at 5%. From the 94 possible pairs $(n_c,\ \zeta_i)$, a selection of five is depicted. As dashed lines, the behaviour of 50 and 100 non-corroded crack elements is shown for comparison, and triangles indicate the peak load.

Despite the constant mean cross-section loss ζ_m, the load-bearing and deformation capacity decreases strongly for a decreasing number of corroded crack elements. This is due to the increasing cross-section loss for each corroded crack element, in order to keep the mean cross-section loss constant. This effect reverses from a specific number of corroded crack elements: For the pairs $(n_c = 10,\ \zeta_i = 50\%)$ and $(n_c = 6,\ \zeta_i = 80\%)$, the residual load-bearing capacity of the 90 and 94 non-corroded crack elements is higher than the load at failure of the corroded crack elements. This is noteworthy, as these structural elements maintain their full deformation capacity at a just slightly reduced failure load.

In Figure 2.8(a), for the same structural element as before, the relative deformation capacity $u_{m,max}$ is plotted for all pairs $(n_c,\ \zeta_i)$ and for various mean cross-section losses ζ_m . The abscissa indicates the cross-section loss ζ_i of the corroded crack elements. To keep the mean cross-section loss constant, the number of corroded crack elements is given by $n_c = 100 \cdot \zeta_m/\zeta_i$. The number of corroded crack elements n_c decreases with increasing ζ_i and vice versa. Figure 2.8(b) shows the corresponding relative load-bearing capacity F_u. Both figures indicate that a critical combination $(n_c, \zeta_i)_{crit}$ exists, for which the structure's load-bearing and deformation capacity is minimum – despite the constant mean cross-section loss – whereas for other combinations (n_c, ζ_i) the load-deformation behaviour is less impaired. Therefore, it is obvious that only indicating the mean cross-section loss ζ_m is insufficient to draw any conclusions on the load-deformation behaviour of a structure, as this depends on the corrosion distribution among the reinforcing bars of all crack elements: Generally, it is less critical to have only a few reinforcing bars corroded to a high extent than vice versa, especially for a severe mean cross-section loss ζ_m.

2.5 Conclusions

Localised corrosion reduces the load-carrying and deformation capacity of reinforced concrete structures due to various effects on different structural levels. A reinforcing bar's load-deformation behaviour can strongly be affected by effects related to the pit morphology, such as a triaxial stress state and local bending moments, leading to disproportionately reduced failure loads. The effect of strain localisation

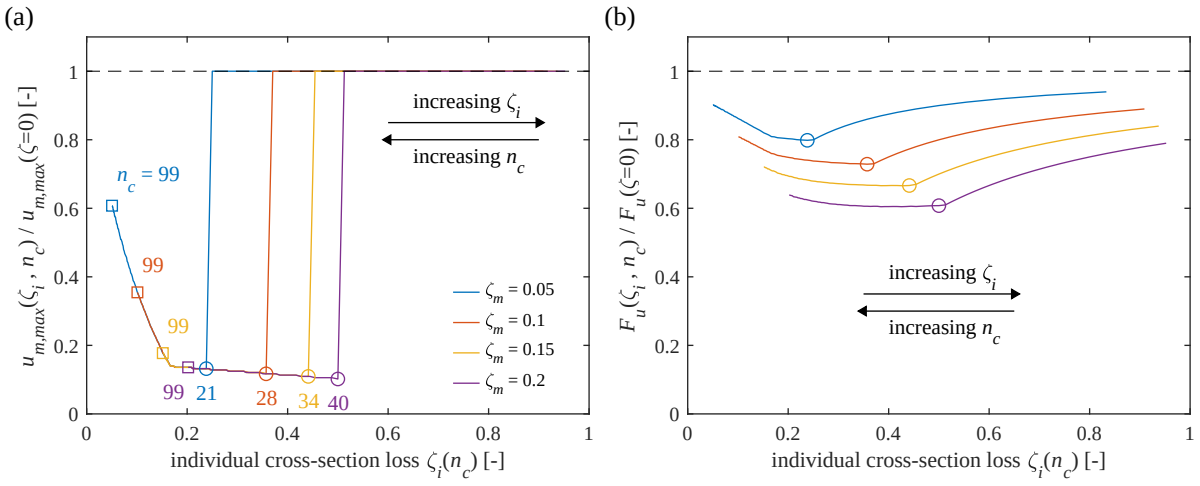

Fig. 2.8 – Structural element assembled of 100 crack elements in parallel with a mean cross-section loss ζ_m, containing n_c reinforcing bars with a cross-section loss $\zeta_i = 100 \cdot \zeta_m / n_c$. (a) relative deformation capacity $u_{m,max}$; (b) relative load-bearing capacity F_u. Circles indicate the critical combination $(n_c, \zeta_i)_{crit}$ with lowest load-bearing and deformation capacity. Note that an HR reinforcing bar was used for calculation.

due to cross-section loss results in a strong reduction of the deformation capacity of the structure, even for very low cross-section losses. This increases the risk of brittle failure for structures whose main loading is deformation dependent or which are statically indeterminate. Their residual deformation capacity therefore needs to be assessed appropriately.

The Corroded Tension Chord Model CTCM combines the effects of tension stiffening effect and strain localisation due to cross-section loss, and therefore allows calculating the load-deformation behaviour of concrete tension chords containing reinforcing bars affected by localised pitting corrosion on a sound mechanical basis. Simple equilibrium considerations lead to the definition of the critical loss of cross-section ζ_{crit} beyond which most of a reinforcing bar's ductility is lost, based solely on the steel yield stress and tensile strength. The CTCM enables estimating the residual deformation capacity at this point. By applying common structural mechanical concepts, corroded and non-corroded tension chords can be assembled serially and in parallel, which enables predicting the load-deformation behaviour of entire structural elements, such as, e. g. cantilever retaining walls.

First exemplary calculations on a structural element indicated a strong influence of the strain localisation effect, leading to a loss of deformation capacity of 83% at merely 17% cross-section loss for a typical pit size and common material characteristics. This reduction is disproportionate to the decrease in load-carrying capacity, which is in this case proportional to the cross-section loss. The calculations further revealed the complexity of structures containing several corroded and non-corroded tension chords with various corrosion damage. Even though the mean cross-section loss of structures may be identical, their load-deformation behaviour can vary considerably, depending on the specific combination of the number of affected reinforcing bars and their specific cross-section loss. Structures with few heavily corroded reinforcing bars seem to be less critical regarding load-bearing and deformation capacity than structures with a large number of slightly corroded reinforcing bars.[1] The indication of a structure's average cross-section loss is therefore not sufficient to draw conclusions about its load-deformation behaviour. This causes considerable uncertainty regarding the accurate assessment of structural safety, as information on the specific spatial distribution of corrosion among the reinforcing bars is mostly missing in practice.

[1] For a specific mean cross-section loss ζ_m, the load-carrying and deformation capacity of a structure decreases (nonlinearly) with a decreasing number of affected bars n_c (and an increasing cross-section loss per bar ζ_i, see Figure 2.8). This trend reverses for $n_c < (\zeta_m + 0.2) \cdot n_{tot}$ (and $\zeta_i > \zeta_m / (\zeta_m + 0.2)$, respectively; n_{tot} = total number of bars), for which the full deformation capacity is reached and the load-carrying capacity increases again [73].

Appendix

TCM-mean strain according to [7] for the constitutive stress-strain relationship of cold-worked (CW) steel given in Equation (2.15)

$$
\begin{aligned}
&\text{for } \sigma_{sr} \le f_{sy} \\
&\quad \varepsilon_m = \frac{\sigma_{sr}}{E_s} - \frac{\tau_{b0} s_r}{E_s \varnothing} + \frac{\varnothing}{2\tau_{b0} s_r} \cdot \frac{1}{(a+1) k_c{}^a} \cdot \left(\sigma_{sr}^{a+1} - \left(\sigma_{sr} - \frac{2\tau_{b0} s_r}{\varnothing} \right)^{a+1} \right) \\
&\text{for } f_{sy} < \sigma_{sr} \le \left(f_{sy} + \frac{2\tau_{b1} s_r}{\varnothing} \right) \\
&\quad \varepsilon_m = \frac{\varnothing}{4 E_s \tau_{b1} s_r} \left\{ (\sigma_{sr} - f_{sy})^2 \left(1 - \frac{\tau_{b0}}{\tau_{b1}} \right) + \frac{2E_s}{(a+1) k_c{}^a} \left[\sigma_{sr}^{a+1} - f_{sy}^{a+1} \left(1 - \frac{\tau_{b1}}{\tau_{b0}} \right) \right. \right. \\
&\qquad \left. \left. - \frac{\tau_{b1}}{\tau_{b0}} \left(f_{sy} + \frac{\tau_{b0}}{\tau_{b1}} (\sigma_{sr} - f_{sy}) - \frac{2\tau_{b0} s_r}{\varnothing} \right)^{a+1} \right] \right\} + \frac{\tau_{b0}}{\tau_{b1}} \left(\frac{\sigma_{sr}}{E_s} - \frac{f_{sy}}{E_s} \left(1 - \frac{\tau_{b1}}{\tau_{b0}} \right) \right) - \frac{\tau_{b0} s_r}{E_s \varnothing} \\
&\text{for } \left(f_{sy} + \frac{2\tau_{b1} s_r}{\varnothing} \right) < \sigma_{sr} \le f_{su} \\
&\quad \varepsilon_m = \frac{\sigma_{sr}}{E_s} - \frac{\tau_{b1} s_r}{E_s \varnothing} + \frac{\varnothing}{2\tau_{b1} s_r} \cdot \frac{1}{(a+1) k_c{}^a} \cdot \left(\sigma_{sr}^{a+1} - \left(\sigma_{sr} - \frac{2\tau_{b1} s_r}{\varnothing} \right)^{a+1} \right)
\end{aligned}
\tag{2.A1}
$$

and for hot-rolled (HR) steel given in Equation (2.16)

$$
\begin{aligned}
&\text{for } \sigma_{sr} \le f_{sy} \\
&\quad \varepsilon_m = \frac{\sigma_{sr}}{E_s} - \frac{\tau_{b0} s_r}{E_s \varnothing} \\
&\text{for } f_{sy} < \sigma_{sr} \le \left(f_{sy} + \frac{2\tau_{b1} s_r}{\varnothing} \right) \\
&\quad \varepsilon_m = \frac{\varnothing}{2\tau_{b1} s_r} \left[\varepsilon_{sh} (\sigma_{sr} - f_{sy}) + k_d (f_{su} - f_{sy}) b \left(1 + z_1 \left(\ln(z_1) - 1 \right) \right) \right] \\
&\qquad + \frac{s_r - 2x^*}{s_r} \left(\frac{f_{sy}}{E_s} - \frac{\tau_{b0} (s_r - 2x^*)}{E_s \varnothing} \right) \\
&\text{for } \left(f_{sy} + \frac{2\tau_{b1} s_r}{\varnothing} \right) < \sigma_{sr} \le f_{su} \\
&\quad \varepsilon_m = \varepsilon_{sh} - \frac{\varnothing}{2\tau_{b1} s_r} k_d (f_{su} - f_{sy}) b \left[z_2 \left(\ln(z_2) - 1 \right) - z_1 \left(\ln(z_1) - 1 \right) \right]
\end{aligned}
\tag{2.A2}
$$

with

$$
\begin{aligned}
x^* &= \frac{(\sigma_{sr} - f_{sy}) \varnothing}{4\tau_{b1}} \\
z_1 &= 1 - \frac{\sigma_{sr} - f_{sy}}{k_d (f_{su} - f_{sy})} \\
z_2 &= 1 - \frac{\sigma_{sr} - f_{sy} - 2\tau_{b1} s_r / \varnothing}{k_d (f_{su} - f_{sy})}
\end{aligned}
$$

with a, b, k_c, k_d according to Equations (2.15) and (2.16). s_r denotes the mean length of the crack element according to Equation (2.19).

Notation

A_c	cross-sectional area of tensile member
A_s, $A_{s,c}$	cross-sectional area of reinforcing bar (in general / in uncorroded section, in corroded section)
E_c, E_s	Young's modulus (of concrete, of steel)
F, F_u	applied tensile force (in general, at ultimate)
e_0, e_a	earth pressure (at-rest, active)
f_{ct}	concrete tensile strength
f_{sy}, f_{su}	steel yield stress, steel tensile strength
k	total number of assembled crack elements
l_{uc}, l_c	length of uncorroded section, length of corroded section
n	modular ratio; $n = E_s/E_c$
n_c	number of corroded crack elements
s_r, s_{r0}	crack element length (in general, maximum)
u_m	elongation of crack element and assembled crack elements, respectively, according to TCM and CTCM; $u_m = \varepsilon_m \cdot s_r$ and $u_m = \varepsilon_{m,c} \cdot s_r$, respectively
u_c	elongation of concrete
u_s, $u_{s,uc}$, $u_{s,c}$	elongation of steel (in general, in uncorroded section, in corroded section)
u_{tot}	sum of elongations
w_r	crack width; $w_r = u_s - u_c \approx u_s$
β	ratio of corroded length of reinforcing bar to length of crack element; $\beta = l_c/s_r$
$\gamma \in [0,1]$	factor to account for reduction of bond stress; $\gamma = \tau_{b,c}/\tau_b$, with $\tau_b = \tau_{b0}$ or τ_{b1}, respectively
δ	bond slip
ε_c	concrete strains
ε_m, $\varepsilon_{m,c}$	mean steel strain of crack element according to TCM and CTCM, respectively
ε_s, $\varepsilon_{s,uc}$, $\varepsilon_{s,c}$	steel strains (in general, of uncorroded section, of corroded section)
ε_{sy}, ε_{sh}, ε_{su}	steel strains at yielding, at onset of hardening, at ultimate
$\lambda \in [0.5,1]$	factor for crack element length; $s_r = \lambda \cdot s_{r0}$
ρ	geometrical reinforcement ratio; $\rho = A_s/A_c$
σ_s, $\sigma_{s,uc}$, $\sigma_{s,c}$	steel stresses (in general, of uncorroded section, of corroded section)
σ_{sr}, $\sigma_{sr,cr}$	steel stress at crack, steel stress at crack for cracking load; $\sigma_{sr} = F/A_s$
τ_{b0}, τ_{b1}	bond stresses (if steel stress $\sigma_s(x) < f_{sy}$, if steel stress $\sigma_s(x) \geq f_{sy}$); $\tau_{b0} = 2\tau_{b1} = 2f_{ct}$
$\tau_{b,c}$	bond stress along corroded section of reinforcing bar
$\zeta, \zeta_i \in (0,1]$	relative loss of cross-sectional area of single reinforcing bar; $\zeta = A_{lost}/A_s$
ζ_{crit}	critical relative loss of cross-sectional area, $\zeta_{crit} = 1 - f_{sy}/f_{su}$
ζ_m	mean relative loss of cross-sectional area for a structural element (assembled of multiple crack elements)
Ø	reinforcing bar diameter

3 Influence of quasi-static strain rate on the stress-strain characteristics of modern reinforcing bars

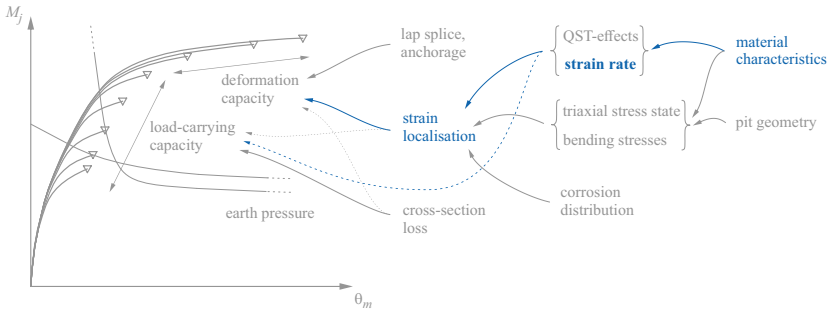

This chapter presents the findings of a comprehensive series of tensile tests on different reinforcing steel types to investigate the influence of various quasi-static strain rates on the apparent yield stress and tensile strength. The study was conducted since preliminary tests on locally damaged reinforcing bars exhibited higher tensile strengths than expected, which was assumed to be partly caused by the locally varying strain rate. The chapter corresponds to the published version of the following article:

> Haefliger, S., Fomasi, S., Kaufmann, W. 'Influence of quasi-static strain rate on the stress-strain characteristics of modern reinforcing bars,' *Construction and Building Materials*, vol. 287, p. 122967, 2021. doi: 10.1016/j.conbuildmat.2021.122967.

The lead author (Severin Haefliger) planned the experiments, conducted them in close collaboration with the second author (Sara Fomasi), evaluated the data, and developed the presented modelling approach under the supervision of the third author (Walter Kaufmann).

Abstract

While it has been known for decades that even for quasi-static loading, increments in strain rate lead to increased stresses in the inelastic range, this effect is often ignored. However, accurate knowledge of the stress-strain characteristics of reinforcing bars is an indispensable prerequisite for the safe design of new structures and the realistic assessment of the structural safety of existing ones, and the strain rate dependency of the reinforcing steel characteristics should thus be accounted for in many situations. An exemplary case is quality control: Reinforcing bars produced today are periodically tested to check their conformity with specifications, determining their stress-strain characteristics in standard tensile tests. However, the applied quasi-static strain rates may vary considerably but are not commonly reported. Hence, the results are subject to considerable uncertainty. Another relevant case is the structural safety assessment of existing structures affected by local corrosion of the reinforcement: Their cross-section (and hence, stiffness) varies considerably along the bar axis and consequently, the strain rate in corroded

sections is significantly higher than in non-corroded sections, leading to higher yield stress and tensile strength.

This study investigates the effect of quasi-static strain rates on the stress-strain characteristics of modern reinforcing bars based on a comprehensive experimental campaign. In four series of experiments, 41 tensile tests on three different types of reinforcing bars were conducted, applying strain rates between 0.004 ‰/s and 1.0 ‰/s. Compared to the static stress, an increase of up to 8% in the dynamic stress was observed, depending on the type of reinforcing bar. Based on these observations, a simplified model for the strain rate dependency was developed and validated against experimental data, showing excellent agreement.

3.1 Introduction

Numerous studies investigated the influence of strain rate on the mechanical behaviour of steel and recognised an increase of stresses in the inelastic range with higher strain rates. The effect is particularly significant for very high strain rates, in the order of $0.1\,\mathrm{s}^{-1}$ to $1000\,\mathrm{s}^{-1}$, which occur in structures in the context of impacts, explosions, and earthquakes. Due to the high damage potential in these situations, researchers thoroughly investigated the related strain rate effects, partially in combination with high temperatures, on reinforcing bars in structural concrete (see, e. g. [30–32, 61, 108, 128, 164]). Studies carried out in the 1970s and 1980s [95, 98] observed quite considerable strain rate effects also at very low, quasi-static strain rates ($10^{-6}\,\mathrm{s}^{-1}$ to $10^{-3}\,\mathrm{s}^{-1}$). However, though important in the context of quality control, corrosion and fatigue of reinforcing bars, no recent studies are known to the authors that consider quasi-static strain rates in modern reinforcing bars.

The effect of quasi-static strain rates is particularly relevant in quality control of reinforcing steel by means of tensile tests. The testing standards EN ISO 6892-1:2016 and EN ISO 15630-1:2017 allow strain rates for quality control between 0.25 ‰/s and 8 ‰/s, which leads to relevant variations in measured yield stress and tensile strength. As it is uncommon to report the strain rate applied in the tensile test, this issue impedes a direct comparison of results among different testing laboratories. Moreover, it introduces a certain amount of arbitrariness when assessing the conformity of a production batch, particularly where the characteristics are close to the required limit values.

Additionally, the effect of quasi-static strain rate may be relevant in experimental campaigns on structural concrete, particularly in the field of corrosion investigations: Reinforcing bars with non-constant cross-section over their length, as commonly investigated in corrosion studies, exhibit different strain rates and therefore different strengths in the intact and corroded sections, respectively. This is due to the varying cross-section reduction along the bar axis and the correspondingly varying tensile stiffness EA. In this context, it is important to note that apart from the effect of strain rate, many other influences have to be considered when assessing the structural safety of corroded reinforced concrete structures. These are in particular various steel microstructures with distinct mechanical properties within the cross-section in quenched and self-tempered (QST) reinforcing bars [55, 71, 82, 139]; three-dimensional stress states near the damage zone for local corrosion [80]; and bending effects for localised corrosion pits due to a shift of the neutral axis [8, 80, 166].

In 1967, Lampert et al. [98] conducted tensile tests on four types of reinforcing bars produced in the 1960s (brand names “Tor”, “Roto”, “Caron” and “Box”) at quasi-static strain rates varying between 0.05 ‰/s and 1.04 ‰/s. They thoroughly analysed the rate dependency of the exhibited stresses and stated that (i) the dynamic stress, with running testing machine, is between 3% and 9% higher than the static stress at halts, depending on the initial stress and the steel type; (ii) even small applied strain rates increase strength considerably; and (iii) static stress is independent of the preceding strain rate. Ten years later, Krempl [95] conducted tensile and relaxation tests on AISI Type 304 steel at low strain rates varying between 10^{-5} ‰/s and 10 ‰/s. He stated that (i) the increase of the inelastic stress depends on the strain rate; (ii) the static stress is independent of the preceding strain rate; and (iii) relaxation

time depends on the applied stress and the preceding strain rate. Krempl hypothesised that a boundary between elastic and inelastic deformation does not exist, but inelasticity is rather a gradually developing process, similar to the modelling approach of Ramberg & Osgood [129].

Contrary to the numerous studies on the influence of medium and high strain rates on the stress-strain characteristics of steel in the past, the data set is scarce for modern reinforcing steel at quasi-static strain rates. This missing data impedes a proper separation of the effects of different phenomena on the stress-strain characteristics of corroded reinforcing bars as described above, and complicates a reliable comparison of test results from different laboratories in production quality control. The present study closes this knowledge gap with a comprehensive experimental campaign on 41 specimens of three types of reinforcing steel, tested at strain rates between 0.004 ‰/s and 1 ‰/s. Stresses were found to increase by 8% from static to dynamic state for a strain rate of 1 ‰/s and by 5% when comparing strain rates of 0.004 ‰/s and 1 ‰/s. Based on these findings, a simplified model is developed to describe the strain rate dependency of the mechanical characteristics of modern reinforcing bars in the inelastic range.

3.2 Experimental programme

The experimental campaign carried out in the structural laboratory at ETH Zurich aimed at investigating the influence of strain rate on the relaxation and stress-strain behaviour of reinforcing bars in the inelastic range. The four test series A1-A4 comprised a total of 41 reinforcing bars of three different types of reinforcement. Series A1 contained 13 cold-worked (CW) reinforcing bars of the product type "BSW-Superring TWR" (B500B) that were hot-rolled, stretched, and coiled for transportation. Series A2 contained 14 hot-rolled, quenched and self-tempered (QST) reinforcing bars of the product type "BSW Tempcore" (B500B) that were delivered as straight bars. Series A3 contained 13 QST reinforcing bars of the product type "Pittini BST500 Jumbo HD" (B500B) which had been coiled for transportation and subsequently straightened before delivery (referred to as QST-R bars). Series A4 contained two reinforcing bars of each type of Series A1 and A2. All reinforcing bars had a nominal diameter of 20 mm and a length of 1200 mm and had been delivered to the laboratory as straight bars with the required length. Reinforcing bars of the same type were taken from the same production batch. CW bars contained a perlitic/ferritic microstructure, whereas QST and QST-R bars consisted of distinct layers of perlite/ferrite (core), bainite (transition zone), and martensite (outer annulus). More information on the different types of reinforcement used, particularly regarding their microstructural composition and its implications on the stress-strain characteristics, can be found in [137] and in a companion paper [71].

All reinforcing bars were loaded displacement controlled until failure, applying varying strain rates, in a universal tensile testing machine of type Schenck 480 kN, containing an Instron controller. They were instrumented with a linear variable differential transformer (LVDT, type WLH50 from Messotron with nominal stroke ±25 mm) of 300 mm gauge length for elongation measurement. After weighing the specimens and installing the LVDT in the middle of the bar's axis, they were installed (clamped) in the testing machine without any further preparation. In Series A1 to A3, the strain rate was kept constant throughout the entire tensile test at either 0.004 ‰/s, 0.01 ‰/s, 0.04 ‰/s, 0.1 ‰/s, 0.4 ‰/s, or 1 ‰/s. To investigate the relaxation behaviour of the reinforcing steel, the displacement of the machine head was stopped, and the elongation of the reinforcing bars was kept constant for at least 2 minutes at a range of strain values (A1: 5 ‰, 20 ‰, and 35 ‰; A2: within yield plateau, 25 ‰, 40 ‰, and 60 ‰; A3: 5 ‰, 20 ‰, and 50 ‰). For Series A4, the strain rate was varied within the same test to validate the results of the previous three series.

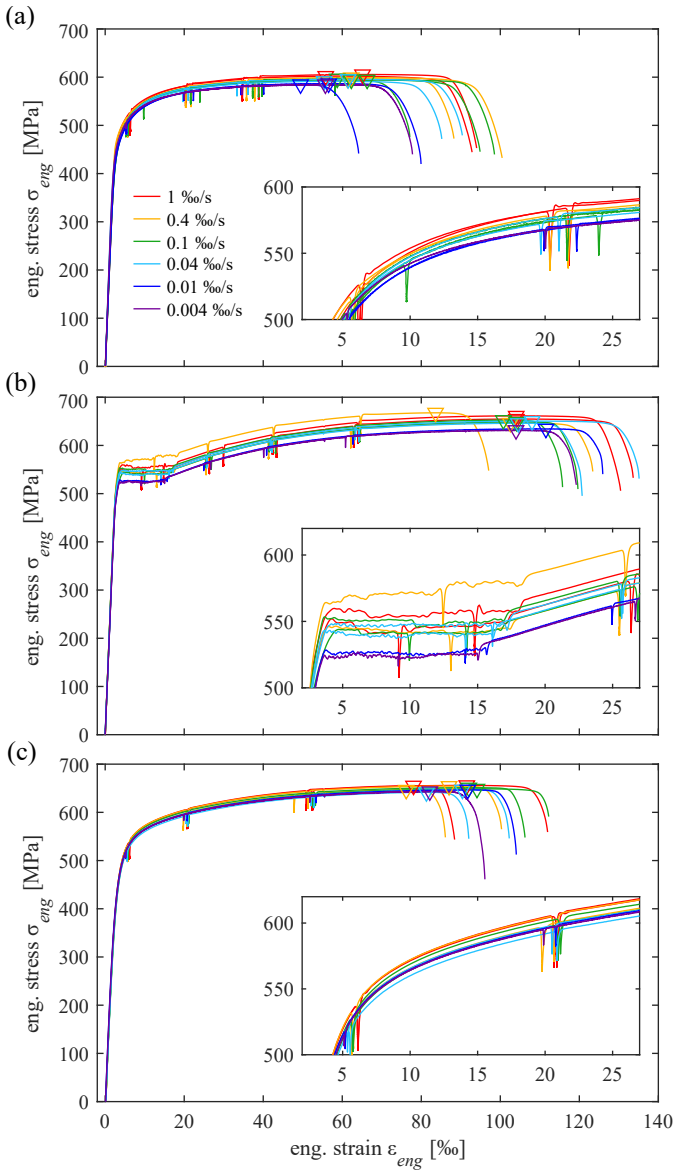

Fig. 3.1 – Stress-strain diagrams of Series A1-A3. Reinforcing bars were tested at the indicated strain rate. Triangles indicate the peak stress and corresponding strain. (a) A1: hot-rolled, cold-stretched reinforcing bar, coiled (CW); (b) A2: QST reinforcing bar, straight; (c) A3: QST-R reinforcing bar, coiled.

3.3 Results and Discussion

3.3.1 Basic observations

Figure 3.1 shows the stress-strain diagrams of Series A1 – A3 with colours indicating the various strain rates. Stresses are calculated using the reinforcing bars effective cross-sectional area determined by their weight. The different curve shapes, evident when comparing the stress-strain curves of Series A1 to A3, are due to the different production methods of the reinforcing bars [71]. The CW reinforcing bars (A1) lack a pronounced yield plateau and exhibit lower strains at peak load due to the cold-working. The QST reinforcing bars (A2) obtain favourable mechanical characteristics by their composed microstructure layers, exhibiting a pronounced yield plateau and higher strain at peak stress. The QST-R reinforcing bars (A3) are produced in the same way as the QST reinforcing bars, except that they are coiled for transportation, which may – but need not – lead to the absence of a yield plateau (as observed in these tests) as the bars undergo plastic deformations when being coiled.

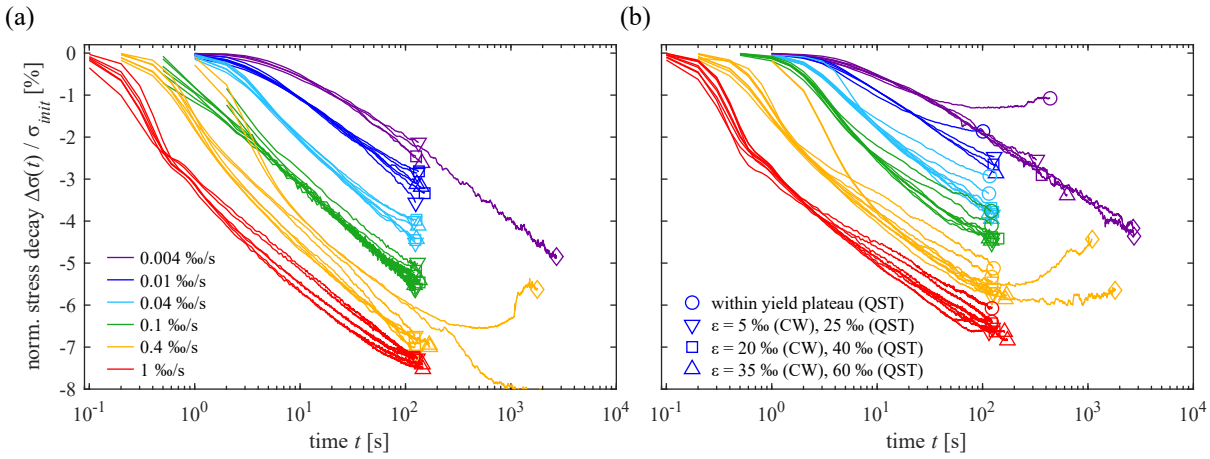

Fig. 3.2 – Normalised stress decay over time for machine stops (at different strain levels) for various strain rates. (a) A1: hot-rolled, cold stretched reinforcing bars (CW); (b) A2: QST reinforcing bars, straight.

The difference in stresses observed at equal strain caused by the varying strain rates is obvious for all Series A1 to A3: The measured stress at a given strain in the plastic phase increases with a higher strain rate. Furthermore, the stress decay from dynamic stress towards static stress due to relaxation when the machine was stopped at various strain levels is clearly visible in Figure 3.1. For a given strain rate, the magnitude of the stress decay between stopping and restarting the machine was found to increase with higher initial stress σ_{init} at the beginning of the machine stop. Therefore, in all further plots, the stress decay is normalised with respect to the initial stress level σ_{init}. Figure 3.2 shows the normalised stress decay over time for CW and QST reinforcing bars for machine stops at various strain levels and for different strain rates. The stop duration was set to 2 minutes for most of the experiments (similar to [98]), and to 45 minutes for the remaining few tests. A logarithmic decay over time, with an increasing slope in the first phase after stopping, was observed. For the higher strain rates of 1 ‰/s and 0.4 ‰/s, the slope decreased after 70...100 s and 400...500 s, respectively. For the slow strain rate of 0.004 ‰/s, the decay kept being logarithmic even after 45 minutes, without showing indications of a decrease of the slope. This leads to the conclusion that the strain rate before stopping influences both, the magnitude of the stress decay and its rate. Furthermore, it indicates that a duration of the machine stop of 2 min, as commonly used in materials testing, is not sufficient for tests conducted at low strain rates to reach a steady state and determine the static stress.

Plastic strains in metals and related strain rate effects are caused by movements of dislocations through the crystalline grains. Orowan was among the first researchers describing the underlying mechanism [81, 96, 159, 160]. He postulated the *Orowan equation* relating the macroscopic plastic shear strain rate to the microscopic parameters:

$$\dot{\gamma}_{pl} = k\rho_m b\bar{v} \tag{3.1}$$

where $k =$ dislocation orientation factor (Schmid factor), $\rho_m =$ mobile dislocation density, $b =$ magnitude of Burgers vector (characterizing the intensity of a dislocation), and $\bar{v} =$ mean dislocation velocity. Further, one may assume that $\bar{v}$ is related to the microscopic shear stress by the power function $\bar{v} = \tau^n$, where n depends on the material properties [96, 160]. On the other hand, the macroscopic plastic shear strain rate $\dot{\gamma}_{pl}$ is proportional to the macroscopic plastic strain rate $\dot{\varepsilon}_{pl}$ in direction of the applied force, which is in turn approximately equal to the total strain rate $\dot{\varepsilon} = \dot{\varepsilon}_{pl} + \dot{\varepsilon}_{el} \approx \dot{\varepsilon}_{pl}$ in the plastic phase of a tensile test [96]. Hence, since the microscopic shear stress τ is proportional to the macroscopic exhibited tensile stress σ and the Taylor factor [136], one gets the proportionalities:

$$\frac{\dot{\varepsilon}_{pl}}{\rho_m} \propto \frac{\dot{\gamma}_p l}{\rho_m} \propto \bar{v} \propto \tau^n \propto \sigma^n \tag{3.2}$$

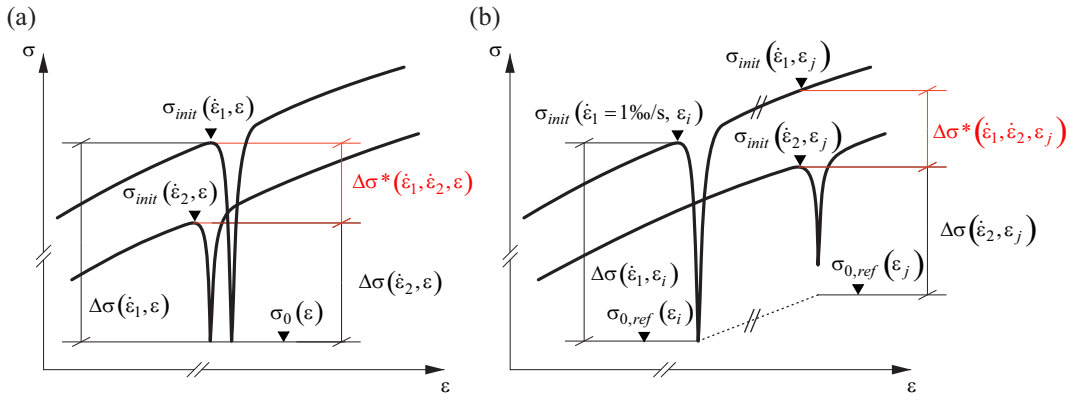

Fig. 3.3 – Approaches to determine stress decay exhibited for reinforcing bars tested with different strain rates: (a) general approach; (b) approach to correct stress decay if stops differ slightly in strain level.

Generally, the mobile dislocation density ρ_m is not constant, but increases with, e. g. plastic deformation [136, 159]. However, it is obvious from equation (3.2) that for equal values of ρ_m (i. e. at a specific strain value in a test), the exhibited tensile stress σ must increase with the strain rate, i. e. $\sigma \propto \sqrt[n]{\dot{\varepsilon}_{pl}}$.

3.3.2 Proposed modelling approach of relaxation behaviour

The influence of strain rate on the stress-strain diagram of a reinforcing bar can be mathematically described using a function depending solely on the applied strain rate, but independent of the strain at stopping. Experimental data and the findings of [95] imply that stresses at a given strain ε decay to the same static stress $\sigma_0(\varepsilon)$, independently of strain rate. The final stress decay therefore can be written as $\Delta\sigma(\dot{\varepsilon},\varepsilon) = \sigma_{init}(\dot{\varepsilon},\varepsilon) - \sigma_0(\varepsilon)$. Normalising with the initial stress yields:

$$\Delta\sigma(\dot{\varepsilon},\varepsilon)/\sigma_{init}(\dot{\varepsilon},\varepsilon) = 1 - \sigma_0(\varepsilon)/\sigma_{init}(\dot{\varepsilon},\varepsilon) = C(\dot{\varepsilon}) \tag{3.3}$$

Here, $C(\dot{\varepsilon})$ denotes a variable only depending on the strain rate. The independence of C from a specific strain value ε is assumed based on the findings in Figure 3.2. The difference in the stress decay $\Delta\sigma^*(\dot{\varepsilon}_1,\dot{\varepsilon}_2,\varepsilon)$ and the ratio between the corresponding dynamic stresses, $\sigma_{init}(\dot{\varepsilon}_2,\varepsilon)/\sigma_{init}(\dot{\varepsilon}_1,\varepsilon)$, for two different strain rates $\dot{\varepsilon}_1$ and $\dot{\varepsilon}_2$ at a specific strain level ε can be determined from Equation (3.4) (see Figure 3.3(a)).

$$\begin{aligned}\Delta\sigma^*(\dot{\varepsilon}_1,\dot{\varepsilon}_2,\varepsilon) &= \sigma_{init}(\dot{\varepsilon}_2,\varepsilon) - \sigma_{init}(\dot{\varepsilon}_1,\varepsilon) = \Delta\sigma(\dot{\varepsilon}_2,\varepsilon) - \Delta\sigma(\dot{\varepsilon}_1,\varepsilon)\\ &= C(\dot{\varepsilon}_2)\sigma_{init}(\dot{\varepsilon}_2,\varepsilon) - C(\dot{\varepsilon}_1)\sigma_{init}(\dot{\varepsilon}_1,\varepsilon)\\ \rightarrow \frac{\sigma_{init}(\dot{\varepsilon}_2,\varepsilon)}{\sigma_{init}(\dot{\varepsilon}_1,\varepsilon)} &= \frac{1-C(\dot{\varepsilon}_1)}{1-C(\dot{\varepsilon}_2)}\end{aligned} \tag{3.4}$$

If $C(\dot{\varepsilon})$ is known, the dynamic stress-strain diagram for any strain rate $\dot{\varepsilon}_2$ can be calculated using the stress-strain diagram determined at any other strain rate $\dot{\varepsilon}_1$.

The value of $C(\dot{\varepsilon})$ presumably depends on the material characteristics of the reinforcing bar. It can be determined empirically using the measured stress decays at various strain rates, applying Equation (3.3). However, while the stress at the beginning of the stress decay $\sigma_{init}(\dot{\varepsilon},\varepsilon)$ was measured, the static stress $\sigma_0(\varepsilon)$ would theoretically only be reached after an infinitely long stop, and clearly was not reached in most of our experiments (see Section 3.3.1). Hence, the following procedure was used to estimate the decay from dynamic to static stress (see Figure 3.3(b)):

The results shown in Figure 3.2 imply that stresses had (almost) fully decayed after machine stops of 2 minutes duration for the experiments with a strain rate of 1 ‰/s. Assuming the static stress $\sigma_0(\varepsilon)$

Tab. 3.1 – Mean and Coefficient of Variation *CoV* for the normalised stress decay $C(\dot{\varepsilon})$ for the three Series A1-A3 (CW, QST and QST-R reinforcing bars).

strain rate [‰/s]		0.004	0.01	0.04	0.1	0.4	1.0
CW	mean [%]	5.32	5.07	6.12	7.13	7.31	8.06
	CoV [%]	19.2	14.9	12.0	36.1	27.7	28.9
QST	mean [%]	2.36	3.18	5.77	5.75	7.31	6.84
	CoV [%]	49.9	37.9	32.3	20.0	36.0	28.9
QST-R	mean [%]	4.99	5.44	4.91	5.51	5.57	6.71
	CoV [%]	5.4	5.6	8.9	9.3	12.9	25.1

to be independent of the applied strain rate, as proposed by [95], its value observed with a strain rate of 1 ‰/s, $\sigma_0(\dot{\varepsilon}_1 = 1\,‰/\text{s}, \varepsilon_i)$, at a specific strain ε_i equals the static stress observed at the same strain ε_i for all experiments of one series conducted with any other strain rate. Thus, the static stress obtained at $\dot{\varepsilon}_1 = 1\,‰/\text{s}$ is used as reference static stress $\sigma_{0,ref}(\varepsilon_i)$. The stress decay in a test with any other strain rate $\dot{\varepsilon}_2$ is then determined by the difference between the stress at the beginning of the machine stop, i. e. $\sigma_{init}(\dot{\varepsilon}_2, \varepsilon_i)$, and $\sigma_{0,ref}(\varepsilon_i) = \sigma_0(\dot{\varepsilon}_1 = 1\,‰/\text{s}, \varepsilon_i)$. Since the machine was stopped manually at distinct strain levels, the actual strains ε_j at stopping differed slightly from the targeted strain level ε_i. Hence, the reference static stress $\sigma_{0,ref}(\varepsilon_j)$ – which was not directly measured at this same strain – was corrected based on the measured dynamic stresses in the experiments with a strain rate of 1 ‰/s, assuming the stress decay $\Delta\sigma(\dot{\varepsilon}_1, \varepsilon_i)$ to be constant.

3.3.3 Determined values for normalised stress decay $C(\dot{\varepsilon})$ and conclusions

Figure 3.4 shows the normalised stress decay $C(\dot{\varepsilon}) = \Delta\sigma(\dot{\varepsilon}, \varepsilon_i)/\sigma_{init}(\dot{\varepsilon}, \varepsilon_i)$ for Series A1, A2 and A3 as a function of the applied strain rate. The symbols indicate the corresponding strain level at which the machine was stopped. Results deviating by more than 40% from the median for Series A2 (QST) or 15% of the median for Series A1 and A3 (CW and QST-R), shown in grey, were treated as outliers and were not considered for the regression of $C(\dot{\varepsilon})$. Table 3.1 contains the mean and coefficient of variation *CoV* for each strain rate and test series.

The results clearly indicate that higher strain rates lead to larger stress decays, approximately following a logarithmic relation. As the static stress $\sigma_0(\varepsilon)$ is constant, the measured dynamic stress thus increases with higher strain rates, to an extent depending on the steel type. Whereas for QST-R reinforcing bars the increase is rather low, it is more pronounced for the CW and quite considerable for QST reinforcing bars. Note that there is a significant difference between dynamic and static stress even for very low strain rates. To correctly validate any calculation model with experimental results, the authors therefore recommend using dynamic rather than static steel characteristics, as in many conducted experiments the applied strain rate – particularly at failure – is still higher than the smallest strain rate applied in the present test series.

A regression of the data shown in Figure 3.4 with a logarithmic formulation yields an empirical estimation of $C(\dot{\varepsilon})$:

$$C(\dot{\varepsilon}) = \frac{\Delta\sigma(\dot{\varepsilon}, \varepsilon_i)}{\sigma_{init}(\dot{\varepsilon}, \varepsilon_i)} = q + m \cdot \log(\dot{\varepsilon}) \geq 0 \qquad \text{with } \dot{\varepsilon} \text{ in } [‰/\text{s}] \tag{3.5}$$

The coefficients q and m can be determined separately for each type of reinforcing steel and are reported in Table 3.2. As $C(\dot{\varepsilon})$ has to be positive to represent a physically meaningful stress decay, the equation is only valid for applied strain rates $\dot{\varepsilon} \geq \dot{\varepsilon}_{min} = 10^{-q/m}$. Table 3.2 also reports the minimum strain rate for the given coefficients.

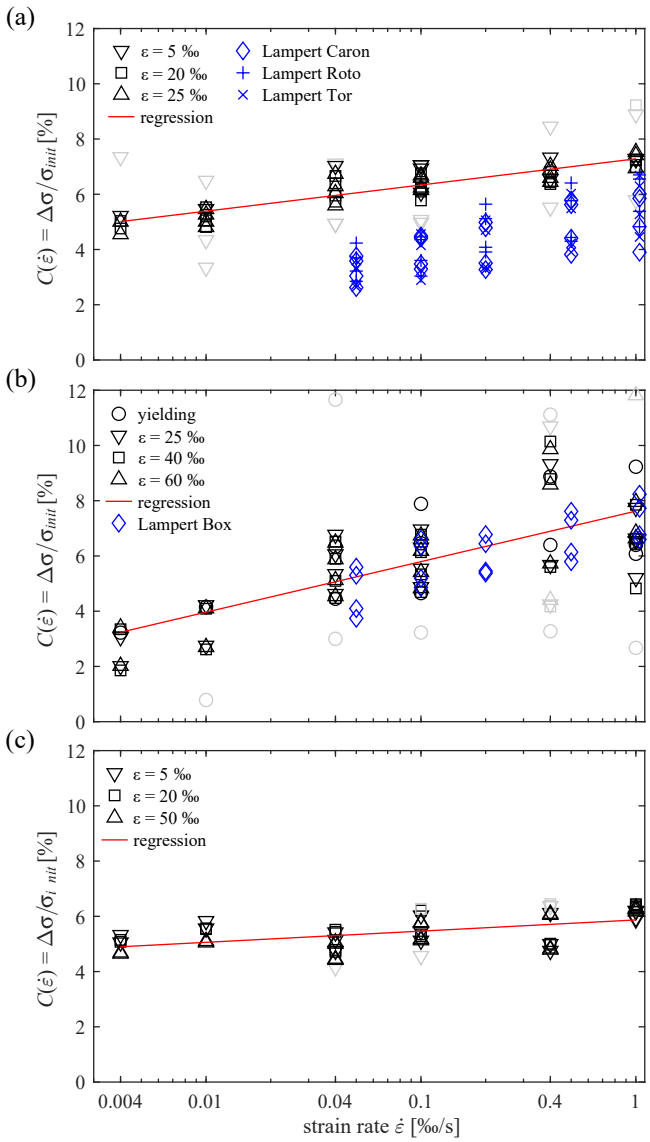

Fig. 3.4 – Normalised stress decay as a function of the applied strain rate in the tensile test. Experimental results are shown in black and grey, the corresponding regression line in red, and the results of Lampert et al. [98] in blue for comparison. (a) A1: hot-rolled, cold stretched reinforcing bars, coiled (CW); (b) A2: QST reinforcing bars, straight; (c) QST-R reinforcing bars, coiled.

The scatter of the data shown in Figure 3.4 differs depending on the reinforcing bar type. While the CW and QST-R series show a comparably low variation, the scatter in the QST series is higher, particularly for higher strain rates. Note that the static stress $\sigma_0(\varepsilon)$ for experiments with strain rates lower than 1 ‰/s was calculated using the procedure described in Section 3.3.2, which may affect the accuracy, and that the given regression coefficients are strictly speaking only valid for the tested samples or production batches of reinforcing steel. Nevertheless, the results can serve as an estimation for calculations using the characteristics of other batches of the same reinforcing bar type.

In Figure 3.4 the results of the experiments of Lampert et al. [98] are included in blue. Their test results obtained for the steel types Caron, Roto, and Tor are compared with the results of the CW series, as they are also cold-worked steels. The relaxation as a function of the strain rate was less pronounced in their tests compared to the CW series, although the slope of a possible regression is similar. The steel type Box is compared with the QST series, although it is not a quenched and self-tempered reinforcing steel, but a hot-rolled steel without further treatment (traded as “naturhart” in German). However, its stress-strain diagram is similar, showing a pronounced yield plateau at about 430 MPa, with a tensile

Tab. 3.2 – Model coefficients for different types of reinforcing steel in Equation (3.5).

		CW	QST	QST-R
q	[-]	0.0728	0.0762	0.0587
m	[-]	0.0095	0.0183	0.0041
$\dot{\varepsilon}_{min}$	[‰/s]	$2.2 \cdot 10^{-8}$	$6.9 \cdot 10^{-5}$	$4.8 \cdot 10^{-15}$

strength of 590 MPa at a strain of 17%. The results of normalised stress decay as a function of the strain rate are almost equal to the QST series.

It is worth noting the implications of the findings on the periodic quality monitoring of reinforcing steel. According to EN ISO 6892-1:2016, the strain rate for determining the tensile strength can be chosen freely among the values 0.25 ‰/s, 2.0 ‰/s or 6.7 ‰/s for method A (control of cross-head via extensometer) or up to 8 ‰/s for method B (control of cross-head via force measurement). To estimate the effect of these high strain rates, the normalised stress decay can be approximated using Equation (3.5), and the stress ratio between two different strain rates can be determined from Equation (3.4) for any given strain. Table 3.3 shows the results of these calculations for the admissible strain rates of EN ISO 6892-1:2016. Assuming that a batch of reinforcing bars exhibits a yield stress f_y of 490 MPa and a tensile strength f_u of 650 MPa at a strain rate of 0.25 ‰/s, a yield stress of approximately 505 MPa and a tensile strength up to 670 MPa will be measured at a strain rate of 8 ‰/s (QST reinforcing bar). With a given minimum threshold of 500 MPa for the yield stress [145], the same batch would either fail or pass the quality control, depending on which strain rate was applied for the tensile test. The authors therefore highly recommend indicating the applied strain rate for every tensile test and, eventually, including a correction factor for the strain rate used in a future revision of EN ISO 6892-1:2016.

3.3.4 Validation of proposed values for $C(\dot{\varepsilon})$

In Series A4, varying strain rates were applied during the tensile test of one reinforcing bar, similar to the experiments of [95]. In Figure 3.5, changes in strain rate at various strain levels and the corresponding sudden change in stress are clearly visible. With the values of Table 3.2 and Equations (3.4) and (3.5), these stress changes can be predicted using the stress before each change in strain rate. Therefore, this test can serve as a validation for the determined regression. Considering the variability of the results of tensile tests even in the same batch of reinforcing bars, the predicted stresses (red lines in Figure 3.5) due to changes in strain rate match the original data very well, except for the QST reinforcing bars at higher load levels.

Tab. 3.3 – Estimated normalised stress decay $C(\dot{\varepsilon})$ and stress ratio for various strain rates, and transformation to absolute stress values for yield stress and tensile strength, f_y and f_u, respectively.

$\dot{\varepsilon}$ [‰/s]	$C(\dot{\varepsilon})$ [%]			$\sigma(\dot{\varepsilon})/\sigma(\dot{\varepsilon} = 0.25‰/s)$ [-]			estimated f_y [MPa]			estimated f_u [MPa]		
	CW	QST	QST-R	CW	QST	QST-R	CW	QST	QST-R	CW	QST	QST-R
0.25	6.7	6.5	5.6	1.000	1.000	1.000	490	490	490	650	650	650
2.0	7.6	8.2	6.0	1.009	1.018	1.004	495	499	492	656	662	653
6.7	8.1	9.1	6.2	1.015	1.029	1.006	497	504	493	660	669	654
8.0	8.1	9.3	6.2	1.016	1.030	1.007	498	505	493	660	670	654

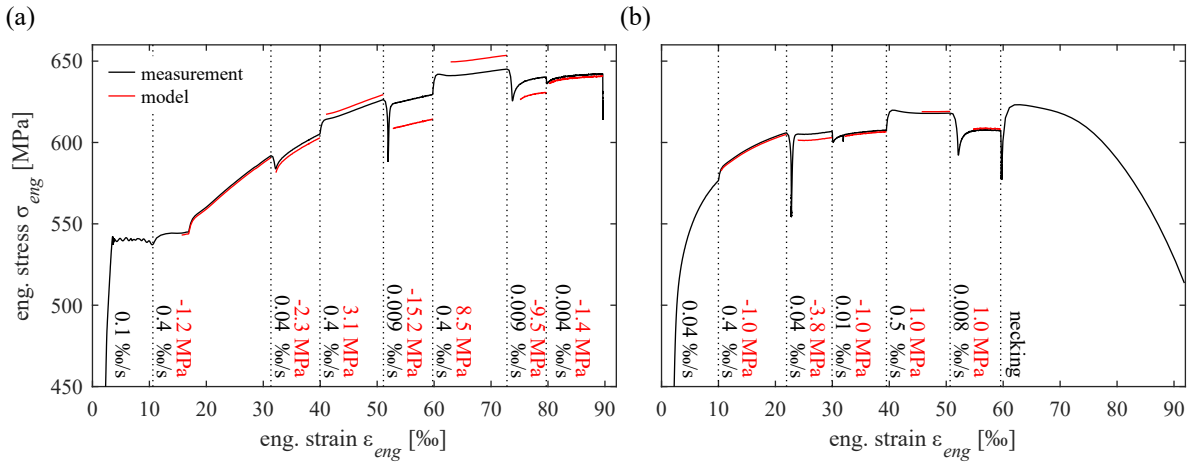

Fig. 3.5 – Stress-strain diagrams of tensile tests of Series A4 at varying strain rates as indicated. In red, the modelled stresses and the deviation from the experimental curve are shown. (a) QST reinforcing bar; (b) CW reinforcing bar.

3.4 Conclusions

This study investigated the effect of quasi-static strain rates between 0.004 ‰/s and 1.0 ‰/s on the stresses in the plastic range for reinforcing bars of three different types (hot rolled & cold-stretched, hot-rolled & QST in straight bars, and hot-rolled & QST on coils). Based on 41 tensile tests with various quasi-static strain rates, it was found that compared to static stresses, dynamic stresses increase logarithmically up to 8% with increasing strain rate. Furthermore, experiments confirmed that the preceding strain rate does not influence the static stress, but affects the relaxation time required to reach the static stress when pausing a displacement-controlled test. A model was proposed which describes the relation between static and dynamic stress by a function $C(\dot{\varepsilon})$ only depending on the strain rate. The coefficients of this function depend on the material characteristics and may vary for different steel types, maybe even among different production batches. Nevertheless, the values given in Table 3.2 can be used as first estimates. The model matches very accurately with the results of the validation tests.

The implications of the findings on the periodic quality monitoring of reinforcing steel production were discussed. Since the definition of yield stress and tensile strength is highly dependent on the applied strain rate, it is highly recommended to document the strain rate used for each tensile test. The authors suggest implementing a correction factor for the strain rate used in a future version of the standard EN ISO 6892-1:2016.

Furthermore, the findings of this study related to the influence of strain rate on the stress-strain behaviour of reinforcing bars are an important step towards a better understanding of the overall response of corroded reinforcing bars. They allow to reliably separate effects induced by the applied strain rate in experiments on corroded reinforcing bars from other effects induced by the corrosion damage. One of these effects, the influence of distinct microstructure layers in QST reinforcing bars, has been investigated in a parallel study, and is discussed in a companion paper [71]; further effects, such as the three-dimensional stress states near localised corrosion pits, or bending moments due to a shift of the neutral axis in case of unilateral damage, are currently being researched by the authors, in order to finally be able to accurately assess the residual safety of corroded reinforced concrete structures.

Notation

$C(\dot{\varepsilon})$	Strain rate coefficient, $C(\dot{\varepsilon}) = 1 - \sigma_0(\varepsilon)/\sigma_{init}(\dot{\varepsilon},\varepsilon)$
b	Magnitude of Burgers vector
f_y, f_u	Steel yield stress, steel tensile strength
k	Dislocation orientation factor (Schmid factor)
m, n, q	Fitting parameters
$\overline{v}$	Mean dislocation velocity
t	Time
$\dot{\gamma}_{pl}$	Macroscopic plastic shear strain rate
ε, ε_{eng}	Steel strain (in general, engineering)
$\dot{\varepsilon}$, $\dot{\varepsilon}_{el}$, $\dot{\varepsilon}_{pl}$	Strain rate (total, elastic amount, plastic amount)
ρ_m	Mobile dislocation density
σ, σ_{eng}	Steel stress (in general, engineering)
$\Delta\sigma(t)$	Steel stress decay over time
$\Delta\sigma(\dot{\varepsilon},\varepsilon)$	Steel stress decay for $t \to \infty$, given strain rate $\dot{\varepsilon}$, and given strain level ε
$\Delta^*\sigma(\dot{\varepsilon}_1,\dot{\varepsilon}_2,\varepsilon)$	Difference in steel stress decay for two different strain rates $\dot{\varepsilon}_1$ and $\dot{\varepsilon}_2$ at a given strain level ε
$\sigma_0(\varepsilon)$, $\sigma_{0,ref}(\varepsilon)$	Static stress and reference static stress at a given strain level ε
$\sigma_{init}(\dot{\varepsilon},\varepsilon)$	Initial stress before stress decay for given strain rate $\dot{\varepsilon}$ and given strain level ε
τ	Microscopic shear stress

4 Influence of cross-section loss on the stress-strain characteristics of corroded quenched and self-tempered reinforcing bars

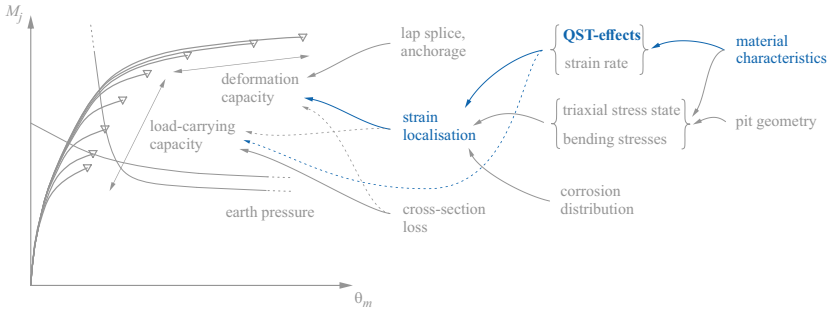

This chapter presents the findings of a comprehensive series of tensile tests on hot rolled, quenched and self-tempered (QST) reinforcing bars to investigate the influence of the varying mechanical characteristics exhibited by the different microstructure layers over the cross-section. Corroding QST bars change their apparent mechanical properties with increasing cross-section loss and thus influence the load-carrying and deformation capacity of a corresponding reinforced concrete member. The chapter corresponds to the published version of the following article:

> Haefliger, S. & Kaufmann, W. 'Influence of cross section loss on the stress-strain characteristics of corroded quenched and self-tempered reinforcing bars,' *Construction and Building Materials*, vol. 282, p. 122598, 2021. doi: 10.1016/j.conbuildmat.2021.122598.

The lead author (Severin Haefliger) planned and conducted the experiments, and developed the presented modelling approaches based on the obtained experimental data under the supervision of the second author (Walter Kaufmann).

Abstract

Many ageing reinforced concrete structures are affected by severe damage of reinforcing bars due to corrosion. Accurate knowledge of the stress-strain characteristics of the installed reinforcing bars is an indispensable prerequisite for the realistic assessment of the structural safety of such structures. The reduction in cross-section does not only reduce the load-bearing capacity of the reinforcing bars, but in case of hot-rolled, quenched and self-tempered (QST, process branded as "Tempcore®" or "Termex®") reinforcing bars also changes their structural characteristics. Since these bars exhibit three distinct microstructures in core, transition zone and outer annulus, each with different mechanical characteristics, the overall stress-strain behaviour of a corroded QST reinforcing bar depends on the composition of its residual area, which varies significantly with ongoing corrosion. As QST reinforcement is widely used in concrete structures worldwide, this effect is of high importance for any structural safety assessment of structures affected by corrosion.

This study investigates the influence of microstructure on the strength and ductility of QST reinforcing bars subjected to axisymmetric cross-section loss. In a comprehensive experimental campaign, 31 tensile tests on QST reinforcing bars with continuously reduced diameters were conducted, exploring the contribution of the concentric layers of the cylindrical cross-section to the overall behaviour. Experimental results indicate a pronounced variation of strength and ductility over the cross-section. Based on these observations, a simplified model was developed for the relationship between loss of cross-section and mechanical characteristics. A validation shows excellent agreement between the model and experimental data.

4.1 Introduction

4.1.1 Overview of the effects of corrosion and on the focus of this study

The reinforcement of many ageing concrete structures is affected by local and /or uniform reinforcement corrosion due to chloride attack and carbonation, respectively. Corrosion reduces the residual load-bearing capacity by several mechanisms [14, 16, 34]. These affect the reinforcement, the concrete, and the interaction between reinforcement and concrete. The initial passive layer of the reinforcement, caused by the high alkalinity of concrete, is either attacked by carbonation of concrete or the presence of chlorides, leading to a uniform or local reduction of the reinforcing bars' cross-section, respectively. Subsequently, concrete may be damaged by splitting or spalling due to the volume expansion of the corrosion products [14, 16, 26], leading to a reduction of the concrete area. Furthermore, bond between reinforcement and concrete is reduced as a result of the reduced cross-section of the reinforcing bars, lubricating effects of the corrosion products, and the presence of cracks parallel to the reinforcement [24, 26, 56], which potentially leads to, e. g. anchorage failures and larger crack openings.

Given this multitude of corrosion effects, the structural safety of corroded structures clearly does not depend exclusively on the residual mechanical properties of the corroded reinforcing bars. Nonetheless, accurate knowledge of the stress-strain characteristics of damaged reinforcing bars is a prerequisite to determine the load-bearing and deformation capacity of corroded structures. The following main effects on this behaviour were identified by the authors: (i) the applied strain rate [69, 95, 98]; (ii) various steel microstructures within the cross-section in quenched and self-tempered (QST) reinforcing bars [11, 12, 55, 82, 139]; (iii) a three-dimensional stress state near the damage zone for local corrosion [80]; and (iv) bending effects for localised corrosion pits due to a shift in the neutral axis [80, 166].

The present paper addresses the effect of cross-section loss on the stress-strain characteristics of QST reinforcing bars, which contain distinct microstructure layers within their cross-section, focusing on the differences in the mechanical characteristics of the distinct layers. Due to these differences, QST reinforcing bars alter their overall mechanical behaviour continuously when corroding, depending on the ratio of areas of the residual layers. Few studies [55, 139] focused on this effect, and only one recent study [82] succeeded in giving a sound mechanical explanation of the resulting stress-strain behaviour.

In order to isolate this influence from the remaining effects, which are closely related to the geometry of the corroded reinforcing bars and have to be superimposed later on, an experimental campaign on reinforcing bars with axisymmetrically reduced cross-section was carried out. The experiments indicate a pronounced variation of strength and ductility over the cross-section. Based on these findings, a simplified model is developed to describe the relationship between the loss of cross-section and mechanical characteristics.

4.1.2 Effects not considered in this study

The further effects (i, iii, iv) mentioned above are beyond the scope of the present paper. The effect of strain rate (i), known for decades, has been revisited and complemented by data for modern reinforcing

steels in a parallel study, and is discussed in a companion paper [69]. Three-dimensional stress states (iii) and bending effects (iv), which are closely related to the geometry of the corroded reinforcing bar and particularly relevant for natural corrosion, are briefly discussed in the following, along with two additional aspects specific to QST reinforcing bars.

Doubtlessly, reinforcing bars embedded in concrete do not corrode axisymmetrically along the bar axis, particularly in the case of pitting corrosion. Despite the widely recognised importance of the pit geometry for the residual reinforcement characteristics, in most studies, the implications of corrosion are treated by means of statistical approaches [10, 20, 46, 53, 83], correlating the global mass loss with the global mechanical properties of the reinforcing bars; this is clearly of limited use for local corrosion. Only few studies [8, 58, 86, 102, 166] consider the variation of the mechanically relevant geometrical properties of corroded reinforcing bars (A_{eff}, I_{yy}, I_{zz}), and even less [8, 58, 166] correlate these properties with experimental results from tensile tests. To the authors' knowledge, Hingorani et al. [80] were the only ones who theoretically studied the effects of bending due to non-axisymmetric corrosion, and investigated the presence of a three-dimensional stress state for localised corrosion. Such investigations on a sound mechanical basis are essential to understand the implications of the pit geometry on the mechanical characteristics of corroded reinforcing bars. Authors are currently working on appropriate models following this approach.

In QST reinforcing bars, corrosion implies further, potentially negative effects on the load-deformation behaviour apart from the different mechanical characteristics of the distinct layers studied in this paper. These effects include a different corrosion behaviour than observed for reinforcing bars with uniform microstructure [21], affecting the pit geometry and hence, the local mechanical behaviour. Furthermore, the production process may cause surface micro cracks and impurities within the microstructure, which in combination with chloride ingress have been associated with stress corrosion [11, 12]. Some studies also point to possible issues related to a potential instability between the different phases of QST reinforcing bars [11, 13]. All these effects are, however, beyond the scope of the present paper.

4.1.3 Production processes and related implications of cross-section loss

Today, mainly two production processes for reinforcing bars are used: Hot-rolling and cold-working (CW) and hot-rolling, quenching and self-tempering (QST). In the CW process, the hot-rolled reinforcing bar slowly cools down after the last rolling, which leads to a homogeneous microstructure over the cross-section, consisting of a mixture of ferrite and perlite with high ductility but low yield stress. To increase the strength, bars are mechanically stretched (cold-worked) after cooling. Due to the plastic deformation induced by the process, such reinforcing bars lack a pronounced yield plateau and exhibit a lower strain at peak stress, as well as a reduced strain hardening, i. e. a lower ratio of tensile strength to yield stress.

Though first produced already in the 1970s [137], QST reinforcing bars have drawn attention only recently, as they have been produced in large quantities mainly since the early 1990s. In the QST process, the hot-rolled reinforcing bar undergoes a brief, controlled water cooling (quenching), which leads to the formation of high strength, low-ductile martensite at the outer part of the bar. This outer annulus of the cross-section is then tempered by the still hot ferritic/perlitic core with lower strength but high ductility. The final reinforcing bar is a composition of ferrite/perlite in the core, bainite in the transition zone and martensite in the outer annulus, combining the mechanical characteristics of these steel microstructures. Hence, a pronounced yield plateau, a higher strain at peak stress and a higher strain hardening are observed for this type of reinforcing bar. Due to these favourable characteristics and the efficient production process, QST reinforcing bars have become the most used type of reinforcement in many regions worldwide.

The mechanical characteristics of QST reinforcing bars with inhomogeneous microstructure over their cross-section thus depend on the characteristics of the different steel microstructures and their relative areas. If a reinforcing bar is damaged, e. g. due to corrosion, its mechanical characteristics alter – continuously in case of progressing corrosion –, starting at the martensitic outer annulus with its higher

strength. Hence, the reduction in load-bearing capacity is higher than the loss of cross-section. Accurate knowledge of the behaviour of damaged QST reinforcing bars is thus essential to accurately assess the residual load-bearing and deformation capacity of structures affected by corrosion.

4.1.4 Current state of research on the static implications of the different microstructures for QST reinforcing bars

Fernandez et al. [55] carried out tensile tests on QST reinforcing bars with initial diameter Ø12 mm and various reduced diameters, and reported variable strengths of the layers (annuli) over the cross-section. They succeeded in calculating the yield stress and tensile strengths of each layer and built up a model based on these stress values. However, they completely ignored the influence of the differing microstructure composition on the ductility of the reinforcing bar. Santos and Henriques [139] conducted tensile and hardness tests on QST reinforcing bars with an initial diameter Ø20 mm and various reduced diameters. They reported the yield stress and tensile strength of the specimens and the hardness over the diameter, which allows for determining the boundaries of the distinct microstructure layers. Additionally, the observed strains at yielding and peak stress are documented, but the results did not indicate any variation regarding the distinct layers. Cadoni et al. [31] thoroughly investigated the hardness over the diameter of a QST reinforcing bar Ø40 mm, including a specification of the microstructure. Moreover, they extracted samples of diameter Ø6 mm and 40 mm length out of the different layers, on which they performed tensile tests. They provide stress-strain diagrams of the different layers, clearly indicating the higher strength and lower ductility of the outer annulus compared to the core and the undamaged reinforcing bar. Rocha et al. [134] performed hardness tests over the diameter and a specification of the microstructure. Hortigón Fuentes et al. [82] performed Vickers hardness tests over the diameter and tensile tests on QST reinforcing bars with an initial diameter Ø14 mm and with reduced diameter. To the authors' knowledge, they were the first and so far only to comprehensively report and discuss the behaviour of the distinct microstructure layers, providing some stress-strain diagrams of the layers' behaviour as well as a finite element model.

Although the importance of the topic was recognised by the research community about a decade ago and several studies and experimental campaigns were carried out, a sound mechanical modelling approach for the influence of the distinct microstructure on the behaviour of corroded QST reinforcing bars was established only recently [82]. This study presents a similar, but more general approach of a consistent mechanical model, which is based on the experimental results of the conducted tensile tests. It is capable of representing the stress-strain behaviour of the distinct microstructure layers and the thereof composed reinforcing bar. The model therefore allows investigating the effects of inhomogeneous microstructure for corroded QST reinforcing bars without any restraints regarding damage geometry. Nevertheless, it is important to notice that other relevant effects in the case of pitting corrosion (pit geometry, impurities in microstructure) are not investigated in this study and thus not covered by the model.

4.2 Experimental programme

The experimental campaign was carried out in the structural laboratory at ETH Zurich and comprised 31 specimens of QST reinforcing bars, similar to those investigated in [69]. The specimens with a nominal (initial) diameter of 20 mm were all taken from the same production batch. Over a length of 250 mm, their cross-section was reduced axisymmetrically by machining on a lathe (turning) to target remaining diameters of 10 mm (3 bars); $\{11, 12, 13, 14, 15, 16, 17\}$ mm (2 bars each); 18 mm (6 bars); and $\{18.5, 19\}$ mm (2 bars each). As reference, 4 bars were tested without any diameter reduction. The total specimen length was generally 500 mm; for small remaining diameters, it was reduced to improve machining precision (to 370 mm for diameters 16 and 17 mm and to 310 mm for smaller diameters, respectively). Constant cooling of the reinforcing bars during turning prevented heat inflow and ensured

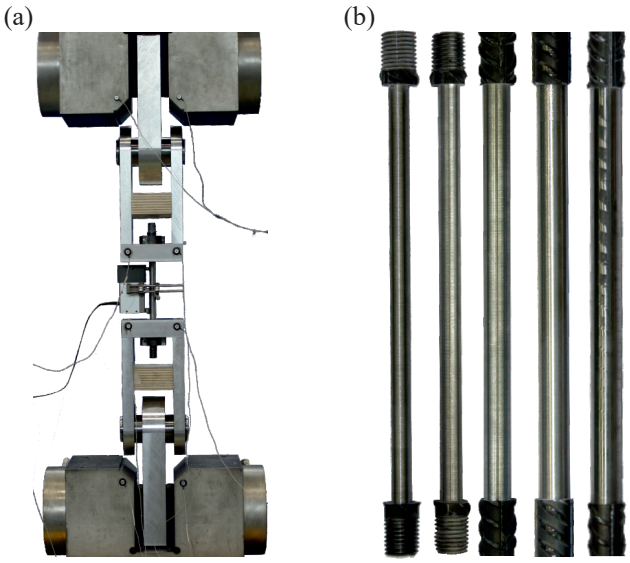

Fig. 4.1 – (a) Heads of universal testing machine with specimen, spherical hinges and LVDT; (b) specimens with residual diameter 11, 13, 16, 18, and 18.5 mm.

that steel microstructure and steel characteristics were not altered. The shape of all reinforcing bars was scanned before testing using an optical three-dimensional scanner (ATOS Core by GOM). This provided a very accurate measurement of the residual diameters, which differed slightly from the target values. The geometry of diameter reduction was chosen to isolate the effect of the different mechanical characteristics of the distinct microstructure layers, rather than trying to simulate the pit geometry of reinforcing bars affected by natural pitting corrosion.

When testing short specimens, it is essential to avoid the influence of bending moments due to any geometrical misalignment of the machine heads or the clamping. For this purpose, load introduction heads with spherical hinges were installed on the tensile testing machine (see Figure 4.1). Specimens were connected to the load introduction heads using stiff slotted steel plates ("two-part washers"). They were loaded displacement controlled until failure at a constant strain rate of 0.1 ‰/s, using an LVDT of 100 mm gauge length for elongation measurement in the part with reduced diameter. Additionally, for this type of reinforcement and for comparison for a cold-worked reinforcing bar presented in [69] (referred to as CW reinforcing bar), Vickers hardness distribution over the cross-section was determined on cut and grinded samples, and the microstructure was analysed after polishing and edging (Nital 3% for 5 s), using a microscope [27].

4.3 Results and Discussion

4.3.1 Microstructure analysis and Vickers Hardness Test

Cuts of the reinforcing bars of this test series and of a CW reinforcing bar reveal the distinct microstructure of the two types of reinforcing bars. Figure 4.2 shows an enlargement of the surface of the different prepared cuts and photos of the corresponding samples (right lower corners). In Figures 4.2(a) and (c), the various material layers of the QST reinforcing bars are visible even by eye (photos), whereas the CW reinforcing bar visually shows a homogeneous surface (Figure 4.2(b)). Figures 4.2(a) and (c) show enlargements of the microstructure of the QST reinforcing bar, for the central zone and for the edge zone. The edge zone exhibits needle-like crystals which are typical for martensite [27]. The central zone exhibits a structure with larger crystals, typical for a mixture of ferrite and perlite [27]. The same crystal structure is found over the whole cross-section for the CW reinforcing bar, see Figure 4.2(b). A Vickers hardness test performed on the QST reinforcing bar (Figure 4.2(d)) exhibits a zone with an

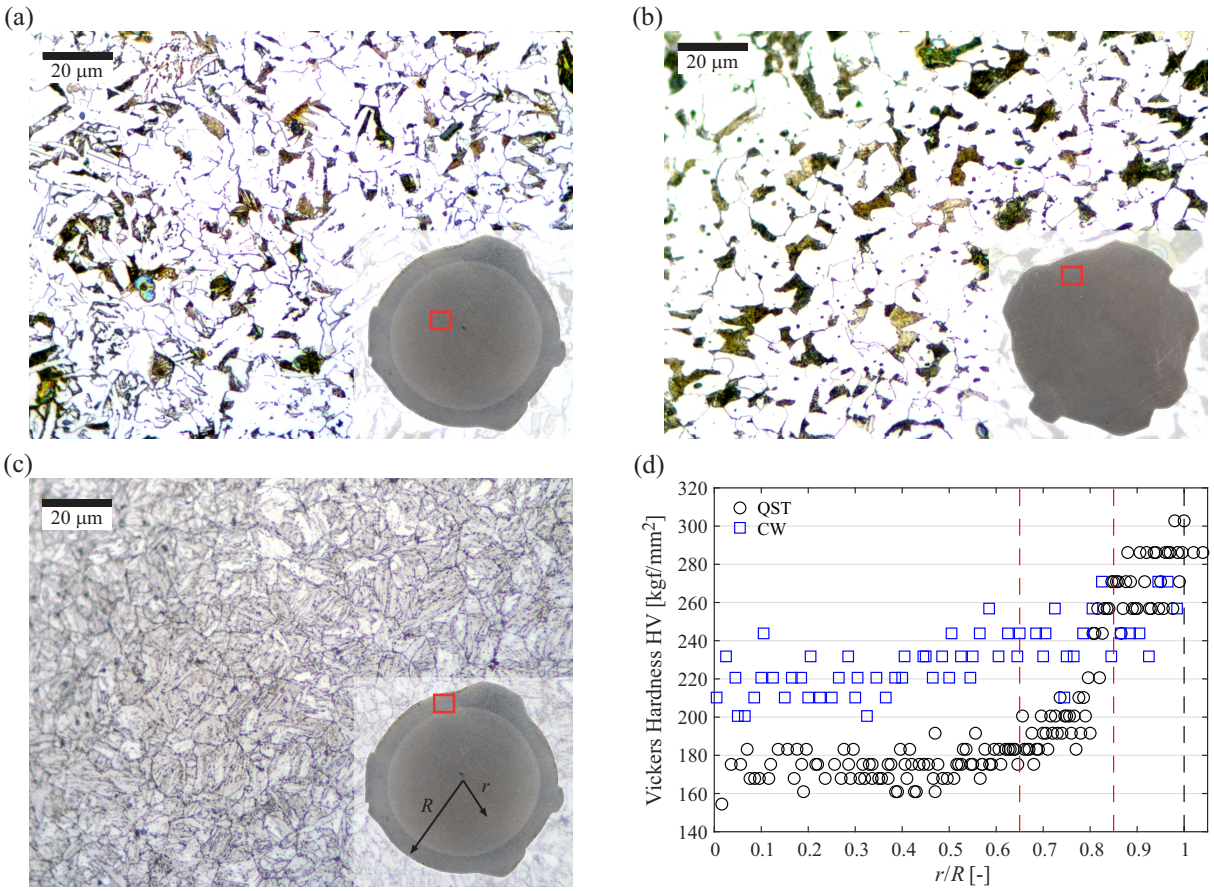

Fig. 4.2 – (a) Microstructure in the centre of QST reinforcing bar; (b) microstructure close to edge of CW reinforcing bar; (c) microstructure close to edge of QST reinforcing bar; (d) results of Vickers hardness tests over cross-section for QST and CW reinforcing bar. Red lines denote layer boundaries of core, transition zone and outer annulus of QST reinforcing bar. For $r/R > 1$, values correspond to the hardness of the adjacent rib.

almost constant hardness of 170 kgf/mm^2 up to a radii ratio $r_{b1}/R = 0.65$, a zone of increasing hardness up to $r_{b2}/R = 0.85$, followed by a zone of again fairly constant hardness of 270 kgf/mm^2. The hardness of the various zones additionally indicates the distinct material layers of the QST reinforcing bars and is consistent with the results of the microstructure analysis. A comparison of the location of the layer boundaries with literature values in Table 4.1 shows a good agreement. Figure 4.2(d) also compares the hardness over the cross-section of the QST and CW reinforcing bars, and illustrates that the CW reinforcing bar exhibits a fairly constant hardness over its cross-section, confirming its uniform microstructure.

Tab. 4.1 – Layer boundaries between core and transition zone, and transition zone and outer annulus, obtained from Vickers Hardness tests in various test series.

Researcher	Cadoni [31]	Cadoni [31]	Santos [139]	Fernandez [55]	Bautista [21]	This study
diameter $2R$ [mm]	40	32	20	12	12	20
core - transition zone r_{b1}/R [-]	0.5	0.5	0.6	0.66	0.79	0.65
transition zone - outer annulus r_{b2}/R [-]	0.85	0.8	0.8	0.92	0.88	0.85

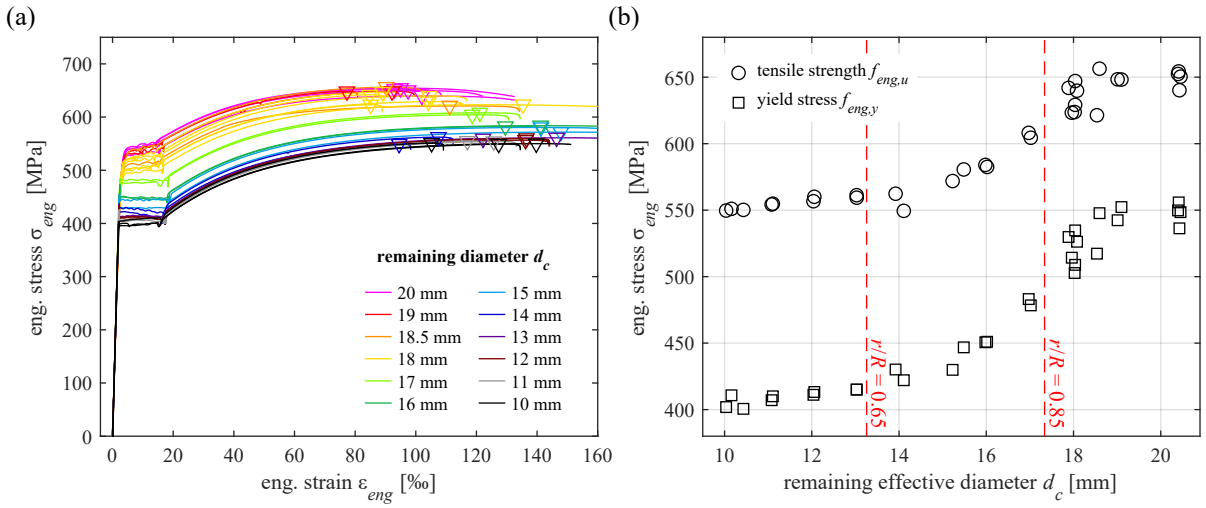

Fig. 4.3 – (a) Stress-strain diagram for specimens with varying residual diameter d_c. Triangles indicate the peak stress and corresponding strain. (b) residual effective diameter of specimens and corresponding yield stress and tensile strength. Red lines denote layer boundaries of core, transition zone and outer annulus.[1]

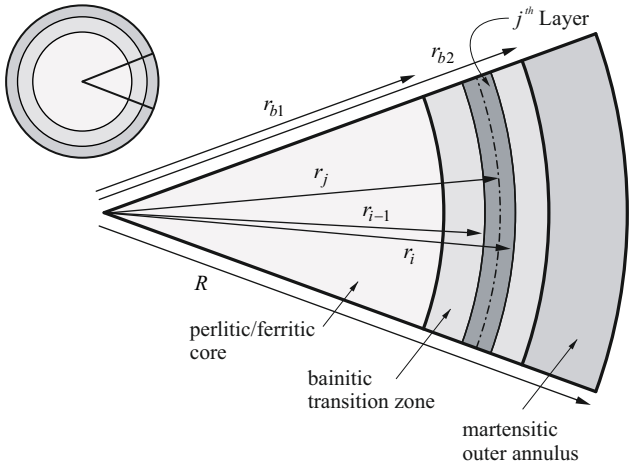

Fig. 4.4 – Definition of variables for the calculation of the characteristics of the distinct layers.

4.3.2 Results of tensile tests

Figure 4.3(a) shows the results of the tensile tests on the specimens for varying residual diameters. Stresses are calculated using the true (as opposed to nominal) residual cross-sectional area determined by laser scanning. It can be seen that the yield stress and tensile strength decrease significantly with reduced residual diameter, while the strain at peak stress exhibits a slight increase. In Figure 4.3(b), the measured yield stresses and tensile strengths are plotted against the residual effective diameter d_c, confirming the higher strength with increasing (i. e. less reduced) diameter. The vertical red lines correspond to diameter ratios $r/R = 0.65$ and 0.85, respectively (with $R = 20.20\,\text{mm}$ being the true equivalent initial bar radius, determined by laser scanning). They separate the three distinct regions determined by Vickers hardness tests. For diameters below $d_c = 13.1\,\text{mm}$ ($= 2\text{x}\ 0.65R$), as well as diameters above $d_c = 17.2\,\text{mm}$ ($= 2\text{x}\ 0.85R$), the tensile strength is fairly constant, with a transition zone of increasing strength between these diameters. This result substantiates the findings of the Vickers hardness tests.

To determine the mechanical characteristics of the distinct layers (annuli), the contribution of Layer j, bounded by diameters $d_{i-1} = 2r_{i-1}$ and $d_i = 2r_i$ (see Figure 4.4), to the total force of the reinforcing bar

[1] The published article contains an error in the legend of Figure 4.3(b) (reversed legend entries). The legend was corrected accordingly.

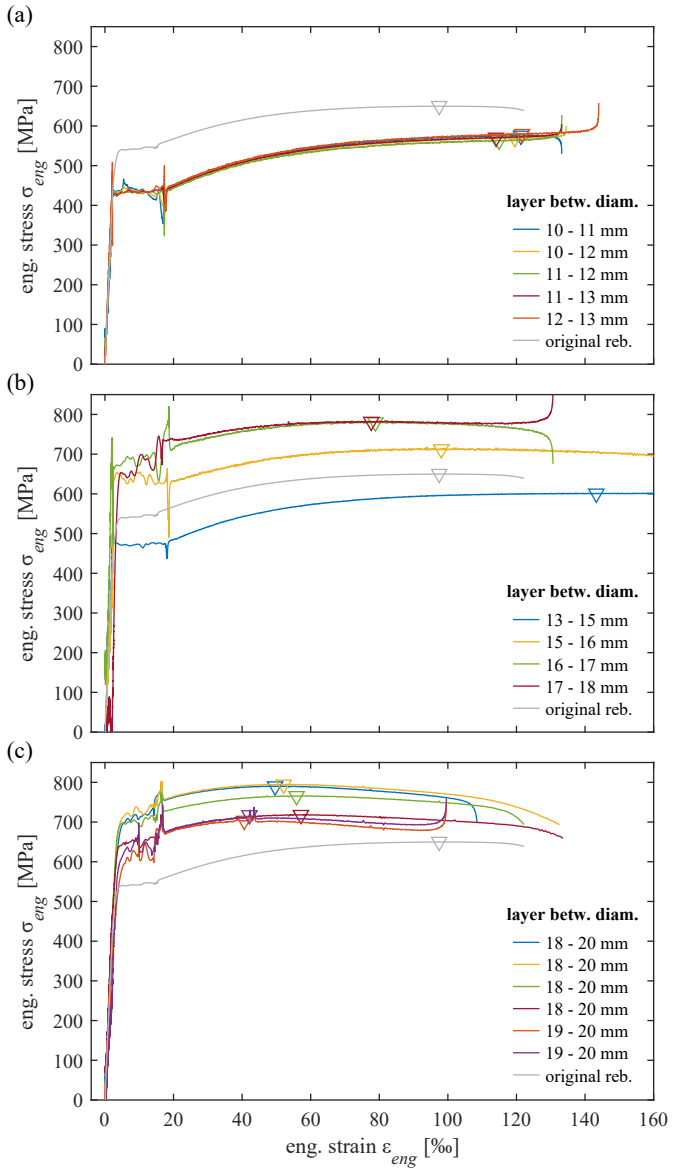

Fig. 4.5 – Calculated stress-strain diagrams for (a) core, (b) transition zone and (c) outer annulus. Triangles indicate peak stress and corresponding strain. In grey, the curve of an original reinforcing bar of the same batch is shown for comparison.

is calculated at specific strain values ε using Equation (4.1):

$$\sigma_j(\varepsilon) = \frac{A_i\sigma_i(\varepsilon) - A_{i-1}\sigma_{i-1}(\varepsilon)}{A_i - A_{i-1}} \tag{4.1}$$

Here, $A_i\sigma_i(\varepsilon)$ denotes the measured force at a specific strain ε for a specimen with residual effective diameter d_i, whereas $A_{i-1}\sigma_{i-1}(\varepsilon)$ denotes the measured force at the same strain ε for a specimen with the consecutive smaller diameter d_{i-1}. The difference in force is attributed to Layer j, having an area of $A_i - A_{i-1}$.

Repeating this calculation for various strain values ε and all tested diameters, one gets the stress-strain diagrams for each Layer j shown in Figures 4.5(a)-(c). All layers up to diameter $d_c = 13\,\text{mm}$ exhibit essentially the same mechanical behaviour; they belong to the perlitic/ferritic core of the reinforcing bar. The results for yield stress and tensile strength match the values of the directly obtained stress-strain diagrams of the corresponding specimens, see Figures 4.3(a) and (b). With increasing diameter,

layers between $d_c = 13$ and 18 mm show an increasing yield stress and tensile strength and a decreasing strain at peak stress. The outer layers, between diameter $d_c = 18$ mm and the initial diameter, again exhibit a more uniform mechanical behaviour. From Figure 4.5(c), it can be seen that the strains at peak stress are very similar, but the yield stress and the tensile strength in the outer layers vary more. The observed differences are presumably due to variations of the martensite content in the outermost layers: The process of a uniform mechanical reduction of the cross-section is initially very demanding due to the ribs, causing uncertainty when determining the centre of the bar area. Hence, the latter may deviate from the bar axis, such that not all material that is removed is indeed part of the martensitic outer annulus. Although having the same effective diameter, these specimens thus exhibit different tensile strengths. However, the exhibited stress values of the outer annulus (between 700 and 800 MPa) are in all cases significantly higher than those of the reinforcing bar without any reduction in cross-section (677 MPa, see grey curve in Figure 4.5). This corresponds to results commonly found in literature ([31, 55, 82]). The undamaged reinforcing bar can be interpreted as a composition of the different layers, and its stress-strain behaviour thus equals the integral of all layer characteristics, i. e. the sum of layer characteristics weighted by their corresponding areas when using discrete layers. Consequently, the martensitic outer annulus has to exhibit a strength higher than the composite bar, as the ferritic/perlitic core exhibits a strength lower than the one of the composite bar.

Comparing the stress-strain diagrams in Figure 4.5, one observes that a pronounced yield plateau exists for the ferritic/perlitic core and the transition zone up to $d_c = 17$ mm, whereas the martensitic outer annulus shows a behaviour similar to hot-rolled and cold-stretched reinforcing bars with a gradual transition to hardening at the end of the elastic phase, lacking a yield plateau.

A substantial difference in the strain at peak stress is visible when comparing the results of the martensitic layer (Figure 4.5(c), $\varepsilon_{eng,mart}(f_{eng,u}) \approx 60‰$) and those of the undamaged reinforcing bar (Figure 4.5(c), grey line, $\varepsilon_{eng,tot}(f_{eng,u}) \approx 100‰$). In the engineering stress-engineering strain diagram – as commonly used in structural engineering –, this point marks the end of uniform elongation in a tensile test, i. e. the beginning of necking in the failure zone, and corresponds to the tensile strength of the specimen, since engineering stresses are related to the initial, constant area. Nevertheless, the material itself undergoes much higher stresses in the necking phase if the true area $A(\varepsilon)$ is considered [136]. If strain compatibility without slip between layers is postulated for the entire reinforcing bar during a tensile test, true strains are equal across any cross-section and consequently, the martensitic layer is stretched beyond its strain at peak engineering stress. As in the experiments neither cracks on the specimens' surface nor local necking were observed, it is highly probable that at strains beyond $\varepsilon_{eng,mart}(f_{eng,u})$, the area of the martensitic layer – supported by the ferritic/perlitic core – was reduced uniformly, leading to an increase in true stress. As soon as the tensile strength of the ferritic/ perlitic core is reached at higher strains, necking over the entire cross-section occurred at the weakest point along the reinforcing bar, leading to a failure of the whole reinforcing bar. Hortigón Fuentes et al. [82] independently set up the same hypothesis, supported by experimental indications obtained from metallographic measurements of the thicknesses of core and outer annulus.

Figure 4.6(a) shows the true stress-true strain diagram for the layers between diameter d_c 18 and 20 mm (similar to Figure 4.5(c), where conventional engineering stresses and strains were used). The general shape of the curve is not altered, but the strain at peak stress increases substantially (compare grey lines in Figure 4.6(a)). The conversion from engineering to true stresses and strains was carried out using the relationships:

$$\varepsilon_{tr} = \ln(1 + \varepsilon_{eng}) \tag{4.2}$$

$$\sigma_{tr} = \sigma_{eng}(1 + \varepsilon_{eng}) \tag{4.3}$$

where Equation (4.2) can be derived by solving the differential equation of the true strains $d\varepsilon_{tr} = dl/l$ [136], and Equation (4.3) follows from the assumption of constant volume [136]. Hence, these equations apply only as long as no local necking (which involves the formation of voids) occurs, i. e. for

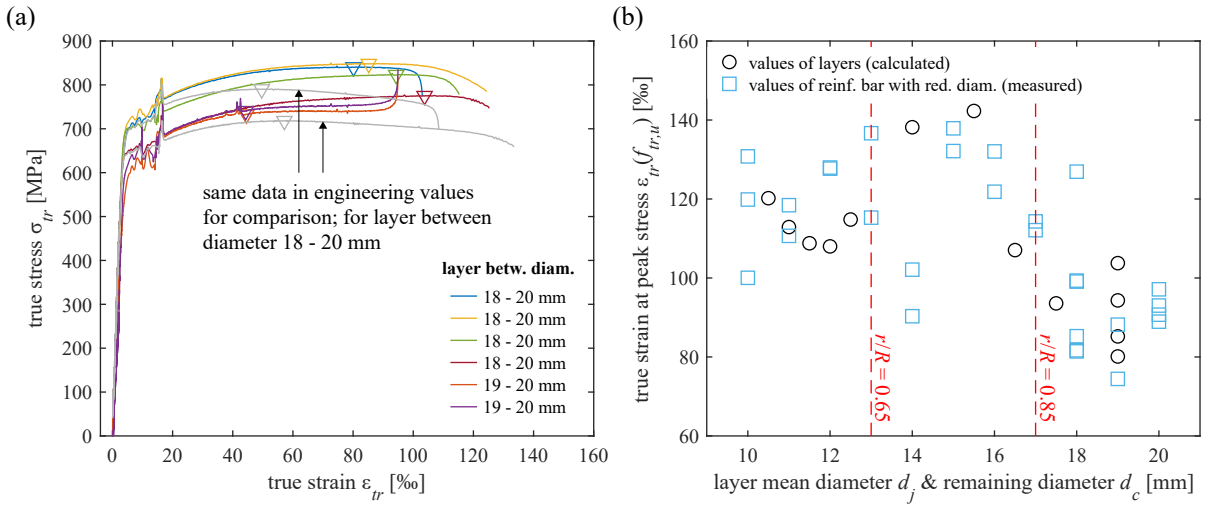

Fig. 4.6 – (a) Response of outer annulus in true stress and strain. Triangles indicate peak stress and corresponding strain. (b) Calculated true strain at true tensile strength for different layers with 1 mm thickness depending on their position (mean diameter $d_j = 2r_j$ acc. to Figure 4.4) and results of tensile tests for specimens with corresponding residual diameter d_c.

$\varepsilon_{tr,max} \leq \ln\left(1+\varepsilon_{eng,tot}(f_{eng,u})\right) \approx \ln(1+0.1) = 0.095$, with $\varepsilon_{eng,tot}(f_{eng,u})$ = strain at peak stress of the undamaged reinforcing bar in engineering values. This value is reached shortly after passing the maximum true stress in Figure 4.6(a).

Figure 4.6(b) compares the true strains corresponding to the true tensile strength of the distinct layers (calculated values) to the results of the tensile tests (measured values). It can be seen that for the martensitic outer annulus between diameter $d_c = 18$ and 20 mm, true strains closely match the true strains of the composite reinforcing bar. This result supports the hypothesis that the martensitic outer annulus is strained above its strain at peak stress determined from the engineering stress-strain diagram, as outlined in the previous section. Since the elongation beyond peak engineering stress of the outer annulus is controlled by the more ductile perlitic/ferritic core, its true strains at peak true stress have to be higher than in engineering values, which represent the behaviour of the material without the support of the core (and for which the true strains at peak true stress are always smaller than in engineering values, see Equation (4.2)).

4.3.3 Constitutive models for ferritic/perlitic core and martensitic outer annulus

In the following, constitutive relationships for the perlitic/ferritic core and the martensitic outer annulus are proposed, that will subsequently be used to model the stress-strain behaviour of the entire reinforcing bar composed of these two materials and bainite. Note that the basic characteristics (yield stress, tensile strength and corresponding strains at yielding, onset of hardening and tensile strength, respectively) have to be determined based on the true stress-true strain diagrams. They cannot be directly back-calculated from the values obtained using engineering stress-strain diagrams as outlined below. However, once the basic values have been obtained from the stress-strain diagram in true values, they can be converted back to their equivalent points in engineering values using Equations (4.2) and (4.3).

The following equations are used to define the constitutive relationships for the perlitic/ferritic core (see Figure 4.7 for notation):

$$\begin{aligned} &\text{elastic phase, i. e. } 0 \leq \varepsilon_{tr} \leq \varepsilon_{tr,y} = \ln\left(\frac{1+\sqrt{1+4f_{tr,y}/E_s}}{2}\right): \\ &\sigma_{tr} = E_s\varepsilon_{eng}\left(1+\varepsilon_{eng}\right) = E_s e^{\varepsilon_{tr}}\left(e^{\varepsilon_{tr}}-1\right) \end{aligned} \tag{4.4}$$

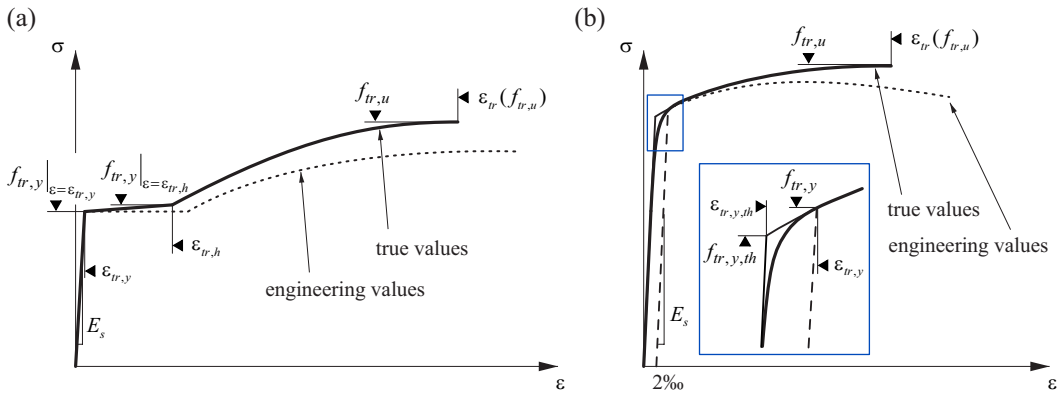

Fig. 4.7 – Definition of material characteristics for the constitutive relationships (a) of the perlitic/ferritic core; (b) of the martensitic outer annulus.

yielding, i. e. $\varepsilon_{tr,y} \leq \varepsilon_{tr} \leq \varepsilon_{tr,h}$:

$$\sigma_{tr} = f_{tr,y} \frac{e^{\varepsilon_{tr}}}{e^{\varepsilon_{tr,y}}} = E_s \left(e^{\varepsilon_{tr,y}} - 1\right) e^{\varepsilon_{tr}} \tag{4.5}$$

hardening, i. e. $\varepsilon_{tr,h} \leq \varepsilon_{tr} \leq \varepsilon_{tr}(f_{tr,u})$:

$$\sigma_{tr} = e^{\varepsilon_{tr}} \left[\frac{f_{tr,u}}{e^{\varepsilon_{tr}(f_{tr,u})}} - \left(\frac{f_{tr,u}}{e^{\varepsilon_{tr}(f_{tr,u})}} - \frac{f_{tr,y}|_{\varepsilon_{tr}=\varepsilon_{tr,y}}}{e^{\varepsilon_{tr,y}}} \right) \left(\frac{e^{\varepsilon_{tr}(f_{tr,u})} - e^{\varepsilon_{tr}}}{e^{\varepsilon_{tr}(f_{tr,u})} - e^{\varepsilon_{tr,h}}} \right)^{\beta} \right] \tag{4.6}$$

In Equation (4.6) (and Equation (4.8) below), β is a model coefficient whose value is determined by regression of the experimental data in true values. Table 4.2 summarises the values of the material characteristics in true values, as determined in our test series.

The constitutive relationships for the martensitic outer annulus are defined as follows:

elastic phase, i. e. $0 \leq \varepsilon_{tr} \leq \varepsilon_{tr,y,th}$:

$$\sigma_{tr} = E_s \varepsilon_{eng} \left(1 + \varepsilon_{eng}\right) = E_s e^{\varepsilon_{tr}} \left(e^{\varepsilon_{tr}} - 1\right) \tag{4.7}$$

hardening, i. e. $\varepsilon_{tr,y,th} \leq \varepsilon_{tr} \leq \varepsilon_{tr}(f_{tr,u})$:

$$\sigma_{tr} = f_{tr,u} - \left(f_{tr,u} - f_{tr,y}\right) \left(\frac{\varepsilon_{tr}(f_{tr,u}) - \varepsilon_{tr}}{\varepsilon_{tr}(f_{tr,u}) - \varepsilon_{tr,y}} \right)^{\beta} \tag{4.8}$$

Figure 4.8 shows the stress-strain curves for each layer back-calculated from experiments (in grey) and the model curves based on the Equations (4.4) – (4.8) for the perlitic/ferritic core and the martensitic outer annulus in engineering (a) and true values (b). The models closely capture the shape of the experimental curves, despite that they contain merely one single fitting parameter (the exponent β). This is particularly noteworthy for the part with negative slope of the martensitic outer annulus in Figure 4.8(a), at strains beyond the engineering tensile strength, which is obtained directly from the model (expressed in true values and transformed into engineering values) by simply inserting the basic characteristics obtained from the experimentally observed true stress-strain diagram. Figure 4.8 nicely demonstrates that for the martensitic outer annulus, the tensile strength (and corresponding strain) determined from true values differs significantly from the tensile strength (and the corresponding strain) obtained directly in

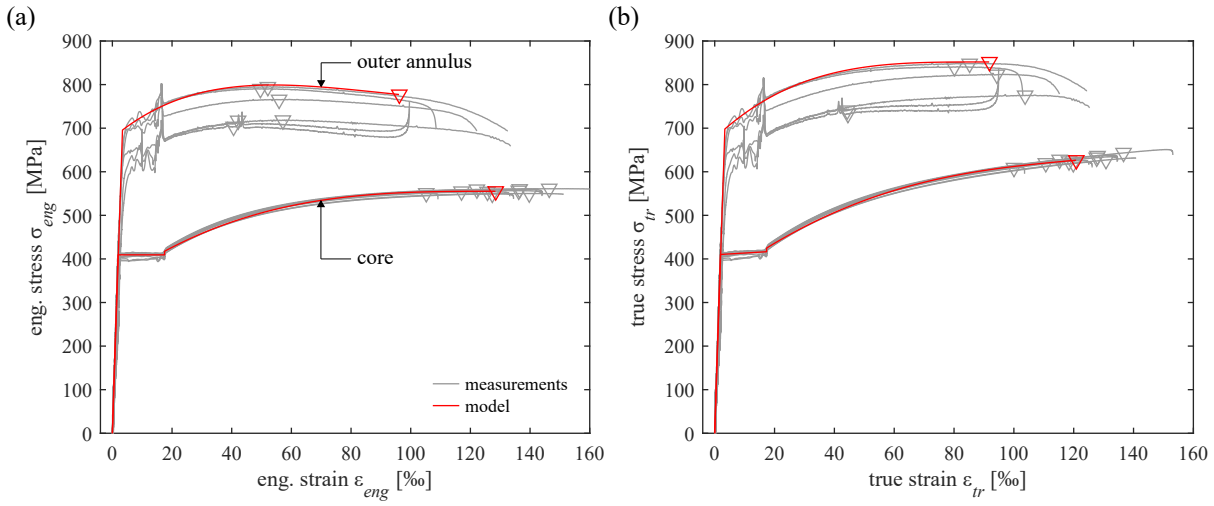

Fig. 4.8 – Stress-strain diagram of perlitic/ferritic core and martensitic outer annulus back-calculated from experiments in grey, and constitutive material model in red in (a) engineering and (b) true values. Triangles denote is the peak stress in the experimental curves and maximum true stress in the model curves (resp. its equivalent in engineering values), and the corresponding strains.

engineering values. Hence, the proper failure point of the material can only be captured correctly from the true stress-strain diagram.

4.3.4 Proposed model for a composed QST reinforcing bar

Based on the two constitutive relationships (Equations (4.4) – (4.8)), the stress-strain behaviour of a reinforcing bar composed of a perlitic/ferritic core, a banitic transition zone and a martensitic outer annulus is obtained by integration over the cross-section. The resulting model allows to describe the behaviour of QST reinforcing bars with intact or reduced cross-section. While all calculations have to be carried out using true stress-strain values, the results can finally be converted to engineering values.

Tab. 4.2 – Material characteristics of perlitic/ferritic core, martensitic outer annulus, and composed original reinforcing bar as determined in the experiments. Stresses and strains are given in true values.

		Core	Outer annulus	Composed reinforcing bar
E_s	[GPa]	205	205	205
$\varepsilon_{tr,y}$	[-]	0.002	0.0055	0.0047
$\varepsilon_{tr,y,th}$	[-]	-	0.0034	-
$\varepsilon_{tr,h}$	[-]	0.017	-	0.016
$\varepsilon_{tr}(f_{tr,u})$	[-]	0.121	0.092	0.0969
$f_{tr,y}\|_{\varepsilon_{tr}=\varepsilon_{tr,y}}$	[MPa]	410	707	542
$f_{tr,y}\|_{\varepsilon_{tr}=\varepsilon_{tr,h}}$	[MPa]	416	-	563
$f_{tr,u}$	[MPa]	627	852	712
β	[-]	2.94	3.4	-

The numerical model is based on the following principles and the notation shown in Figure 4.4 and Figure 4.7:

1. Determine r_{b1} and r_{b2} denoting the border of the core and the transition zone.
2. Obtain the constitutive relationships for perlite/ferrite and martensite (Equations (4.4) – (4.8)).
3. Determine the constitutive relationship of the bainitic transition zone, using the relationship derived for perlite/ferrite (Equations (4.4) – (4.6)), but assuming a linear variation of yield stress and tensile strength from ferrite/perlite at $r = r_{b1}$ to martensite at $r = r_{b2}$:

$$
\begin{aligned}
&\text{for } r_{b1} < r \leq r_{b2}: \\
&\quad f_{tr,y,bain}(r) = \left(f_{tr,y,mart} - f_{tr,y,core}\right)(r - r_{b1}) \,/\, (r_{b2} - r_{b1}) + f_{tr,y,core} \\
&\quad f_{tr,u,bain}(r) = \left(f_{tr,u,mart} - f_{tr,u,core}\right)(r - r_{b1}) \,/\, (r_{b2} - r_{b1}) + f_{tr,u,core} \\
&\quad \varepsilon_{tr,y,bain} = f_{tr,y,bain}/E_s \\
&\quad \varepsilon_{tr,h,bain} = \varepsilon_{tr,h,core} \\
&\quad \varepsilon_{tr,bain}\left(f_{tr,u}\right) = \varepsilon_{tr,core}\left(f_{tr,u}\right) \\
&\quad E_s = 205\,\text{GPa} \\
&\quad \beta = 3.8
\end{aligned}
\tag{4.9}
$$

4. Calculate sum of stresses in all layers for a specific strain value ε, weighted by their area A in the cross-section with total area A_{tot}:

$$
\sigma_{tr,tot}\left(\varepsilon_{tr}\right) = \frac{A_{core}}{A_{tot}}\sigma_{tr,core}\left(\varepsilon_{tr}\right) + \sum_j \frac{A_{bain}\left(r_j\right)}{A_{tot}}\sigma_{tr,bain}\left(r_j, \varepsilon_{tr}\right) + \frac{A_{mart}}{A_{tot}}\sigma_{tr,mart}\left(\varepsilon_{tr}\right) \tag{4.10}
$$

Note that the contribution of the bainitic transition zone is nonlinear, as the strength of the bainite is linear in r, and the total bainitic area is quadratic in r. To determine the behaviour of a reinforcing bar with a non-axisymmetrically reduced cross-section, the area of the damaged zone can be discretised over r and the weighted stresses of each element summed up. In the special case of a uniform, all-sided reduction of the cross-section, Equation (4.10) can be simplified and a discretisation be avoided. With $\tilde{r}$ denoting the outermost radius of the (remaining) bainitic transition zone ($r_{b1} < \tilde{r} \leq r_{b2}$) and $\alpha = \tilde{r}/r_{b1}$ the ratio of radii, integration of the total yield load and tensile resistance of the transition zone yields:

$$
\begin{aligned}
F_{tr,y,bain}(\tilde{r}) &= \int_{r_{b1}}^{\tilde{r}} 2r\pi f_{tr,y,bain}(r)dr \\
&= \frac{\pi r_{b1}^3}{3\left(r_{b2} - r_{b1}\right)}(\alpha - 1)^2(2\alpha + 1)\left(f_{tr,y,mart} - f_{tr,y,core}\right) + \left(\alpha^2 - 1\right)\pi r_{b1}^2 f_{tr,y,core} \\
F_{tr,u,bain}(\tilde{r}) &= \int_{r_{b1}}^{\tilde{r}} 2r\pi f_{tr,u,bain}(r)dr \\
&= \frac{\pi r_{b1}^3}{3\left(r_{b2} - r_{b1}\right)}(\alpha - 1)^2(2\alpha + 1)\left(f_{tr,u,mart} - f_{tr,u,core}\right) + \left(\alpha^2 - 1\right)\pi r_{b1}^2 f_{tr,u,core}
\end{aligned}
\tag{4.11}
$$

Dividing by the total area of the transition zone

$$
A_{bain}(\tilde{r}) = \int_{r_{b1}}^{\tilde{r}} 2r\pi dr = \pi\left(\tilde{r}^2 - r_{b1}^2\right) = \left(\alpha^2 - 1\right)\pi r_{b1}^2 \tag{4.12}
$$

one gets the mean yield stress and tensile strength, $\overline{f_{tr,y,bain}}(\tilde{r})$ and $\overline{f_{tr,u,bain}}(\tilde{r})$, respectively:

$$\begin{aligned}
\overline{f_{tr,y,bain}}(\tilde{r}) &= F_{tr,y,bain}(\tilde{r}) \big/ A_{bain}(\tilde{r}) \\
&= \frac{\pi r_{b1}}{3\,(r_{b2}-r_{b1})} \frac{(\alpha-1)(2\alpha+1)}{(\alpha+1)} \left(f_{tr,y,mart} - f_{tr,y,core}\right) + f_{tr,y,core} \\
\overline{f_{tr,u,bain}}(\tilde{r}) &= F_{tr,u,bain}(\tilde{r}) \big/ A_{bain}(\tilde{r}) \\
&= \frac{\pi r_{b1}}{3\,(r_{b2}-r_{b1})} \frac{(\alpha-1)(2\alpha+1)}{(\alpha+1)} \left(f_{tr,u,mart} - f_{tr,u,core}\right) + f_{tr,u,core}
\end{aligned} \tag{4.13}$$

Yield stress and tensile strength, $f_{tr,y,bain}(r)$ and $f_{tr,u,bain}(r)$, can then be substituted in Equation (4.9) by their mean values (Equation (4.13)), and the constitutive model for bainite be written accordingly, resulting in an average stress in the bainitic transition zone $\overline{\sigma_{tr,bain}}(\tilde{r},\varepsilon_{tr})$ independent of the discretised radius r. The second term of the sum in Equation (4.10) can thus be rewritten as:

$$\sum_j \frac{A_{bain}(r_j)}{A_{tot}} \sigma_{tr,bain}(r_j,\varepsilon_{tr}) = \frac{A_{bain}(\tilde{r})}{A_{tot}} \overline{\sigma_{tr,bain}}(\tilde{r},\varepsilon_{tr}) \tag{4.14}$$

After having developed the model outlined above, the authors became aware of a publication of Hortigón Fuentes et al. [82], who presented a similar approach for modelling the stress-strain behaviour of a reinforcing bar by summing up weighted true stresses in concentric layers. However, they considered only two zones with distinct thicknesses and material characteristics, and their model, requiring finite element calculations to obtain the behaviour of the composite reinforcing bar, neither captures reinforcing bar rupture nor the behaviour of damaged zones. These issues are overcome with the approach proposed here, which considers all three relevant zones of an intact or damaged QST reinforcing bar and can easily be implemented in a simple spreadsheet. Nevertheless, the similarity of both independently developed models and their good correlation with experimental data show their potential and confirm the underlying hypotheses.

4.3.5 Comparison of proposed model with experimental data

Figure 4.9 compares the experimental curves with the calculations of the model proposed in Section 4.3.4. Calculations were done in true stress-strain values and the results transformed to engineering values. Model predictions and experimental data are in almost perfect agreement.

The observed behaviour at the transition from the elastic phase to yielding (see the zoomed-in region in Figure 4.9 (b)) merits a closer look and discussion: A distinct upper yield point with subsequent serrated flow at a fairly constant average stress was clearly observed for the perlitic/ferritic core and the bainitic transition zone. As documented in literature [81, 132, 136], this is typical for the plastic flow of metals with dissolved atoms of sufficient diffusivity (e. g. interstitial carbon atoms in ferritic steel) in a displacement-controlled tensile test. Without applied stress, the interstitial atoms diffuse to the metal's defects at an atomic level, known as dislocations, and subsequently impede movements along gliding planes at low applied stresses. Once the applied stresses exceed the upper yield point, dislocations can break free and move freely, causing an immediate drop of the stress to the lower yield point. This process starts in a small number of crystalline grains with optimally oriented gliding planes, where local deformations build up. Dislocations then accumulate at the boundaries to the adjoining grains and stress increases again, until the dislocations of the adjacent grain break free, leading to a cascaded formation of strain localisations known as Lüders bands. The process continues at variable stress – between upper and lower yield point – until all dislocations are unpinned and able to move. At this point, the yielding phase ends, i. e. the end of the yield plateau in the stress-strain diagram has been reached, and the phase of strain hardening begins subsequently.

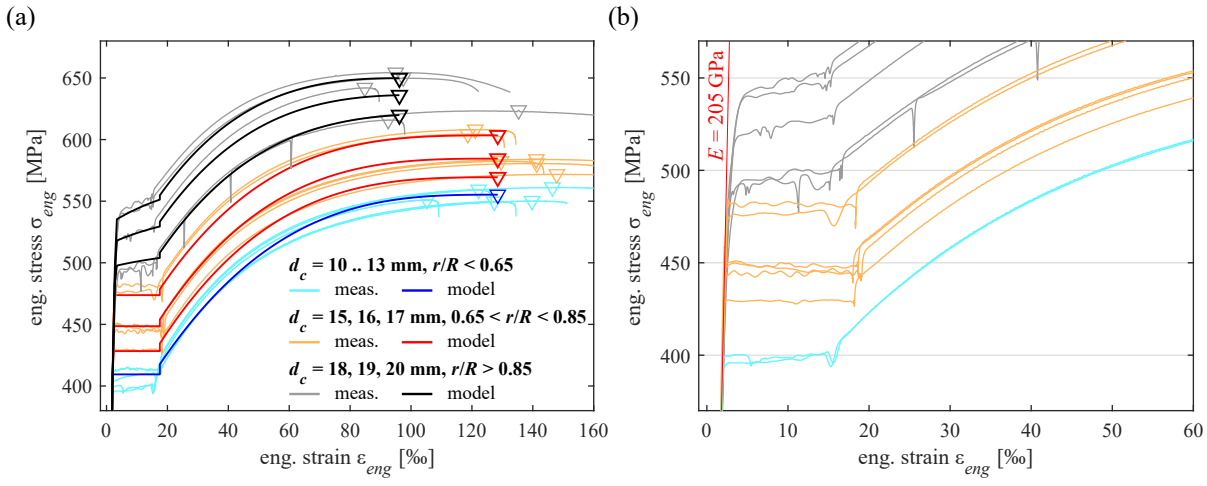

Fig. 4.9 – (a) Comparison of model and experimental curves of reinforcing bars with uniformly reduced diameter d_c; (b) zoomed-in region between yielding and hardening of selected experimental curves.

If the composed reinforcing bar includes a martensitic outer annulus, the observed behaviour changes markedly. Rather than exhibiting a distinct upper yield point, the slope of the stress-strain curve decreases gradually, and the stress clearly increases during the yielding phase with increasing strain. This change in behaviour can be explained by the fact, that the stress-strain curve of the martensitic outer annulus does not exhibit any yield plateau when reaching the yield stress. Instead, strain hardening in the martensitic layer immediately follows the elastic phase. Furthermore, the yield stress for martensite is almost twice as high as the yield point of the perlitic/ferritic core ($f_{eng,y,mart} = 706\,\text{MPa} \gg f_{eng,y,core} = 409\,\text{MPa}$ in the used samples). Consequently, the stress-strain curve of the composite reinforcing bar becomes flatter at 409 MPa (core is yielding, outer annulus is still elastic). Once the end of the elastic phase of the outer annulus is reached (706 MPa for the martensitic outer annulus or 548 MPa on average of the composed material), the curve flattens again. In the following phase, stresses increase since the martensitic outer annulus strain hardens, whereas the perlitic/ferritic core and the bainitic transition zone yield at constant stress. At the end of the yield plateau of core and transition zone, these layers start strain hardening, causing the stress-strain curve of the composite bar to become markedly steeper again. The proposed model represents these phenomena very well.

4.3.6 Influence of microstructure on the residual tensile strength of a corroded reinforcing bar

Figure 4.10 compares the remaining tensile resistance of a unilaterally and uniformly damaged QST reinforcing bar for a given loss of cross-sectional area $\zeta = A_{lost}/A_{tot}$ (a) to the tensile resistance of an original reinforcing bar, and (b) to the residual tensile resistance of a cold-worked CW reinforcing bar with the same initial strength and equal damage. Whereas due to its homogeneous composition, the residual strength of the CW reinforcing bar is directly proportional to the loss of cross-section, the uniformly damaged QST reinforcing bar reveals a disproportionate loss of strength. This behaviour directly results from the loss of the martensitic and bainitc layers, which are responsible for the high strength of a QST reinforcing bar. At a residual cross-sectional area of 43 % of the original area ($\zeta = 0.57$), only the perlitic/ferritic core remains, having a markedly lower strength than the composite material. With further degradation beyond this point, the residual force ratio between the QST and the CW reinforcing bar remains constant (slightly above 0.85, see Figure 4.10(b)).

A unilaterally damaged QST reinforcing bar also exhibits a disproportionate strength degradation up to a cross-section loss of 50%, but much less drastically than the uniformly damaged bar (minimum strength ratio of 0.98 between a QST and a CW bar at $\zeta = 0.2$). This is due to an approximately even removal of martensitic and perlitic/ferritic material. For cross-section losses higher than 50%, the strength

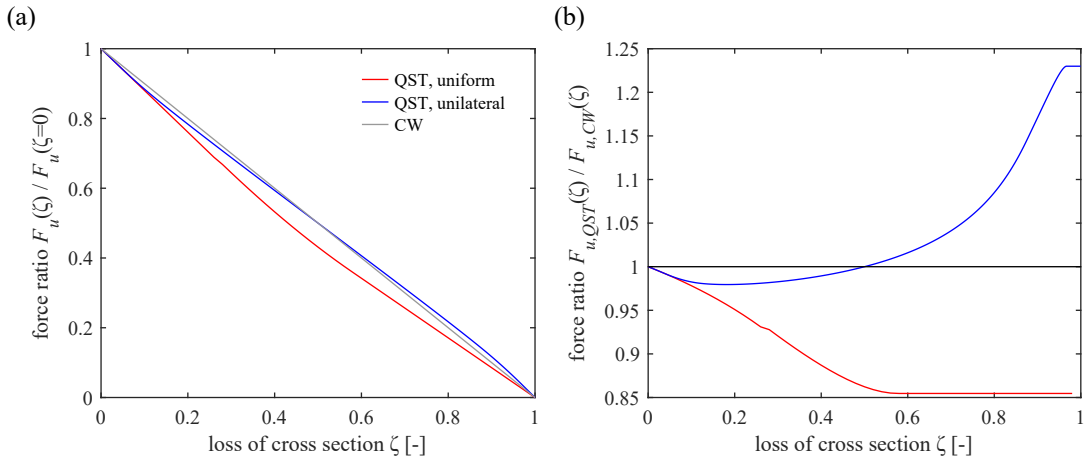

Fig. 4.10 – (a) Remaining tensile resistance of a uniformly damaged QST, a unilaterally damaged QST, and a cold-worked CW reinforcing bar as a function of the cross-section loss, compared to the tensile resistance of an original reinforcing bar; (b) ratio of remaining tensile resistance of a uniformly and a unilaterally damaged QST reinforcing bar compared to a CW reinforcing bar with the same initial strength and equal damage as a function of the cross-section loss.

ratio between a QST and an equally damaged CW reinforcing bar is even higher than 1, as the area of the martensitic layer prevails.

The findings of Figure 4.10 highlight that depending on the damage geometry, QST reinforcing bars can disproportionally lose strength if the martensitic layer is lost. Especially for uniformly corroded reinforcing bars, this effect has to be taken into account when assessing the structural safety. In contrast, unilaterally damaged QST reinforcing bars do not lose more strength than equally damaged CW reinforcing bars. This is of high practical relevance, as chloride-induced corrosion leads in the majority of cases to unilateral damage of reinforcing bars. However, it has to be noted that with severe unilateral damage, other effects occur, such as local bending moments, which may significantly affect the bearing capacity of the reinforcing bar [8, 58, 80, 166].

4.3.7 Estimation of model parameters for predicting the strength of damaged QST reinforcing bars

In the validation above, the results of the model match the experimental curves very well since the input values (yield stress and tensile strength and corresponding strains) could be obtained from the tensile tests. Obviously, carrying out such an expensive experimental campaign to determine these input values for a practical case, e. g. where the stress-strain characteristics of corroded reinforcing bars in an existing structure should be assessed, can hardly be justified. Therefore, a simplified approach to calculate the strength of a damaged composite reinforcing bar based on the results of conventional tensile tests is proposed, distinguishing three levels of approximation. In all of them, the ratios

$$\begin{aligned} f_{eng,u,core} / f_{eng,y,core} &= 1.36 \\ f_{eng,u,mart} / f_{eng,y,mart} &= 1.10 \end{aligned} \tag{4.15}$$

between tensile strength and yield stress, as observed in this study, are used. Furthermore, for simplicity, it is assumed that the composite reinforcing bar consists of only two layers, i. e. a ferritic/perlitic core and a martensitic outer annulus; the area of the bainitic layer in between is assigned equally to core and outer annulus. This simplification can be justified as follows: The tensile strength of the composed reinforcing bar is made up – according to the above simplification – proportionally by the tensile strength of core

and outer annulus, i. e.

$$a \cdot f_{eng,u,core} + (1-a) \cdot f_{eng,u,mart} = f_{eng,u,tot} \tag{4.16}$$

where a denotes a proportionality factor, which is equal to $a = 0.58$ for the tensile strength of the tested specimens. On the other hand, the weighted area of the core and half of the adjacent bainitic zone, i. e.

$$b = \frac{A_{core} + A_{bain}/2}{A_{tot}} \tag{4.17}$$

equals $b = 0.57 \approx a$ for the tested specimens. Hence, the simplification introduced above will yield reasonable results.

First level of approximation

1. Determine the tensile strength $f_{eng,u,tot}$ and the yield stress $f_{eng,y,tot}$ of the composite reinforcing bar from a conventional tensile test.

2. Assume that the true strain corresponding to the tensile strength of the martensitic layer coincides with the true strain corresponding to the tensile strength of the composite bar, i. e. $\varepsilon_{tr,mart}(f_{tr,u}) = \varepsilon_{tr,tot}(f_{tr,u})$. Assume – as observed in the present test series – the true strain at peak stress of the perlitic/ferritic core to be 7 % larger than the true strain at peak stress of the composite bar, i. e.

   $$\varepsilon_{tr,core}(f_{tr,u}) = 1.07 \ln(1 + \varepsilon_{eng,tot}(f_{eng,u})) \tag{4.18}$$

   The true strain at hardening of the core can be obtained from the engineering strain at hardening of the composite bar, i. e. $\varepsilon_{tr,h,core} = \ln(1 + \varepsilon_{eng,h,tot})$.

3. Assume that the relative area of the simplified core is $\tilde{A}_{core} = b = 0.57$ (as observed in the experiments, see above) and the relative area of the simplified outer annulus is $\tilde{A}_{mart} = 1 - b = 0.43$.

4. Using Equation (4.15), determine the yield stress and the tensile strength of the ferritic/perlitic core, $f_{eng,y,core}$ and $f_{eng,u,core}$, and of the martensitic layer, $f_{eng,y,mart}$ and $f_{eng,u,mart}$, respectively, by solving the following linear system of equations:

   $$\begin{aligned} f_{eng,y,tot} &= \tilde{A}_{core} \cdot f_{eng,y,core} + \tilde{A}_{mart} \cdot f_{eng,y,mart} \\ f_{eng,u,tot} &= \tilde{A}_{core} \cdot f_{eng,u,core} + \tilde{A}_{mart} \cdot f_{eng,u,mart} \end{aligned} \tag{4.19}$$

   Alternatively, the yield stress of the core material $f_{eng,y,core}$ could also be estimated using the stress-strain diagram of the composite reinforcing bar, as it coincides with the point where the elastic region ends and the curve begins to flatten (see Figure 4.9(b)). This observation may be used to verify the appropriateness of the assumptions and simplifications made.

5. The true values of the yield stress and the tensile strength can be calculated using Equation (4.2) and (4.3), i. e.

   $$\begin{aligned} f_{tr,y,core} &= f_{eng,y,core} e^{\varepsilon_{tr,y,core}} \\ f_{tr,y,mart} &= f_{eng,y,mart} e^{\varepsilon_{tr,y,mart}} \\ f_{tr,u,core} &= f_{eng,u,core} e^{\varepsilon_{tr,core}(f_{tr,u})} \\ f_{tr,u,mart} &= f_{eng,u,mart} e^{\varepsilon_{tr,mart}(f_{tr,u})} \end{aligned} \tag{4.20}$$

Second level of approximation

The values of the yield stress and the tensile strength of the core material, $f_{eng,y,core}$ and $f_{eng,u,core}$, respectively, are obtained by carrying out additional tensile tests on reinforcing bars with sufficiently reduced cross-section to eliminate the transition zone (e. g. 50% reduction in diameter) over a length of about 10 times the original diameter. With these values, the assumption of the strength ratios (Equation (4.15)) can be avoided, which will improve the approximation for the yield and tensile strength of the outer annulus obtained from Equation (4.19). Additionally, the true strain at peak stress of the core can be set to its experimentally determined value, rather than approximating it using Equation (4.18).

Third level of approximation

Performing a Vickers Hardness test over the cross-section of the sample, the relative areas of the core and the outer annulus, $\tilde{A}_{core}$ and $\tilde{A}_{mart}$, respectively, are obtained. Using this information, combined with the results of the tensile tests on the reinforcing bar with reduced diameter, the yield stress and the tensile strength of the martensitic outer annulus $f_{eng,y,mart}$ and $f_{eng,u,mart}$ can be determined with good accuracy.

4.4 Conclusions

This study investigated the influence of the steel microstructure on the stress-strain behaviour of hot-rolled, quenched and self-tempered (QST) reinforcing bars. As documented in literature, three distinct material layers could be identified: A ferritic/perlitic core, a bainitic transition zone and a martensitic outer annulus. Thicknesses of the distinct material layers, determined by Vickers hardness tests, were found to closely correspond to values found in literature. Tensile tests on QST reinforcing bars with gradually reduced diameters were used to reveal the stress-strain behaviour of the different microstructure layers. Constitutive relationships for the ferritic/perlitic core, the bainitic transition zone and the martensitic outer annulus were shown, together with experimental stress-strain diagrams. Experimental results confirmed that models composing a reinforcing bar out of its distinct layers cannot be formulated in conventional engineering stress and strain, but true stress and true strain must be used. A simplified model to predict the stress-strain behaviour of a QST reinforcing bar based on the constitutive relationships of its layers was proposed and validated against the experimental results, revealing excellent agreement. Finally, three levels of approximation were suggested to determine the strength of damaged QST reinforcing bars if no detailed information is available.

Knowledge about the stress-strain behaviour of the distinct layers of QST reinforcing bars and their interaction is crucial to assess the residual strength and ductility of concrete structures affected by reinforcement corrosion. Experiments and calculations reveal that the strength of uniformly damaged QST reinforcing bars is reduced up to 15% more than what would be expected if merely the loss of cross-section were considered since the inner core has much lower strength than the outer layers. In combination with the loss of cross-section area, the strength is thus disproportionately reduced. On the other hand, if QST reinforcing bars are damaged unilaterally, the direct tensile strength does not alter significantly. Therefore, the different stress-strain behaviour of the distinct microstructure layers only has a minor influence in case of pitting corrosion, as this corrosion type leads in the majority of cases to unilateral damage of reinforcing bars. However, other effects resulting from the pit geometry, such as bending due to a shift of the neutral axis, may strongly affect the bearing capacity [80, 166].

The findings of this study related to the influence of microstructure on the stress-strain behaviour of corroded reinforcing bars are a first important step towards a better understanding of the structural response of concrete structures affected by reinforcement corrosion. Nonetheless, further effects need to be considered, such as, e. g. the strain rate dependent strength of reinforcing bars [69], three-dimensional stress states in the vicinity of localised corrosion pits, or bending moments in case of unilateral damage. The authors are currently investigating these additional effects, in order to finally be able to accurately assess the residual safety of corroded reinforced concrete structures.

Notation

A_{tot}	Cross-sectional area of reinforcing bar (with original or reduced diameter), $A_{tot} = \sum A_i$
A_i	Cross-sectional area of a circle with diameter d_i, $A_i = \left(d_i^2 \pi\right) / 4$
A_{core}, A_{bain}, A_{mart}	Cross-sectional area of core, bainitic transition zone, and martensitic outer annulus
$\tilde{A}_{core}$, $\tilde{A}_{mart}$	Cross-sectional area of simplified core and simplified outer annulus
A_{lost}	Cross-sectional area lost by corrosion
E_s	Young's modulus of reinforcing steel
HV	Vickers Hardness
R	Original radius of reinforcing bar, $R = Ø / 2$
a, b	Proportionality factors determining $\tilde{A}_{core}$ and $\tilde{A}_{mart}$
d_c	Residual diameter of specimen
d_i	Outermost diameter of Layer j, $d_i = 2r_i$
$f_{eng,y}$, $f_{eng,u}$	Steel yield stress and tensile strength (engineering value)
$f_{tr,y}$, $f_{tr,y,core}$, $f_{tr,y,bain}(r)$, $f_{tr,y,mart}$	Yield stress (true values; in general, of core, bainitic transition zone, and martensitic outer annulus); note that the value for the bainitic transition zone is a function of r
$f_{tr,u}$, $f_{tr,u,core}$, $f_{tr,u,bain}(r)$, $f_{tr,u,mart}$	Tensile strength (true values; in general, of core, bainitic transition zone, and martensitic outer annulus); note that the value for the bainitic transition zone is a function of r
$f_{tr,y,th}$	Theoretical value of yield stress used for martensitic outer annulus (true value)
$\overline{f_{tr,y,bain}}(\tilde{r})$, $\overline{f_{tr,u,bain}}(\tilde{r})$	Mean yield stress and mean tensile strength of bainitic transition zone (true values)
r, r_i, r_j, $\tilde{r}$	Radius in general, outermost radius of Layer j, mean radius of Layer j, outermost radius of bainitic transition zone
r_{b1}, r_{b2}	Outermost radius of core and bainitic transition zone, respectively
α	Radii ratio, $\alpha = \tilde{r} / r_{b1}$
β	Fitting parameter of constitutive relationship
ε_{eng}, ε_{tr}	Steel strain (engineering value, true value)
$\varepsilon_{tr,y}$, $\varepsilon_{tr,y,core}$, $\varepsilon_{tr,y,bain}$, $\varepsilon_{tr,y,mart}$	Strain at yield stress (true value; in general, of core, bainitic transition zone, and martensitic outer annulus)
$\varepsilon_{tr,h}$, $\varepsilon_{tr,h,core}$, $\varepsilon_{tr,h,bain}$	Strain at onset of hardening (true value; in general, of core, and bainitic transition zone)
$\varepsilon_{tr}(f_{tr,u})$, $\varepsilon_{tr,core}(f_{tr,u})$, $\varepsilon_{tr,bain}(f_{tr,u})$, $\varepsilon_{tr,mart}(f_{tr,u})$	Strain at tensile strength (true value; in general, of core, bainitic transition zone, and martensitic outer annulus)
$\varepsilon_{tr,y,th}$	Strain at theoretical yield stress $f_{tr,y,th}$ (true value)
σ_{eng}, σ_{tr}	Steel stress (engineering value, true value)
σ_{tot}	Total stress exhibited by reinforcing bar with residual cross-sectional area A_{tot}
σ_j	Stress exhibited by Layer j
$\overline{\sigma_{tr,bain}}(\tilde{r}, \varepsilon_{tr})$	Average stress in bainitic transition zone (true value) in function of $\tilde{r}$ at specific strain
ζ	Relative cross-section loss of reinforcing bar
$Ø$	Original diameter of reinforcing bar

5 Influence of a triaxial stress state on the load-deformation behaviour of corroded reinforcing bars

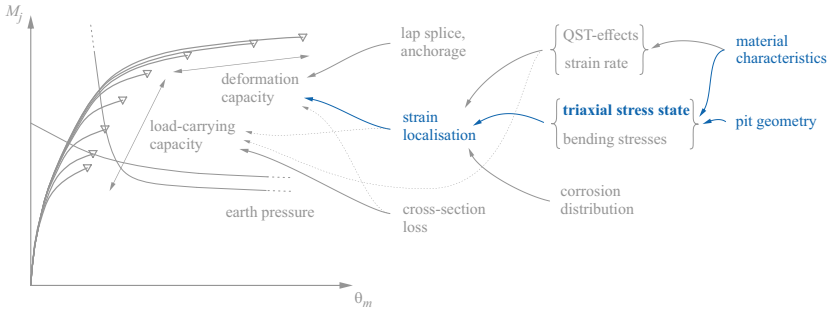

This chapter presents the findings of a series of tensile tests on locally, axisymmetrically damaged reinforcing bars and a comprehensive series of nonlinear finite element analyses of locally damaged bars to investigate the influence of a varying axisymmetric pit geometry on the bar load-carrying and deformation capacity. The investigation revealed a significant attenuation of the strain localisation effect and a pronounced increase in the uniaxial tensile strength for locally damaged bars depending on the geometrical parameters. The chapter corresponds to the submitted version (preprint) of the following manuscript:

> Haefliger, S., Thoma, K., Kaufmann, W. 'Influence of a triaxial stress state on the load-deformation behaviour of corroded reinforcing bars,' submitted to *Construction and Building Materials*, 2022.

The lead author (Severin Haefliger) planned and conducted the experiments, did literature review on the metallurgic background regarding the different types of yielding and the behaviour of Lüders bands, and developed the presented models, which are based on a parametric nonlinear finite element (NLFE) analysis. The latter he conducted in collaboration with the second author (Karel Thoma), who set up the generic NLFE model, such that it could be controlled and evaluated with *Matlab* (by the lead author). The third author (Walter Kaufmann) supervised the conducted research.

Abstract

Local corrosion damage reduces the load-bearing capacity of reinforcing bars and, even more severely, their deformation capacity. These effects are mainly attributed to the reduced cross-sectional area and the accompanying strain localisation. However, several experimental studies found an altered load-deformation behaviour of naturally corroded as well as artificially damaged reinforcing bars, including an apparently increased tensile strength, which cannot be explained solely by strain localisation. Accordingly, in an experimental campaign carried out by the authors on locally axisymmetrically damaged reinforcing bars, the observed peak load increased with decreasing damage length, and the deformation capacity was much less impaired than predicted by established strain localisation models. A series of

nonlinear FE analyses was carried out to investigate a potential effect of the local stress state in the vicinity of the local corrosion damage. The results indeed revealed a triaxial stress state in this region, caused by the local deviation of the stress trajectories, explaining the experimental observations on a mechanical basis, and indicating a pronounced influence of the triaxial stresses on the uniaxial stress-strain behaviour of the bar in the vicinity of the corrosion pit. A parametric study was conducted to investigate a broader range of corrosion damage geometries and the corresponding triaxial stresses. The results indicate that the transverse stresses strongly affect the apparent uniaxial mechanical steel properties (yield stress, tensile strength, deformation capacity, loss of yield plateau) for short damage lengths typically found for pitting corrosion. A simplified modelling approach is proposed to capture the governing effects on the apparent uniaxial stress-strain curve of locally corroded reinforcing bars.

5.1 Introduction

Uniform and local corrosion reduce the load-bearing capacity of reinforcing bars and reinforced concrete (RC) structures due to the loss of cross-sectional area. In contrast to uniform corrosion, local corrosion additionally impairs the deformation capacity, as shown in many experimental campaigns on naturally corroded and artificially damaged reinforcing bars [8, 15, 34, 39, 58, 80, 83, 85, 122, 163, 166]. Recent studies [39, 72, 74, 122, 163] attributed the reduced ductility to strain localisation, proposing independently similar modelling approaches [72, 163]. They introduced a critical cross-section loss beyond which most of the deformation capacity of a reinforcing bar is lost [39, 72]. These studies also found that the deformation capacity is reduced disproportionally to the cross-section loss, with one study reporting a drastic reduction of the elongation at ultimate force by more than 80% for a cross-section loss of merely 17% [72].

The reduced deformation capacity of corroded reinforcing bars directly impairs the deformation capacity of the affected RC structure, depending on the variation of the residual cross-sectional area of the bars [72, 74]. This is particularly crucial for structural safety assessment strategies applying the lower bound theorem of the plasticity theory, which – though often only implicitly – presumes sufficient deformation capacity. Furthermore, quantifying the residual deformation capacity of corroded structures is essential to successfully apply performance-based assessment strategies, i. e. to compare the deformation capacity of a structure to its deformation demand. Such assessments are typically used for the analysis of plastic load redistributions in statically indeterminate structures (e. g. imposed deformations in multi-span bridges), and where the actions on the structure depend on its deformations (e. g. earth pressure on a retaining wall, seismic loading). Therefore, the mechanical understanding and the accurate modelling of the deformation capacity of corroded reinforcing bars is key for a safe assessment of corroded RC structures.

5.1.1 Strain localisation effects

As mentioned above, strain localisation plays a crucial role in the mechanical explanation of the reduced deformation capacity. It can readily be explained by modelling a corroded reinforcing bar as a chain of tension members having different lengths, with equal normal force F but varying tensile stiffness $E_s A_s$, where E_s = tangent modulus of the reinforcing steel, and A_s = cross-sectional area of the reinforcing bar (reduced by corrosion where applicable). If the tensile stiffness of a member is strongly reduced – which may be caused by severe cross-section loss and/or yielding of the reinforcement – much higher strains $\varepsilon_s = N/E_s A_s$ occur in this weak member than in the remaining members, i. e. the strains localise in the weak member. If this weak member is short, even very high localised strains cause only a small overall elongation (see, e. g. [72]). This typically applies to reinforcing bars affected by severe pitting corrosion, whose cross-section is reduced over a short length. It is particularly pronounced in cases where the tensile strength in the damaged section is reached (i. e. the bar ruptures) while the tensile stress

in the regular cross-section is still below the yield stress: substantial deformation occurs only in the short damaged part, and the total elongation of the bar at ultimate load is strongly reduced.

Cross-section loss and damage length are thus decisive parameters regarding strain localisation. For reinforcing bars affected by local corrosion, the extent of strain localisation further depends on the material characteristics of the steel: The ratio of yield stress to tensile strength determines the critical cross-section loss beyond which no plastic strains occur in the undamaged part of the reinforcing bar [39, 72]). For smaller cross-section losses, the shape of the steel stress-strain curve, particularly the slope in the strain-hardening phase, is highly relevant as well.

Models based on the strain localisation effect have been developed and successfully applied by [163] to describe the behaviour of corroded bare reinforcing bars, and by [72] to describe the response of concrete tension members containing locally corroded reinforcing bars, accounting for tension stiffening. However, experimental results [8, 39, 58, 80, 84, 166] indicate that strain localisation alone cannot explain the observed differences in the load-deformation behaviour of bars with varying pit geometry (pit length and pit shape) but equal cross-section loss.

5.1.2 Effects beyond strain localisation: Influence of pit geometry

The pit geometry affects (i) the triaxial stress state in the pit region caused by the local deviation of the stress trajectories and, in case of non-axisymmetric corrosion, (ii) local bending moments caused by the shift of the centroidal axis in the pit region.

Triaxial stress states occurring in the vicinity of geometry variations are well investigated in material and mechanical engineering, and their influence on the apparent uniaxial steel characteristics is well-known [9, 19, 59, 60, 78, 105, 120]. The occurring stress concentrations can lead to unforeseen failures (especially by fatigue) or undesired plastic deformations in mechanical parts, and considerable efforts have been made to quantify them (see, e. g. [127]). Since the stress concentration and the triaxial stress state strongly depend on the local geometry, closed-form solutions can at most be derived for simple geometries and linear elastic behaviour. For general geometries and nonlinear material behaviour, such as that of steel beyond the yield point, Finite Element analyses are applied nowadays, making use of incremental plasticity models including von Mises' J2-plasticity model and material damage models [9, 19]. With such analyses, the effects related to a triaxial stress state can be investigated, ranging from an increase or decrease of the apparent uniaxial yield stress and tensile strength to larger strains at peak stress.

Evidently, these effects are not limited to mechanical parts exhibiting geometrical variations, but equally affect locally damaged reinforcing bars. Indeed, some of the mentioned effects have been observed in experimental campaigns on corroded reinforcing bars: Zhu et al. [166] specifically investigated bars with different pit geometries, reporting significant differences in the stress-strain behaviour among the different geometries despite equal residual cross-sections and, hence, an equal degree of strain localisation. Several studies [39, 62, 83, 151] reported a slight to moderate increase of the apparent uniaxial tensile strength (defined as ultimate load divided by the actual residual cross-sectional area in the damaged zone) with increasing cross-section loss. These observations were either attributed to a variation of material characteristics along the bar, or accounted for by using an average of the reduced and initial cross-sectional areas, but maintaining the nominal uniaxial strength [84]. Only few researchers investigated the triaxial stress state in the vicinity of corrosion pits to date, and to the authors' knowledge, FE analyses investigating the mechanical properties of reinforcing bars containing corrosion pits have only been conducted by [54, 80], with [80] pointing out the effect of different pit geometries on the results.

In addition to the triaxial stress state caused by the deviation of the stress trajectories, bending stresses occur in the vicinity of unilateral corrosion pits due to a shift of the centroidal axis at the pit. This effect was observed in some experimental campaigns on bare reinforcing bars [8, 58], indicating a significant influence on the stress-strain behaviour, and on concrete structures instrumented with fibre optic strain

sensing [74], where the strains caused by the bending stresses were measured. Presumably, the superposition of bending stresses leads to a premature steel rupture in the case of unilateral corrosion when compared to an axisymmetrically corroded bar with equal cross-section loss: due to the non-uniform tensile stresses caused by bending, the ultimate elongation on the tensile side of the cross-section is reached while the average stress in the residual cross-section is below the tensile strength. However, a quantification is complicated by the triaxial stress state in the vicinity of the corrosion pit, and would thus require a parametric study based on FE analyses (similar to those carried out in this study for axisymmetric damage, but requiring much more time and resources).

5.1.3 Focus of this study

This study investigates the influence of a triaxial stress state on the apparent uniaxial stress-strain behaviour and material characteristics of reinforcing bars with local corrosion damage. It focuses solely on axisymmetric damage and deliberately excludes unilateral corrosion pits to avoid any superimposed effects of bending stresses, which the authors intend to address in a future study.

An experimental campaign on reinforcing bars of two different steel types was conducted, with each specimen having an artificially created local damage of different lengths. The specimens were instrumented using a three-dimensional digital image correlation system, enabling the observation of the stress-strain behaviour in different regions near the pit, which are discussed and compared to simple engineering approaches for strain localisation. In a second step, the experiments were modelled with the FE software Ansys, using von Mises' J2-plasticity model beyond the yield point. The effects of the occurring triaxial stress state are discussed in detail. A comprehensive parametric study including 270 different datasets for each steel type demonstrates the influence of a triaxial stress state for varying geometrical parameters. Finally, a simplified modelling approach is presented, which allows estimating the stress-strain behaviour of an axisymmetrically corroded reinforcing bar accounting for the effects of the triaxial stress state.

5.1.4 Further effects

A considerable amount of reinforcing bars used since the 1990s [137] are produced as quenched and self-tempered (QST) bars, sold under the labels "Tempcore®" or "Thermex®". In the last step of their production process, these hot-rolled bars are quenched with water and then cooled under ambient conditions. During the cooling period, the hot core of the reinforcing bar tempers the quenched outer annulus. This process forms a reinforcing bar with distinct microstructure over the cross-section: The ferritic/perlitic core with high ductility but moderate strength is surrounded by a bainitic transition zone and a martensitic outer annulus with high strength but moderate ductility. The composed bar exhibits favourable material characteristics of higher strength and ductility [92, 121, 130, 133]. However, QST reinforcing bars change their apparent material characteristics during the corrosion degradation process due to changes in the relative areas of the different microstructures.

This effect is well-investigated [54, 71, 82, 139], and a simple model to consider this influence for corroded reinforcing bars is presented in [71], including different levels of approximation depending on the available material data. This model is used to describe the stress-strain behaviour of one of the investigated reinforcing steels; however, an in-depth analysis of the effect of distinct microstructure is beyond the scope of this study.

5.2 Experimental programme

The experimental campaign was designed to investigate the influence of a triaxial stress state in the vicinity of an axisymmetric cross-section reduction induced by corrosion. The diameter of the reinforcing bar samples was reduced axisymmetrically to isolate the effect of triaxial stresses on their load-deformation

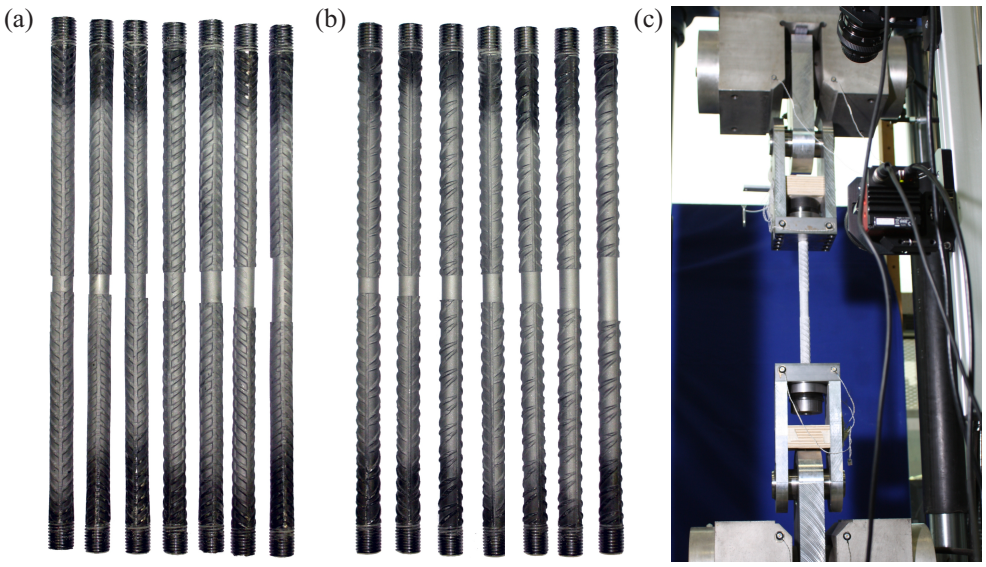

Fig. 5.1 – Experiments on reinforcing bars with reduced diameter. Specimens of (a) CW series and (b) QST series after sandblasting; (c) tensile testing machine with spherical hinges and DIC cameras mounted on front side.

behaviour, rather than trying to simulate the pit geometry found in reinforcing bars affected by natural corrosion, see Sections 5.1.2 and 5.1.3.

The experimental campaign was carried out in the structural laboratory at ETH Zurich and comprised two series of QST and cold-worked (CW) reinforcing bars with 7 specimens each (see Figures 5.1(a) and (b)). The 500 mm long specimens originated from the same production batch per series, and batches were identical to those of [69, 71]. The initial (nominal) diameter of the bars was reduced from $Ø = 20\,\text{mm}$ to a remaining (target) diameter of $Ø_c = 19\,\text{mm}$ over a distinct length L_c per specimen. The targeted cross-section reduction of 10% was chosen to ensure that the bar outside the damage zone still undergoes plastic deformation to attenuate the strain localisation. The diameter was reduced mechanically by machining on a lathe (turning). During turning, the specimens were constantly cooled to prevent heat inflow and an unintended alteration of steel microstructure and characteristics. The ratio $(L_c/2)/Ø_c$ varied between 0.4 and 1.6, which resulted in the damage lengths L_c reported in Table 5.1; note that the numbers of the specimen designation correspond to the damage length in millimetres. The geometry of all reinforcing bars was scanned before testing using a three-dimensional optical scanner (ATOS Core by GOM). The accurate measurements of initial and residual diameter allowed to precisely determine the cross-sectional areas of the bars (see Table 5.1). With the effective initial diameter being a bit larger than 20 mm and the precision of the mechanical diameter reduction, the effective cross-section loss was slightly higher than targeted.

The specimens were tested deformation controlled until failure in a universal testing machine at a constant strain rate of $10^{-4}\,\text{s}^{-1}$ (Figure 5.1(c)). Load introduction heads with spherical hinges were installed on the testing machine to minimise unintentional bending moments in the specimens due to geometrical misalignment of either the machine heads or the clamping, which can hardly be avoided and could otherwise have affected the test results. Threads were provided at the specimen ends, which were connected to the load introduction heads using spherical washers and nuts. A three-dimensional digital image correlation system (DIC) with two ProSilica GT600-cameras containing a sensor of 6576 x 4384 Px = 29 MPx was used to capture the specimen deformations. To this end, the specimens were sandblasted and subsequently painted white and speckled black (see Figures 5.1(a) and (b)). The cameras were placed vertically at a distance of 900 mm from the specimen, with an inter-camera distance of 300 mm to enable optimal correlation of the curved bar surface. The system setup resulted in a resolution of approximately 0.014 mm/px. The data was post-processed with a subset size of 29 px and a step size of 7 px, providing data points at a distance of 0.4 mm.

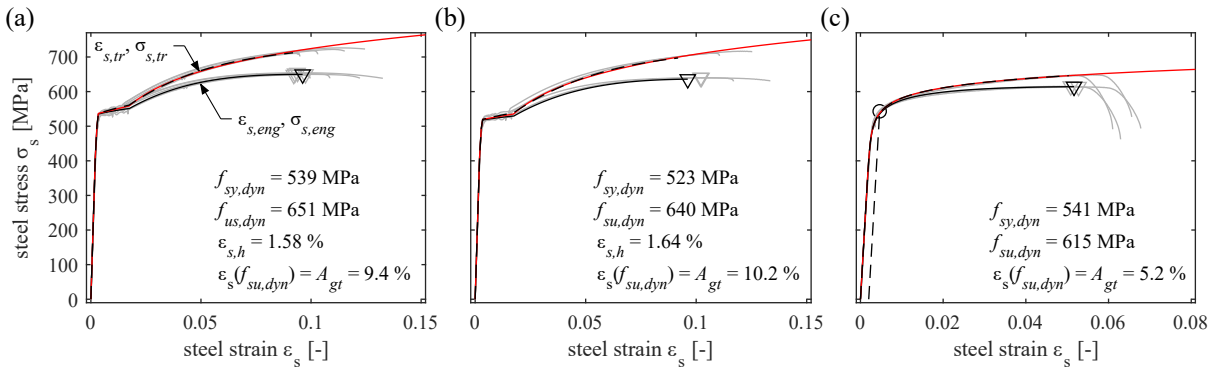

Fig. 5.2 – Stress-strain relationships and material characteristics from standard tensile tests of (a) QST reinforcing bar Ø20, (b) QST reinforcing bar Ø19, (c) CW reinforcing bar Ø20. The plots show true and engineering stress-strain curves of the test samples (grey curves, $\varepsilon_{s,tr}$, $\sigma_{s,tr}$ and $\varepsilon_{s,eng}$, $\sigma_{s,eng}$, respectively), the steel characteristics (dynamic yield stress $f_{sy,dyn}$, dynamic tensile strength $f_{su,dyn}$ and corresponding strain A_{gt} (marked with a triangle), and strain at onset of hardening $\varepsilon_{s,h}$) and the corresponding constitutive relationships (black and red curves), see Section 5.3.2

Standard tensile tests were conducted on 1200 mm long bar samples at a constant strain rate of $10^{-4}\,s^{-1}$ to determine the material characteristics of the reinforcing bars, using an LVDT of 300 mm gauge length to measure the deformations. Figure 5.2 shows the steel stress-strain relationships (true and engineering strains and stresses, $\varepsilon_{s,tr}$, $\sigma_{s,tr}$ and $\varepsilon_{s,eng}$, $\sigma_{s,eng}$, respectively) together with the corresponding characteristics and the constitutive models (see Section 5.3.2) for (a) the QST reinforcing bars with an initial diameter of 20 mm, (b) the QST reinforcing bars with a reduced diameter of 19 mm, and (c) the CW reinforcing bars (diameter 20 mm). Although originating from the same production batch as the specimens in [69, 71], the plotted stress-strain relationships and the steel characteristics were determined from additional tensile tests conducted near-term to the experiments to avoid any influence of strain ageing, which commonly affects CW reinforcement and is indeed evident when comparing the

Tab. 5.1 – Specimen specifications: CW = hot-rolled and cold-worked, QST = hot-rolled, quenched and self-tempered; A_s, $A_{s,c}$ = initial and reduced cross-sectional area obtained from GOM-Scan; Ø, $Ø_c$ = initial and reduced diameter; L_c = damage length; ζ = cross-section loss; and $(L_c/2)/Ø_c$ = normalised damage length.

Specimen	L_c [mm]	A_s [mm^2]	$A_{s,c}$ [mm^2]	Ø [mm]	$Ø_c$ [mm]	ζ [-]	$(L_c/2)/Ø_c$ [-]
CW-15	15	316.9	278.5	20.09	18.83	0.121	0.40
CW-19	19	316.6	270.7	20.08	18.56	0.145	0.51
CW-23	23	316.3	276.5	20.07	18.76	0.126	0.61
CW-27	27	316.9	279.7	20.09	18.87	0.118	0.72
CW-30	30	317.5	275.4	20.11	18.72	0.133	0.80
CW-38	38	317.5	276.5	20.11	18.76	0.129	1.01
CW-61	61	317.0	274.7	20.09	18.70	0.133	1.63
QST-15	15	329.6	285.7	20.48	19.07	0.133	0.39
QST-19	19	332.0	289.0	20.56	19.18	0.130	0.50
QST-23	23	330.8	289.4	20.52	19.20	0.125	0.60
QST-27	27	328.0	280.8	20.43	18.91	0.144	0.71
QST-30	30	328.1	280.6	20.44	18.90	0.145	0.79
QST-38	38	327.9	278.5	20.43	18.83	0.151	1.01
QST-61	61	328.1	279.9	20.44	18.88	0.147	1.62

characteristics presented in Figure 5.2(c) to those reported in [69] (e. g. increase of yield stress by 5% over time).

For the QST bars, separate constitutive relationships for Ø20 and Ø19 are shown in Figures 5.2(a) and (b) to capture the effect of the distinct microstructure over the cross-section (see Section 5.1.4), which needs to be considered in the analysis. Note that the relationship and characteristics of the QST bar Ø19 (Figure 5.2(b)) were taken from [71] since no strain ageing effect was observed for the QST reinforcing bars Ø20 (comparing the results of Figure 5.2(a) to those reported in [69, 71]).

5.3 Definitions and basic theoretical models

5.3.1 Used definition of stress

Throughout this paper, the apparent uniaxial stress in the corroded damage zone (subscript c; in general and at peak load) is defined as

$$\begin{aligned} \sigma_{s,c} &= \frac{F}{A_{s,c}} \\ \sigma_{s,c,max} &= \frac{F_u}{A_{s,c}} \end{aligned} \tag{5.1}$$

and the stress in the undamaged part of the bar (uncorroded regular cross-section, subscript uc) as

$$\begin{aligned} \sigma_{s,uc} &= \frac{F}{A_s} \\ \sigma_{s,uc,max} &= \frac{F_u}{A_s} \end{aligned} \tag{5.2}$$

with F, F_u = load and peak load, and A_s, $A_{s,c}$ = initial and reduced cross-sectional areas of the bar (Table 5.1). The relative cross-section loss is defined as

$$\zeta = \frac{A_s - A_{s,c}}{A_s} \in [0,1] \tag{5.3}$$

and hence, the stress in the damaged and undamaged parts is related by equilibrium

$$\sigma_{s,uc} = \sigma_{s,c}(1-\zeta) \tag{5.4}$$

The corresponding strains in the damaged and undamaged part, $\varepsilon_{s,c}$ and $\varepsilon_{s,uc}$, follow from the stress-strain relationships of Figure 5.2 or any constitutive material relationship.

5.3.2 Constitutive material relationships

The stress-strain relationships of the QST reinforcing bars Ø20 and Ø19 are approximated using the constitutive model described in [71]. The input parameters for the model evaluation (i. e. characteristics of the distinct microstructure layers perlite/ferrite, bainite, and martensite, as well as their amount on the total cross-sectional area) are also taken from [71] since the specimens of both studies originate from the identical production batch, and no strain ageing was observed in the QST bars. The model response is shown in Figures 5.2(a) and (b) as solid black lines, virtually identical to the material test results.

The following constitutive relationship is used to approximate the results of the material tests of the CW reinforcing bars:

$$\begin{aligned}
\varepsilon_s(\sigma_s) &= \frac{\sigma_s}{E_s} + \left(\frac{c_1}{c_2 - \sigma_s}\right)^{1/c_3} + c_4 \\
c_1 &= \frac{K {c_4}^{c_3} f_{su}}{K - c_4^{c_3}} \\
c_2 &= \frac{c_1}{c_4^{c_3}} \\
K &= \left(A_{gt} - \frac{f_{su}}{E_s} + c_4\right)^{c_3} \\
&\varepsilon_s,\ A_{gt} \text{ in [-]},\ \sigma_s,\ f_{su},\ E_s \text{ in [MPa]}
\end{aligned} \tag{5.5}$$

with f_{su}, A_{gt} = tensile strength and corresponding strain from the material tests, $E_s = 205\,\text{GPa}$ = steel Young's modulus, and c_3, c_4 = model parameters. The proposed relationship extends the one proposed by Ramberg and Osgood [129] such that the curve accurately captures the behaviour of modern European reinforcing steel. The model parameters were determined such that the material tests are closely approximated, which resulted in $c_3 = 3.2 \cdot 10^{-10}$ and $c_4 = 2.0 \cdot 10^{-14}$ (in true stresses and true strains, which can be reformulated to engineering stresses and strains, see Section 5.5.1). The model response is shown in Figure 5.2(c) as a solid black line.

5.3.3 Strain localisation model (SLM)

Strain localisation is modelled by idealising the bars as tension members consisting of several sub-members with different lengths, cross-sectional areas and stress-strain behaviour, which are serially connected and, hence, subjected to an equal normal force. The stresses in the sub-members at any given load are determined with respect to their actual cross-sectional areas (e. g. using Equations (5.1) and (5.2)). The corresponding strains follow from the constitutive material model (e. g. Equation (5.5)), and the sub-member elongations are obtained by multiplying the strains with the sub-member length. Summing up the elongations of all sub-members and dividing by the total length yields the mean strain of the entire tension member. For a reinforcing bar of total length L_{tot} and initial cross-sectional area A_s, which contains a locally reduced cross-sectional area $A_{s,c}$ over the damage length L_c, the mean strain obtained by the SLM is (using the notation of Equations (5.1)-(5.3)):

$$\varepsilon_{s,m}^{SLM}(\sigma_{s,c}) = \frac{L_c \varepsilon_s(\sigma_{s,c}) + (L_{tot} - L_c)\,\varepsilon_s(\sigma_{s,uc})}{L_{tot}} = \frac{L_c \varepsilon_s(\sigma_{s,c}) + (L_{tot} - L_c)\,\varepsilon_s(\sigma_{s,c}(1-\zeta))}{L_{tot}} \tag{5.6}$$

where $\varepsilon_s(\sigma_s)$ denotes the constitutive material model. A detailed description of the concept, including example calculations and accounting for tension stiffening in concrete tension members, can be found in [72]. An identical model was successfully applied to bare reinforcing bars with artificially reduced cross-sections by Zeng et al. [163].

5.4 Experimental results

5.4.1 Strain measurements and influence of ribs

The field of view of the DIC setup described in Section 5.2 covered almost the entire projection of half the circumferential bar surface, as illustrated in Figures 5.3(a) and (b) for the surface geometry of the

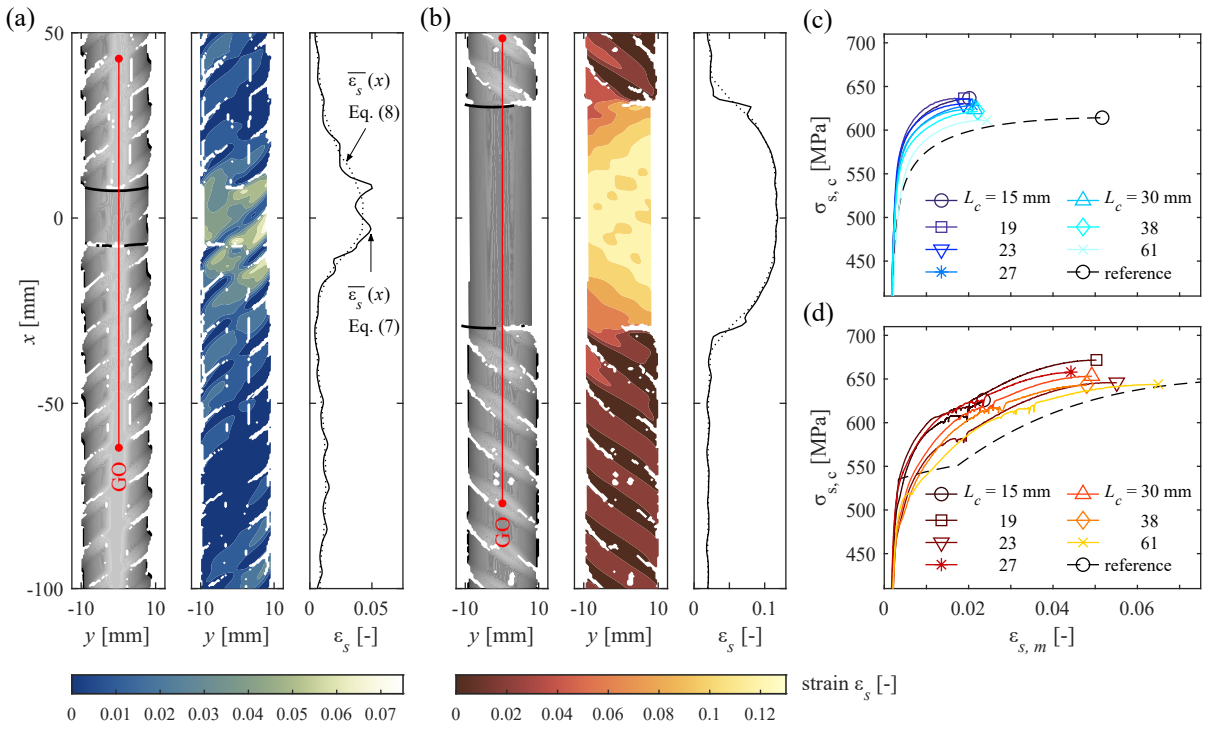

Fig. 5.3 – Strain measurements using DIC of Specimens (a) CW-15 and (b) QST-61, showing the bar geometry (grey), the full-field strains at peak load (coloured), and the corresponding mean strain over the bar width according to Equation 5.7; stress-mean strain curves $\sigma_{s,c}$ vs $\varepsilon_{s,m}$ of all specimens of (c) CW and (d) QST reinforcing bars using the virtual gauges GO indicated in red in (a) and (b), with a length L_{tot} reported in Table 5.2. Note: white areas in (a) and (b) could not be correlated.

Specimens CW-15 and QST-61 (in grey). The correlation of the images of the two cameras was very satisfying; only the white areas below or above a rib could not be correlated since they were hidden by the corresponding rib and out of sight for either of the cameras.

DIC provides deformation measurements of a specimen surface, which can deviate from the average specimen deformation over the cross-section, especially if the surface exhibits elevations such as the ribs of a reinforcing bar. This issue can be observed in the full-field strains at peak load shown in colour in Figures 5.3(a) and (b). In the undamaged part, the location of the areas exhibiting small strains matches the location of the ribs perfectly, indicating that the ribs deform much less than the bar on average. The measured strains on the ribs do not necessarily need to represent the specimen deformation over the cross-section, which is evident when comparing to the strains on the left and right side of a rib (at a horizontal cross-section, e. g. at $x = -50\,\text{mm}$). Similar effects are known from other near-surface measurement techniques, e. g. from fibre optic strain sensing on reinforcing bars, see [63, 100].

To overcome this issue, the mean strain over the instrumented bar width is calculated as

$$\overline{\varepsilon_s}(x) = \frac{\int_{y_{min}}^{y_{max}} \varepsilon_s(x,y)\,dy}{(y_{max} - y_{min})} \tag{5.7}$$

Results obtained from Equation (5.7) are shown as solid lines in Figures 5.3(a) and (b) for the strains at peak load. While the mean strain is a simple and intuitive measure to qualitatively compare the strains of different bar sections or between different specimens at equal load, it is inadequate to determine strains and stresses quantitatively since the ribs still affect the calculated strain distribution $\overline{\varepsilon_s}(x)$ (as seen in Figures 5.3(a) and (b)), as a specific strain value $\overline{\varepsilon_s}(x)$ depends on the number of measurement points laying on or next to a rib.

Tab. 5.2 – Lengths L_{tot} of Gauge GO (Figure 5.3) per specimen, bridging the damaged section with length L_c and instrumenting a length L_{uc} with regular cross-section.

Specimen	L_c [mm]	L_{uc} [mm]	L_{tot} [mm]
CW-15	15	90	105
CW-19	19	86	105
CW-23	23	73	96
CW-27	27	73	100
CW-30	30	73	103
CW-38	38	79	117
CW-61	61	68	129
QST-15	15	88	103
QST-19	19	82	101
QST-23	23	93	116
QST-27	27	87	114
QST-30	30	81	111
QST-38	38	89	127
QST-61	61	65	126

A more robust measure for strains was found to be the integral of axial strains along the bar axis (or a parallel to the latter) over an axial distance equal to the rib spacing, divided by this distance (essentially corresponding to virtual strain gauges with the rib spacing as base length). For any lateral position $y = y_1$, this strain measure is defined as

$$\overline{\varepsilon_s}\,(x, y = y_1) = \frac{\int_{x-c/2}^{x+c/2} \varepsilon_s\,(x, y = y_1)\,dx}{c} \tag{5.8}$$

with c = rib spacing. The ribs only negligibly influence the results since the number of measurement points laying on or next to a rib is approximately constant for all locations x. However, if Equation (5.8) is used continuously over x, it strongly underestimates steep strain gradients, e. g. in the cross-section transition at the end of the damage zone (see Figure 5.3). To avoid this issue, discrete virtual gauges with gauge length = rib spacing were placed along the bar, paying attention that no gauge overlaps the cross-section transition (except for the gauge GO in Figure 5.3, which spans the entire bar), and strains are calculated in this paper according to Equation (5.8) for the virtual gauges.

The lengths L_{tot} of the longest gauge GO (shown in red in Figures 5.3(a) and (b)), bridging the damaged section with length L_c and a length L_{uc} with regular cross-section, was approximately constant for all experiments; the exact values are reported in Table 5.2. L_{tot} was chosen such that the gauge endpoints were located at least one diameter away from the damage zone (where possible two or more diameters, but observing the limitation by the field of view of the cameras).

Figures 5.3(c) and (d) show the stress-mean strain curves ($\sigma_{s,c}$ vs $\varepsilon_{s,m}$) of all CW- and QST-specimens, respectively, with $\varepsilon_{s,m}$ = strain measured at the virtual gauge GO. The strain at peak stress is reduced by approximately 50% compared to the corresponding A_{gt} = 5.2% (CW), 9.4% (QST, Ø19) and 10.2% (QST, Ø20, see Figure 5.2) of the undamaged bars (dashed lines in Figures 5.3(c) and (d)), which is a direct consequence of strain localisation. However, the variation of the strain at peak stress among the same steel type is remarkably small, considering their different damage lengths L_c (except for QST-15, which failed prematurely). Moreover, the apparent uniaxial peak stress appears to increase with decreasing damage length L_c, which is remarkable since the cross-section reduction was equal for all specimens (small variations in the cross-sectional area, see Table 5.1, were accounted for in determining

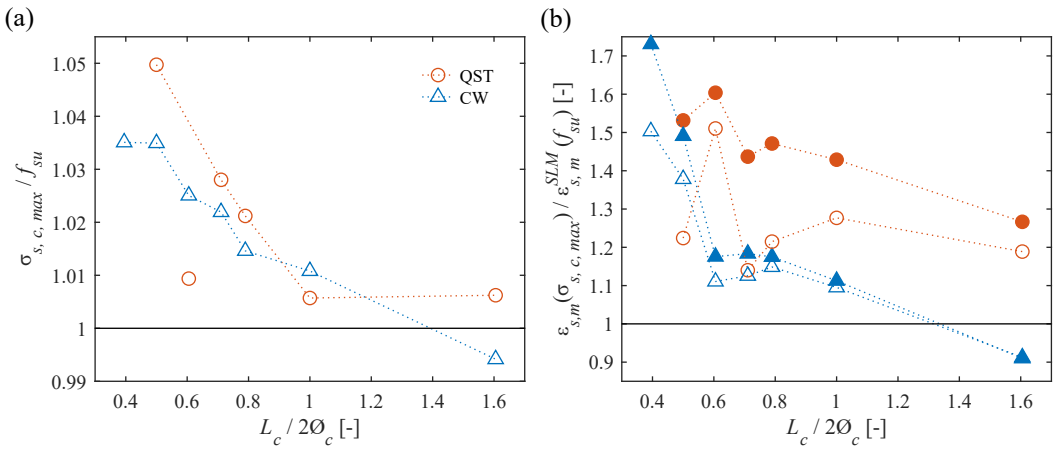

Fig. 5.4 – Experimental results of tension tests: (a) peak stress normalised with uniaxial tensile strength and (b) mean strain at peak stress, normalised with mean strain predicted by SLM (Equation 5.6). Filled markers result from evaluating Equation 5.6 with $\sigma_{s,uc} = (1-\zeta) f_{su}$, and empty markers for $\sigma_{s,uc} = (1-\zeta)\sigma_{s,c,max}$.

the stresses). These effects are attributed to a triaxial stress state in the vicinity of the damage zone, which is further analysed in the following sections.

5.4.2 Increase in tensile strength and corresponding deformation

Figure 5.4(a) shows the peak stress in the damage zone measured in the experiments, normalised with the tensile strength f_{su} of the material tests, vs the normalised damage length. The actual cross-sectional areas (Table 5.1) were used to determine the stresses, and the tensile strength of the reduced cross-section Ø19 (listed in Figure 5.2(b)) for the normalisation of the results of the QST reinforcing bars. While the ratio $\sigma_{s,c,max}/f_{su}$ is close to 1 ($\pm 1\%$) for $L_c/(2Ø_c) \geq 1$, a significant increase in the peak stress is observed for both steel types with decreasing damage length, with peak stresses exceeding the material tensile strength by up to 5%.

In Figure 5.4(b), filled blue and red markers indicate the observed strains at peak stress $\varepsilon_{s,m}(\sigma_{s,c,max})$ of the virtual gauge GO (Figure 5.3 and Table 5.2), plotted vs the normalised damage length. The measured strains are normalised with the strains expected according to the SLM (Equation (5.6)), assuming $\sigma_{s,c} = f_{su}$. For the QST reinforcement (filled red markers), a steady increase of the strain at peak stress, compared to the theoretical strains of the SLM, is observed with decreasing damage length, with a pronounced strain increase even for the longest damage length ($L_c/(2Ø_c) = 1.6$). For the CW-reinforcement (filled blue markers), the increase in peak strain is less pronounced for $L_c/(2Ø_c) \geq 0.6$ but increases sharply for shorter damage lengths.

Evidently, the strains at peak stress in the undamaged parts were higher than assumed by the calculations underlying the solid markers (using $\sigma_{s,c} = f_{su}$) due to the increased peak stress for shorter damage lengths (see Figure 5.4(a)). To eliminate this effect and visualise a potentially altered stress-strain behaviour, the actually measured load is considered in a second step for determining the theoretically expected strains, replacing the term $\sigma_{s,uc} = f_{su}(1-\zeta)$ in Equation (5.6) with $\sigma_{s,uc} = \sigma_{s,c,max}(1-\zeta)$. The results are depicted in Figure 5.4(b) with empty markers in red and blue for the QST and CW reinforcement, respectively. While the strain increase compared to the predictions of the SLM is somewhat reduced, particularly at short damage lengths, the overall tendencies remain the same, indicating an altered stress-strain behaviour.

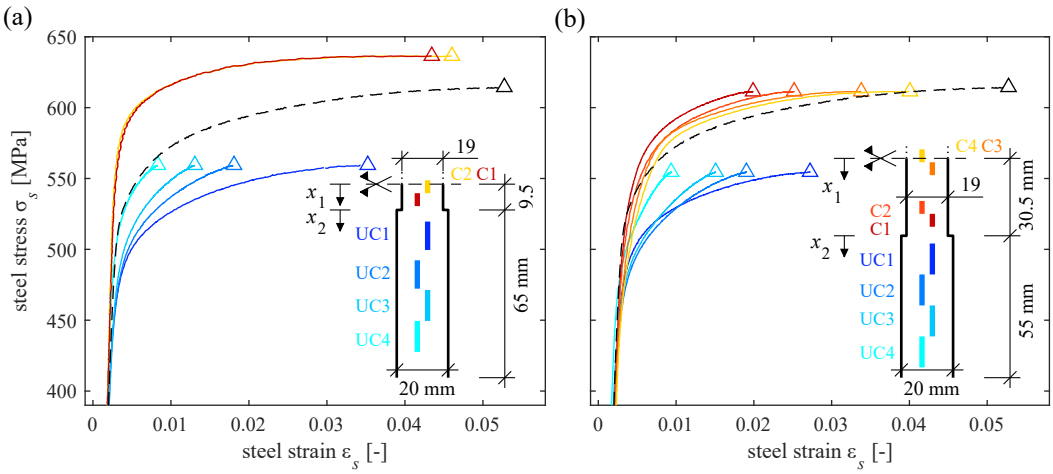

Fig. 5.5 – Stress-strain curves of different virtual gauges along the bar axis in the damage zone (red, yellow) and the adjacent undamaged zone (blue) for the Specimens (a) CW-19 and (b) CW-61, with schematic positions of the gauges shown to the right. The dashed black lines represent the reference curves of the material tests. Stresses refer to the reduced cross-sectional area in the damage zone and to the initial cross-sectional area in the undamaged part according to Equations (5.1) and (5.2), and Table 5.1.

5.4.3 Analysis of stress-strain behaviour inside and close to the damage zone

Figure 5.5 shows the stress-strain curves of several virtual strain gauges for the specimens (a) CW-19 (short damage length) and (b) CW-61 (long damage length). The gauges in the undamaged part span one rib distance (as suggested in Section 5.4.1), while the gauge lengths in the damage zone without ribs are shorter (11-12 mm and 5 mm, respectively); the gauge positions and lengths are shown schematically in the figures and are reported in Table 5.3. Stresses (referred to the reduced cross-sectional area (Equation (5.1)) and strains in the damage zone are depicted in red and yellow; stresses (referred to the initial cross-sectional area (Equation (5.2)) and strains in the adjacent undamaged parts are shown in blue. The stress-strain curve of the corresponding material test is shown as a dashed black curve for comparison, and the peak load is marked with triangles.

In Specimen CW-19 (short damage length, Figure 5.5(a)), the curves of the gauges in the damage zone (yellow and red) almost coincide, with slightly smaller strains at peak stress of the gauge closer to cross-section transition (C1, red). The stresses of both curves are significantly higher than in the material tests, and the apparent uniaxial yield stress and tensile strength are clearly increased. After passing the

Tab. 5.3 – Gauge length L_G and position of gauge centre of the gauges shown in Figures 5.5 and 5.6 (x_1 = distance from damage zone centre, x_2 = distance from cross-section transition, see Figures 5.5 and 5.6).

Gauge	CW-15			CW-61			QST-15			QST-61		
	L_G [mm]	x_1 [mm]	x_2 [mm]	L_G [mm]	x_1 [mm]	x_2 [mm]	L_G [mm]	x_1 [mm]	x_2 [mm]	L_G [mm]	x_1 [mm]	x_2 [mm]
C4				5.3	0.2	-30.3				5.2	0.2	-30.2
C3				5.0	5.3	-25.2				4.8	5.2	-25.3
C2	3.8	0.3	-9.2	5.0	20.1	-10.4	4.9	0.0	-9.5	5.2	20.2	-10.3
C1	4.2	4.3	-5.2	5.6	25.4	-5.1	4.2	4.6	-4.9	5.6	25.6	-4.9
UC1	10.9	17.6	8.1	10.9	38.8	8.3	13.6	20.9	11.4	10.8	37.3	6.8
UC2	10.9	32.7	23.2	12.0	50.2	19.7	12.4	33.9	24.4	12.9	45.8	15.3
UC3	12.0	44.1	34.6	11.9	62.1	31.6	12.7	46.4	36.9	12.4	58.4	27.9
UC4	11.9	56.1	46.6	12.2	74.2	43.7	12.3	58.9	48.5	12.7	71.0	40.5

yield point, the curves flatten pronouncedly and continue almost horizontally until the peak stress. On the other hand, the stress-strain curves in the undamaged part exhibit a significantly softer behaviour compared to the material test, with lower stiffnesses and, accordingly, higher strains at peak stress the closer the gauges are located to the damage zone. Hence, while the curve of Gauge UC4 (light blue), away from the damage zone, closely follows the material reference curve, the strains of UC1 are roughly four times higher at equal stress. The strain of UC1 at peak stress is thus similar to the one of Gauge C1 in the damage zone although the cross-sectional area at UC1 was roughly 17% higher than at C1 in the damage zone (compare Table 5.1).

In Specimen CW-61 (long damage length, Figure 5.5(b)), other than in Specimen CW-19, the peak stresses in the damage zone are almost identical to the tensile strength of the material tests. Still, the stress-strain curves in the damage zone show a stiffer behaviour closer to the cross-section transition (Gauges C4 to C1, yellow to red): while Gauge C4 in the middle of the damage zone exhibits a stress-strain behaviour similar to the reference curve, the strain at peak stress of Gauge C1 is reduced approximately by a factor of 2. The curves of the gauges in the undamaged part (UC1 to UC4, blue) are very similar to the corresponding curves of Specimen CW-19 (Figure 5.5(a)), with a softer stress-strain behaviour close to the damage zone. Again, the strains in Gauge UC4 (light blue) are similar to the reference curve, whereas the strains in Gauge UC1 (dark blue) are comparable to those in the damage zone, and even higher than the strains of Gauges C1 and C2. The strains at peak stress measured in the Gauges UC2 to UC4 are almost identical for both specimens CW-19 and CW-61, irrespective of the different damage lengths.

Figures 5.6(a) and (b) show the results of Specimens QST-19 and QST-61, respectively, with a zoom to the yield point in (c) and (d). As a reference, the dashed lines show the stress-strain curve of the material test on a bar Ø20, applying to the results of the gauges in the undamaged part (UC1 to UC4), and the dash-dotted lines refer to the material test on a bar with reduced diameter Ø19, applying to the results of the gauges in the damage zone (C1 to C4).

The results obtained for Specimen QST-19 (short damage length, Figure 5.6(a)) are similar to those of Specimen CW-19 in Figure 5.5(a). The strains in Gauge C1 are similar to those of Gauge C2, and both curves show a stiffer behaviour at the beginning of the inelastic phase. Nevertheless, strains at peak stress are even higher in this specimen than in the reference test, and the peak stresses are again increased compared to the tensile strength of the reference test. The stress-strain curves of the Gauges UC1 to UC4 in Figure 5.6(c) in the adjacent undamaged part differ less from the reference curve than those in Figure 5.5(a), except for Gauge UC1 closest to the damage zone, which clearly exhibits a softer behaviour.

The stress-strain curves of the gauges in the damage zone (red, yellow) of Specimen QST-61 (long damage length, Figure 5.6(b)) follow the curves of the reference test even closer than in Specimen QST-19. Nevertheless, a stiffer behaviour is observed closer to the cross-section transition (C4 to C1), with Curve C1 (red) differing significantly, exhibiting merely about 60% of the strain at peak stress compared to C4. The curves of the gauges in the adjacent undamaged part UC1 to UC4 differ much less than in Specimen CW-61 (Figure 5.5(b)) and closely follow the reference curve in the elastic range and at hardening onset.

An interesting observation in Figure 5.6 is the loss of the yield plateau (i. e. of the approximately horizontal part of the black reference stress-strain curve between the yield point and the hardening onset). The same observation was made in tension tests of reinforcing bars with natural, unilateral corrosion pits [62]. In the undamaged part, the yield plateau is absent for all gauges close to the cross-section transition (UC1, UC2, C1 and C2). For UC1 of QST-19 and UC1 and UC2 of QST-61, the yield point is lowered from 540 MPa to approximately 450 to 470 MPa, directly followed by the strain hardening phase. Except for UC1 of QST-19, the curves pass the point (ε_{sh}, f_{sy}) and then follow the reference curves again. This stress-strain behaviour contrasts that of gauges further away from the damage zone (UC3, UC4), which closely follow the reference curve and exhibit a yield plateau. Similarly, in all gauges of the damage zone close to the cross-section transition (C1 and C2 for QST-19 and C1 for QST-61), the strain hardening

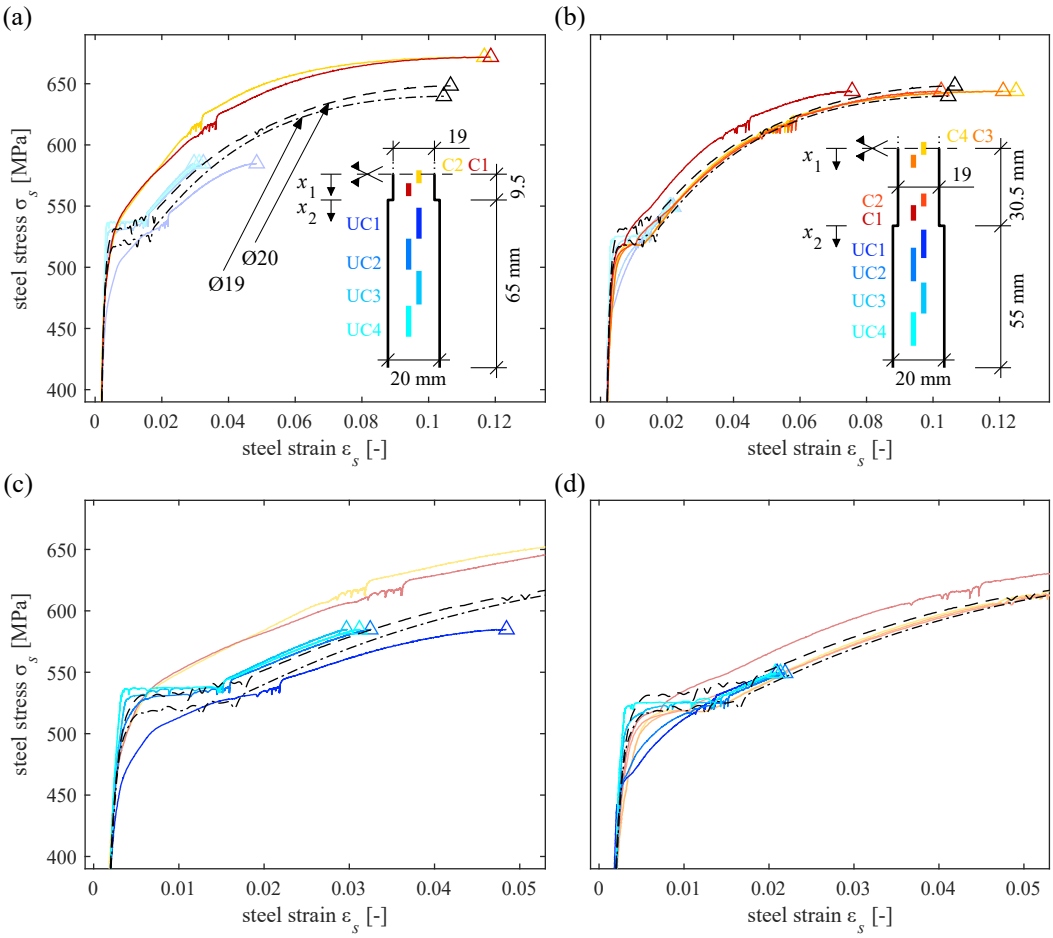

Fig. 5.6 – Stress-strain curves of different virtual gauges along the bar axis in the damage zone (red, yellow) and the adjacent undamaged zone (blue) for the Specimens (a) QST-19 and (b) QST-61, with schematic positions of the gauges shown to the right. The dashed black lines represent the reference curve of the material tests for Ø20, and the dash-dotted lines that for Ø19. Stresses refer to the reduced cross-sectional area in the damage zone and to the initial cross-sectional area in the undamaged part according to Equation (5.1) and (5.2), and Table 5.1.

phase directly seems to follow the yield point, while the curves observed at Gauges C3 and C4 in QST-61, away from the transition, again follow the reference curve and exhibit a yield plateau.

A macroscopically visible yield plateau is related to the occurrence of Lüders bands and is associated with discontinuous yielding. Presumably, the triaxial stress state at the cross-section transition influences the deformation behaviour of crystal grains in the steel, preventing macroscopically visible discontinuous yielding. The phenomenon is further investigated in Section 5.5.5, after analysing the triaxial stress state near a local damage.

5.5 Analysis of triaxial stress state near local damages

5.5.1 Introduction and FE model description

For the assessment of the experiments, the reinforcing bars were modelled with the FE-software Ansys Mechanical as concatenated smooth cylinders, with two cylinders of diameter Ø enclosing a cylinder of length L_c and reduced diameter $Ø_c$ (diameters according to Table 5.1). The composed bar has a total length of 200 mm and is fixed at one end, whereas an increasing displacement is imposed at the other end. The structure is meshed with PLANE183-elements at a size of 1.0 mm, which allows to exploit the

Tab. 5.4 – Fitting parameters for extrapolation of the hardening branch of constitutive material curves according to Equation (5.10).

Material constitutive relationship	b_1 [-]	b_2 [-]	Material constitutive relationship	b_1 [-]	b_2 [-]
CW	37.9	759.4			
QST, Ø20	94.7	942.6			
QST, Ø19	98.8	935.7			
QST, Ø19.5	96.7	939.2	QST, Ø15.5	112.1	894.1
QST, Ø18.4	101.4	931.3	QST, Ø14.8	113.5	887.5
QST, Ø17.9	104.1	926.6	QST, Ø14.1	114.9	882.5
QST, Ø17.3	107.2	921.2	QST, Ø13.4	115.9	879.9
QST, Ø16.7	108.9	910.5	QST, $\leq$ Ø12.7	116.3	879.9
QST, Ø16.1	110.5	901.9			

axial symmetry and reduce the calculation time. Von Mises' J2-plasticity model (see Section 5.1.3) with isotropic hardening was implemented as a material model, and the analyses accounted for geometrical nonlinearity. A possible mesh-size dependency was not analysed since a similar study reported no such influence for the chosen mesh size [9].

For material input, the engineering stress-strain relationships shown in Figure 5.2 need to be converted to true values. True strains result from considering the deformations on a differential element, leading to $d\varepsilon_{tr} = dl/l$. For true stresses, the force is referred to the actual cross-sectional area, which decreases with increasing axial deformation due to volume conservation. The conversion can be approximated by (see, e. g. [136])

$$\begin{aligned} \varepsilon_{s,tr} &= \ln\left(1+\varepsilon_{s,eng}\right) \\ \sigma_{s,tr} &= \sigma_{s,eng}\left(1+\varepsilon_{s,eng}\right) \end{aligned} \tag{5.9}$$

Assuming a homogeneous bar (no variation of mechanical properties along the bar axis), Equation (5.9) can be applied to the data of the material tests up to the onset of necking, which occurs after having reached the tensile strength. Figure 5.2 shows the converted stress-strain curves of the material tests in grey and the constitutive material models in true values as dashed black lines.

Following the concept of [9], the input material curve is not limited to the tensile strength and the corresponding strain, but extrapolated from the constitutive relationships (formulated in true values) up to $\varepsilon_{s,tr} = 0.2$. Since the application range of the constitutive relationships is limited to the tensile strength and cannot be evaluated beyond this point, a logarithmic equation of the form

$$\begin{aligned} &\sigma_{s,tr} = b_1 \ln\left(\varepsilon_{s,tr}\right) + b_2 \\ &\varepsilon_{s,tr} \text{ in [-]}, \ \sigma_{s,tr} \text{ in [MPa]} \end{aligned} \tag{5.10}$$

is fitted to the constitutive relationships in the hardening branch, i. e. in the range $[\varepsilon_{sh}, A_{gt}]$ for the QST reinforcement and $[0.02, A_{gt}]$ for the CW reinforcement, with the parameters b_1 and b_2 summarised in Table 5.4. The resulting curves are shown in Figure 5.2 as solid red lines. The second part of Table 5.4 contains the parameters for bars with a cross-section reduction beyond 19 mm, which are used for the parametric study in Section 5.6.

The force-elongation diagram resulting from the FE analyses is not monotonically increasing, as one might assume from the input material relationship. Since the FE-analysis considers the lateral contraction of the bar in the damage zone due to the high axial strains, the cross-section is continuously reduced with

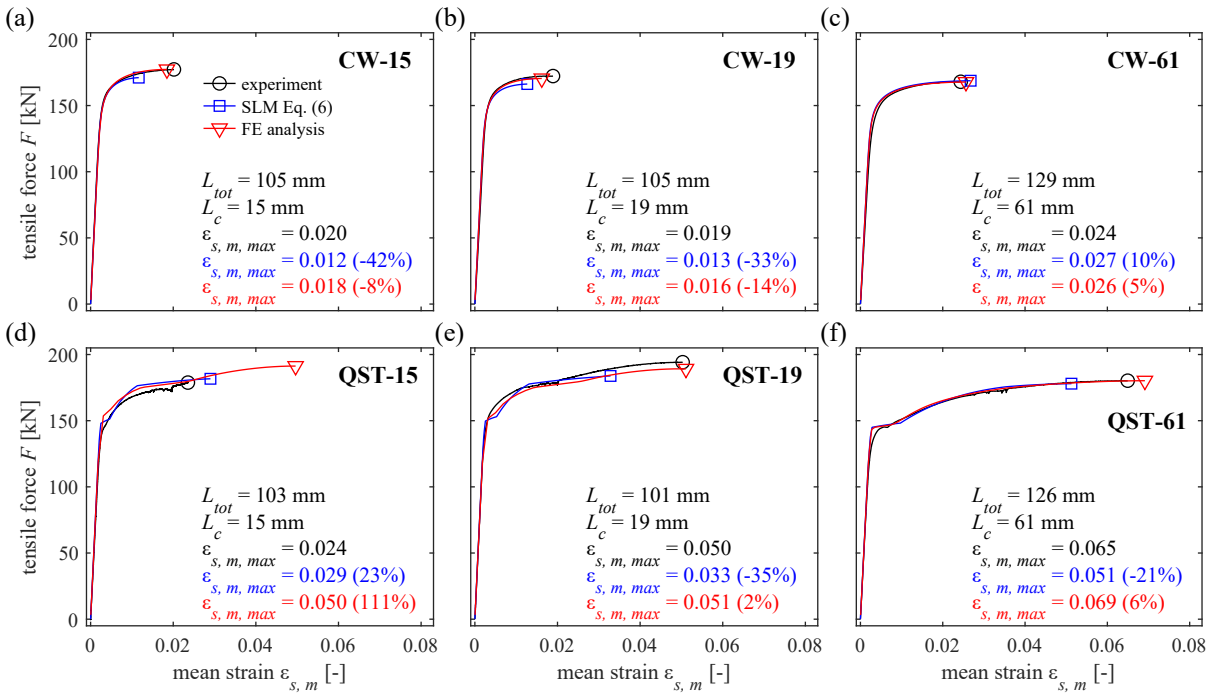

Fig. 5.7 – Comparison of experimental results (black) with the SLM (Equation (5.6), blue) and the FE analyses (red): (a)-(c) Series CW; (d)-(f) Series QST, specimens with damage lengths L_c = 15, 19, and 61 mm. The markers indicate the peak loads. Additionally, the total gauge length L_{tot} and the mean strain at peak load $\varepsilon_{s,m,max}$ are reported, as well as the relative deviation between the models and the experimental result.

increasing axial deformation, and beyond a certain elongation, the force decreases despite that the axial stresses keep increasing. The elongation at the peak load – similar to the onset of necking in a tensile test – is considered representative for comparison with the experimental results.

5.5.2 Comparison of experiments with different models

Figure 5.7 compares the force-mean strain curves obtained from the experiments (black) with the response of the SLM (blue, see Section 5.3.3) and the FE analyses of Section 5.5.1 for the CW (Figures 5.7(a) to (c)) and the QST reinforcement (Figures 5.7(d) to (e)) with damage lengths L_c = 15, 19, and 61 mm. The markers indicate the peak loads. The results of the remaining experiments with L_c = 23, 27, 30, and 38 mm are enclosed in the appendix. The gauge lengths L_{tot} used for evaluating the experimental data are reported in Table 5.2 and indicated in Figure 5.7. Equation (5.6) is used for the SLM in combination with the constitutive material relationships of Section 5.3.2 and Table 5.1.

The results of Figures 5.7(a), (b), and (e) confirm the observation of Section 5.4.2 that the SLM strongly underestimates the strain at peak stress (up to 40%) for short damage lengths and, to a minor extent, also the peak stress. With increasing damage length, the accuracy of the SLM increases (compare also Figure 5.A1), with the SLM being almost identical to the experimental results in Figure 5.7(c) for L_c = 61 mm. In contrast, the responses of the FE analyses capture the experimental curves for all damage lengths regarding curve shape, peak stress, and corresponding strain, except for Specimen QST-15 (Figure 5.7(d)), which failed prematurely. Accordingly, both models overestimate the peak stress and elongation of this experiment.

The results of the FE analyses support the hypothesis that the triaxial stress state at the cross-section transition considerably alters the stress-strain behaviour of reinforcing bars containing local corrosion damage. The hypothesis is further confirmed by the increasing prediction accuracy of the SLM for longer damage lengths, where the local effects of the transition zones become less relevant.

5.5.3 Analysis of the triaxial stress state

Figure 5.8 illustrates the stress state for Specimens (a) CW-15 and (b) CW-61 at the peak load, showing the engineering values of the von Mises stress $\sigma_{vM}(r,x)$, the axial, radial, and tangential stresses, $\sigma_x(r,x)$, $\sigma_r(r,x)$, and $\sigma_\varphi(r,x)$, the non-zero shear stress $\tau_{rx}(r,x)$, and the distribution of the axial and von Mises stresses averaged over the cross-section, i. e.

$$\begin{aligned}
\overline{\sigma_x}(x) &= \frac{\int_A \sigma_x(r,x)dA}{A} \\
\overline{\sigma_{vM}}(x) &= \frac{\int_A \sigma_{vM}(r,x)dA}{A} \\
A &= \begin{cases} A_{s,c} & \text{in damage zone} \\ A_s & \text{elsewhere} \end{cases}
\end{aligned} \tag{5.11}$$

The results are shown for a section between the bar axis and the bar surface in cylindrical coordinates. The maximum and minimum stress and the corresponding location are indicated per stress variable with a circle (at the cross-section transition, a small distance from the edge was chosen to avoid reporting potential singularities related to the FE mesh). Since the problem is axially symmetric and only a tensile force is applied, stresses do not depend on the rotation angle φ in the $r\varphi$-plane perpendicular to the x-axis, and the shear stresses in φ-direction vanish, $\tau_{r\varphi} = \tau_{x\varphi} = 0$. Hence, the von Mises stress simplifies to

$$\sigma_{vM} = \sqrt{\frac{1}{2}\left(\left(\sigma_x - \sigma_r\right)^2 + \left(\sigma_r - \sigma_\varphi\right)^2 + \left(\sigma_\varphi - \sigma_x\right)^2\right) + 6\tau_{rx}^2} \tag{5.12}$$

The von Mises stresses $\sigma_{vM}(r,x)$ are similar for both specimens, with the maximum value in the range of the material tensile strength $f_{su} = 615\,\text{MPa}$ occurring at the centre of the damage zone. While they are fairly constant along the damage length, the von Mises stresses start decreasing near the cross-section transition, tending to a constant value (over both the cross-section and along the axis) at a distance $\geq 1Ø$ away from the damage zone, where the stress state is essentially uniaxial. At the centre of the damage zone ($x = 0$), the von Mises stress is approximately constant over the cross-section for CW-61, whereas it decreases towards the bar surface for CW-15.

The occurrence of a triaxial stress state within the damage zone (CW-15) or at its ends (CW-61) can easily be seen from the radial and tangential stresses, $\sigma_r(r,x)$ and $\sigma_\varphi(r,x)$. They are maximum near the cross-section transition, with a positive sign (tensile stresses) at the ends of the damage zone and a negative sign (compressive stresses) in the adjacent undamaged parts. The absolute shear stress (its value depends on the coordinate system) is highest at the edge of the cross-section transition and decreases radially and axially. For a short damage length, the radial and tangential stresses are much higher than for a long damage length and extend over the entire damage zone, whereas an essentially uniaxial stress state is reached at the centre of a long damage length. Considering the considerable radial and tangential tensile stresses at $x = 0$ and Equation (5.12), it is evident that the axial stress can be substantially increased for a short damage length until the von Mises stress reaches the material uniaxial tensile stress. In contrast, no such increase is possible at the centre of a long damage length, where the axial stress approximately equals the von Mises stress.

At the peak load, the von Mises stress averaged over the cross-section (Equation (5.11)) exactly reaches the material uniaxial tensile strength for both specimens. This is noteworthy since the input material curve was not limited to the material tensile strength. This result indicates excellent model accuracy since the von Mises stress is the representative value for comparing a triaxial stress state with uniaxial steel characteristics.

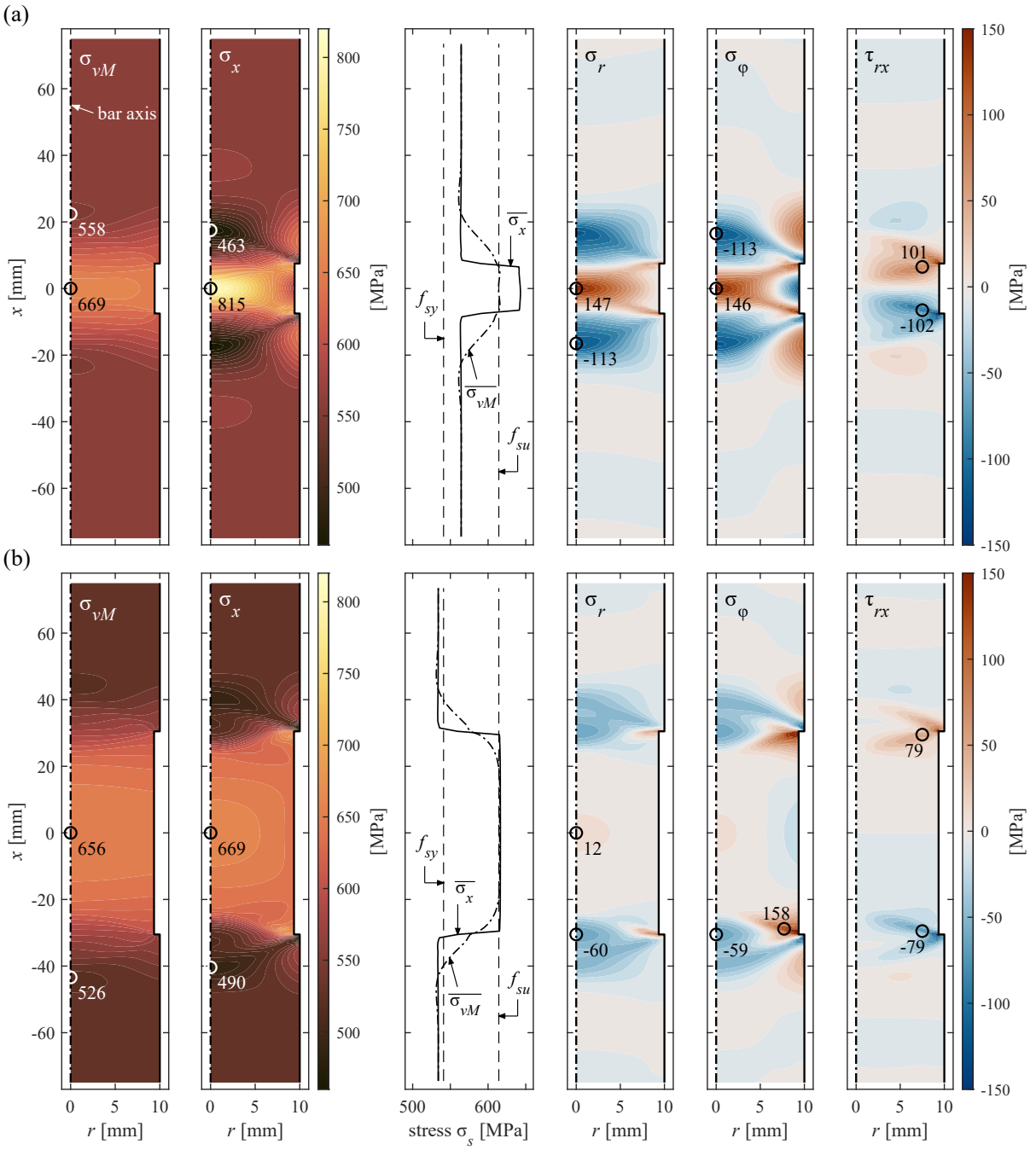

Fig. 5.8 – Visualisation of triaxial stress state: Von Mises stress σ_{vM}, axial, radial and tangential stresses, σ_x, σ_r, and σ_φ, non-zero shear stresses τ_{rx}, and axial and von Mises stresses averaged over cross-section (Equation (5.11)) for (a) CW-15 and (b) CW-61. Location of maximum and minimum stress are indicated with circles.

For CW-61, the mean axial stress at $x = 0$, coinciding with the von Mises stress, evidently also reaches the tensile strength and remains fairly constant over the entire damage length. At the cross-section transition, the mean axial stress drops sharply, whereas a gradual decrease is obtained for the von Mises stress in this zone. Both stress values are slightly below the uniaxial yield stress in the undamaged part, reaching a tensile stress of 534 MPa. This value can be validated by Equation (5.4), i. e. $\sigma_{s,uc} = \sigma_{s,c}(1-\zeta) = 533\,\text{MPa}$ (with $\sigma_{s,c} = f_{su} = 615\,\text{MPa}$, and $\zeta = 0.133$ according to Table 5.1).

In the damage zone of CW-15, the mean axial stress reaches a peak value of 643 MPa, which is 4.5% higher than the uniaxial tensile strength (coinciding with the von Mises stress). This result matches well with the experiment, where an increase in peak stress of 3.5% was observed compared to the uniaxial

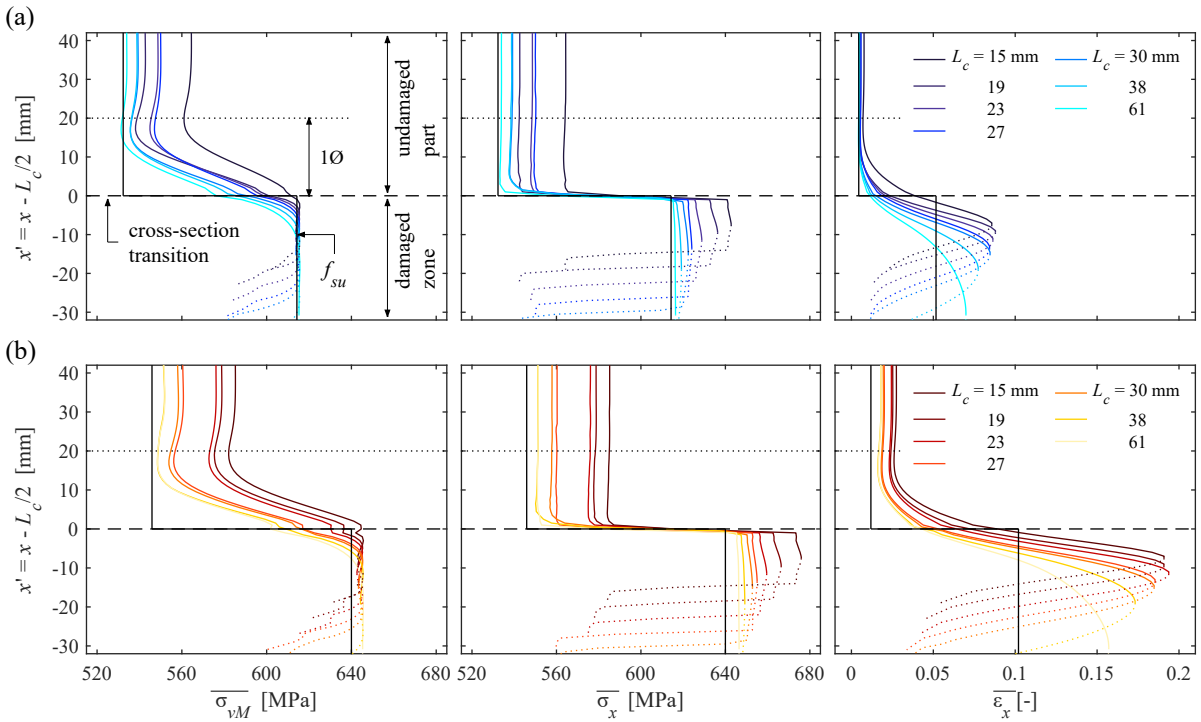

Fig. 5.9 – Influence of triaxial stress state on the mean von Mises and mean axial stress $\overline{\sigma_{vM}}(x)$ and $\overline{\sigma_x}(x)$, and the mean axial strain over cross-section $\overline{\varepsilon_x}(x)$ for (a) the CW and (b) the QST reinforcement.

tensile strength. As for CW-61, the mean axial stress drops sharply at the ends of the damage zone, whereas the von Mises stress gradually decreases over a length of approximately 1Ø from the damage zone end. Both stresses reach a value of 564 MPa in the undamaged part in the FE analysis, which corresponds well to the 565 MPa obtained from Equation (5.4) ($\sigma_{s,c} = 642$ MPa and $\zeta = 0.121$).

The FE analyses thus confirm the presence of a triaxial stress state near corrosion pits and underline its significant influence on the apparent uniaxial tensile strength of bars containing a short damage length, as it enables the activation of axial stresses exceeding the uniaxial tensile strength of the material. For long damage lengths, a uniaxial stress state is again reached at the centre of the damage zone, with conditions equal to those in a standard tensile test, and the apparent uniaxial peak stress cannot exceed the uniaxial tensile strength of the material. The influence of the triaxial stress state on the deformation behaviour is analysed in Section 5.5.4, and Section 5.6 explores for which damage geometries triaxial stresses potentially develop.

5.5.4 Influence of a triaxial stress state on stresses and deformations

The left two columns of Figure 5.9 show the mean von Mises and mean axial stresses according to Equation (5.11) at the peak load along the bar obtained from the FE analyses simulating (a) the CW series and (b) the QST series. The black lines indicate the uniaxial tensile strength from the material tests (shown in the damaged part) and the corresponding theoretical, reduced stress in the undamaged part (determined from Equation (5.4)) as reference values. The plots in the right column of Figure 5.9 show the mean axial engineering strains over the cross-section $\overline{\varepsilon_x}(x)$, along with the strain at the peak stress of the material tests in the damaged part and the corresponding theoretical value in the undamaged part as reference (black lines). Results are shown for only half of the modelled reinforcing bar (with the symmetry axis laying in the middle of the damage zones), and continuation is indicated with dotted lines. Note that a different coordinate is used along the bar axis than in Figure 5.8, $x' = x - L_c/2$, i. e. the cross-section transition is positioned at $x' = 0$, which facilitates the comparison between the different damage lengths.

For all damage lengths, the mean von Mises stress in the damages zone exactly matches the uniaxial tensile strength for the CW series and is in good agreement for the QST series (indicating a slightly weaker FE model accuracy for the QST series). In the adjacent undamaged part, the stress decreases and reaches a constant value at a distance approximately 1Ø away from the damage zone, independently of the damage length. This is noteworthy since the peak load of the specimens increases with decreasing damage length, as indicated by the von Mises stresses at $x = 40\,\text{mm}$, and confirms the principle of de Saint-Venant, stating that stress discontinuities generally attenuate over a length equal to the element width.

The mean axial stresses in the damage zone, hence the peak load, decrease with increasing damage length, reducing to the uniaxial material tensile strength for the damage lengths $L_c = 38$ and 61 mm (again almost exactly for the CW series and in good agreement for the QST series). Unlike for the von Mises stresses, there is a pronounced stress decrease at the cross-section transition, $x' = 0$. Nevertheless, the axial stress in the undamaged part equals the corresponding von Mises stress at a distance $> 1Ø$ from the damage zone.

The mean strain starts to increase in the undamaged part at a distance of approximately 0.5...1.0Ø from the cross-section transition and reaches its maximum at the centre of the damage zone. The maximum strains are much higher than observed in the material tests, $\overline{\varepsilon_{x,max}} \approx 2A_{gt}$ for $L_c = 15\,\text{mm}$ and $\overline{\varepsilon_{x,max}} = 1.5A_{gt}$ for $L_c = 61\,\text{mm}$. However, with increasing damage length, the mean strain is lower than A_{gt} over a considerable length at the ends of the damage zone, partly compensating the high maximum strain at the centre. On the other hand, as mentioned above, the mean strain in the undamaged part is higher than the expected theoretical strain over a length of 0.5...1.0Ø from the damage zone; hence the bar exhibits additional deformation in this region. Further away from the damage zone, the mean strain for specimens with long damage length equals the expected theoretical value, while it is higher for shorter damage lengths due to the increased peak load (compare the increased mean axial stresses). This strain increase is more pronounced for the QST bars due to the different shape of the stress-strain curve.

Figure 5.10 compares the experimental results (markers) with the FE analyses (solid lines) at the peak load, plotting them against the normalised damage length: (a) peak stress in the damage zone, (b) mean strain over the damage zone, (c) mean strain over the first 20 mm in the undamaged part adjacent to the cross-section transition (between $0 \leq x' \leq 20\,\text{mm}$ in Figure 5.9), and (d) mean strain at the Gauge GO extending over the damage zone and the undamaged part, as shown in Figure 5.3. The results are normalised with their corresponding theoretical values (f_{su}, A_{gt}, $\varepsilon_s(\sigma_{s,uc} = (1-\zeta)f_{su})$, and $\varepsilon_{s,m}^{SLM}(\sigma_{s,c}) = f_{su}$) according to the SLM and Equation (5.6)). Note that the experimental results in Figures 5.10(a) and (d) correspond to those in Figures 5.4(a) and (b).

The results of the FE analyses match the experimentally observed increased peak stresses very well, for the CW as well as the QST bars, see Figure 5.10(a). Regarding the mean strain over the damage length (Figure 5.10(b)), the FE analyses predict the experimental results of the QST bars fairly well, particularly compared to the conventional prediction (= A_{gt}), which underestimates the experimentally observed mean strain in the damage zone by up to 40%. The experimentally observed strains for the CW series do not show a clear tendency regarding damage length, but all strains are below A_{gt}. The FE analyses predict strains slightly lower than A_{gt} for long damage lengths, but a moderate increase for shorter damage lengths. The mismatch might be due to a model inaccuracy or secondary effects having influenced the strain measurements in the experiments (influence of ribs, presence of bending stresses caused by a slight shift of the centroidal axis due to tolerances when reducing the diameter).

The experimentally observed mean strains measured over the first 20 mm (1Ø) of the undamaged part (Figure 5.10(c)) – which are strongly underestimated by the SLM (roughly 20% for long damage lengths and up to a factor of 3 for short damage lengths) – are fairly well predicted by the FE analyses for both, the CW and the QST reinforcement. However, the large scatter of the experimental results reflects the challenge of accurately measuring strains in reinforcing bars over a short reference length, even with advanced measurement technologies.

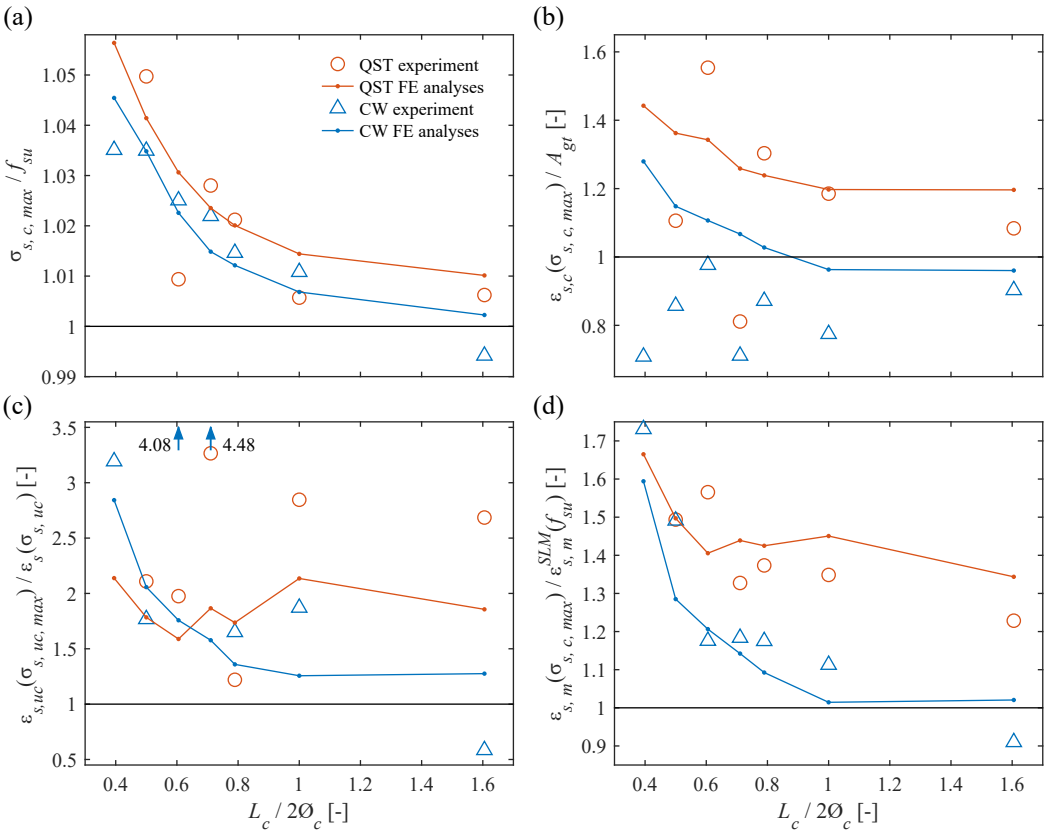

Fig. 5.10 – Influence of triaxial stress state on peak stress and deformation, depending on damage length: (a) peak stress normalised by uniaxial material tensile strength; (b) strain in damage zone at peak stress, normalised with strain at peak stress of material tensile tests; (c) mean strain in adjacent undamaged part at peak stress, measured over a distance of one diameter from the cross-section transition, normalised with strain corresponding to a stress $\sigma_{s,uc} = (1-\zeta) f_{su}$ (Equation (5.4)); positions of outlying values are indicated with arrows; (d) strain of Gauge GO (Figure 5.3) at peak stress, normalised by strain according to SLM.

Figure 5.10(d) shows the experimentally measured, normalised mean strain in Gauge GO of Figure 5.3 and the corresponding results of the FE analyses. The FE analyses match the experimental data accurately for the CW reinforcement and slightly overpredict the results for the QST reinforcement. The experimental results as well as the FE analyses indicate that for damage lengths shorter than twice the reduced diameter, i. e. $L_c \leq 2Ø_c$, the SLM tends to strongly underestimate the deformation capacity of damaged reinforcing bars, by 10...70% in the cases investigated here. This is due to the beneficial effects of the triaxial stress state at the cross-section transition, which partly compensates for the strain localisation effect described by the SLM (Equation (5.6)).

5.5.5 Influence of a triaxial stress state on the yield behaviour

The strain measurements of gauges near the cross-section transition of QST bars illustrated in Figure 5.6 revealed (i) a reduced yield stress and (ii) a loss of the yield plateau (see Section 5.4.3). The yield stress increased again further away from the damage zone, and a yield plateau was retrieved. Both effects directly result from the triaxial stress state near the cross-section transition.

The apparently reduced yield stress in the undamaged part adjoining the damaged zone follows from the distribution of the von Mises stresses $\overline{\sigma_{vM}}$ in Figure 5.8(b), where the von Mises yield criterion $\overline{\sigma_{vM}} = f_{sy}$ is reached or exceeded for $30 \leq |x| \leq 40\,\text{mm}$, and hence, yielding occurs, whereas the mean axial stress is still below the yield stress, i. e. $\overline{\sigma_x} = 534\,\text{MPa} < f_{sy}$. In contrast, if one scales the mean von Mises and mean axial stress distributions in Figure 5.8(a), it evolves that a stress state $\overline{\sigma_{vM}} \leq f_{sy} < \overline{\sigma_x}$

exists where no plastic deformations occur in the damaged part, although the mean axial stresses exceed the yield stress. Hence, the apparent yield stress is increased.

The macroscopic occurrence of a yield plateau in low carbon steel is related to the formation of Lüders bands, i. e. discrete local bands of high deformation increase (discontinuous yielding) due to a sudden break free of the dislocations from the interstitial carbon atoms (Cottrell-Bilby clouds), which propagate along the reinforcing bar (see, e. g. [43, 45, 81, 132, 136, 165]). It has been shown that the Lüders band front orients in the direction of the maximum shear stress (i. e. 45° to the bar axis for pure tension) [45, 165]. The presence of shear stresses τ_{xr} at the cross-section transition (see Figure 5.8) causes the stress trajectories to rotate, leading to a variation of the maximum shear stress direction over the cross-section. This could hinder the Lüders bands from propagating in an ordered manner [101]. Moreover, it is probable that the varying von Mises stress (which represents the yield criterion) over the cross-section triggers the dislocations to break free from their interstitial atoms in only a few grains simultaneously. This hypothesis is supported by the fact that in the FE analyses simulating bars with short damage lengths – for which a wide range of stress values is exhibited over the cross-section, see Figure 5.8 – no yield plateau was obtained either (see curves for $L_c/2Ø_c = 0.2$ in Figure 5.11(b)). Hence, these issues presumably hinder the occurrence of macroscopically visible Lüders bands (i. e. a yield plateau) and favour continuous yielding with strain hardening near the cross-section transition, as also observed in a recent study in the context of bond [101].

5.6 Parametric study

5.6.1 Aim and setup

Besides the material characteristics, the formation of a triaxial stress state is mainly governed by the diameter of the residual cross-section $Ø_c$ and the length of the damage zone L_c. To investigate the influence of these parameters on the triaxial stress state, a parametric study was conducted, investigating the force-elongation behaviour of a reinforcing bar with a total length $L_{tot} = 150\,\text{mm}$ and exhibiting a cross-section loss $\zeta = 0.05...0.8$ over a variable length $L_c/(2Ø_c) = 0.2...1.4$. The bar behaviour was simulated using the FE model described in Section 5.5.1 and adopting the two material models of Section 5.3.2. The initial diameter was held constant at $Ø = 20\,\text{mm}$, yielding $Ø_c = 8.95...19.5\,\text{mm}$ and $L_c = 3.6...54.6\,\text{mm}$. By normalising with $Ø_c/Ø$, $Ø_c^2/Ø^2$, and $L_c/2Ø_c$, respectively, the results apply to other bar and damage geometries within the limitation set in this paper, i. e. an axisymmetric cross-section reduction. A total number of 544 simulations (272 per steel type) were run and evaluated.

5.6.2 General results

As an overview, Figure 5.11 shows selected force-mean strain curves resulting from the parametric study for (a) CW and (b) QST reinforcing bars with different damage lengths ($L_c/(2Ø_c)$ = 0.2, 0.6, and 1.0, indicated with different markers) and different cross-section losses (ζ = 0.1, 0.2, and 0.4, indicated with different colours). The stress-strain curves of the undamaged bars are shown in black as a reference.

As expected, the peak load generally decreases with increasing cross-section loss. However, for a specific cross-section loss, it varies considerably and increases with decreasing damage length. Similar to the maximum load, the strain at peak stress generally decreases with increasing cross-section loss. However, the results indicate that the peak strain for a short damage length (circular markers) can even be larger than for a longer damage length (square and triangular markers) for small or moderate cross-section loss (blue and red curves). This result contradicts the SLM (Equation (5.6)) and is caused by the triaxial stress state.

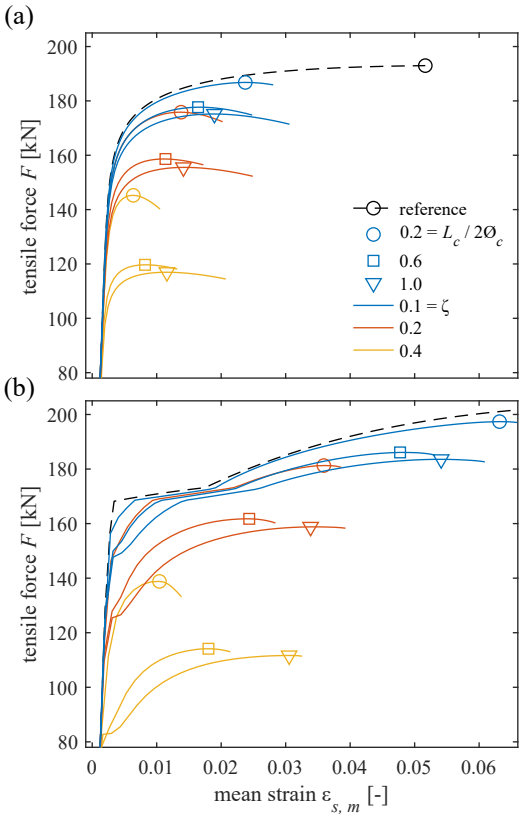

Fig. 5.11 – Selected force-mean strain curves of parametric study to illustrate the strong influence of a triaxial stress state, depending on damage length $L_c/(2Ø_c)$ and cross-section loss ζ, for (a) CW and (b) QST reinforcement.

5.6.3 Load-carrying and deformation capacity compared to the SLM

Figures 5.12(a) and (b) show contour plots of the ratio $\sigma_{s,c,max}/f_{su}$, i. e. the deviation of the peak stress obtained by the FE analyses from the uniaxial material tensile strength, for (a) the CW and (b) the QST reinforcing steel. Results are shown in the parameter range of the cross-section loss ζ and the normalised damage length $L_c/(2Ø_c)$ as defined in Section 5.6.1. Red colours indicate an underestimation of the peak load; note that the colour map is limited to $1.1f_{su}$ for a higher resolution in the main part of the diagram. The maximum and minimum values and their locations are indicated with circles. Black lines indicate constant normalised damage lengths L_c; they are curved because the residual bar diameter $Ø_c$ and thus the ratio $L_c/(2Ø_c)$ constantly vary with the cross-section loss ζ. Isolines are plotted in grey, with an equidistance of 0.05 in (a) and (b), and 0.5 in (c) and (d).

For damage lengths longer than 1Ø, the load-carrying capacity is underestimated by less than 5% for both steel types, almost independently of the cross-section loss. The load-carrying capacity is underestimated by 5...10% for damage lengths in the range of 0.5Ø to 1Ø, and by 10...35% for shorter damage lengths.

Figures 5.12(c) and (d) show contour plots of the strain ratio $\varepsilon_{s,m}(\sigma_{s,c,max})/\varepsilon_{s,m}^{SLM}(\sigma_{s,c}=f_{su})$, i. e. the deviation of the strain at peak load obtained by the FE analyses from the strain at peak load according to the SLM (Equation (5.6)), for (c) the CW and (d) the QST reinforcing steel. Red colours indicate an underestimation of the strain at peak stress by the SLM, and blue colours an overestimation. Note that the colour map is limited to 0.8 and 1.5 for a higher resolution of the main part of the diagram. The dashed line in Figure 5.12(d) indicates the critical cross-section loss ζ_{crit}, denoting the maximum cross-section loss for which the undamaged cross-section still reaches the yield stress at maximum load according to the SLM (see [72]). Additionally, the cross-section loss ζ_{mart} indicates the complete loss

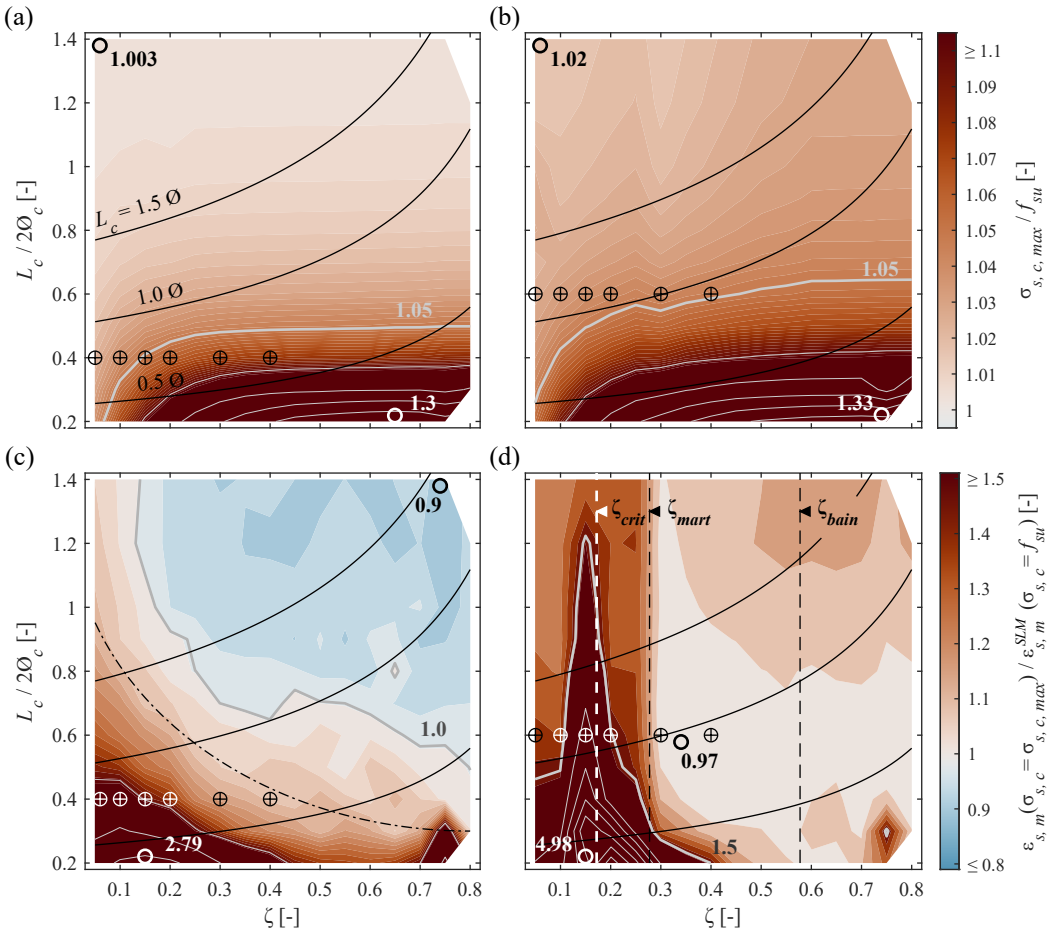

Fig. 5.12 – Load-carrying and deformation capacity predicted by the FE analyses compared to the uniaxial tensile strength and the SLM. (a), (b) ratios of the peak stress (FE) to the uniaxial material tensile strength for CW and QST bars, respectively. (c), (d) ratios of strain at peak stress of the FE analyses to that of the SLM for CW and QST bars, respectively. Solid black lines correspond to constant damage lengths, circular markers show extreme values, and target markers correspond to the parameter sets analysed in Figure 5.13. Isolines are plotted in grey, with an equidistance of 0.05 in (a, b) and 0.5 in (c, d).

of the martensitic outer annulus for the QST bar, and ζ_{bain} indicates the complete loss of the bainitic transition zone (see [71]).

For the CW reinforcing steel in Figure 5.12(c) and the chosen parameter range, an empirical, elliptical relationship was found, above which the error made by using an SLM is less than $\pm 10\%$:

$$R(\zeta, L_c) = \left(\frac{\zeta}{0.8} - 1\right)^2 + \left(\frac{L_c}{2Ø\sqrt{1-\zeta}} - 1.3\right)^2 \leq 1 \tag{5.13}$$

The limit $R(\zeta, L_c) = 1.0$ is shown in Figure 5.12(c) with a dash-dotted line. For shorter damage lengths and smaller cross-section losses, the SLM underestimates the deformation capacity, especially for $\zeta < 0.4$ and $L_c/(2Ø_c) < 0.4$, where the peak strain ratio reaches a maximum value of $\varepsilon_{s,m}/\varepsilon^{SLM}_{s,m} = 2.8$.

For QST reinforcing bars, Figure 5.12(d) indicates that the underestimation of the deformation capacity by the SLM is acceptable, i. e. $\varepsilon_{s,m}/\varepsilon^{SLM}_{s,m} < 1.2$, for cross-section losses $\zeta > \zeta_{mart}$ (and $L_c/(2Ø_c) > 0.3$); this might be an artefact of the constitutive material model formulated in [71], with an increase of the strain at peak stress as soon as the martensitic outer annulus is completely lost. Independent of the damage length, the SLM underestimates the deformation capacity most pronouncedly around the critical

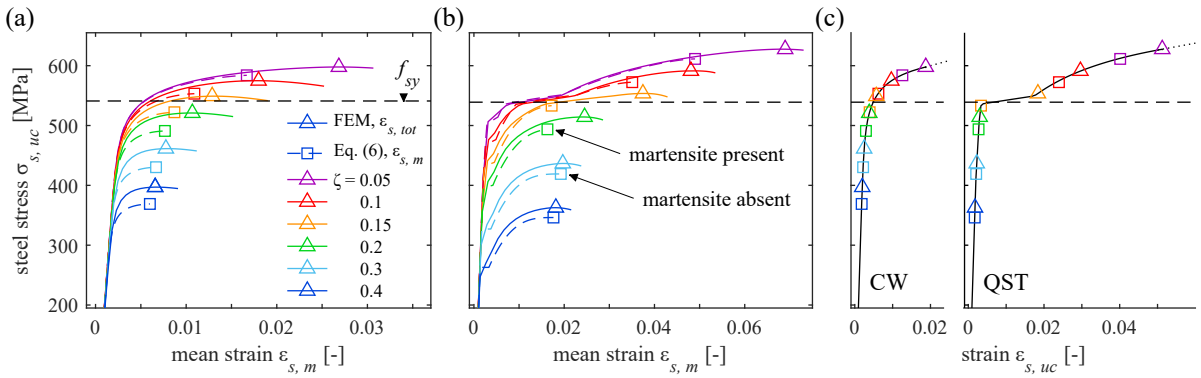

Fig. 5.13 – Stress-mean strain diagrams for the damage conditions indicated with black markers in Figure 5.12 for (a) the CW and (b) the QST reinforcement. Solid lines correspond to the FE analyses, and dashed lines to the SLM; (c) peak stresses and corresponding strains of FE analyses (triangles) and SLM (squares) in the undamaged part far away from the damage zone together with the constitutive material relationships (black) for validation. All stresses refer to the initial cross-sectional area.

cross-section loss ζ_{crit}, with a maximum ratio $\varepsilon_{s,m}/\varepsilon_{s,m}^{SLM} \approx 5$ for short damage lengths $L_c \leq \text{Ø}$, and peak strain ratios > 1.5 even for long damage lengths.

Figures 5.13(a) and (b) show the stress-mean strain diagrams for the simulated CW bars with $L_c/(2\text{Ø}_c) = 0.4$, and QST bars with $L_c/(2\text{Ø}_c) = 0.6$, respectively, for cross-section losses $\zeta = 0.05...0.4$. These damage conditions (parameters $(\zeta|L_c/(2\text{Ø}_c))$) are depicted with target markers in Figure 5.12. Solid lines show the behaviour obtained from the FE analyses, and dashed lines show the predictions according to the SLM (Equation (5.6)), with triangular (FE) and square (SLM) markers indicating the peak stress and corresponding strain. The stress is related to the undamaged, initial cross-sectional area A_s (Equation (5.2)). Figure 5.13(c) shows the constitutive material relationships (black lines) and the stresses and strains observed in the undamaged parts (far away from the damage zone) at the peak forces of the calculations shown in Figures 5.13(a) and (b).

Figures 5.13(a) and (b) show a significantly decreasing load-carrying capacity with increasing damage, and a substantial decrease in deformation capacity already for low cross-section losses. This is a direct consequence of the strain localisation described in Section 5.1.1. The concept of the critical cross-section loss [72] explains why the deformation capacity is almost entirely lost as soon as the stress in the undamaged part drops below the yield stress.

For the CW bars, Figures 5.13(a) and (c) show that the difference in the mean strain at peak stress between the FE analyses and the SLM is highest for low cross-section losses $\zeta < \zeta_{crit}$, where the undamaged part of the bar also exhibits significant plastic strains. Since load variations in the plastic strain range can lead to significantly different strains, it is evident that the FE analyses, which unlike the SLM account for the increased maximum load due to the triaxial stress state, lead to significantly larger deformations than the SLM. As soon as the undamaged part is not reaching the yield stress, the predicted strains at peak stress of both models start converging, although the predicted peak loads still differ significantly.

The same observations apply to the QST reinforcing bars, Figures 5.13(b) and (c), where again significant differences in strain at peak stress are observed for small cross-section losses, i. e. where the undamaged part also exhibits plastic strains, with the largest difference between the two models occurring for $\zeta = 0.2$. For this cross-section loss, the undamaged part reaches strains at the onset of hardening in the FE analyses (accounting for a higher peak load due to the triaxial stress state), whereas the strains according to the SLM – with a 4% lower maximum load – are just below the elastic limit (yield point). The FE- and SLM-strains in the undamaged zone thus differ by the length of the yield plateau (Lüders strain, see Figure 5.13(c)). This explains the considerable differences (i. e. the high ratios) observed in Figure 5.12(d) for QST bars with a cross-section loss $\zeta \approx \zeta_{crit}$, irrespective of the damage length. Moreover, the loss of the martensitic outer annulus for $\zeta > 0.28$ has a visible influence on the differences between the model predictions, as can be seen from Figure 5.13(b).

5.7 Simplified modelling approach to estimate the influence of the triaxial stress state

While FE analyses of reinforcing bars with local damage are well suited to investigate and explain the effects of a triaxial stress state, modelling entire concrete structures containing locally corroded reinforcement on such a level of detail is not expedient, particularly due to the immense computational effort. Hence, simplified models are needed to capture the governing effects with reasonable accuracy. Such a simplified approach is proposed in this section, valid for the parameter ranges set in Section 5.6.1 and following the model strategy illustrated in Figure 5.14.

5.7.1 General model strategy

As seen in the previous sections, a shorter damage length leads to a considerable increase in the apparent uniaxial tensile strength $\sigma_{s,c,max}$ (Equation (5.1)), which is decisive for the differences between the FE analyses and the SLM. The effect is captured in the following by the parameter p_σ, defined as the ratio of the maximum apparent uniaxial stress and the material tensile strength:

$$p_\sigma = \frac{\sigma_{s,c,max}}{f_{su}} \tag{5.14}$$

The proposed approach is based on the observation that in all FE analyses, the triaxial stress state had a limited influence length, defined as the length between the cross-section transition and the point where $\overline{\sigma_{vM}}(x) \approx \overline{\sigma_x}(x)$ (see Figures 5.8 and 5.9) and corresponding to 0.75...1.0Ø and $\min(L_c/2,\ 0.7...0.9Ø_c)$ for the undamaged and damaged parts, respectively.

The results of the FE analyses align well with the principle of de Saint-Venant, whose direct application would result in influence lengths of one diameter. For simplicity, this value is adopted in the following. The strains near the cross-section transition of the FE analyses were thus averaged over lengths of 1Ø and $\min(L_c/2,\ Ø_c)$ in the undamaged and damaged part, respectively, resulting in the following mean strains $\overline{\varepsilon_{s,c}}$ (damaged part) and $\overline{\varepsilon_{s,uc}}$ (undamaged part) at peak load $F = F_u$ (see Figure 5.14):

$$\begin{aligned} \overline{\varepsilon_{s,c}} &= \int_0^s \overline{\varepsilon_x}(x, F = F_u)\, dx \Big/ s \\ s &= \min\left(L_c/2, Ø_c\right) \end{aligned} \tag{5.15}$$

$$\overline{\varepsilon_{s,uc}} = \int_{-Ø}^{0} \overline{\varepsilon_x}(x, F = F_u)\, dx \Big/ Ø \tag{5.16}$$

The stresses corresponding to these mean strains are determined from the stress-strain diagram of the material tensile tests. By dividing the applied maximum force by these stresses, one gets the equivalent cross-sectional areas $A_{s,c}^{eq}$ and A_s^{eq}, i. e. the cross-sectional area of a fictitious bar exhibiting these mean strains at peak load (Figure 5.14):

$$\begin{aligned} A_{s,c}^{eq} &= \frac{F_u}{\sigma_s\left(\varepsilon_s = \overline{\varepsilon_{s,c}}\right)} = \frac{A_{s,c} f_{su} p_\sigma}{\sigma_s\left(\varepsilon_s = \overline{\varepsilon_{s,c}}\right)} \\ p_{\varepsilon,c} &= \frac{A_{s,c}^{eq}}{A_{s,c}} = \frac{f_{su} p_\sigma}{\sigma_s\left(\varepsilon_s = \overline{\varepsilon_{s,c}}\right)} \end{aligned} \tag{5.17}$$

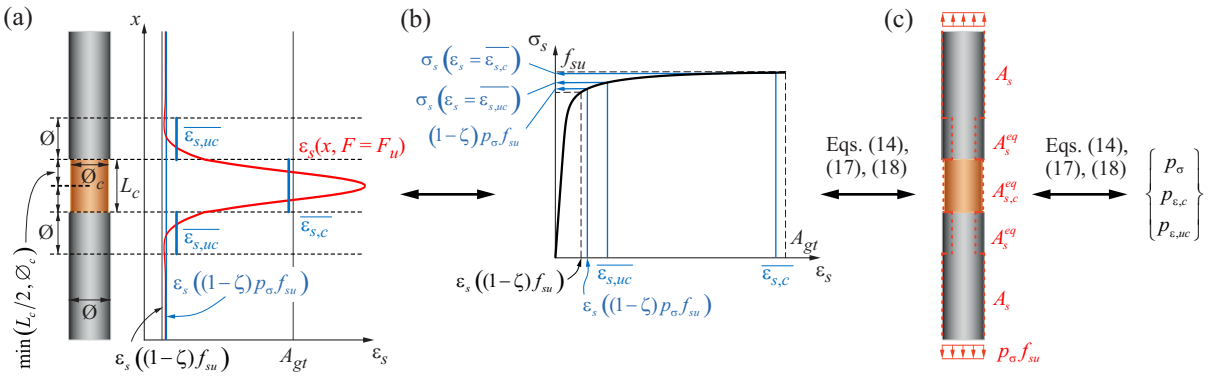

Fig. 5.14 – Schematic representation of model strategy: (a) strain distribution at peak load (red) and mean strains in the vicinity of the cross-section transition according to Equations (5.15) and (5.16); (b) stresses resulting from material stress-strain curve for mean strains; (c) equivalent cross-sectional areas (red dotted lines) according to Equations (5.17) and (5.18).

$$A_s^{eq} = \frac{F_u}{\sigma_s\left(\varepsilon_s = \overline{\varepsilon_{s,uc}}\right)} = \frac{A_{s,c} f_{su} p_\sigma}{\sigma_s\left(\varepsilon_s = \overline{\varepsilon_{s,uc}}\right)}$$
$$p_{\varepsilon,uc} = \frac{A_s^{eq}}{A_s} = \frac{A_{s,c}}{A_s} \frac{f_{su} p_\sigma}{\sigma_s\left(\varepsilon_s = \overline{\varepsilon_{s,uc}}\right)} \tag{5.18}$$

The parameters $p_{\varepsilon,c}$ and $p_{\varepsilon,uc}$ are the ratios between the equivalent and the actual cross-sectional areas. The parameters p_σ, $p_{\varepsilon,c}$, and $p_{\varepsilon,uc}$ thus represent the effect of the triaxial stress state regarding peak stress and corresponding strain on the bar load-deformation behaviour, i. e. the differences compared to the SLM (Equation (5.6)). They were determined for every FE analysis and are analysed in the following section.

5.7.2 Model parameter evaluation

Figure 5.15(a) illustrates the parameters p_σ obtained for the CW bars with different ratios $Ø_c/Ø$ in blue, plotted vs the normalised damage length. The peak stress increases strongly with decreasing damage length and residual diameter, while the influence of the triaxial stress state evidently vanishes at large damage lengths, with no increase in the peak stress for $L_c \geq (2Ø_c)$, irrespective of the residual diameter.

The FE analyses showed that the parameters p_σ and $p_{\varepsilon,c}$ are virtually identical, and there are only marginal differences between the CW and the QST bars despite the strongly differing steel characteristics. The distribution of both parameters, p_σ and $p_{\varepsilon,c}$, can thus be approximated by the same empirical relationship, valid for the CW and the QST bars:

$$p_\sigma = p_{\varepsilon,c} = a e^{-b(L_c/(2Ø_c))} + c \tag{5.19}$$

with a, b, c = fitting parameters depending on the diameter ratio $Ø_c/Ø$ and the steel type (CW or QST). The parameter c is set equal to unity for the CW bars, as expected for long damage lengths, and slightly higher ($c = 1.01$) to achieve a better fit for the QST bars. Figures 5.15(b) and (c) show the distribution of the parameters a and b, respectively, found by linear regression, as functions of $Ø_c/Ø$ and $(Ø_c/Ø)^2$, respectively, with triangles indicating the results for p_σ and circles those for $p_{\varepsilon,c}$. The parameters for the QST reinforcing steel are shown in blue, and those of the CW reinforcing steel in red. The virtually identical values of both parameters and reinforcing steel types are seen in both figures.

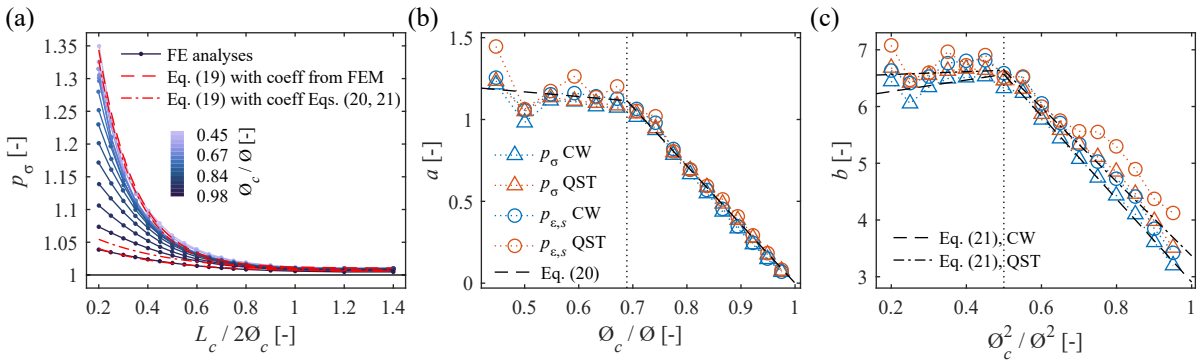

Fig. 5.15 – Simplified model approximating the effects of the triaxial stress state: (a) parameter p_σ for the CW bars as a function of normalised damage length and diameter ratio (blue), and evaluation of Equation (5.19) (red); (b, c) regression parameters a and b, respectively, as functions of linear and squared diameter ratios (coloured), and fits according to Equations (5.20) and (5.21) (dashed and dash-dotted black lines).

As a further simplification, the fitting parameter a is assumed to be bilinear in $\mathcal{Ø}_c/\mathcal{Ø}$, independent of the steel type:

$$a = \begin{cases} -0.3\mathcal{Ø}_c/\mathcal{Ø} + 1.3 & \text{for } \mathcal{Ø}_c/\mathcal{Ø} \leq 0.69 \\ -3.6\mathcal{Ø}_c/\mathcal{Ø} + 3.6 & \text{for } \mathcal{Ø}_c/\mathcal{Ø} > 0.69 \end{cases} \tag{5.20}$$

and the fitting parameter b is assumed to be bilinear in $\mathcal{Ø}_c^2/\mathcal{Ø}^2$, and slightly dependent on the steel type:

$$b(\text{CW}) = \begin{cases} 1.0\mathcal{Ø}_c^2/\mathcal{Ø}^2 + 6.1 & \text{for } \mathcal{Ø}_c^2/\mathcal{Ø}^2 \leq 0.5 \\ -7.3\mathcal{Ø}_c^2/\mathcal{Ø}^2 + 10.2 & \text{for } \mathcal{Ø}_c^2/\mathcal{Ø}^2 > 0.5 \end{cases}$$
$$b(\text{QST}) = \begin{cases} 0.2\mathcal{Ø}_c^2/\mathcal{Ø}^2 + 6.5 & \text{for } \mathcal{Ø}_c^2/\mathcal{Ø}^2 \leq 0.5 \\ -6.5\mathcal{Ø}_c^2/\mathcal{Ø}^2 + 9.9 & \text{for } \mathcal{Ø}_c^2/\mathcal{Ø}^2 > 0.5 \end{cases} \tag{5.21}$$

where the fitting coefficients were again obtained by regression. Figure 5.15(a) includes the results obtained from Equation (5.19) as red lines for $\mathcal{Ø}_c/\mathcal{Ø} = 0.98$ ($\zeta = 0.05$) and $\mathcal{Ø}_c/\mathcal{Ø} = 0.45$ ($\zeta = 0.8$), once using the parameters a and b found by the linear regression of the FE analyses (i. e. the values indicated with red triangles in Figures 5.15(b) and (c)), and once using the bilinear parameters defined by Equations (5.20) and (5.21). Both parameter sets fit the results of the FE analyses almost equally well.

Figure 5.16(a) shows the parameter $p_{\varepsilon,uc}$ of the CW reinforcing steel in blue for different normalised damage lengths $L_c/(2\mathcal{Ø}_c)$ vs the diameter ratio $\mathcal{Ø}_c/\mathcal{Ø}$. The curves are serrated for low $\mathcal{Ø}_c/\mathcal{Ø}$-ratios, i. e. high cross-section losses, most probably due to the chosen load steps in the FE analyses. For a specific damage length, $p_{\varepsilon,uc}$ increases with the residual diameter, i. e. as the residual cross-sectional area approximates the initial cross-sectional area, and the influence of the triaxial stress state in the adjacent undamaged parts reduces. Similarly, $p_{\varepsilon,uc}$ increases with the damage length, but only up to $L_c = \mathcal{Ø}_c$ beyond which it is independent of L_c. This observation indicates that the damage length influences the triaxial stress state in the adjacent undamaged part much less than the cross-section loss.

The parameter $p_{\varepsilon,uc}$ was found to be roughly proportional to the diameter ratio, and can thus be approximated by a straight line with the slope m

$$p_{\varepsilon,uc} = m\,(\mathcal{Ø}_c/\mathcal{Ø} - 1) + 1 \tag{5.22}$$

Figure 5.16(b) shows the slopes obtained by linear regression of the FE analyses shown in Figure 5.16(a) (blue = CW bars, red = QST bars). The parameter m strongly depends on the type of reinforcing steel, with the QST steel showing higher values than the CW steel, indicating a stronger influence

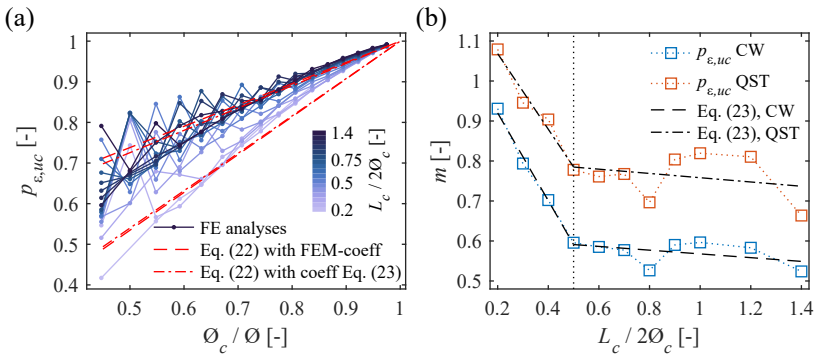

Fig. 5.16 – Simplified model approximating the effects of the triaxial stress state: (a) parameter $p_{\varepsilon,uc}$ for the CW bars as a function of damage length and diameter ratio (blue), and evaluation of Equation (5.22) (red); (b) regression parameter m as a function of normalised damage length (coloured) and fits according to Equation (5.23) (dashed and dash-dotted black lines).

of the triaxial stress state. The slope stays approximately constant for $L_c > \varnothing_c$, i. e. the parameter $p_{\varepsilon,uc}$ merely depends on the diameter ratio, except for very short damage lengths.

The parameter m is assumed to be bilinear in $L_c/(2\varnothing_c)$, hence one gets by regression:

$$m(\mathrm{CW}) \approx \begin{cases} -1.10\,(L_c/2\varnothing_c) + 1.14 & \text{for } L_c/2\varnothing_c \leq 0.5 \\ -0.05\,(L_c/2\varnothing_c) + 0.62 & \text{for } L_c/2\varnothing_c > 0.5 \end{cases}$$
$$m(\mathrm{QST}) \approx \begin{cases} -0.95\,(L_c/2\varnothing_c) + 1.26 & \text{for } L_c/2\varnothing_c \leq 0.5 \\ -0.05\,(L_c/2\varnothing_c) + 0.81 & \text{for } L_c/2\varnothing_c > 0.5 \end{cases} \tag{5.23}$$

Figure 5.16(a) shows the results of Equation (5.22) as red lines for $L_c/\varnothing_c = 0.2$ and $L_c/\varnothing_c = 1.4$. The dashed lines are obtained for the parameter m found by the linear regression of the FE analyses (i. e. the values indicated with red squares in Figure 5.16(b)), and the dash-dotted lines if m is chosen according to Equation (5.23).

5.7.3 Model application

To assess the influence of the triaxial stress state on the force-elongation behaviour of a damaged reinforcing bar, the SLM (Equation (5.6)) is enhanced with (i) the increased apparent uniaxial tensile strength and (ii) the equivalent cross-sectional areas of the bar sections above and below the cross-section transition, see Figure 5.17.

The material stress-strain relationship ε_s - σ_s (e. g. from a conventional tensile test, black curve in Figure 5.17) is converted into the relationship ε_s' - σ_s' accounting for strain localisation and the triaxial stresses, which applies for the bar over a length $L_{tot} = L_c + 2\varnothing$. For $\varnothing = 18\,\mathrm{mm}$, $\varnothing_c = 17\,\mathrm{mm}$, and $L_c = 10\,\mathrm{mm}$, the blue solid line results according to the SLM in Equation (5.6), exhibiting severe strain localisation mainly due to the reduced strain outside the pit (dashed blue line). The red solid line results from the simplified modelling approach, described in the following, and applying the model parameters p_σ, $p_{\varepsilon,c}$, and $p_{\varepsilon,uc}$ to account for the effects of the triaxial stress state.

1. Estimate the fitting parameters a, b, m using Equations (5.20), (5.21), and (5.23), depending on the steel type, with c = 1.0 (CW) or c = 1.01 (QST).

2. Use Equations (5.19) and (5.22) to determine the parameters p_σ, $p_{\varepsilon,c}$, and $p_{\varepsilon,uc}$

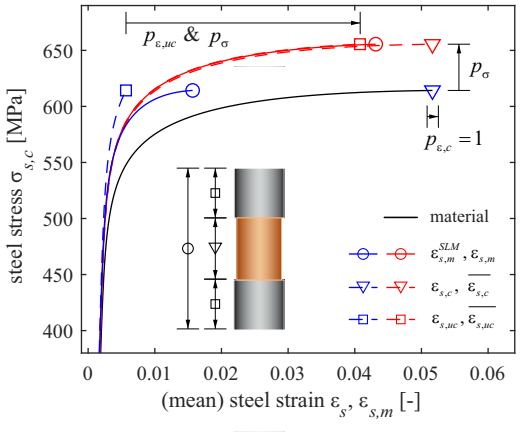

Fig. 5.17 – Comparison of material stress-strain relationship ε_s - σ_s (black), stress-mean strain relationship over the length $L_{tot} = L_c + 2\text{Ø}$ according to the SLM (Equation (5.6)), blue) and the simplified modelling approach accounting for the triaxial stress state ε'_s - σ'_s (red). Example for $\text{Ø} = 18\,\text{mm}$, $\text{Ø}_c = 17\,\text{mm}$, $L_c = 10\,\text{mm}$, and constitutive material relationship defined in Equation (5.5).

3. Determine the vector of apparent uniaxial stress σ'_s, and the auxiliary stress vectors $\overline{\sigma_{s,c}}$ and $\overline{\sigma_{s,uc}}$:

$$\begin{aligned} \sigma'_s &= p_\sigma \sigma_s \\ \overline{\sigma_{s,c}} &= \frac{\sigma'_s}{p_{\varepsilon,c}} = \frac{p_\sigma}{p_{\varepsilon,c}} \sigma_s \\ \overline{\sigma_{s,uc}} &= \frac{\sigma'_s A_{s,c}}{p_{\varepsilon,uc} A_s} = \frac{p_\sigma}{p_{\varepsilon,uc}} \frac{A_{s,c}}{A_s} \sigma_s \end{aligned} \tag{5.24}$$

4. Obtain the strain vectors $\varepsilon_{s,c}$, $\overline{\varepsilon_{s,c}}$, $\overline{\varepsilon_{s,uc}}$, corresponding to the stresses determined in Step 3 from the material stress-strain curve:

$$\begin{aligned} \varepsilon_{s,c} &= \begin{cases} \varepsilon_s(\sigma'_s) & \text{if } \sigma'_s \le f_{su} \\ A_{gt} & \text{if } \sigma'_s > f_{su} \end{cases} \\ \overline{\varepsilon_{s,c}} &= \begin{cases} \varepsilon_s(\overline{\sigma_{s,c}}) & \text{if } \overline{\sigma_{s,c}} \le f_{su} \\ A_{gt} & \text{if } \overline{\sigma_{s,c}} > f_{su} \end{cases} \\ \overline{\varepsilon_{s,uc}} &= \begin{cases} \varepsilon_s(\overline{\sigma_{s,uc}}) & \text{if } \overline{\sigma_{s,uc}} \le f_{su} \\ A_{gt} & \text{if } \overline{\sigma_{s,uc}} > f_{su} \end{cases} \end{aligned} \tag{5.25}$$

5. Determine the strain vector ε'_s by weighting and summing up the strains of Step 4:

$$\begin{aligned} \varepsilon'_s &= \frac{(L_c - 2\text{Ø}_c)\,\varepsilon'_{s,c} + 2\text{Ø}_c \overline{\varepsilon_{s,c}} + 2\text{Ø}\overline{\varepsilon_{s,uc}}}{L_{tot}} && \text{for } L_c > 2\text{Ø}_c \\ \varepsilon'_s &= \frac{L_c \overline{\varepsilon_{s,c}} + 2\text{Ø}\overline{\varepsilon_{s,uc}}}{L_{tot}} && \text{for } L_c \le 2\text{Ø}_c \end{aligned} \tag{5.26}$$

Note the similarity of Equations (5.26) and (5.6). Inserting the stress $\sigma_{s,c} = F/A_{s,c}$ (Equation (5.1)) in the ε'_s - σ'_s relationship yields the mean strain exhibited by the bar section with length L_{tot}, accounting for the effects of the triaxial stress state. Failure of the bar at the pit occurs, if $\sigma_{s,c} = p_\sigma f_{su}$.

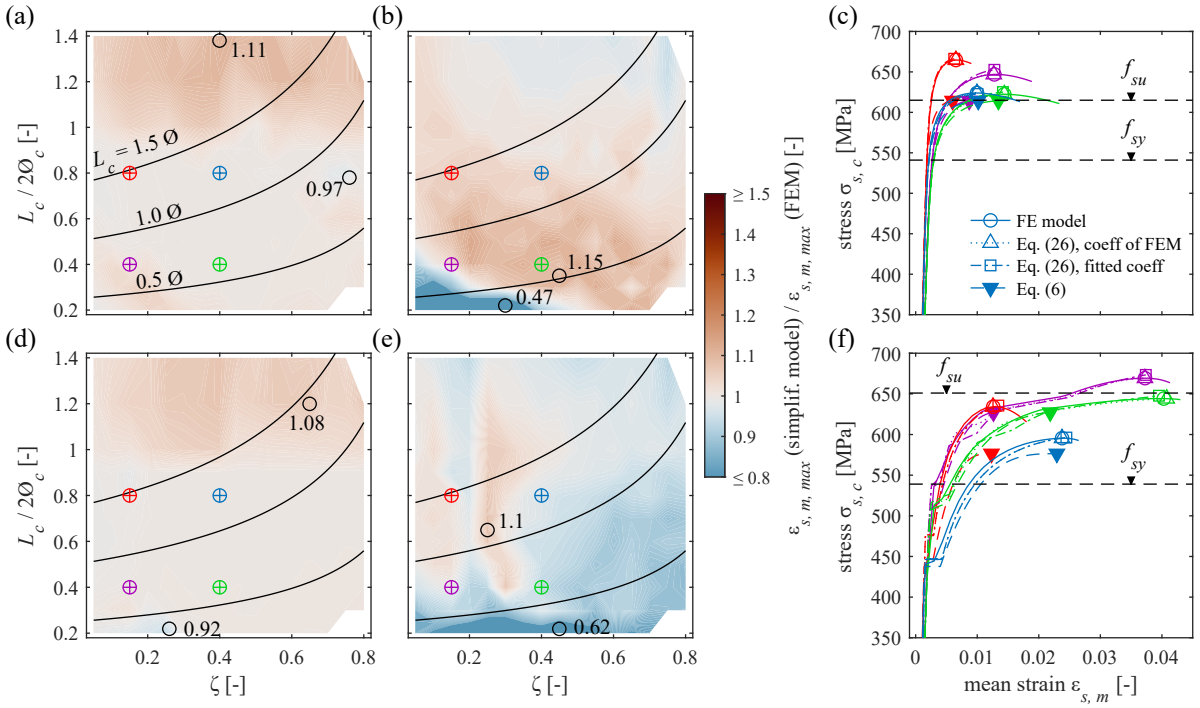

Fig. 5.18 – Comparison of the strain at peak stress predicted by the FE analyses and the simplified model of Sections 5.7.2 and 5.7.3 for (a, b) CW and (d, e) QST bars. For (a, d), model coefficients for the simplified model were chosen according to the FE analyses; for (b, e), coefficients were chosen according to Equations (5.20), (5.21), and (5.23). (c, f) stress-mean strain curves of the FE analyses, the simplified model, and the SLM at the points indicated with target markers in (a, b, d, e).

5.7.4 Model evaluation

Figures 5.18 (a, b, CW bars) and (d, e, QST bars) show the deviation in the strain at peak stress of the simplified model from the FE analyses, similar to the comparison between FE analyses and the SLM illustrated in Figure 5.12. The black lines correspond to constant normalised damage lengths, and circles indicate the maximum and minimum ratios found in the parameter range.

Figures 5.18(a) and (d) show the results obtained using the individual regression parameters of each FE analysis for evaluating Equations (5.19) and (5.22), while Figures 5.18(b) and (e) are based on the regression parameters approximated with Equations (5.20), (5.21), and (5.23). In the former case, the strain at peak stress is slightly underestimated; in the latter case, deviations are generally higher (as expected, since two regression steps are now included), and the strain at peak stress is more pronouncedly underestimated for very short damage lengths $L_c/(2Ø_c) = 0.2...0.3$. However, the deviations are still much smaller than those of the SLM neglecting the effects of the triaxial stress state, see Figure 5.12.

Figures 5.18(c) and (f) show the stress-strain curves of the FE analyses, the SLM, and the simplified model with original and approximated model parameters for the four coloured target markers included in Figures 5.18(a, b, d, e), i. e. for the combinations $\zeta = 0.15,\ 0.4$ and $L_c/(2Ø_c) = 0.4,\ 0.8$. It is observed that the stress-strain curves of the FE analyses and both simplified models are virtually identical, whereas the curve based on the SLM underestimates the peak load and the strain at peak stress, particularly for shorter damage lengths.

The presented simplified model thus appears to reasonably capture the altered stress-strain behaviour of bars containing axisymmetric corrosion damage, accounting for both strain localisation as well as the effect of triaxial stresses near the cross-section transition. However, it needs to be validated in a larger experimental campaign for different material behaviour and a wider range of geometrical parameters, and extended to non-axisymmetric damage in future studies.

5.8 Conclusions

Numerous experimental campaigns aiming to characterise the stress-strain behaviour of reinforcing bars affected by local corrosion have been conducted to date, using both naturally corroded and artificially damaged bars. However, the behaviour has been described mainly empirically, and only few researchers tried to derive mechanically consistent models. However, such models are essential to understand and describe the various effects caused by local corrosion damages.

This paper investigated the influence of a triaxial stress state on the stress-strain behaviour of reinforcing bars affected by local corrosion, focusing on axisymmetric damage. It was found that the triaxial stress state inside and near the damage zone of a corroded bar strongly influences the apparent uniaxial stress-strain behaviour, typically enhancing the tensile strength and deformation capacity, which explains experimental observations that cannot be attributed to strain localisation alone. Likewise strain localisation, the triaxial stress state is mainly governed by the material characteristics, especially in the inelastic phase, and the geometrical characteristics of the damage. Therefore, if local corrosion is considered, it is all the less expedient to describe damage of a bar merely by its mass loss, as it is still common practice in many experimental campaigns despite having been criticised in former studies [58, 80, 102]. An effort should therefore be made to a better characterisation of the corrosion damage geometry and its mechanical influence on the apparent uniaxial stress-strain behaviour of affected bars, as previously suggested by other researchers [39, 58, 166].

The following findings emerged from experiments and theoretical considerations of this study:

- Due to the local deviation of the stress trajectories, a triaxial stress state occurs inside and near the damage zone of reinforcing bars affected by local corrosion. The significant radial, tangential and shear stresses present in the vicinity of the cross-section transition change the local steel stress-strain behaviour, particularly for short damage lengths.
- For axisymmetric damage, the triaxial stress state mainly depends on the shape of the steel stress-strain curve in the inelastic phase, the damage length and the cross-section reduction. Its effects are most pronounced for severe cross-section losses and short damage lengths. For damage lengths exceeding twice the residual diameter, the influence of the triaxial stresses on the apparent uniaxial peak stress and deformation capacity is negligible.
- For short damage lengths, the triaxial stress state leads to a considerable increase of the apparent uniaxial peak stress, which can be up to 35% higher than the uniaxial tensile strength for high cross-section losses, with experimental evidence of up to 4% higher peak stresses even for slight cross-section losses of merely 10...15%. Similar experimental findings were reported in previous studies [39, 62, 84, 151], and are mechanically substantiated by this study.
- Experimental observations show that the tensile stiffness of a bar is reduced in the undamaged part near the cross-section transition, but increased in the adjoining parts of the damage zone. This is explained by the radial and tangential compressive and tensile stresses acting on the undamaged and damaged side of the cross-section transition, respectively. The length over which the altered behaviour is observed comprises approximately one bar diameter.
- The triaxial stress state was found to alter the yield behaviour near the corrosion damage of reinforcing steels exhibiting a yield plateau, as previously reported by [62]. The yield plateau (due to the propagation of Lüders bands) is lost, and strain hardening directly follows the elastic phase. The loss of the yield plateau might be caused by the rotating principal directions as a direct consequence of the deviated stress trajectories, preventing the Lüders bands to progress.
- The lower stiffness and reduced yield strength in front of the damage zone, combined with the higher peak stress, can lead to a significantly higher deformation capacity of damaged bars than would be assumed by established concepts of strain localisation. This particularly applies to short damage lengths and small to moderate cross-section losses below 15...20%.

- While the triaxial stress state was investigated with a nonlinear FE model considering von Mises / J_2-plasticity in this study, such a model is deemed inadequate for application to entire structures due to its high computational cost. Hence, a simplified modelling approach is proposed to estimate the combined influence of strain localisation and the triaxial stress state on the stress-strain behaviour of damaged reinforcing bars.
- The simplified modelling approach correlates well with the FE analyses carried out in this study. However, it is restricted to axisymmetric damage and needs to be validated in a larger experimental campaign regarding different material characteristics and damage geometries.
- The application range of this study is limited to axisymmetric local damage of reinforcing bars, and the results may not directly apply to bars exhibiting unilateral corrosion damage. It was shown that unilateral damages additionally cause bending stresses in the pit vicinity [8, 74], which may soften the stress-strain behaviour in this part of the bar (yield stress is reached at lower load), but may also reduce the failure load.

Appendix

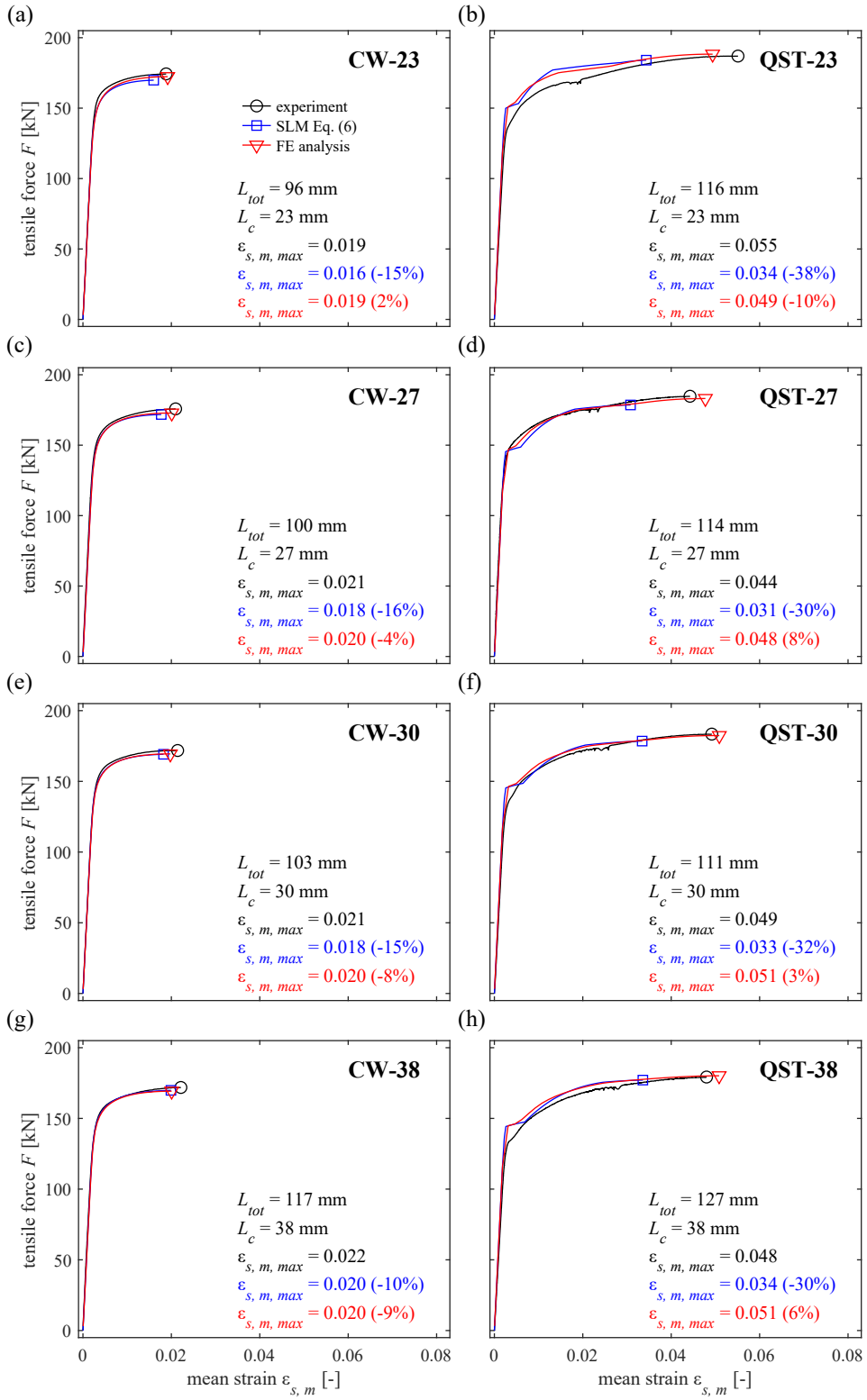

Fig. 5.A1 – Comparison of experimental results (black) with the SLM (Equation (5.6), blue) and the FE analyses (red): (a, c, e, g) Series CW; (b, d, f, h) Series QST, specimens with damage lengths L_c = 23, 27, 30, and 38 mm. The markers indicate the peak loads. Additionally, the total gauge length L_{tot} and the strain at peak load $\varepsilon_{s,m,max}$ are reported, as well as the relative deviation between the models and the experimental result.

Notation

$A_{gt} = \varepsilon\left(f_{su,dyn}\right)$	Strain at steel tensile strength
A_s, $A_{s,c}$	Reinforcing bar cross-sectional area (initial, reduced)
A_s^{eq}, $A_{s,c}^{eq}$	Equivalent cross-sectional areas in (undamaged, damaged) section, for simplified modelling approach
E_s	Young's modulus of reinforcing steel
F, F_u	Axial normal force (in general, maximum)
K	Coefficient for steel constitutive relationship
L_{tot}, L_c, L_{uc}	Total bar length, length of damaged section, length of section with initial diameter (undamaged)
a	Fitting parameter
b, b_1, b_2	Fitting parameters
c	Rib distance, fitting parameter
c_1, c_2, c_3, c_4	Coefficients for steel constitutive relationship
f_{sy}, $f_{sy,dyn}$	Steel yield stress (in general, dynamic value)
f_{su}, $f_{su,dyn}$	Steel tensile strength (in general, dynamic)
m	Fitting parameter
p_σ, $p_{\varepsilon,c}$, $p_{\varepsilon,uc}$	Parameters to simplified modelling approach to account for the influence of the triaxial stresses on the apparent uniaxial stress and axial strains
x, x', x_1, x_2	Coordinates (parallel to bar axis), with $x' = x - L_c/2$
$\varepsilon_{s,eng}$, $\varepsilon_{s,tr}$	Steel strain (engineering, true, with $\varepsilon_{s,tr} = \ln\left(1+\varepsilon_{s,eng}\right)$)
ε_s, $\varepsilon_{s,c}$, $\varepsilon_{s,uc}$	Steel strain in general, steel strain in section with (reduced, initial) cross-sectional area
$\varepsilon_{s,h}$	Steel strain at hardening
$\varepsilon_{s,m}$, $\varepsilon_{s,m}^{SLM}$	Mean strain over total bar length (measured, or according to strain localisation model (SLM))
$\overline{\varepsilon_c}$, $\overline{\varepsilon_{uc}}$	Mean strain over 1Ø_c of damaged zone, and over 1Ø of adjacent undamaged section, respectively, for simplified modelling approach
$\sigma_{s,eng}$, $\sigma_{s,tr}$	Steel stress (engineering, true, with $\sigma_{s,tr} = \sigma_{s,eng}\left(1+\varepsilon_{s,eng}\right)$)
σ_s, $\sigma_{s,c}$, $\sigma_{s,uc}$	Steel stress in general, steel stress referred to (reduced, initial) cross-sectional area
$\sigma_{s,c,max}$, $\sigma_{s,uc,max}$	Steel stress at maximum load referred to (reduced, initial) cross-sectional area
σ_{vM}, $\overline{\sigma_{vM}}$	Von Mises stress (in general, mean over cross-section)
σ_x, $\overline{\sigma_x}$, σ_r, σ_φ	Axial stress (in general, mean over cross-section), radial, and tangential stress
τ_{rx}, $\tau_{r\varphi}$, $\tau_{x\varphi}$	Shear stresses
ζ, ζ_{crit}	Relative cross-section loss of reinforcing bar (in general, critical)
ζ_{mart}, ζ_{bain}	Relative cross-section loss of reinforcing bar for which (martensitic, bainitic) microstructure layer is lost
Ø, Ø_c	Reinforcing bar diameter (initial, reduced)

6 Load-deformation behaviour of locally corroded reinforced concrete retaining wall segments: Experimental results

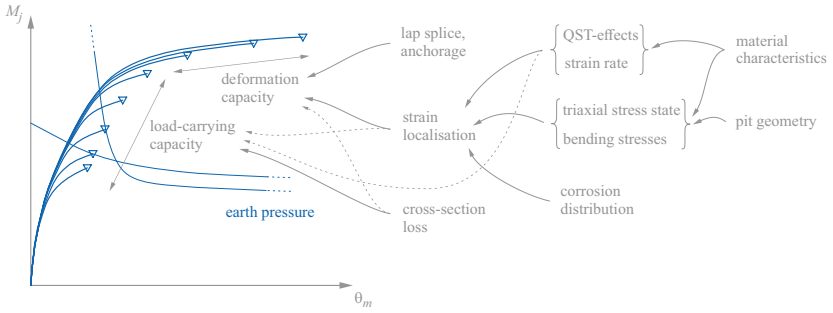

This chapter presents the findings of a series of large-scale experiments conducted in the Large Universal Shell Element Tester LUSET on cantilever retaining wall segments containing reinforcing bars with artificial local damage. The study investigated the load-deformation behaviour of the specimens regarding a varying cross-section loss and different loading conditions, revealing a pronounced influence of the distribution of the corrosion damage among the reinforcing bars. Furthermore, local effects at the corrosion pits, such as local bending moments, were visualised using fibre optic strain sensing. In two hybrid tests, the cross-section loss was increased during the experiment and the applied load simultaneously decreased, depending on the measured deformations, to realistically simulate the earth pressure loading occurring for cantilever retaining walls. The chapter corresponds to the published version of the following article:

> Haefliger, S. & Kaufmann, W. 'Load-deformation behavior of locally corroded reinforced concrete retaining wall segments: Experimental results,' *fib Structural Concrete*, vol. 24, no. 1, pp. 288-317, 2023. doi: 10.1002/suco.202200405.

The lead author (Severin Haefliger) planned and conducted the experiments and analysed the measured data under the supervision of the second author (Walter Kaufmann).

Abstract

Local reinforcement corrosion damage reduces the load-bearing capacity of reinforced concrete structures and, even more severely, their deformation capacity. This problem is of particular concern for cantilever retaining walls, whose loading is dominated by earth pressure and hence, depends on the wall deformations. With a limited deformation capacity at the ultimate limit state due to the locally corroded reinforcement, the earth pressure may not drop to its reduced value typically assumed in design, and simultaneously, the structural resistance may be severely impaired by the cross-section loss. Load redistributions are impeded since retaining walls are statically determined vertically and typically segmented longitudinally. This increases the risk that affected structures collapse, exhibiting a brittle failure. The

situation is aggravated by the fact that the wall deformations prior to failure are too small to be detected by conventional monitoring, as indicated by a previous study.

To improve the basis for quantifying the related risks and the magnitude of pre-failure deflections, this study investigates the load-deformation behaviour of cantilever retaining walls affected by local pitting corrosion, focusing on (i) the influence of the corrosion pit distribution among different reinforcing bars on the load-bearing and deformation capacity and (ii) the interdependence of corrosion, reduced deformation capacity and deformation-dependent loading. To this end, eight large-scale experiments on retaining wall segments were conducted in the Large Universal Shell Element Tester (LUSET), simulating the lower part of a 4.65 meter tall cantilever retaining wall. Five specimens contained initial damage (pitting corrosion simulated by a spherical mill). In the remaining three specimens, artificial corrosion damage was induced during the experiments. For two of the latter specimens, the loading was adapted in real-time control depending on their deformation to simulate the decreasing earth pressure. These are the first large-scale hybrid tests in the field of corrosion research to our knowledge.

The experiments confirmed that the ultimate load and the corresponding deformation strongly differ depending on the corrosion pit distribution, even among specimens with equal mean cross-section loss. Furthermore, it was found that the deformation increase due to corrosion damage depends on the loading and, hence, on the compaction of the backfill. The observed deformation increase ranged between 0.8 mm and 1.4 mm per meter height at 40% cross-section loss, with loose soil causing a larger deformation increase. The load transfer between the damaged and undamaged reinforcing bars was found to take place in the first two crack elements above the construction joint. Local bending moments occurred in the reinforcing bars in the vicinity of the corrosion pits due to the shift of the centre of gravity of the bar at the pit. Fibre optic strain sensing allowed visualising the bending moment decrease in the embedded part of the damaged bars as a consequence of a lateral bearing pressure.

6.1 Introduction

Many cantilever retaining walls built in the 1960s and 1970s along Swiss motorways and railroads are affected by severe local pitting corrosion, as revealed, e. g. by a pilot study of the Swiss Federal Roads Office [52] on 36 retaining walls carried out in 2013. According to this study, the corrosion pits are located exclusively at the construction joint between the footing and the wall and primarily affect the main tensile reinforcement on the rear side, see Figures 6.1(a) and (b). The corrosion is most likely caused by honeycombs resulting from poor concrete compaction in this region, which impeded the passivation of the reinforcement and enabled local ingress of water and oxygen. The electric connection between the relatively small part of unprotected reinforcement (acting as anode) with the large amount of passivated reinforcement in the remaining part of the retaining wall (acting as cathode) led to the formation of a strong macro element and rapidly progressing pitting corrosion [25] (see Figure 6.1(c)), affecting approximately 25% of the main tensile reinforcement with a mean cross-section loss of 37% (total cross-section loss: 9.5%) [52]. The wall thickness above the footing (for many objects between 0.5 and 1.2 m) impedes detecting the corroding reinforcement at the wall's rear side with conventional methods applied at the front side, such as potential mapping or georadar measurements [52]. Therefore, even severe corrosion damage is likely to remain undetected until failure.

Retaining walls are mainly loaded by earth pressure, whose magnitude depends on the deformation of the loaded structure. Code provisions in the 1960s and 1970s (in Switzerland, SIA 162 [144]) recommended designing cantilever retaining walls for reduced earth pressure, often assuming merely active earth pressure at the ultimate limit state (ULS). Hence, it was implicitly assumed that the deformation capacity is sufficient for the earth pressure to drop from pressure at rest to active pressure. However, the occurrence of pitting corrosion not only reduces the load-bearing capacity of a structure but also – and much more pronouncedly – impairs its deformation capacity [17, 35, 51, 103, 110]: recent studies [39, 72] show that limited cross-section losses of only 17% might reduce deformation capacity by as much as 82% due to strain localisation in the vicinity of the corrosion pit. Hence, considerable uncertainty

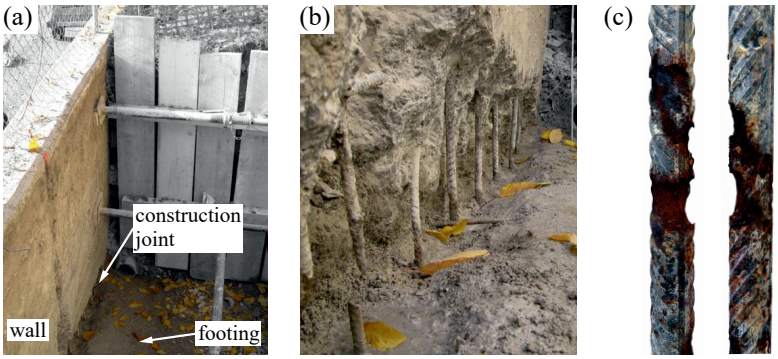

Fig. 6.1 – Retaining walls with locally corroded reinforcement: (a) affected wall along motorway (picture from [52]); (b) detail of construction joint with corroded reinforcement (picture from [52]); (c) example of reinforcing bar with local corrosion damage, extracted during the pilot study.

arises whether the residual deformation capacity of corroding retaining walls is sufficient to reach active earth pressure at ULS. Otherwise, affected structures are at risk of failing in a brittle manner since (i) the reduced load-bearing capacity will hardly be sufficient to resist an earth pressure substantially exceeding the value assumed in design (active pressure), and (ii) most retaining walls are segmented by closely spaced dilatation joints. Although sometimes provided with (rather weak) shear dowels, this segmentation impedes the activation of plate bending and a corresponding load redistribution in the longitudinal direction. Moreover, the potentially small deformation increase due to corrosion until failure challenges a successful application of the observation method [138], i. e. permanent monitoring of a structure's deformation to detect the exceeding of a predefined limit at an early stage.

The assessment of the residual deformation capacity of corroding structures is demanding, as it depends on various aspects on different structural levels [72]. On the level of the reinforcing bar, the microstructural composition of the bar and the pit morphology are most relevant. Quenched and self-tempered (QST) reinforcing bars, making up for most modern reinforcement, reveal a distinct microstructure over their cross-section, and hence, change their mechanical properties continuously for an increasing cross-section loss [55, 71, 82, 139]. The pit morphology strongly influences the behaviour of reinforcing bars in the pit region by two distinct mechanisms. Depending on the pit length, a triaxial stress state can influence the apparent mechanical steel characteristics and potentially lead to (i) a higher strength of the bar than nominally expected [80] and (ii) an altered tensile stiffness (higher or lower) in the pit vicinity. Furthermore, for unilateral corrosion damage, local bending moments occur in the vicinity of the pit due to the shift of the centroidal bar axis, which can disproportionally impair the load-bearing capacity [8, 58, 86, 166].

On the level of a reinforced concrete cross-section, the distribution of the corrosion damage among the reinforcing bars strongly influences the deformation capacity. When comparing two identical structures with the same mean cross-section loss but different corrosion pit distribution, a recent study [72] concluded that the deformation capacity for the structure with few severely corroded bars is much higher than that of the structure with many slightly corroded bars. This is due to a varying influence of strain localisation and implies that knowledge of the mean cross-section loss of a corroded structure is insufficient to draw reliable conclusions on its load-deformation behaviour, particularly regarding deformation capacity.

The pit morphology and pit distribution significantly influence the load (re-)distribution in a reinforced concrete cross-section between reinforcing bars with and without cross-section loss, and govern a structure's load-deformation behaviour in case of pure pitting corrosion (where in contrast to uniform or mixed corrosion, no appreciable deterioration of bond due to corrosion is expected). Experimental studies on damaged bare reinforcing bars with different pit geometries and structural elements with systematically varied pit distributions are needed to develop and validate models for the corresponding structural effects. Whereas individual experimental results and first modelling approaches exist for bare

reinforcing bars [8, 58, 76, 80, 86, 166], experimental data reflecting these effects is scarce for structural elements.

The hazard potential of locally corroding retaining walls is substantial due to the large number of potentially affected structures, the difficulty of corrosion detection, and the various critical aspects, particularly the interdependence of corrosion, altered load-deformation behaviour and deformation-dependent loading. Since this interdependence and the underlying load-transfer mechanisms have barely been investigated on a structural level, a comprehensive experimental campaign on retaining walls with locally damaged reinforcement was set up at ETH Zurich. It aimed at investigating (i) the general load-deformation behaviour of uncorroded retaining walls as a reference (behaviour of construction joint, footing and lap splice), (ii) the influence of the corrosion pit distribution on the load-deformation behaviour, and (iii) the interaction between the deformation increase due to corrosion damage and the deformation-dependent loading. For this purpose, eight large-scale experiments on retaining wall segments of two meters in width and height were conducted in the Large Universal Shell Element tester (LUSET) [88], simulating the lower part of 4.65 m tall retaining walls. Five specimens with varying initial corrosion damage were loaded until failure. The three remaining specimens were loaded to characteristic load, and corrosion damage was subsequently increased. Two of the latter were tested in a hybrid mode, with the load being adapted depending on the actual wall deflection, to simulate the decrease of the earth pressure loading with increasing deformation due to corrosion. To the authors' knowledge, these are the first large-scale hybrid tests conducted in corrosion research.

This paper presents the design of the specimens (Section 6.2) and the experimental setup (Section 6.3), including details on the instrumentation and the hybrid testing. The experimental results are comprehensively discussed in Section 6.4, focusing on the influence of the corrosion pit distribution on the load-deformation behaviour, the load-transfer mechanism in the pit region, and the occurrence of local bending effects. A comprehensive discussion of the load-deformation behaviour of the footing and lap splice region, and the theoretical assessment of the experimental data based on the Corroded Tension Chord Model [70, 72], is envisaged for a future separate publication. The geotechnical aspects of the problem, particularly the relation between earth pressure and a structure's deformation, are part of a separate research project; comprehensive information can be found in the corresponding publication [125].

Tab. 6.1 – Number of assessed cantilever retaining walls for parametric analysis by location and year of construction.

Origin (Canton)	Number of assessed walls
Berne	12
Grisons	1
St. Gallen	5
Vaud	11
Zurich	1
Year of construction	**Number of assessed walls**
1968 - 1970	7
1971 - 1975	11
1976 - 1980	3
1981 - 1985	7
1996	1

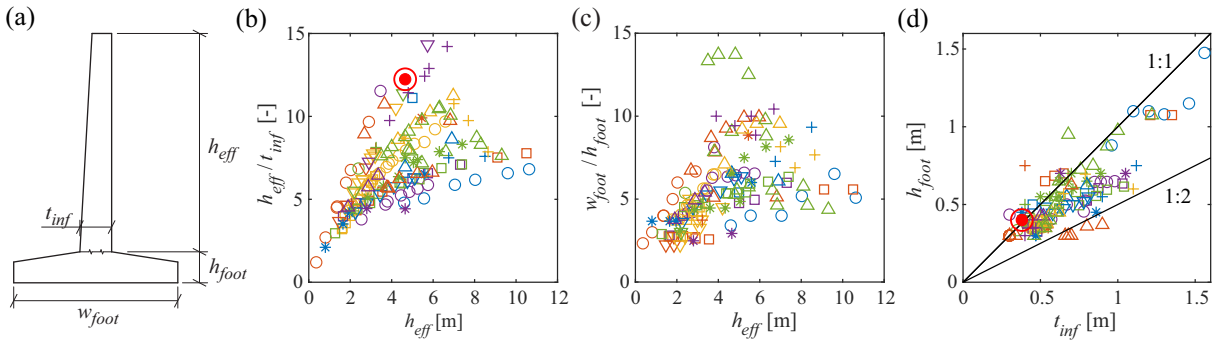

Fig. 6.2 – Geometry of assessed retaining walls: (a) parameter definition; (b)-(d) relations between different geometrical parameters. The solid red dots in (b) and (d) indicate the parameters chosen for the specimens of the experimental campaign.

6.2 Design of existing retaining walls

Accurate knowledge of typical design parameters of existing cantilever retaining walls is indispensable for producing representative specimens for experimental purposes. Therefore, prior to the experimental campaign, a parametric study was carried out based on 158 sections of 30 cantilever retaining walls located in different regions of Switzerland and built in different years, mainly between 1968 and 1985 (Table 6.1). The data was collected mainly from the original construction plans of retaining walls, including those assessed in the pilot study [52].

Figure 6.2 shows the relations between the different geometric parameters of the assessed walls, with Figure 6.2(a) defining the parameters (h_{eff} = wall height above footing, t_{inf} = wall thickness above footing, t_{foot} = thickness of footing, and w_{foot} = width of footing). All sections of one retaining wall are indicated with a marker of identical shape and colour. As seen from Figure 6.2(b), retaining walls with heights (above footing) up to 3 m typically exhibit a slenderness between 1:4 and 1:7, whereas the slenderness of higher walls varies roughly between 1:5 and 1:12. This is presumably owed to a minimum wall thickness due to the detailing rules (e. g. minimum bar spacing), causing lower walls to be less slender. The wide range of slenderness is potentially also caused by the various boundary conditions of the respective projects. According to Figure 6.2(c), the slenderness of footings tends to be smaller and less correlated to the wall height, with most values between 1:3 and 1:10. Figure 6.2(d) indicates that the footing thicknesses range from 0.5 to 1 times the wall thickness at its base. This is reasonable, as the wall base moment is carried by one side or shared between two sides of the footing depending on its position (L-shaped or reversed-T-shaped wall).

Most of the analysed retaining walls are segmented longitudinally at distances of roughly 0.7 to 2 times the wall height. The segments are sometimes connected with shear dowels (e. g. Ø20@500) to avoid differential deformations of two neighbouring segments in service. However, these dowels are neither designed for nor sufficient to compensate for a reduction in structural resistance of a segment. Hence, cantilever retaining walls are statically determined vertically and cannot redistribute substantial loads in the longitudinal direction by plate action.

Figure 6.3 shows the reinforcement properties of the analysed retaining walls. The design values of the bending moment due to active earth pressure (assuming a triangular distribution) acting on a retaining wall m_{Ed} and the bending resistance m_{Rd} can be approximated by

$$\begin{aligned} m_{Ed} &= \gamma_q \cdot \frac{1}{6} K_{ah} \gamma_{soil} h_{eff}^3 \\ m_{Rd} &= z \cdot a_s f_{yd} \approx 0.8 t_{inf} \cdot \rho t_{inf} f_{yd} \end{aligned} \tag{6.1}$$

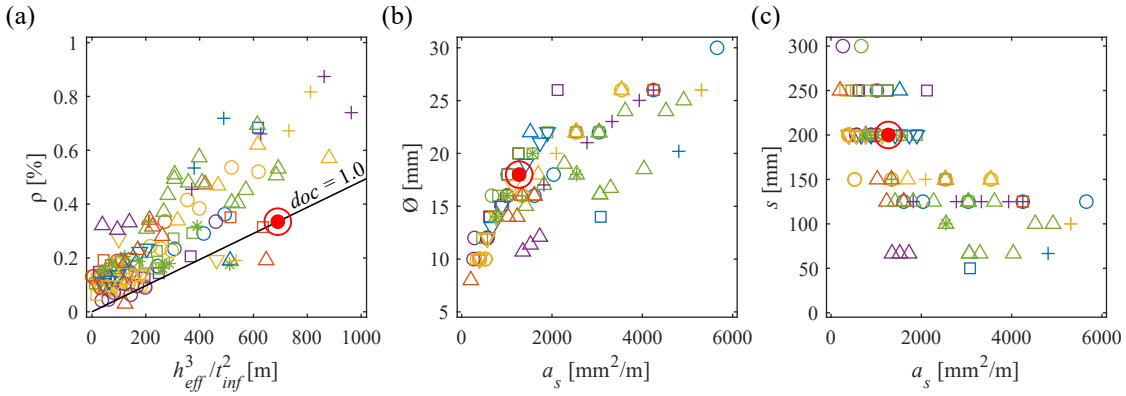

Fig. 6.3 – Reinforcement of assessed walls: (a) relation between reinforcement ratio and geometrical parameters according to Equation (6.3); (b, c) reinforcing bar diameters and spacings vs cross-sectional area of reinforcement. The solid red dots indicate the parameters chosen for the specimens of the experimental campaign.

with γ_{soil} = specific weight of soil, γ_q = partial safety factor, $z \approx 0.8 \cdot t_{inf}$ = lever arm of internal forces, a_s = reinforcement cross-sectional area per unit length, $\rho = a_s/t_{inf}$ = reinforcement ratio at wall base, f_{yd} = design value of reinforcing steel yield stress, and K_{ah} = Coulomb's horizontal earth pressure coefficient [99]

$$K_{ah} = \left(\frac{\cos\varphi}{1 + \sqrt{\frac{\sin(\delta+\varphi)\sin\varphi}{\cos\delta}}} \right)^2 \tag{6.2}$$

where φ = internal angle of friction and δ = wall friction angle. Setting $m_{Ed} = m_{Rd}$, one gets the reinforcement ratio required to ensure structural safety:

$$\rho \approx \frac{K_{ah}\gamma_{soil}}{6 \cdot 0.8 \cdot f_{yd}} \frac{h_{eff}^3}{t_{inf}^2} \tag{6.3}$$

which is proportional to the geometrical parameter h_{eff}^3/t_{inf}^2. Note that the actual yield stress of the reinforcement (depending on the time it was produced) needs to be used in Equation (6.3). Figure 6.3(a) illustrates the correlation of the reinforcement ratios in the assessed walls with Equation (6.3), along with a black line indicating a degree of compliance $doc = 1.0$ when assuming typical values of $K_{ah} = 0.28$ (gravel sand with $\varphi = 30°$ and $\delta = 2/3\varphi$), $\gamma_{soil} = 20\,\mathrm{kN/m^3}$, $f_{yd} = 240\,\mathrm{MPa}$, and $\gamma_q = 1.0$ according to the Swiss Design Code SIA 162 of 1968 [144] (in vigour until 1989). The reinforcement ratio of almost all analysed wall sections lies above the minimum, with tall and slender walls exhibiting higher safety margins than low and compact walls. Figures 6.3(b) and (c) illustrate the reinforcing bar diameters Ø and spacings s used depending on the cross-sectional area of reinforcement.

6.3 Experimental design

Eight cantilever retaining wall segments were prepared and subsequently tested in the LUSET [88] at the structures laboratory of ETH Zurich. Representative dimensions and reinforcement layouts were chosen based on the parametric study described in Section 6.2. The test specimens represented the lower part of a 4.65 m tall retaining wall segment, which was achieved by applying the corresponding bending moment and shear force, caused by earth pressure on the upper (not physically represented) part of the wall, along the top edge of the specimens with the LUSET. All specimens were identical except

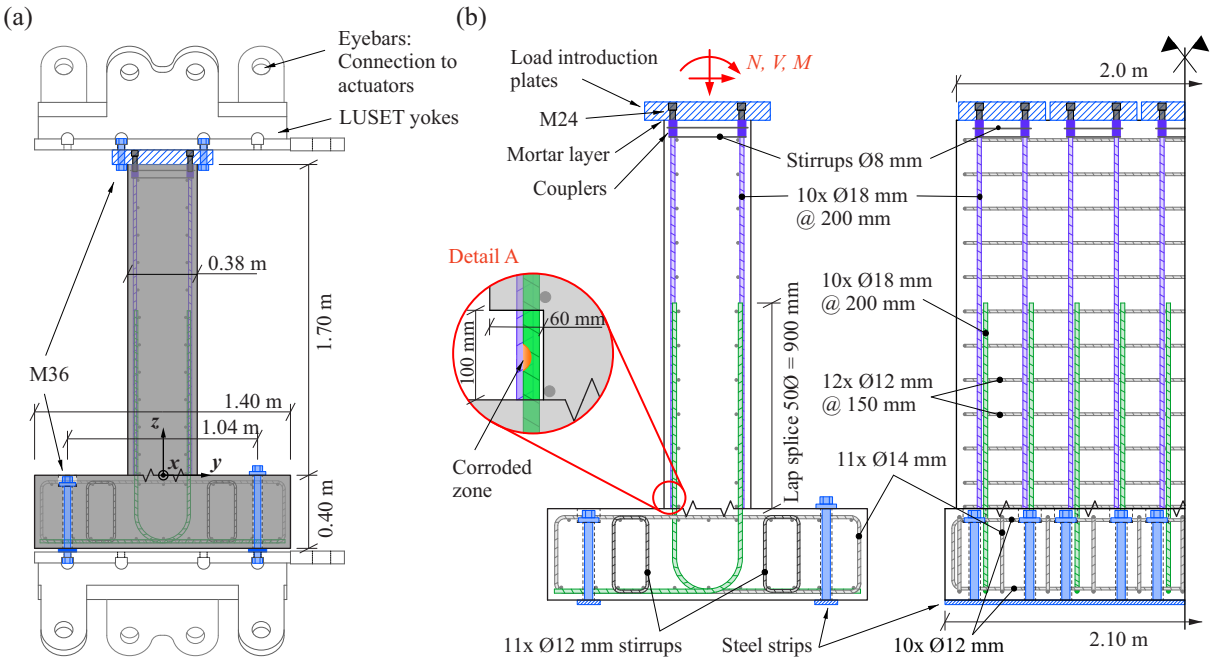

Fig. 6.4 – Drawings of test setup in the Large Universal Shell Element Tester (LUSET): (a) specimen dimensions, connection to LUSET yokes, and definition of the coordinate system; (b) reinforcement layout and detail of a reinforcing bar in the region of the corroded zone.

for the corrosion damage and the loading, which were the only parameters that varied throughout the experimental campaign.

6.3.1 Geometry and reinforcement layout

As shown in Figure 6.4(a), the specimens consisted of a 1.7 m tall and 2.0 m wide wall with a thickness of 0.38 m, built on a footing measuring $1.4 \cdot 2.1 \cdot 0.4\,\text{m}^3$. The specimens are rather slender ($h_{eff}/t_{inf} = 4.65/0.38 \approx 12:1$) compared to the assessed walls, as illustrated in Figure 6.2(b). This slenderness was deliberately chosen to explore the behaviour of a typical bending element, minimising the influence of shear deformations and avoiding the formation of a direct compression strut. The height of the footing was defined with the ratio $h_{foot}/t_{inf} = 1$ using Figure 6.2(d), and its length was bounded by the yoke dimensions of the testing machine.

Figure 6.4(b) illustrates the schematic reinforcement layout; the photos in Figures 6.5(a) and (b) show the footing and the wall before casting, and Figure 5 (c) shows the reference specimen prior to testing. The reinforcement ratio of the main tensile reinforcement was chosen such that the degree of compliance according to the design code SIA 162 of 1968 [144] with the parameters defined in Section 6.2 equalled $doc = 1.0$ (Figure 6.3(a)). This led to a ratio $\rho = 0.33\%$, which was achieved with reinforcing bars of diameter Ø = 18 mm and a typical bar spacing of $s = 200$ mm (see Figures 6.3(b) and (c)). The specimens were cast in two steps, as common for retaining walls, starting with the footing and continuing with the wall. Therefore, the vertical reinforcement was anchored in the footing and spliced just above the construction joint over a length of 50Ø, representing the typical detailing of existing retaining walls (no seismic design), see Figure 6.5(b).

Additional transverse reinforcement Ø14, longitudinal reinforcement Ø12, and stirrups Ø12 were placed in the footing to account for shrinkage and ensure a proper transfer of the moment and shear force from the construction joint to the supports. In the wall, shrinkage reinforcement Ø12@150 was placed longitudinally, and the load introduction zone at the wall head was confined with stirrups Ø8. No shear reinforcement was placed in the wall. All reinforcing bars had a minimum concrete cover of 30 mm.

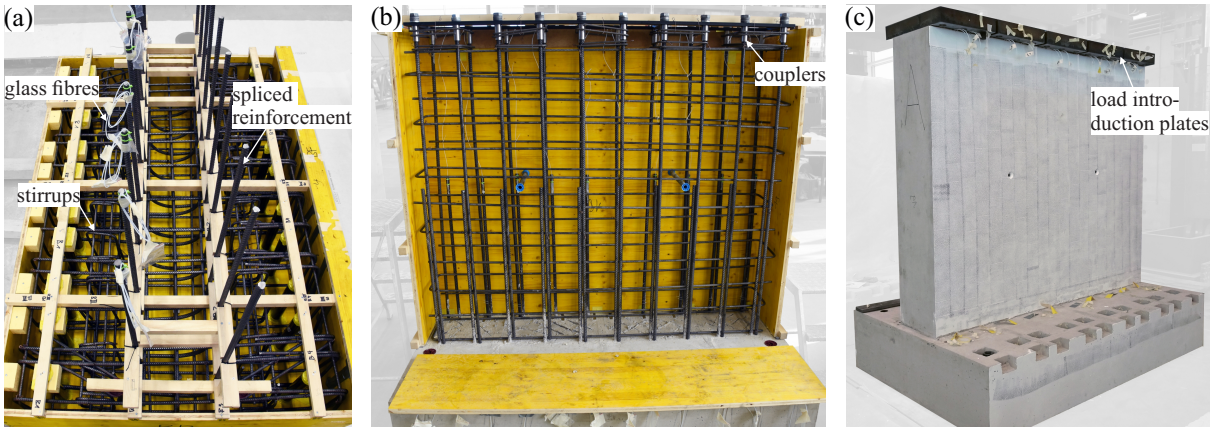

Fig. 6.5 – Test specimens: (a) footing before casting; (b) wall before casting; (c) Specimen CD-0 with installed load introduction plates.

6.3.2 Experimental programme

The experimental campaign consisted of two test series, with five and three specimens, respectively. Series CD ("Corrosion Distribution") aimed at investigating the influence of different corrosion pit distributions on the load-deformation behaviour of cantilever retaining walls since theoretical studies indicated a pronounced influence [72]. Series EP ("Earth Pressure") addressed the influence of a decreasing earth pressure loading with increasing wall deformation due to corrosion damage. The experimental programme is summarised in Table 6.2, where the individual cross-section loss per reinforcing bar ζ_i and the mean cross-section loss ζ_m per specimen are defined as

$$\zeta_i = \frac{A_{s,lost}}{A_s}$$
$$\zeta_m = \frac{\sum\limits_{n_c} A_{s,lost}}{\sum\limits_{n_{tot}} A_s} = \frac{\sum\limits_{n_c} \zeta_i}{n_{tot}} \tag{6.4}$$

with $A_{s,lost}$ = lost cross-sectional area of the reinforcing bar, A_s = original cross-sectional area of the bar, n_c = number of damaged (corroded) bars, and n_{tot} = total number of reinforcing bars (damaged and undamaged, all with the same nominal diameter).

In the specimens of Series CD, the cross-sections of a number of reinforcing bars were reduced before casting, and the load was increased during the experiments until failure (without further reduction of the bar cross-sections). After the reference test CD-0 without any damaged reinforcing bars, Specimen CD-3-10 ($\zeta_m = 0.03$, $\zeta_i = 0.1$) provided insight into the behaviour of a segment with few slightly damaged reinforcing bars. In the following three specimens (CD-9-15/30/var), the mean cross-section loss was held constant at $\zeta_m = 0.09$, similar to that found in the pilot study [52], by providing (i) a few severely damaged reinforcing bars (CD-9-30, $\zeta_i = 0.3$), (ii) many slightly damaged bars (CD-9-15, $\zeta_i = 0.15$), and (iii) many bars with different cross-section losses (CD-9-var).

In the specimens of Series EP, the cross-section of four reinforcing bars was reduced with drilling machines after applying the characteristic load (see Sections 6.3.5 and 6.3.7 for more details). In Specimen EP-CL, the load was held constant during drilling and increased to failure after the bars had been completely drilled through. In the Tests EP-LD ("Low Density", loose soil) and EP-HD ("High Density", compacted soil), a different characteristic load was applied and subsequently decreased during drilling, depending on the increasing wall deformation (see Section 6.3.7). Again, the load was increased to failure after the four bars had been completely drilled through.

Tab. 6.2 – Experimental programme. The cross-section loss per bar and the mean cross-section loss are defined according to Equation (6.4).

Test name	Mean cross-section loss ζ_m [-]	Affected bars n_c	Cross-section loss per bar ζ_i [-]	Loading	Remarks
CD-0	0	0/10	0	Increasing load	Reference test
CD-3-10	0.03	3/10	0.1		Few affected bars, slight damage
CD-9-30	0.09	3/10	0.3		Few affected bars, severe damage
CD-9-15	0.09	6/10	0.15	Increasing load	Many affected bars, slight damage
CD-9-var	0.09	5/10	0.1 (1x), 0.15 (2x), 0.2 (1x), 0.3 (1x)		Many affected bars, various damage
EP-CL	0…0.4	4/10	0…1.0	Constant characteristic load caused by loose soil	
EP-LD	0…0.4	4/10	0…1.0	Characteristic load caused by loose soil (“Low Density”), decreasing with increasing deformation	Increasing damage, starting after application of characteristic load
EP-HD	0…0.4	4/10	0…1.0	Characteristic load caused by compacted soil (“High Density”), decreasing with increasing deformation	

6.3.3 Material properties

The main tensile reinforcement Ø18 originated from the same production batch for all specimens. It consisted of B500B cold-worked bars with the product name “BSW-Superring TWR” (producer: Badische Stahlwerke GmbH). For this type of reinforcing bar, the microstructure is homogeneous over the entire cross-section, other than in QST bars that exhibit a distinct microstructure over the cross-section. Conventional tension tests were carried out at a strain rate of 0.01 %/s to determine the steel stress-strain characteristics. The results are shown in Figure 6.6 along with the typical values of the dynamic yield stress $f_{y,dyn}$, dynamic tensile strength $f_{u,dyn}$, and strain at peak stress $A_{gt} = \varepsilon(f_{u,dyn})$, as well as the static values $f_{y,stat}$ and $f_{u,stat}$ determined by stopping the deformation-controlled loading for two min after reaching the yield stress and close to the tensile strength, respectively.

A conventional concrete C25/30 with a maximum aggregate size of 16 mm was used. On the day of each experiment, two cube and three cylinder compression tests and two double punch tests [113] were carried out to determine the concrete compressive (f_{cc} and f_c) and tensile strength f_{ct}. This was done separately for the footing and the wall since the wall was cast approximately 30 days after the footing (see Section 6.3.1) and thus exhibited different concrete properties. Table 6.3 summarises the mean values of the concrete material tests, along with the maximum absolute deviation in parentheses.

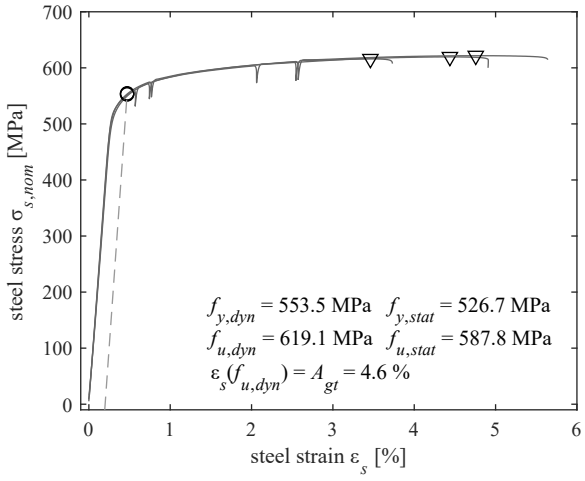

Fig. 6.6 – Stress-strain characteristics of main tensile reinforcement (3 test samples illustrated) with typical values. The circles indicate the dynamic yield stress $f_{y,dyn}$ at 0.2% plastic deformation, and the triangles mark the dynamic tensile strength $f_{u,dyn}$ and the corresponding strain A_{gt}. Note that all stress values were determined with the nominal cross-sectional area.

Tab. 6.3 – Results of concrete material tests for footing and wall of each specimen in [MPa]: mean values and maximum absolute deviation (in parentheses).

Test name	Footing			Wall		
	Cube compressive strength f_{cc}	Cylinder compressive strength f_c	Double punch tensile strength f_{ct}	Cube compressive strength f_{cc}	Cylinder compressive strength f_c	Double punch tensile strength f_{ct}
CD-0	36.9 (0.2)	31.0 (2.1)	2.3 (0.2)	41.1 (0.3)	34.3 (0.2)	2.7 (0.1)
CD-3-10	38.7 (1.1)	34.0 (2.2)	2.9 (0.3)	43.7 (1.4)	36.7 (1.4)	3.3 (0.3)
CD-9-30	40.3 (0.6)	36.3 (1.1)	2.7 (0.2)	43.6 (0.2)	43.7 (0.6)	3.3 (0.2)
CD-9-15	39.8 (0.6)	33.4 (2.6)	2.9 (0.1)	43.8 (1.2)	40.8 (3.0)	3.5 (0.1)
CD-9-var	40.8 (0.5)	35.6 (1.0)	3.1 (0.1)	41.8 (0.9)	39.2 (1.5)	2.9 (0.3)
EP-CL	39.3 (2.3)	35.9 (0.8)	2.8 (0.2)	38.7 (2.0)	37.9 (2.0)	2.8 (0.1)
EP-LD	45.4 (0.2)	41.5 (0.2)	3.2 (0.1)	41.7 (0.3)	36.6 (0.6)	2.9 (0.1)
EP-HD	44.4 (0.2)	41.5 (0.3)	3.1 (0.2)	42.5 (0.7)	38.0 (0.6)	2.8 (0.4)

6.3.4 Artificial corrosion damage

The cross-section of the $n_c = 0...6$ reinforcing bars per specimen affected by corrosion, as indicated in Table 6.2, which were anchored in the footing and passing into the wall, was reduced mechanically just above the construction joint using a spherical mill to simulate corrosion damage. This procedure had already been successfully applied by [34]. It has the advantage that the diameter of the mill and the penetration depth define the cross-section loss and the pit geometry. Preceding pilot tests on bare reinforcing bars and tension chords comparing this degradation method to others, e. g. electrochemically induced corrosion damage, showed only minor differences regarding the load-deformation behaviour [161]. No accumulation of corrosion products and resulting cracks or spalling of the concrete cover are to be expected in case of honeycombs, since (i) no pressure can build up in the highly porous concrete and (ii) most products are washed away with the entering water [25].

The mill diameter was chosen to be 20 mm, closely matching the average pit length found in the pilot study [52]. The bars were provided with a single pit (in contrast to several pits in series) since several bars extracted from existing walls during the pilot study [52] exhibited this pit configuration. Moreover,

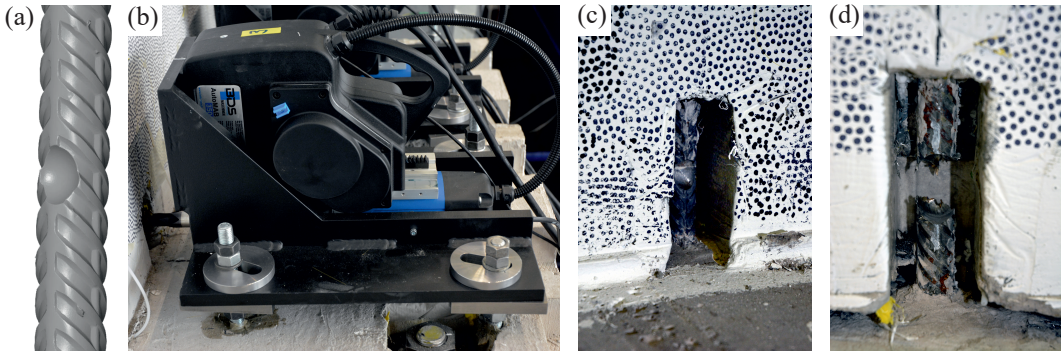

Fig. 6.7 – Details of artificial corrosion: (a) 3D scan of a reinforcing bar Ø18 mm with corrosion pit generated by drilling, corresponding to a maximum cross-section loss $\zeta_i = 0.1$; (b) drilling machine with automatic feed used for hybrid tests, positioned in front of recess and fixed with concrete anchors; (c) recess with reinforcing bar damaged prior to experiment ($\zeta_i = 0.3$); (d) recess with reinforcing bar drilled through during the experiment, after removal of drilling machine.

a study on the influence of the pit geometry on the bar load-deformation behaviour indicated that a single pit is the worst possible configuration regarding the loss of deformation capacity [58].

In Series CD, the cross-section of the $n_c = 0...6$ bars per specimen was reduced before casting, and the region around the pit was scanned using the 3D-scanning system ATOS Core® by GOM to have a reference measurement of the calculated cross-section loss (see Figure 6.7(a)). In Series EP, the cross-section of $n_c = 4$ reinforcing bars per specimen was reduced simultaneously in steps of $\Delta\zeta_i = 0.05$ during each experiment. To this end, four industrial drilling machines fitted with an automatic feed and a high-precision laser distance sensing system were fixed to the footing by means of four concrete anchors per machine (see Figure 6.7(b)). By combining the measured penetration depth with the radii of the reinforcing bar and spherical mill, the removed and remaining cross-sectional areas were precisely known throughout the entire experiment.

In order to provide access to the reinforcing bars to be drilled during the experiment, a recess of 100 mm height, 60 mm depth and 40 mm width was provided around the future corrosion pit during casting by means of a styrofoam formwork inlay (see Figure 6.4(b), Detail A, and Figures 6.7(c) and (d)). Identical recesses were also provided in the Series CD for reinforcing bars containing initial damage to have comparable experimental conditions. While the recesses facilitate access for precisely controlled drilling, they have the apparent disadvantage of a locally missing bond. However, this is no major concern here since the bond strength in the affected region is also reduced in the real retaining walls due to the honeycombs triggering the corrosion damage (see Section 6.1).

6.3.5 Test setup and instrumentation

Figure 6.8(a) shows one of the specimens of Series EP installed in the LUSET; the identical setup, but without drilling machines at the base, was used in Series CD. The specimen footing was placed onto two steel strips positioned on the bottom yokes of the LUSET, which ensured a properly defined load introduction, and clamped with preloaded M36 bolts (see Figure 6.4(a)). At the top edge of the specimen, five load introduction plates were placed onto a mortar layer, connecting the tensile reinforcement at the specimen head to the plates by means of reinforcing bar couplers (BARTEC ® Type X18-24) fixed with M24 bolts (Figure 6.4(b)). This ensured a direct contact of the plates to the specimen and a slip-free moment and shear force introduction. Each of the five load introduction plates was subsequently connected to the corresponding top yoke of the LUSET using preloaded M36 bolts.

All reinforcing bars of the main tensile reinforcement were instrumented with a fibre optic strain sensing system (Odisi 6104 from Luna Inc. [106]), which enabled a quasi-continuous strain sensing along the entire length of the bars using a virtual gauge length of 1.3 mm [63, 100, 116]. To this end,

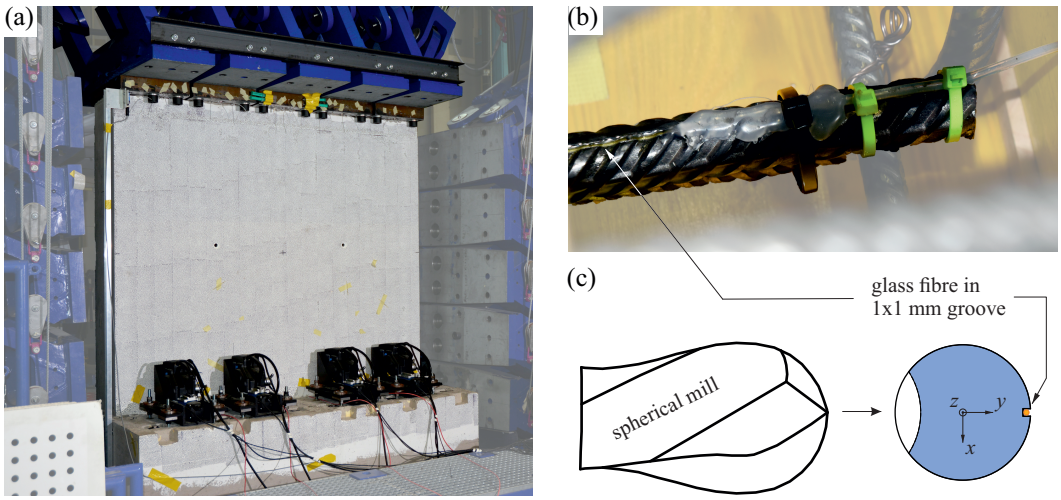

Fig. 6.8 – Test setup and detail of instrumentation: (a) specimen in the Large Universal Shell Element Tester (LUSET) with installed drilling machines for hybrid test; (b) glass fibre glued in groove, with adjacent transition zone where the fibre continues in protecting tube; (c) location of fibre in the reinforcing bar with respect to drilling direction, with global coordinate system shown for reference.

optical glass fibres were placed into small grooves of 1x1 mm cross-section carved along the inner side of the reinforcing bars (opposite the present or future artificial corrosion pit) and glued with epoxy resin [63, 100, 116] (see Figures 6.8(b) and (c)). Note that a transition zone of approximately 10 cm length exists at both ends of each bar where the glass fibre leaves the groove and continues in a protecting tube and, therefore, is not bonded to the bar (Figure 6.8(b)). Hence, the fibre optic measurements do not extend over the full reinforcing bar length. Measurements were carefully post-processed using the consolidating methods and filters described in Appendix B1.

A three-dimensional digital image correlation (DIC) system (VIC-3D of Correlated Solutions [42], FLIR Grasshopper 3 cameras with a resolution of 4096x3000 px) was used to measure the surface deformations of the specimens. To this end, the footing and wall's surface (at the side in tension) were primed white and speckled black. Besides recording the overall deformations, the kinematics of the cracks occurring during the tests were automatically determined from the deformation field using the Automated Crack Detection and Measurement tool ACDM [65, 66, 116]. Different correlation parameters were used depending on the purpose, resulting in a measurement precision of approximately 20...40 µm for the out-of-plane displacement and 10 µm for the crack kinematics (see Appendix B2).

The applied loads were measured using the load pins installed at the 50 actuators of the LUSET (out of 100) used in this configuration, and the resultants were calculated with the actuator's position measurements. Lagrangian optimisation was used to reduce possible noise (see Appendix B3).

6.3.6 Boundary conditions and loading

As a boundary condition, it was assumed that the simulated retaining wall is built on rock or stiff, compacted ground such that wall deflections resulting from a rotation of the footing can be neglected. Consequently, the bottom yokes of the LUSET were controlled to zero rotation and displacement throughout all experiments. The top yokes applied a combination of normal force, out-of-plane shear force and bending moment at the specimen head. Figure 6.9(a) shows the triangular loading of the simulated 4.65 m tall retaining wall (blue and light grey) and that of the specimen (red and dark grey), along with the corresponding shear force and moment lines, bending stiffness, and deflection. The loading of the specimens was chosen such that the moment at the construction joint M_j and the displacement at the specimen head $v_{exp}(z = h)$ were equal to that of a retaining wall with $h_{eff} = 4.65$ m subjected to a triangular earth pressure distribution $q_{eff}(z)$. The bending moment M_{top} and shear force V_{top} to be applied at

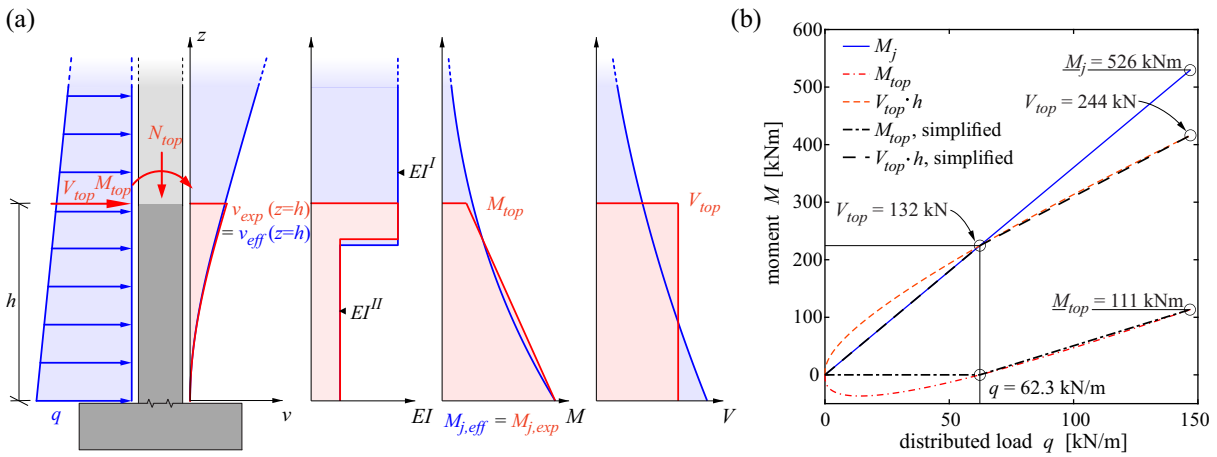

Fig. 6.9 – Applied loads: (a) loading, deflection, bending stiffness, moment, and shear force distribution over height for the simulated retaining wall (blue) and the specimen (red), illustrated for a moment at the joint $M_j = 460\,\text{kNm}$ ($q = 128\,\text{kN/m}$); (b) load path for moment and shear force at the top, M_{top} and V_{top}, respectively, resulting from Equation (6.5). Red curves show the theoretically exact path, black lines represent the simplified path implemented in the control system of the Large Universal Shell Element Tester (LUSET).

the specimen head can thus be determined by solving the following two equations for M_{top} and V_{top} (see Figure 6.9(a)):

$$\begin{aligned} M_{j,exp} &= M_{top} + h \cdot V_{top} \overset{!}{=} M_{j,eff} = \iint_0^{h_{eff}} q_{eff}(z)dz \\ v_{exp}(z=h) &= \iint_0^{h} \frac{M(z)}{EI(z)}dz \overset{!}{=} v_{eff}(z=h) = \iint_0^{h} \frac{M_{eff}(z)}{EI(z)}dz \end{aligned} \tag{6.5}$$

The solution of Equation (6.5) is plotted in red in Figure 6.9(b) as a function of the distributed load q (earth pressure) acting at the location of the construction joint. The analytical solution can be found in the appendix. A simplified, bilinear load path was implemented in the control system of the LUSET, yielding a good approximation (see Figure 6.A1 and black lines in Figure 6.9(b)). A quasi-static loading rate of $dM_j/dt = 5\,\text{kNm/min}$ was chosen.

The specimens were first loaded with a normal force of $N_{top} = (h_{eff} - h)bt_{inf}\gamma_{conc} = -56\,\text{kN}$, simulating the self-weight of the fictitious upper part of the retaining wall (geometry of wall with $h_{eff} = 4.65\,\text{m}$, $h = 1.7\,\text{m}$, $t_{inf} = 0.38\,\text{m}$, $b = 2.0\,\text{m}$, and $\gamma_{conc} = 25\,\text{kN/m}^3$) but neglecting wall friction. As an exception, Specimen CD-0 was tested without normal force. Subsequently, the shear force at the specimen head was increased continuously at a rate of $dV_{top}/dt = 2.95\,\text{kN/min}$ (corresponding to $dM_j/dt = 5\,\text{kNm/min}$) until a shear force $V_{top} = 132\,\text{kN}$ was reached. Subsequently, the shear force was increased at $dV_{top}/dt = 1.96\,\text{kN/min}$ (corresponding to $dM_j/dt = 3.33\,\text{kNm/min}$), and an additional bending moment was applied at the specimen head at a rate of $dM_{top}/dt = 1.66\,\text{kNm/min}$; the total bending moment rate at the construction joint thus remained constant at $dM_j/dt = 5\,\text{kNm/min}$.

In Series CD, the load was monotonically increased until failure. The specimens of Series EP were first loaded to the characteristic load following the load path of Figure 6.9(b), and subsequently, four reinforcing bars were damaged by drilling while the load was either kept constant (EP-CL) or reduced as a function of the deformations (EP-LD and EP-HD, see Table 6.2). For Specimens EP-CL and EP-LD, the characteristic moment at the construction joint $M_{j,k}$ was determined assuming loose soil with $\varphi = 30°$, $\gamma = 22\,\text{kN/m}^3$ and $\delta = 2/3\varphi$ from

$$M_{j,k} = \overline{K}\gamma\frac{h_{eff}^3 b}{6} \tag{6.6}$$

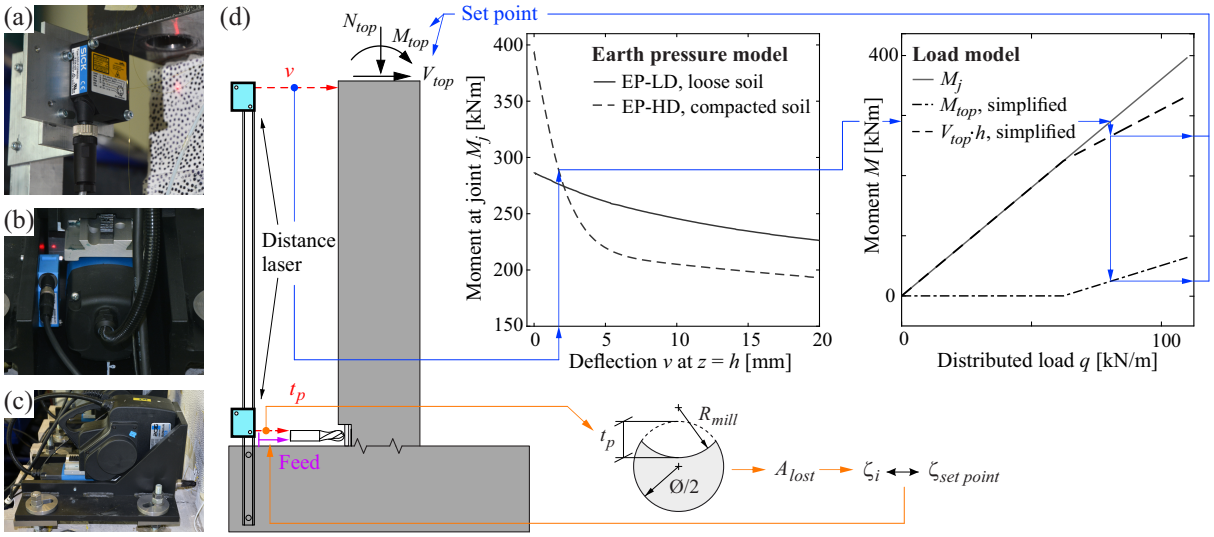

Fig. 6.10 – Control loops for hybrid tests: (a)-(c) details of high-precision laser measurements of the wall head displacement and drill feed; (d) overview of feedback loops for drilling machines (orange) and deformation-dependent load (blue) based on the earth pressure model developed by [125] for loose (Specimen EP-LD) and compacted (Specimen EP-HD) soil.

with $K_0 = 1 - \sin\varphi$, K_{ah} = horizontal earth pressure coefficient (see Equation (6.2)), and $\overline{K} = (K_{ah} + K_0)/2$ = mean earth pressure coefficient, as often used in serviceability limit state (SLS) design. This resulted in a bending moment at the construction joint of $M_{j,k} = 288\,\text{kNm}$ ($q = 39.9\,\text{kN/m}^2$). For Specimen EP-HD, the same soil parameters were assumed, but the earth pressure was determined assuming compaction in five layers using a model provided by [125], resulting in $M_{j,k} = 394\,\text{kNm}$ ($q = 54.7\,\text{kN/m}^2$). If the specimen did not fail after drilling through the reinforcing bars, the load was subsequently increased again, following the load path illustrated in Figure 6.9(b).

6.3.7 Hybrid tests

Series EP, including the two hybrid tests, aimed at investigating (i) the deflection increase in the SLS due to corrosion and, hence, an expected decrease in stiffness, and (ii) the interaction between corrosion, increasing deflection and decreasing earth pressure, i. e. the soil-structure interaction with increasing corrosion damage.

Figure 6.10 shows the control loops for the hybrid tests. The feed of the drilling machines was controlled using the penetration depth measurement resulting from the corresponding distance laser (orange loop in Figure 6.10). Together with the bar diameter and the mill radius, the current cross-section loss was obtained from the penetration depth by integration, which was compared to the current set point. Subsequently, the controller regulated the corresponding machine feed to meet the set point.

To simulate the decreasing earth pressure with increasing deformation, the load applied during the drilling phase in the Tests EP-LD and EP-HD was controlled in function of the specimen head displacement (blue loop in Figure 6.10). The displacement was measured using an additional high-precision distance laser, which was installed on a stiff rod connected to the specimen footing (to avoid any errors due to potential unwanted movements of the specimen base in the LUSET). The model describing the earth pressure behaviour was developed within a companion project at the Chair of Geomechanics at ETH Zurich [125] and customised to fit the input-output structure of the hybrid tests. It relates the displacement at $z = h = 1.7\,\text{m}$ of the simulated wall with $h_{eff} = 4.65\,\text{m}$ to an earth pressure distribution and the resulting bending moment acting at the construction joint M_j, see Figure 6.10. As outlined in Section 6.3.6, two different earth pressure distributions were adopted, simulating loose soil (EP-LD) and compacted soil (EP-HD). The base moment M_j was converted to an equivalent shear force and bending moment at the specimen head, M_{top} and V_{top}, respectively, which were forwarded to the LUSET control system as new set points.

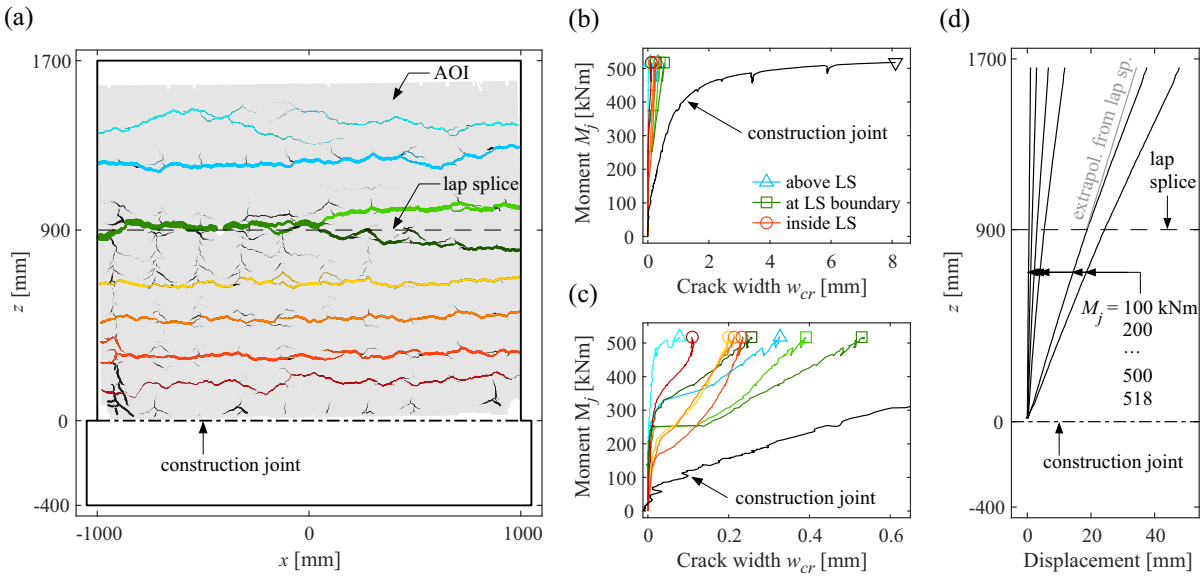

Fig. 6.11 – Crack widths and deformations of cantilever retaining walls with a lap splice (LS): (a) Specimen CD-0 with crack pattern at end of test (yellow and red = cracks in LS region, green = cracks at upper LS boundary, blue = cracks above the LS; line thicknesses proportional to scaled-up (36:1) crack opening; (b, c) crack openings and opening of construction joint at different scale of abscissa; (d) deflections for different load steps.

6.4 Experimental results and discussion

6.4.1 General load-deformation behaviour

This section elaborates on the general load-deformation behaviour of the specimens and, hence, cantilever retaining walls with a similar reinforcement layout, independent of a potential corrosion damage. The particularities in the case of pitting corrosion damage are described in Section 6.4.2.

Figure 6.11(a) shows a front view of specimen CD-0 with the crack pattern at the end of the test. The grey shaded area illustrates the area of interest (AOI) evaluated in the DIC post-processing; a dash-dotted line marks the construction joint, and a dashed line indicates the top end of the lap splice (LS) region. Bending cracks occurring in the LS region are shown in yellow and red, those at the upper LS boundary in green, and bending cracks above the LS in blue, whereas all other cracks are plotted in black. The thickness of the crack lines is proportional to the (scaled-up, 36:1) crack opening. Figures 6.11(b) and (c) show the measured opening of the construction joint (black) and the bending cracks (coloured according to Figure 6.11(a)) vs the moment at the construction joint M_j at different scales of the abscissa. The bending crack opening was extracted from the DIC data using the ACDM techniques described in Section 6.3.5. The latter was not possible to determine the crack opening of the construction joint since it is located at the border of the AOI. Therefore, it was determined as displacement of the lower part of the AOI with reference to two plates fixed at the side of the footing. This results in a slightly higher noise level compared to the ACDM data.

Figures 6.11(b) and (c) show that the opening of the construction joint is one order of magnitude larger than that of the remaining bending cracks. This is due to the crack-width contribution of (i) the footing, where the reinforcement is anchored with its deformation accumulating towards the crack at the joint, and (ii) the lower LS boundary, which concentrates the deformation of the adjacent 1-2 crack elements in the crack at the LS boundary, as outlined in a recent study [75]: the boundary elements of a LS contribute most to its total deformation, whereas the inner elements behave approximately as conventional crack elements with twice as much reinforcement. This is also reflected by the opening of the cracks at the upper end of the LS ($z = 900\,\text{mm}$), which are more than twice as large as the crack openings inside the LS (compare green and red lines in Figure 6.11(c)), despite the much lower bending moment at

Tab. 6.4 – Peak moment at construction joint $M_{j,u}$ and corresponding displacement of the specimen head $v_{top,u}$.

Test name	$M_{j,u}$ [kNm]	$v_{top,u}$ [mm]
CD-0	518	43.2
CD-3-10	532	38.5
CD-9-30	450	25.6
CD-9-15	507	33.2
CD-9-var	481	30.6

this location. The latter underlines the much stiffer behaviour of the LS compared to an element with continuous reinforcement. Additionally, the crack spacing inside the LS is significantly smaller than above the LS, confirming the theoretical approach of [75] regarding the double reinforcement ratio.

Figure 6.11(d) shows the deflections of Specimen CD-0 for different load steps. The curves are almost linear for all load steps, with the wall essentially rotating as a rigid body around the construction joint. This behaviour is due to a combination of the disproportionally decreasing bending moment in z and the significantly increased stiffness in the LS region. At the upper end of the LS ($z = 900$ mm), an additional kink occurs in the deflection curve (clearly visible for $M_j = 500$ kNm, where a grey straight line representing the extrapolation of the deformation of the lower part was added as reference). These observations are in accordance with the comparably large crack opening at this location, seen in Figures 6.11(a) and (c) (green lines).

Overall, the deformation of a cantilever retaining wall containing a LS right above the construction joint (which is the typical case in practice) can be well approximated by a rigid body rotating around the joint. This observation is independent of a potential corrosion damage, which merely affects the (maximum) rotation angle but does not influence the general shape of the deflection curve. Consequently, the LS placed at the construction joint significantly stiffens the lowest part of the retaining wall and strongly reduces its deformation capacity.

6.4.2 Implications of corrosion on load-deformation behaviour

Figure 6.12(a) shows the load-deformation behaviour in terms of the moment at the construction joint M_j vs displacement of the specimen head v_{top} in the five experiments of Series CD with increasing load at constant cross-section loss. The behaviour of the reference test CD-0 without any cross-section loss is shown in black, and that of Specimen CD-3-10 with a slight mean cross-section loss ($\zeta_m = 0.03$) in blue. The tests CD-9-30, CD-9-15 and CD-9-var, with a varying number of corroded bars of different residual cross-sectional areas but equal mean cross-section loss of $\zeta_m = 0.09$, are shown in green, orange and purple, respectively. Triangles indicate the maximum moment at the construction joint $M_{j,u}$ and the corresponding displacement of the specimen head $v_{top,u}$; the corresponding numerical values are compiled in Table 6.4. Compared to the reference test CD-0, the displacement at maximum load of Specimen CD-3-10 was reduced by 11% (-4.7 mm), whereas the maximum load itself slightly increased by 2.9% ($+15$ kNm). The latter effect is presumably due to a triaxial stress state at the corrosion pit, leading to an increase of the exhibited tensile strength for slight cross-section losses; the related effects are currently being investigated by the authors. In the specimens CD-9-30, CD-9-var, and CD-9-15, the displacement at maximum load was reduced by 40.8%, 29.1%, and 23.2% (-12.6 mm, -10.0 mm, -7.6 mm), respectively, and the maximum load decreased by 13.0%, 7.1%, and 2.1% (-68 kNm, -37 kNm, -11 kNm), respectively.

Figure 6.12(b) summarises the results by comparing the Tests CD-3-10 and CD-9-15/30/var with the reference test CD-0 in terms of the variation of the deformation capacity (ratio $v_{top,u}(\zeta)/v_{top,u}(\zeta = 0)$, circles) and the moment capacity (ratio $M_{j,u}(\zeta)/M_{j,u}(\zeta = 0)$, squares) with the mean cross-section loss ζ_m. The results confirm that (i) the reduction of moment capacity is approximately proportional to

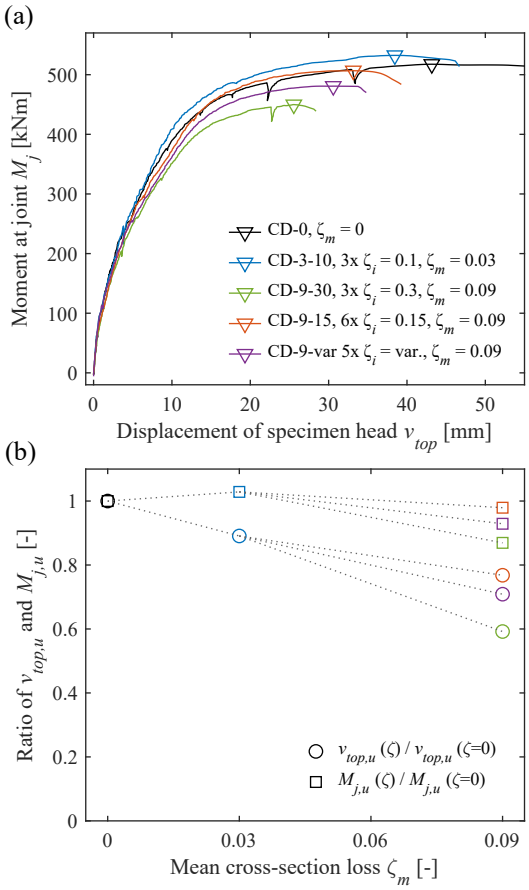

Fig. 6.12 – Results of Series CD: (a) load-deformation behaviour (ζ_i = cross-section loss of individual reinforcing bars and ζ_m = mean cross-section loss for the entire specimen, see Equation (6.4) and Table 6.2; maximum load and corresponding displacement indicated with a triangle); (b) variation of moment capacity ratios (squares) and deformation capacity ratios (circles) with mean cross-section loss.

the mean cross-section loss, (ii) the deformation capacity is disproportionally reduced, and (iii) neither of the two capacity losses can be explained merely by the mean cross-section loss, as evidenced by the different results obtained in the Tests CD-9-15/30/var, all with equal mean cross-section loss of $\zeta_m = 0.09$. Accordingly, among two corroding structures exhibiting an identical mean cross-section loss, the one containing few corroded reinforcing bars with a severe cross-section loss tends to exhibit lower capacities than the structure containing a larger number of corroding reinforcing bars with a smaller cross-section loss. This effect is due to a more severe strain localisation for larger cross-section losses and depends on the individual pit distribution among the reinforcing bars. It was theoretically explained by the authors in [72] for tension chords, including the tension stiffening effect, and in [39] for bare reinforcing bars and is validated for members subject to bending by the experiments presented in this paper. Note, however, that theoretical calculations [72] predict a trend reversal for structures containing an even smaller amount of damaged bars with larger cross-section loss (exemplified in the mentioned study [72] for 20% of bars at $\zeta_i = 0.45$ or 10% of bars at $\zeta_i = 0.9$).

The specimens of the CD series were provided with a varying number of recesses, i. e. an unbonded length of 100 mm (three for CD-3-10 and CD-9-30, five for CD-9-var, and six for CD-9-15). Since the deformation capacity is closely related to the bond conditions, a part of the observed deformations of these specimens may have been due to the unbonded length. Hence, the already reduced deformation capacity observed in the experiments even overestimates that of the real retaining walls. On the other hand, the honeycombs cause a substantial reduction of the bond stresses (though not to zero as in the case of a recess), partly counteracting the overestimation.

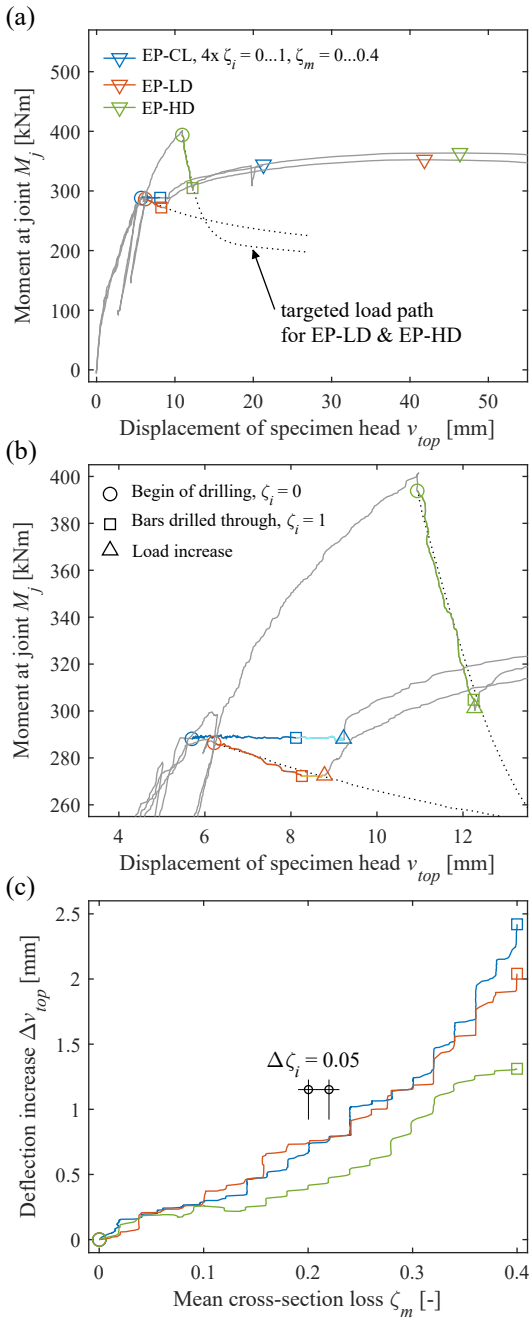

Fig. 6.13 – Results of Series EP: (a, b) load-deformation behaviour, drilling phase highlighted in colour (EP-CL = constant load in drilling phase, EP-LD and EP-HD = hybrid tests with deformation-dependent decreasing load, see Section 6.3.7); (c) displacement increase during drilling vs mean cross-section loss.

Figures 6.13(a) and (b) show the load-deformation behaviour of the three experiments of Series EP with increasing cross-section loss during the entire experiments and in detail during the drilling phase, respectively; note that the part of the experiments where the four reinforcing bars were drilled is shown in colour. Before the cross-section reduction, Specimens EP-CL and EP-HD were subjected to one unloading-reloading cycle in the elastic load range. For these tests, a downwards-pointing triangle indicates the maximum load and the corresponding displacement reached upon increasing the load after all four artificially corroded bars had been drilled through, i. e. at failure of the remaining, uncorroded reinforcing bars.

As described in Section 6.3.7, after loading the specimens to a specified moment at the construction joint in load control mode, the control system was switched to the hybrid mode for the drilling phase.

The load was either kept constant for EP-CL (blue line) or decreased for EP-LD and EP-HD (orange and green lines) in function of the displacement of the specimen head. The black dotted curves indicate the targeted load paths according to the model [125], which the control system followed very well. A circle marks the beginning of the drilling phase, and a square indicates its end, i. e. the point where the bars were completely drilled through.

When switching from load control mode to hybrid mode, the system was set to hold the current actuator positions for a short time (approximately 6 minutes). A slight drop in the load was observed for EP-HD (compare the locations of load peak and the circle in Figure 6.13(b)), as frequently observed in structural testing and investigated, e. g. in [69]. This relaxation is caused by the change in the strain rate (in this case, by the machine stop and the subsequent constant position holding) and occurs pronouncedly for reinforcing steel loaded in its inelastic range. For a moment of $M_j = 400\,\text{kNm}$, the ten reinforcing bars exhibited a steel stress at the wall base of $\sigma_s \approx 477\,\text{MPa}$ and a corresponding total strain of $\varepsilon_s = 0.26\%$ (according to Figure 6.6), i. e. they were just at the beginning of the inelastic load range with a plastic steel strain $\varepsilon_{s,pl} = \varepsilon_s - \sigma_s/E_s = 0.03\%$.

After the four reinforcing bars had been drilled through, the system was switched back to load control, keeping the last applied load constant. Subsequently, the load was increased until the undamaged bars failed. Upwards pointing triangles in Figure 6.13(b) indicate the start of the load increase. For the specimens EP-CL and EP-LD, the time between switching to load control and the start of the load increase was approximately 23 min and 19 min, respectively. A significant deformation increase was observed during this time in both specimens, which can be attributed to creep of (mainly) the reinforcing bars under constant load: while the stresses in the concrete were relatively low, the remaining six reinforcing bars exhibited steel stresses of $\sigma_s \approx 547\,\text{MPa}$ (EP-CL) and $\sigma_s \approx 511\,\text{MPa}$ (EP-LD; total strain $\varepsilon_s = 0.44\%$ and $\varepsilon_s = 0.31\%$, using Figure 6.6), and hence, a plastic steel strain of $\varepsilon_{s,pl} = 0.17\%$ and $\varepsilon_{s,pl} = 0.06\%$, respectively. In line with the shorter duration under constant load and lower stress [69], the creep deformation was lower for Specimen EP-LD compared to EP-CL. In Specimen EP-HD, the time between switching the control mode and the subsequent start of the load increase was only 2 minutes, and accordingly, no significant creep deformation was observed.

Figure 6.13(c) shows the displacement increase of the specimen head vs the mean cross-section loss; note that the displacement is considered between the start of drilling and the complete cross-section loss of the damaged bars, without the subsequent creep deformation (i. e. the displacement measured between the circle and the corresponding square in Figures 6.13(a) and (b)). The shape of the curves reflects the reduction of the cross-section in steps of $\Delta\zeta_i = 0.05$. The displacement increase was highest under constant load (EP-CL), whereas it was significantly lower under deformation-dependent, decreasing load (-16% and -46% for EP-LD and EP-HD, respectively). This lower increase is likely due to the global unloading of specimens: although the six reinforcing bars without cross-section loss could compensate for the strength loss of the four drilled bars and, therefore, exhibited higher stresses near the construction joint, the loading of the entire structure decreased, resulting in significantly reduced deformations. In addition to the load decrease, smaller deformations were presumably also caused by the stiffer unloading behaviour, as observed in the unloading branches prior to the drilling phase for EP-CL and EP-HD (see Figure 6.13(a)). This stiffer behaviour is due to partial slip reversal and a corresponding reversal of bond stresses (see, e. g. [7, 94]) and appears to clearly outweigh the loss of stiffness caused by the cross-section loss of the damaged bars, as outlined in the following section.

6.4.3 Load-transfer mechanism and load distribution among bars

Figure 6.14 shows the stress distribution obtained from the fibre optic strain sensing data in reinforcing bars of the hybrid tests (a) EP-CL, (b) EP-LD, and (c) EP-HD for various individual cross-section losses ζ_i. For each specimen, one undamaged and one damaged pair of reinforcing bars is shown, with a pair consisting of the reinforcing bar crossing the construction joint (L) and its corresponding splicing bar (S; note the different scale of the abscissa for L- and S-bars). The black curve corresponds to the state without

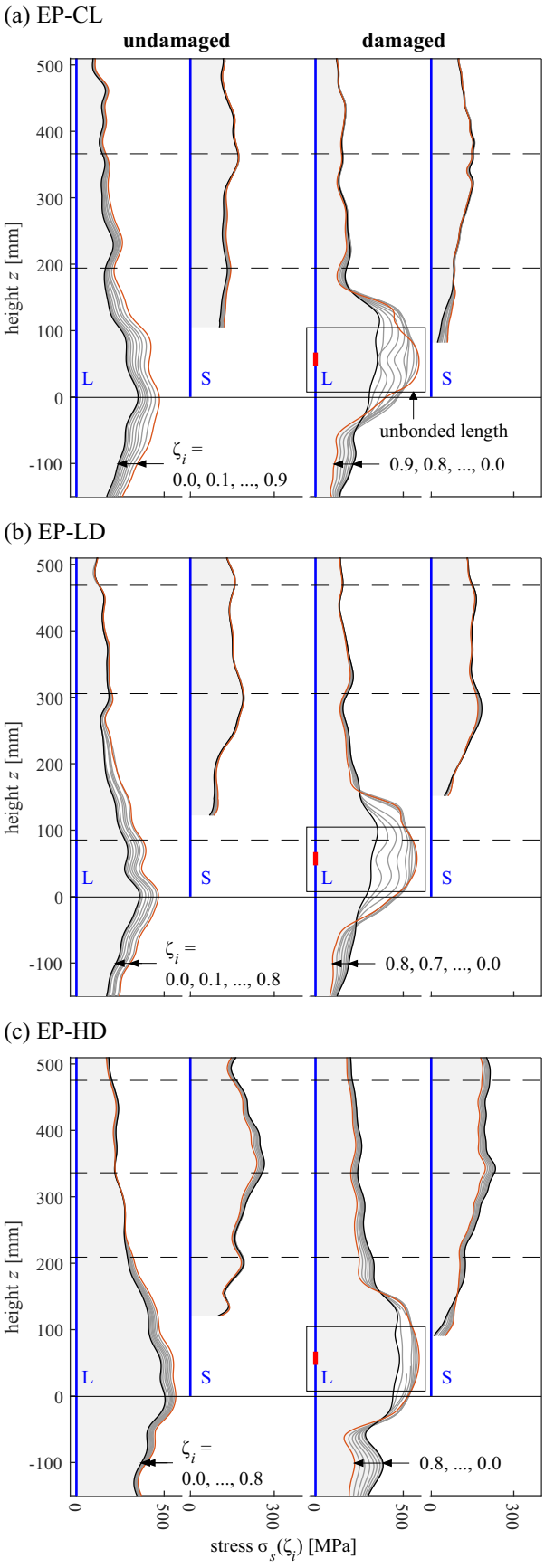

Fig. 6.14 – Steel stresses determined from fibre optic strain sensing data in undamaged (left) and damaged (right) pairs of reinforcing bars in the specimens (a) EP-CL (constant load in drilling phase), (b) EP-LD, and (c) EP-HD (hybrid tests with deformation-dependent decreasing load). Each pair of reinforcing bars (blue lines) consists of a bar crossing the construction joint (L) and the corresponding splicing bar (S). The red area indicates the drilled section, and the solid and dashed horizontal black lines indicate the construction joint and the location of observed bending cracks, respectively. Note the different scale of the abscissa for L- and S-bars.

any cross-section loss prior to drilling ($\zeta_i = 0$), and the orange curve corresponds to a cross-section loss of the damaged bars of $\zeta_i = 0.9$ for Specimen EP-CL and $\zeta_i = 0.8$ for EP-LD and EP-HD. The grey curves correspond to cross-section losses between these values, shown at intervals of $\Delta\zeta_i = 0.1$. The blue vertical lines represent the reinforcing bars; a red area indicates the section penetrated by the mill. A square indicates the recess around the corrosion pit and marks the unbonded length of the damaged reinforcing bar. A solid horizontal line at $z = 0$ specifies the construction joint, and the dashed horizontal lines visualise the mean crack locations extracted from the ACDM data. The fibre optic measurements are missing for the lowest part of the spliced reinforcing bars (S) since the bars were not instrumented there (see Figure 6.8(b)).

The measurements of the damaged L-bars in the pit region $-50\,\text{mm} \leq z \leq 180\,\text{mm}$ reveal a superposition of tensile and bending stresses and cannot directly be compared to other results of the graph. For this reason, the pit region is excluded from the following interpretations and analysed in detail in Section 6.4.4.

For all three experiments, a stress increase (difference between the orange and the black curve) for the undamaged L-bar and a stress decrease for the damaged L-bar (for $z > 180\,\text{mm}$) is visible with increasing cross-section loss ζ_i: the cross-section loss was accompanied by a loss of tensile stiffness of the affected L-bars in the pit region, which triggered a load transfer towards the stiffer undamaged bars. This load transfer is facilitated by a difference in bond shear stresses acting along the individual bars over a certain transfer length, whose extent is mainly governed by the in-plane wall stiffness and the bond strength. It approximately corresponded to the first two crack elements in the experiments: The stress increase in the undamaged L- and S-bars started within the second crack element ($z = 370$, 300, and 240 mm for EP-CL, EP-LD, and EP-HD) and extended in negative z-direction towards the construction joint. At the joint, the stress increase was highest in the L-bar, whereas the S-bar must exhibit zero stress at its end by equilibrium. The damaged L-bars exhibited a stress decrease over the same length (for $z > 180\,\text{mm}$, see Section 6.4.4 for the part below). The corresponding S-bars were unloaded in the upper part of the transfer length and loaded closer to the construction joint. The latter occurred due to the stiffness loss of the neighbouring damaged L-bars, for which the S-bars partly compensated.

In the footing, at depths $-50\,\text{mm} \geq z \geq -150\,\text{mm}$, the reinforcing bars essentially exhibited a pull-out behaviour without a pronounced load transfer between the bars along the short embedment length between the construction joint ($z = 0$) and the beginning of the bent part at $z = -217\,\text{mm}$.

The load transfer mechanism between corroded and uncorroded reinforcing bars has to be superimposed with the load transfer due to the lap splice [75] and with the global loading of the specimens. In the Specimens EP-LD and EP-HD, the load-transfer length was shorter than in Specimen EP-CL due to the pronounced unloading of the former specimens. Accordingly, the stress increase of the undamaged L-bar at the joint in Specimen EP-HD was approximately half of that in EP-CL. All other bars of Specimen EP-HD exhibited a stress decrease, i. e. they were unloaded. Considering the generally stiffer unloading behaviour commented in Section 6.4.2, the findings of Figure 6.14(c) are in line with the lower displacement increase in Specimen EP-HD illustrated in Figure 6.13(c).

Figure 6.15(a) shows the variation of the mean stresses of the undamaged L-bars at the construction joint $\sigma_{s,uc}$ in the specimens of Series CD vs the bending moment at the joint M_j. A cross marks the rupture of the glass fibres (not to be confused with the failure of the specimens). Figure 6.15(b) shows the difference in the mean stresses at the construction joint of the specimens of Series CD compared to Specimen CD-3-10. The latter is used as a reference in this plot since some of the fibre optical strain data of specimen CD-0, which would be the natural choice of reference, contained excessive noise due to technical issues during the test. Again, the fibre failure is marked with a cross, and the failure of a specimen is indicated with three triangles indicating possible failure stress levels (whose actual value is unknown since the glass fibres had ruptured at this point).

Deviations of the steel stresses in the uncorroded bars (Figure 6.15(a)) from the reference test, and a persisting stress difference in Figure 6.15(b), indicate a load transfer from the damaged to the undamaged reinforcing bars. Note that assessing this load transfer by directly comparing the stresses in the damaged

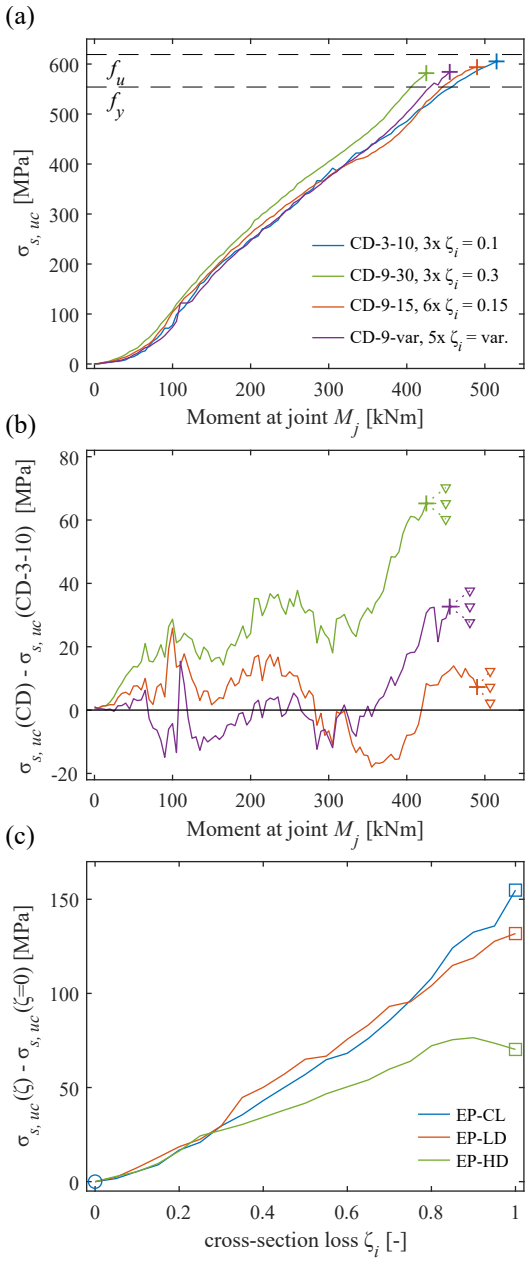

Fig. 6.15 – Mean steel stresses obtained from strain sensing data in L-bars at construction joint: (a) mean stresses in undamaged reinforcing bars of Series CD; (b) difference of mean stresses in undamaged reinforcing bars between Specimens CD-9-15/30/var and CD-3-10 (used as reference); (c) difference of mean stress at a particular cross-section loss and mean stress prior to drilling in Series EP.

bars in the vicinity of the construction joint is not possible due to the superimposed bending effects in the pit region mentioned before. As shown in Figure 6.15(b), the mean steel stresses in the specimens CD-9-15 (red line) and CD-3-10 (reference) were virtually identical. This is remarkable since the total steel cross-sectional area of CD-9-15 is 6% lower than that of CD-3-10, and hence, a more pronounced load transfer to the undamaged bars would have been expected. As the load transfer between damaged and undamaged reinforcing bars is related to a difference in tensile stiffness, this observation implies an almost equal stiffness of the damaged bars in Specimens CD-3-10 and CD-9-15 despite the obviously different steel cross-sectional areas. This apparent contradiction can be resolved by considering that the stress trajectories in the vicinity of the corrosion pit are strongly deviated due to the local change in cross-section (corrosion pit), causing triaxial stress states, which affect the local tensile stiffness and yield behaviour (considering, e. g. von Mises plasticity). Furthermore, it can be observed from Fig-

ure 6.15(b) that the steel stress differences of the specimens CD-9-15/30/var vary despite their identical total steel cross-sectional area, with CD-9-30 (green line) containing few bars with high cross-section loss exhibiting a stronger load transfer than CD-9-var (magenta) or CD-9-15 (red), which contain more bars with smaller cross-section losses. These findings confirm the conclusions drawn from Figure 6.12, i. e. the load-deformation behaviour cannot be explained based on the mean cross-section loss alone. The results can be attributed to the superposition of the influence of the mentioned triaxial stress state and the local bending moments in the pit region, combined with the resulting variation of the localisation effect explained in [72].

Figure 6.15(c) shows the observed stress increase in the undamaged L-bars at the construction joint for the tests of Series EP as a function of the individual cross-section loss ζ_i. The increase was calculated as the difference in the mean steel stress of all undamaged L-bars at a given cross-section loss and at the beginning of the drilling phase (without cross-section loss). The curves in Figure 6.15(c) are similar to those of Figure 6.13(c) and confirm the findings of Figure 6.14: (i) The stresses in the undamaged reinforcing bars at the joint increased with the cross-section loss due to the load transfer from the less stiff damaged bars; (ii) the global unloading of the Specimens EP-LD and EP-HD resulted in a significantly lower stress increase compared to Specimen EP-CL tested under constant load.

6.4.4 Bending effects in the reinforcing bars near the corrosion pit

In reinforcing bars loaded in tension and affected by unilateral corrosion, bending moments in the vicinity of the corrosion pits have been encountered in experimental campaigns [8, 102, 166] (note that throughout this section, the terms bending moment and shear force, as well as deflections, refer to the individual reinforcing bars, rather than the wall). Several models have been developed that adjust the effective reinforcing steel parameters to account for the altered strength of the affected reinforcing bars [8, 58, 166]. The bending moments are a second-order effect caused by the shift of the centre of gravity of the bar near the unilateral pit, causing the reinforcing bar to act essentially as a bending-resistant tie (see Figure 6.16(a) showing the deflection, moment, and shear force distributions for a bar in tension). The embedment of the reinforcing bar in the surrounding concrete restrains its lateral deformation, causing lateral reactions (bearing pressure) and corresponding variations of the bending moment along the bar axis, as in a beam on an elastic foundation, see Figure 6.16(b). The magnitude of the bearing pressure, corresponding to the second derivative of the bending moments, depends on the tensile force, the maximum pit depth, and the stiffness of the surrounding concrete.

Figure 6.17 illustrates the observed behaviour of selected damaged L-reinforcing bars of Series EP (same bars as shown in Figure 6.14). The left graph in the figures (a) and (b) shows the stress variation, measured at the backside of the bar, in the vicinity of the pit for a varying cross-section loss ζ_i with respect to the state prior to drilling ($\zeta_i = 0$), i. e.

$$\Delta\sigma_s\big(M_j, z, \zeta_i\big) = \sigma_s\big(M_j, z, \zeta_i\big) - \sigma_s\big(M_j, z, \zeta_i = 0\big) \tag{6.7}$$

In Specimen EP-CL (Figure 6.17(a)), the stress variation depends solely on the cross-section loss since the moment at the joint $M_j = 288\,\text{kNm}$ was held constant during drilling, i. e. $\Delta\sigma_s = \Delta\sigma_s(z, \zeta_i)$. The same holds in good approximation for Specimen EP-LD (Figure 6.17(b)) considering the minor moment reduction during drilling. The blue curves indicate the stress distribution for $\zeta_i = 0.1$, and the orange curves show the stress distribution for $\zeta_i = 0.9$ (EP-CL) and $\zeta_i = 0.8$ (EP-LD), respectively. The grey curves show the stress variation for intermediate cross-section losses at intervals of $\Delta\zeta_i = 0.1$. Two black horizontal lines indicate the construction joint and the end of the recess, marking the unbonded length of the reinforcing bar. The drilling axis and the diameter of the mill are shown as red stripes, and a green area indicates the region with steel stresses above the yield strength $f_y = 554\,\text{MPa}$. Its edge is curved since the plots show the difference between the yield strength and the stresses prior to drilling (see Figure 6.14), which varied along the bar axis primarily due to bond, but also slightly in the recess.

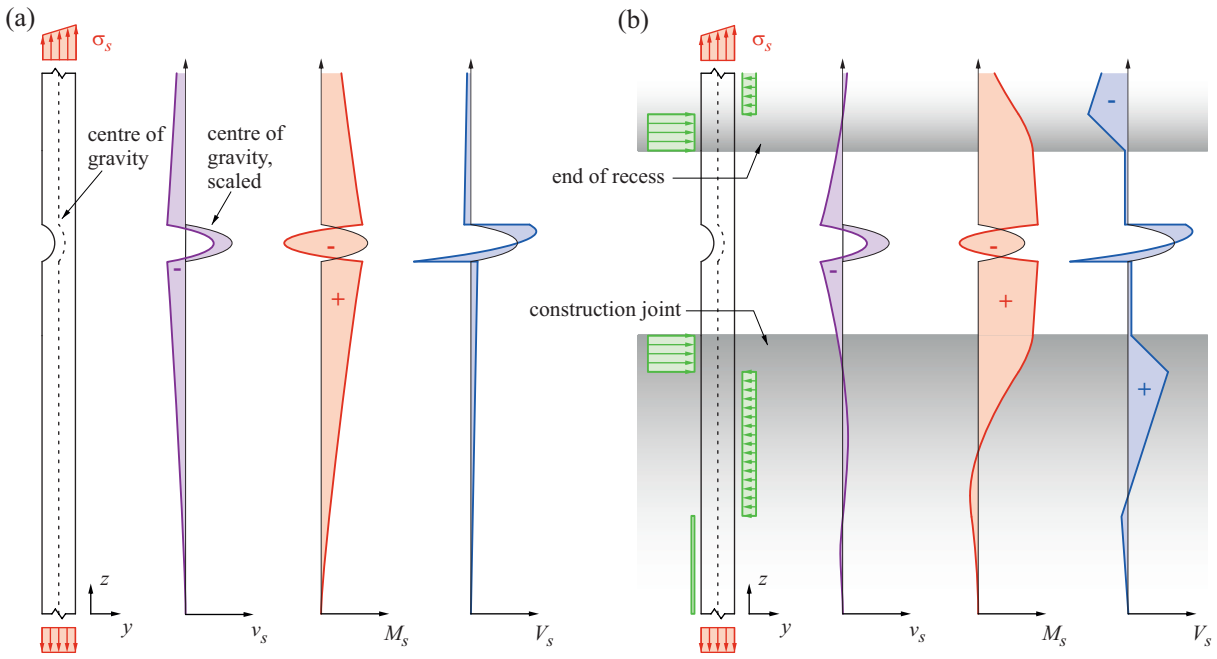

Fig. 6.16 – Second-order effect for reinforcing bars with unilateral corrosion pit: Deflection, moment, and shear force distributions (a) for a reinforcing bar in tension and (b) for one of the damaged reinforcing bars in the specimens. The embedment above and below the recess restrains the bar deformation and causes lateral bearing pressure (green).

Since the glass fibre is glued on the reinforcing bar side opposite to the mill (see Figure 6.8(c)), the measured stresses are caused by the normal force N_s and the bending moment M_s in the reinforcing bar. For steel stresses below the yield strength, i. e. $\Delta\sigma_s \leq \left(f_y - \sigma_s\left(\zeta_i = 0\right)\right)$, the stress variation is thus

$$\Delta\sigma_s\left(z,\zeta_i\right) = \frac{\Delta N_s\left(z,\zeta_i\right)}{A_s} + \frac{\Delta M_s\left(\Delta N_s, z, \zeta_i\right)}{I_x}\frac{\varnothing}{2} \tag{6.8}$$

with ΔN_s and ΔM_s = variation of normal force and bending moment and I_x = second moment of inertia of the reinforcing bar cross-section, all at a specific location along the bar axis. As usual in second-order analyses, the bending moment and its variation depend on the normal force, which in this case is influenced by the cross-section loss, as the latter influences the internal load transfer between the bars. The bending moment also depends on the maximum pit depth (hence, the cross-section loss) and the location z due to the bearing pressure. The normal force varies along the length of the bar due to the bond stresses and, therefore, generally also depends on the location z. Note that Equation (6.8) only approximates the actual steel stresses in the immediate vicinity of the pit: the effects of the triaxial stress state would have to be considered over a length corresponding to 1-2 bar diameters on either side of the pit edges.

Figures 6.17(a) and (b) show that at the pit, a local steel stress reduction – compared to the steel stresses in the adjoining parts of the reinforcing bars – occurred for cross-section losses below $\zeta_i =$ 0.4...0.6. This is due to the bending moment caused by the local shift of the centre of gravity and the acting tensile force (see Figure 6.16(a)). For larger cross-section losses, the steel stresses approached the yield stress, and the local steel stress reduction vanished, presumably because a local plastic hinge formed. Away from the drilling axis and in the embedded parts close to the recess, the steel stress variation increased with the cross-section loss but decreased with the distance from the recess.

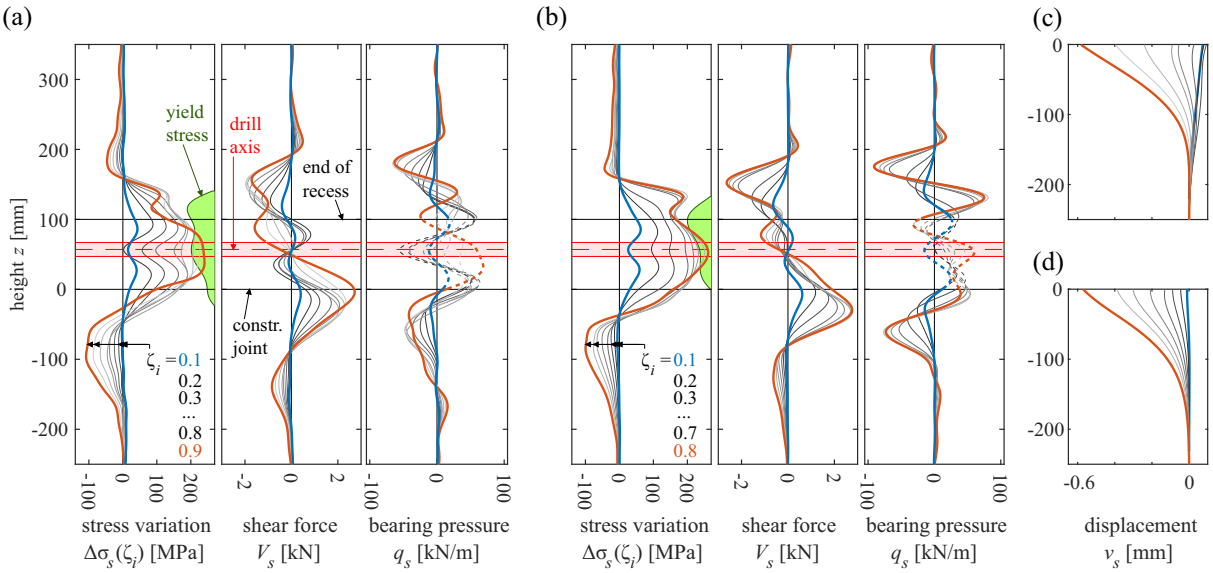

Fig. 6.17 – Variation of steel stresses opposite the mill, estimated shear force (based on Equation (6.12)) and bearing pressure (based on Equation (6.14)) along one damaged reinforcing bar in (a) Specimen EP-CL (constant load in drilling phase) and (b) Specimen EP-LD (hybrid test with deformation-dependent decreasing load) for varying cross-section losses, referred to the state prior to drilling (drilled section indicated by red stripes); (c, d) lateral deflection of the reinforcing bar in Specimens EP-CL and EP-LD, respectively, for varying cross-section losses.

The embedded parts of the reinforcing bars remained elastic for all measurements, i. e. $\Delta\sigma_s \leq \left(f_y - \sigma_s\left(\zeta_i = 0\right)\right)$. Rewriting Equation (6.8), one gets the bending moment in the reinforcing bar

$$M_s\left(N_s, z, \zeta_i\right) = \frac{2I_x}{\text{Ø}}\left(\sigma_s\left(z, \zeta_i\right) - \frac{N_s\left(z, \zeta_i\right)}{A_s}\right) \tag{6.9}$$

and, using the relationship $dN_s = \pi \text{Ø} \tau_b dx$ [114], its derivative corresponds to the shear force

$$V_s\left(N_s, z, \zeta_i\right) = \frac{dM_s}{dz} = \frac{2I_x}{\text{Ø}}\left(\frac{d\sigma_s\left(z, \zeta_i\right)}{dz} - \frac{4}{\text{Ø}}\tau_b\left(z, \zeta_i\right)\right) \tag{6.10}$$

with τ_b = bond shear stress. However, the shear force cannot be directly determined from the measured data (i. e. the steel stresses obtained from fibre optic strain measurements) since the share of steel stress variations caused by (i) bond shear stresses and (ii) bending moment variations due to the shear force is unknown. Nevertheless, a good estimation can be found using the shear force variation

$$\Delta V_s\left(N_s, z, \zeta_i\right) = V_s\left(N_s, z, \zeta_i\right) - \underbrace{V_s\left(N_s, z, 0\right)}_{=\,0} = V_s\left(N_s, z, \zeta_i\right) \tag{6.11}$$

which is identical to the shear force since the latter is zero (in good approximation) prior to drilling. Inserting Equation (6.10) in Equation (6.11) yields the shear force

$$V_s\left(N_s, z, \zeta_i\right) = \frac{2I_x}{\text{Ø}}\left(\frac{d\Delta\sigma_s\left(z, \zeta_i\right)}{dz} - \frac{4}{\text{Ø}}\Delta\tau_b\left(z, \zeta_i\right)\right) \tag{6.12}$$

where $\Delta\tau_b$ = variation of bond stresses due to cross-section loss. As $\Delta\tau_b$ tends to be much smaller than τ_b, this formulation improves the estimation quality of the shear force. Additionally, many bond models assume a zone of reduced (or even absent) bond in the vicinity of cracks or a surface perpendicular to the bar (e. g. Eligehausen et al. [49] suggested a reduced bond over a distance of 5Ø = 90 mm from

the crack). This further reduces the influence of bond in Equation (6.12) since the considered region is located at the construction joint, where a crack is present. The middle plots in Figures 6.17(a) and (b) show the shear forces calculated using Equation (6.12) with $\Delta\tau_b = 0$, with maxima of 2.7 kN near the recess in both specimens. Considering a strong bond stress variation of $\Delta\tau_b = -5$ MPa or -10 MPa, the maximum shear force would merely change by 0.2 and 0.4 kN to 2.9 and 3.1 kN, respectively, confirming the subordinate influence of bond on the results.

Differentiating Equation (6.10) with respect to z yields the bearing pressure acting on the bar and the surrounding concrete

$$q_s(N_s, z, \zeta_i) = \frac{2I_x}{Ø}\left(\frac{d^2\sigma_s}{dz^2} - \frac{4}{Ø}\frac{d\tau_b(z,\zeta_i)}{dz}\right) \tag{6.13}$$

which can be reformulated, again using Equations (6.11) and (6.12), as

$$q_s(N_s, z, \zeta_i) = \frac{2I_x}{Ø}\left(\frac{d^2\Delta\sigma_s}{dz^2} - \underbrace{\frac{4}{Ø}\frac{d\Delta\tau_b(z,\zeta_i)}{dz}}_{\approx 0}\right) \approx \frac{2I_x}{Ø}\frac{d^2\Delta\sigma_s}{dz^2} \tag{6.14}$$

Neglecting the second term in the parentheses in Equation (6.14) is justified since the variation of the bond stresses along the bar axis is almost constant at a specific section under increasing load in the elastic range (see, e. g. [47, 142, 143]).

The right plots in Figures 6.17(a) and (b) show the bearing pressure obtained from Equation (6.14). Since differentiating experimental data leads to high variability, a low pass filter with a lower cut-off frequency (compared to the post-processing of the other fibre optic measurements) was used to compensate for additional noise, with the drawback of flattening the maxima (see Section B1 in the appendix). Hence, the absolute values are subject to higher uncertainty, whereas the overall distribution (location of roots and maxima) remains unaffected. Positive values of the bearing pressure correspond to forces directed towards the concrete surface, and negative values to forces directed to the specimen's inside. The values along the recess are artefacts of measurement inaccuracy in the pit region and the calculation procedures and, therefore, are shown as dotted lines. Relevant bearing pressures occurred over a distance of 100...150 mm on either side of the recess, changing their signs twice for lower cross-section losses and three times for larger cross-section losses, in line with the increase in the acting bending moment.

Figures 6.17(c) and (d) show the estimated deflection of the corresponding reinforcing bars in Specimens EP-CL and EP-LD, obtained by integrating the curvatures corresponding to the steel stress variations twice. Since the negative stresses may partly be overestimated due to the superimposed unloading of the damaged bars, the plotted deflections are merely an approximation. Nevertheless, Figure 6.17 gives a valuable insight into the processes evolving in the pit region and the neighbouring concrete sections despite the uncertainties.

Figure 6.18(a) shows the absolute bearing pressure and (b) the bending moment and the bending stress in the reinforcing bar at the transitions to the recess, i. e. at $z = 0$ mm (solid lines) and $z = 100$ mm (dashed lines), for an increasing cross-section loss. Despite the uncertainty regarding the absolute values due to the low pass filter, these sections of the reinforcing bar exhibit an increasing bending moment (and consequently increasing local lateral forces) up to a cross-section loss of $\zeta_i = 0.55$ for EP-CL and $\zeta_i = 0.4$ for EP-LD, respectively. Subsequently, the bending moment remains constant, indicating that the normal force in the bar (transferred over the pit) decreased at a similar rate as the eccentricity of the centre of gravity, i. e. approximately half the maximum pit depth, increased.

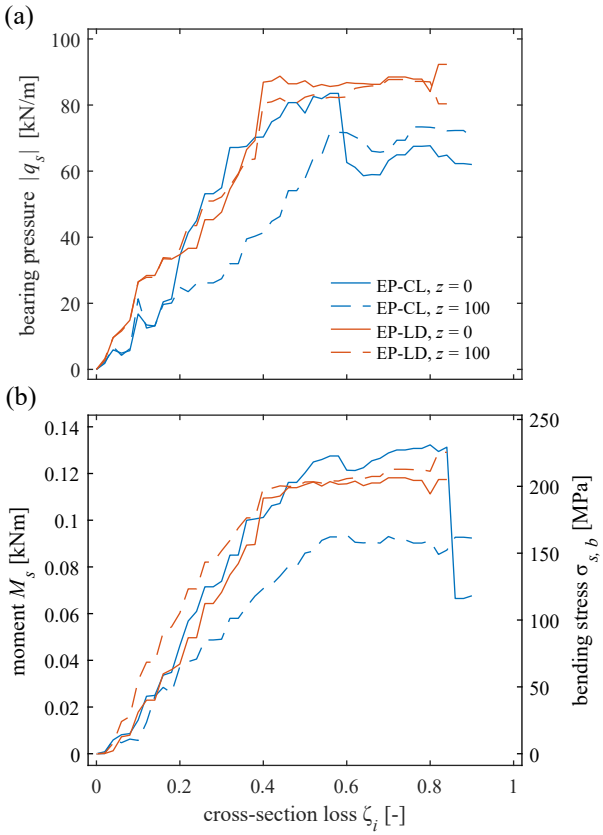

Fig. 6.18 – (a) Absolute bearing pressure and (b) local bending moment and bending stresses at the transition to the recess as a function of the cross-section loss.

6.5 Conclusions and recommendations for future research

The structural safety of cantilever retaining walls with locally corroded reinforcement is concerning due to considerable uncertainties: Corrosion at the rear of the wall base is difficult to detect with standard techniques due to the common wall dimensions, but the related localised damage strongly reduces the load-bearing and deformation capacity. On the other hand, the earth pressure (a retaining wall's main loading) is typically deformation dependent, and many walls have been designed for loads at the lower limit of the possible range (active pressure) relying on a sufficient deformation capacity. Thus, if the residual deformation capacity is insufficient, the actual load acting on the walls will be higher than assumed in design. The situation is further aggravated by the fact that many aspects related to the quantification of the residual deformation capacity are scarcely investigated, such as, e. g. the influence of the corrosion pit distribution among different reinforcing bars and the influence of the local stress state in the vicinity of corrosion pits. This complicates a comparison of deformation capacity and deformation demand, whereas the latter is still under investigation itself (see [125]). Moreover, the statically determined system of cantilever walls in the vertical direction, along with the closely spaced segmentation in the longitudinal direction, impedes substantial load redistributions. In conclusion, the risk for a brittle failure of affected structures – presumably without prior detectable deformations – is high.

In order to improve the basis for the quantification of the related risks and the deformations prior to failure, this study investigated the load-deformation behaviour of retaining walls with localised corrosion of the main tensile reinforcement, focusing on (i) the influence of the corrosion pit distribution among different reinforcing bars and (ii) the interdependence of deformation-dependent loading, corrosion, and deformation capacity. To this end, eight large-scale experiments on retaining wall segments with varying corrosion pit distribution were conducted in the LUSET [88][20], revealing the following results:

- Cantilever retaining walls containing a lap splice right above the construction joint deform almost as a rigid body rotating around the joint. This is caused by the significantly higher bending stiffness in the lap splice region, leading to a large crack opening at the construction joint, amounting to several millimetres in the present experimental series. Hence, lap splices placed directly at the construction joint impair the deformation capacity of the walls.

- The load-deformation behaviour, specifically the maximum load and corresponding deformation, strongly depends on the corrosion pit distribution: The deformation capacity is lower for a structure containing few bars with a large cross-section loss (here, 30% of bars at $\zeta_i = 0.3$) than one containing many bars with lower cross-section loss (here, 60% of bars at $\zeta_i = 0.15$)[1]. This result confirms previous theoretical studies [72] and can, i.a., be attributed to a varying localisation effect. It demonstrates that merely indicating the mean cross-section loss of a structure (here in both cases equal $\zeta_m = 0.09$) is insufficient to draw reliable conclusions on its load-deformation behaviour. Note, however, that theoretical calculations [72] predict a trend reversal for structures containing an even smaller amount of damaged bars with larger cross-section loss (exemplified in that study [72] for 20% of bars at $\zeta_i = 0.45$ or 10% of bars at $\zeta_i = 0.9$).

- The relative reduction of the deformation capacity observed in the tests is more pronounced than the relative reduction in load-bearing capacity, as predicted by [39, 72]. However, it is to note that a part of the exhibited deformation of the specimens might be attributed to the unbonded length in the recess, and hence, the reduced deformation capacity of the tests might even be overestimated.

- Stresses in the undamaged reinforcing bars back-calculated from the measured strains indicate that the local tensile stiffness in the vicinity of the corrosion pit is higher than could be assumed when merely considering the reduction of cross-sectional area. This effect may be attributed to a triaxial stress state caused by the strongly deviated stress trajectories in the pit region. Together with locally acting bending moments in the pit vicinity, the latter effect presumably also influences the yield behaviour of damaged bars in the pit region (considering, e. g. von Mises plasticity).

- The displacement increase of the specimen head due to an increasing cross-section loss was found to be non-linear, laying in the range of 0.8 to 1.4 mm per meter height for a maximum cross-section loss of 40% (40% of bars drilled through, i. e. $\zeta_i = 1.0$), depending on the actual earth pressure. This corresponds to a total displacement of 3.7 to 6.5 mm at the head of a 4.65 m tall retaining wall, considering that the deformation localises in the construction joint. This magnitude of displacement is potentially too small for a successful application of the observation method, as it is highly challenging to recognise an increasing displacement trend resulting from an increasing cross-section loss in field data, and distinguish it from displacements caused by many other effects (seasonal and daily temperature variations, temporary water pressure, etc.).

- The displacement increase of the specimen head due to an increasing cross-section loss was lower in the hybrid test simulating compacted soil than in that simulating loose soil, although the earth pressure is higher in the first case. This was attributed to a more pronounced decrease of the earth pressure in compacted soil with increasing wall deformation [125]: the load increase of the undamaged reinforcing bars due to the internal force redistribution caused by corrosion damage is balanced or even outweighed by the strong decrease of the total applied load. The latter observation was confirmed by the fibre optic strain measurements of the undamaged reinforcing bars. However, further investigations are needed to confirm these findings.

[1] This conclusion refers to the context of the published article, where the maximum cross-section loss per bar was $\zeta_i = 0.3$. Regarding larger cross-section losses per bar, the trend may reverse (see Figure 2.8): Structures containing many reinforcing bars with slight cross-section losses ($\zeta_i < \zeta_{crit}$) or only a few heavily corroded bars ($n_c < (\zeta_m + 0.2) \cdot n_{tot}$ and $\zeta_i > \zeta_m / (\zeta_m + 0.2)$; n_c = number of affected bars, n_{tot} = total number of bars) exhibit a larger load-carrying and deformation capacity for a specific mean cross-section loss ζ_m than structures with a moderate number of affected bars. Both capacities are minimum for $n_c \approx (\zeta_m + 0.2) \cdot n_{tot}$ and $\zeta_i \approx \zeta_m / (\zeta_m + 0.2)$ [73].

- The load transfer between the damaged and the undamaged reinforcing bars for an increasing cross-section loss was found to occur in the region up to the first or second crack above the construction joint (depending on the total external load).
- As stated in previous works [8, 166], unilateral local corrosion damage leads to bending moments in the vicinity of the pit. Additional strains attributed to such bending moments present at the pit and in the adjacent embedded part of the reinforcing bars were measured with fibre optic strain sensing. The results allow conclusions on the bearing pressure distribution acting laterally on the bar and the length over which the bending moment decreases to zero (roughly 120 to 150 mm in this study, corresponding to 6. . . 8 bar diameters).

This study outlines the importance of further research on reinforcing bars affected by pitting corrosion and describing their load-deformation behaviour on a sound mechanical basis. The authors are currently investigating the influence of the triaxial stress state due to deviated stress trajectories (axial tensile stiffness and apparent tensile strength) and the influence of local bending moments due to the shift of the centre of gravity in the pit region on the tensile resistance. A publication detailing the modelling approach outlined in [70] for locally corroded structural elements in bending based on the Corroded Tension Chord Model [72] is envisaged.

Appendix A: Derivation of graphical results in Figure 6.9 from Equation (6.5)

The distribution of shear force and bending moment for a simulated, effective retaining wall of height h_{eff}, loaded by a triangular distributed load $q_{eff}(z)$ (see Figure 6.9(a)), i. e. $V_{eff}(z)$ and $M_{eff}(z)$, are given with

$$\begin{aligned} q_{eff}(z) &= \frac{q}{h_{eff}}(h_{eff}-z) \\ V_{eff}(z) &= \int q_{eff}(z)dz = \frac{q}{h_{eff}}\frac{(h_{eff}-z)^2}{2} \\ M_{eff}(z) &= \int -V_{eff}(z)dz = -\frac{q}{h_{eff}}\frac{(h_{eff}-z)^3}{6} \end{aligned} \tag{6.A1}$$

For a specimen of height h, loaded at the top by a force V_{top} and a bending moment M_{top}, the shear force and bending moment distributions, $V_{exp}(z)$ and $M_{exp}(z)$, are

$$\begin{aligned} V_{exp}(z) &= V_{top} \\ M_{exp}(z) &= -M_{top} - V_{top}(h-z) \end{aligned} \tag{6.A2}$$

The rotation $\varphi(z)$ and the deflection $v(z)$ in Equation (6.A3) follow by integrating Equations (6.A1) and (6.A2), respectively,

$$\begin{aligned} \varphi(z) &= \int -\frac{M(z)}{EI(z)}dz \\ v(z) &= \int \varphi(z)dz \end{aligned} \tag{6.A3}$$

with the bending stiffness

$$\begin{aligned} EI(z) &= EI^I && \text{for } M(z) < M_{cr} \\ EI(z) &= EI^{II} = \alpha_{cr}EI^I && \text{for } M_{cr} \le M(z) < M_y \\ EI(z) &= EI^y = \alpha_y EI^I && \text{for } M_y \le M(z) \end{aligned} \tag{6.A4}$$

where M_{cr} = cracking moment and M_y = yielding moment. Equations (6.A1) and (6.A2) yield the height z_{cr} where the bending moment equals the cracking moment:

$$\begin{aligned} M_{eff}(z_{cr,eff}) &= -\frac{q}{h_{eff}}\frac{(h_{eff}-z_{cr,eff})^3}{6} = -M_{cr} && \rightarrow z_{cr,eff} = h_{eff} - \sqrt[3]{\frac{6M_{cr}h_{eff}}{q}} \\ M_{exp}(z_{cr,exp}) &= -M_{top} - V_{top}(h-z_{cr,exp}) = -M_{cr} && \rightarrow z_{cr,exp} = h - \frac{M_{cr}-M_{top}}{V_{top}} \end{aligned} \tag{6.A5}$$

As a second condition, Equation (6.5) sets the displacement of the specimen head equal to the deflection of the simulated retaining wall at the same height, i. e. $v_{exp}(z=h) = v_{eff}(z=h)$. This condition can be approximated in the elastic range by setting the height where the bending moment equals the cracking moment equal for the specimen and the effective retaining wall, i. e. $z_{cr,exp} = z_{cr,eff}$. This approximation is sufficiently accurate (also for the plastic range, as shown below) since the cracked part at the bottom

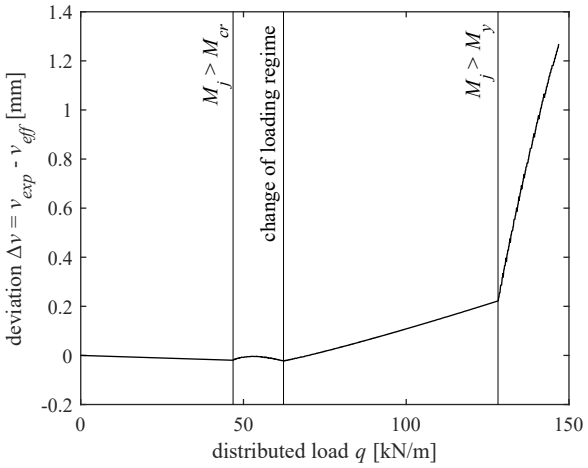

Fig. 6.A1 – Deviation between the expected displacement of the specimen head and of a 4.65 m tall retaining wall at $z = h$ (assuming $\alpha_{cr} = 1/3$ and $\alpha_y = 1/9$). The loading is given in Figure 6.9(a) (triangular) and (b) (black curves).

of the wall contributes most to the deflection. Thus, Equation (6.A5) is replaced by

$$\begin{aligned} &M_{exp}(z=0) = M_{eff}(z=0) \\ &z_{cr,exp} = z_{cr,eff} \end{aligned} \tag{6.A6}$$

yielding the following solution for V_{top} and M_{top}:

$$\begin{aligned} V_{top} &= \frac{M_{eff}(z=0) - M_{cr}}{z_{cr,eff}} = \frac{qh_{eff}^2 - 6M_{cr}}{6\left(h_{eff} - \sqrt[3]{\frac{6h_{eff}M_{cr}}{q}}\right)} \\ M_{top} &= M_{eff}(z=0)\left(1 - \frac{h}{z_{cr,eff}}\right) + M_{cr}\frac{h}{z_{cr,eff}} \\ &= \frac{qh_{eff}^2}{6}\left(1 - \frac{h}{h_{eff} - \sqrt[3]{\frac{6h_{eff}M_{cr}}{q}}}\right) + M_{cr}\frac{h}{h_{eff} - \sqrt[3]{\frac{6h_{eff}M_{cr}}{q}}} \end{aligned} \tag{6.A7}$$

With the cracking moment

$$M_{cr} = \frac{t_{inf}^2 b}{6} f_{ct} \tag{6.A8}$$

and $h = 1.7\,\text{m}$, $h_{eff} = 4.65\,\text{m}$, $t_{inf} = 0.38\,\text{m}$, $b = 2.0\,\text{m}$, and assuming $f_{ct} = 3.5\,\text{MPa}$, Equation (6.A7) yields the red curves plotted in Figure 6.9(b).

As mentioned in Section 6.3.6, the loading path of Figure 6.9(b), red curves, was further simplified (black curves) for the implementation in the control system of LUSET. Whereas the first condition of Equation (6.A6) was exactly met, the second condition was approximated. Figure 6.A1 shows the deviation between the expected displacement of the specimen head and the 4.65 m tall retaining wall at $z = h$ (assuming $\alpha_{cr} = 1/3$ and $\alpha_y = 1/9$). For the elastic range, the expected absolute deviation is < 0.2 mm, and for the plastic range, it increases with a peak value at failure of approximately 1.2 mm. Given the uncertainties of the assumptions (bending stiffness, effective cracking moment, etc.), these values are acceptable.

Appendix B: Data post-processing and data accuracy

B1 Fibre optic strain data

The strain data of the fibre optic measurement recorded with 1.25 Hz (1 measurement every 0.8 s) was first consolidated to 0.104 Hz (1 measurement every 9.6 s) using the median in the time domain. This procedure reliably rejects outlying data. Afterwards, the influence of the ribs of the reinforcing bar surface on the local strains was reduced by applying a moving average filter in the space domain (see [63]). A window size of 16 for a virtual gauge length of 1.3 mm was chosen to approximately meet the double rib spacing of 10.5 mm ($16 \cdot 1.3\,\text{mm} = 20.8\,\text{mm} \approx 21\,\text{mm} = 2 \cdot 10.5\,\text{mm}$). A low-pass filter with a cutoff frequency of 0.05 mm^{-1} (the sampling frequency is 1/1.3 = 0.77 mm^{-1}) was applied in the space domain to reduce noise further. The chosen frequency corresponds to keeping a periodic signal with a wavelength larger than 1/0.05 = 20 mm, and attenuating signals with smaller wavelengths. For a bar diameter of 18 mm, this cutoff frequency leads to results at low noise without losing relevant information: For slender instrumented elements with negligible shear deformations, like reinforcing bars, strain data at a spatial resolution smaller than the thickness of the instrumented carrier material does not provide useful additional information. However, note that for the evaluations shown in Section 6.4.4, a low-pass filter with a cutoff frequency of 0.02 mm^{-1} was applied to prevent a substantial noise increase for the derivatives. The curve's shape remains valid for this cutoff frequency, but the absolute values have to be interpreted with care.

B2 Deformation data of DIC

The sampling frequency of the DIC system during the experiments was 0.1 Hz (1 picture every 10 s). For correlating the pictures, a subset size of 31 pixels and a step size of 8 pixels were chosen for the deformation measurements, and a subset size of 15 pixels and a step size of 2 pixels for evaluating the crack kinematics with ACDM. The different correlation parameters enabled high accuracy for measuring the out-of-plane deformations (where it is essential to determine the absolute movement of the top and the bottom part of the specimen with little noise) and simultaneously a high accuracy for detecting the cracks and determining their kinematics (where it is essential to localise connecting strain peaks with a high spatial resolution). A moving average filter was subsequently applied in the time domain (same virtual subset over several pictures) with a window size of 15 for the deformation measurements and 5 for the crack kinematics. Since the specimens slightly rotated as rigid bodies at the beginning of the experiment (due to slip in the clamping), a rigid body motion removal technique based on Sorkine-Hornung and Rabinovich [147] was applied using the data of the front side of the footing.

Prior to each experiment, a Zero-Displacement-Test (ZDT) and a Zero-Strain-Test (ZST) were carried out following the recommendations by Mata-Fálcon et al. [116] and technical guidelines of VDI [158]. Whereas the ZDT gives information on the noise floor depending on the correlation parameters (subset size and step size), the ZST gives information on the noise floor depending on the displacement of the area of interest (AOI) for one specific set of correlation parameters. For the ZDT, the specimen was held in place, and approximately 80 pictures were taken; for the ZST, the specimen was moved stress-free in the YZ-plane, following a virtual square of 100 mm side length, and approximately 700 pictures were taken.

In the ZDT, where the measured mean virtual displacement $\overline{u_k}$ is almost zero for all subsets, the standard deviation s_k of the virtual displacement in z-direction estimates the noise floor for the actual in-plane displacement field during the experiment for a given calibration parameter set; the standard deviation in y-direction estimates the noise floor out-of-plane

$$s_k = \sqrt{\frac{\sum_{i=1}^{n} \left(u_{i,k} - \overline{u_k}\right)^2}{n-1}} \approx \sqrt{\frac{\sum_{i=1}^{n} u_{i,k}^2}{n-1}} \tag{6.B1}$$

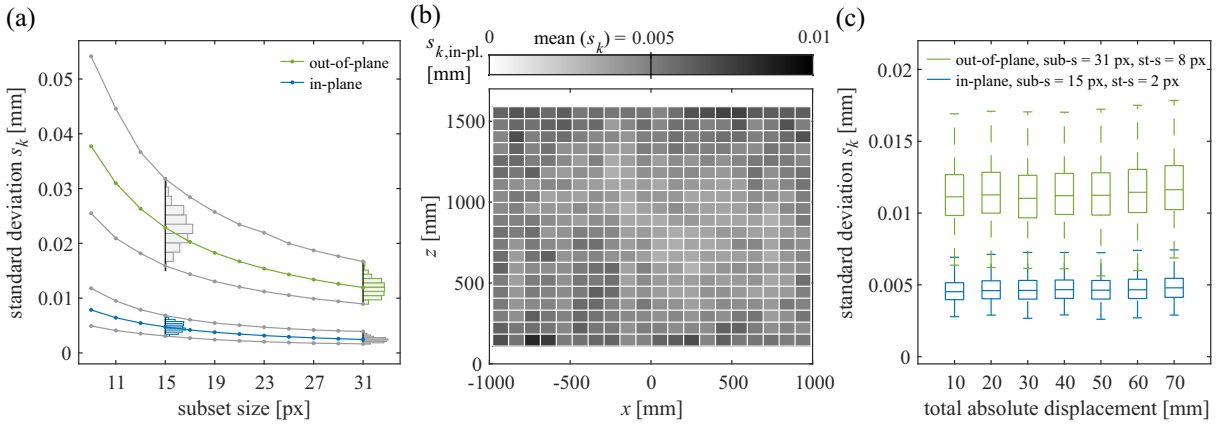

Fig. 6.B1 – Results of zero-displacement test ZDT and zero-strain test ZST of CD-9-30: (a) standard deviation according to Equation (6.B1) of ZDT in function of chosen subset size for in-plane and out-of-plane displacements; (b) standard deviation of ZST per subarea; (c) standard deviation distribution of ZST at specific absolute displacements of specimen for in-plane and out-of-plane displacement.

with $k = k^{th}$ subset, $i = i^{th}$ picture, n = total number of pictures of ZDT, $u_{i,k}$ = measured displacement (in y or z-direction) in k^{th} subset and i^{th} picture. Figure 6.B1(a) shows the in-plane and out-of-plane standard deviation for CD-9-30 as a function of the chosen subset size. The blue line represents the median of the in-plane standard deviation, i. e. the standard deviation of the virtually measured displacements in the z-direction, evaluated over all subsets of the AOI; the blue line represents the median of the out-of-plane standard deviation (y-direction). Four histograms characterise the standard deviation distributions for two specific subset sizes, and grey lines indicate the maximum and minimum histogram boundaries. The noise floor decreases logarithmically for larger subset sizes due to the stronger averaging effect for bigger subsets, at a trade-off of an increasing information loss. Therefore, as explained above, two different correlation parameter sets were chosen for different purposes (in-plane crack kinematics and out-of-plane displacement measurements).

For the evaluation of the ZST, the rigid body motion was removed from the displacement data (leading to zero mean displacements). Hence, the remaining measured virtual displacement in each subarea corresponds to noise. The AOI was divided into $20 \cdot 20 = 400$ subareas; Figure 6.B1(b) shows the standard deviation of the virtual displacement of CD-9-30 per subarea, evaluated with the in-plane correlation parameters (subset size 15, step size 2). Here, the standard deviation s_k was calculated according to Equation (6.B1), with $k = k^{th}$ subarea (instead of subset) and n = total number of pictures of ZST. A slightly higher noise is visible at the border of the AOI, which can be attributed to a distortion of the camera lenses. Nevertheless, the average noise of 5 µm for the whole AOI is very low.

In Figure 6.B1(c), box plots characterise the distribution of the standard deviation s_k for the measured virtual displacements among the 400 subareas at specific absolute displacements of the specimen. Again, it is distinguished between measured in-plane and out-of-plane displacement and correlation parameters (z-direction, subset size 15, step size 2, and y-direction, subset size 31, step size 8, respectively). As expected, the noise for the measured out-of-plane displacements is higher than for the in-plane displacements, and its corresponding distribution (characterised by the interquartile range and the neighbouring values) is broader. Nevertheless, the result is not influenced by the absolute displacement of the specimen. Hence, the noise floor can be assumed constant for the experimental results and is approximately 11 µm out-of-plane and 4 µm in-plane on average.

Table 6.B1 summarises the analysed noise values for all experiments. In conclusion, the out-of-plane displacement can be determined with a measurement precision of approximately $2\widetilde{s_k} = 20...40$ µm. The crack opening and slip (in-plane displacement) can be determined with a measurement precision of approximately $2\widetilde{s_k} = 10$ µm.

Tab. 6.B1 – Median and standard deviation (in parentheses) of distribution of s_k according to Equation (6.B1) for in-plane and out-of-plane displacement, in µm.

Test name	In-plane		Out-of-plane	
	ZDT	ZST	ZDT	ZST
CD-0	6.9 (2.1)	6.5 (1.7)	26.1 (13.9)	22.5 (7.5)
CD-3-10	6.1 (1.1)	6.5 (1.5)	16.5 (2.6)	18.0 (3.7)
CD-9-30	4.7 (0.8)	4.7 (1.0)	11.8 (1.5)	11.5 (2.3)
CD-9-15	4.3 (0.6)	4.4 (0.9)	10.9 (1.5)	11.1 (2.8)
CD-9-var	3.6 (0.6)	4.0 (2.3)	9.0 (1.3)	10.1 (4.4)
EP-CL	3.8 (0.5)	3.9 (1.2)	12.8 (2.9)	11.7 (3.9)
EP-LD	3.7 (0.6)	4.3 (2.5)	11.4 (2.7)	11.4 (4.3)
EP-HD	4.2 (0.8)	4.3 (1.6)	14.6 (3.8)	14.0 (4.4)

B3 Force data

The Lagrangian optimisation method was applied to the 50 independently measured force signals during the experiment to account for possible noise and non-linearities of the load pins. The six global equilibrium conditions served as equality constraints. The three force and moment resultants were calculated accounting for the displaced yoke positions, i. e. using the actuator stroke and the corresponding direction vector calculated by the LUSET control system.

Notation

$A_{gt} = \varepsilon\left(f_{u,dyn}\right)$	Strain at steel tensile strength
$A_s, A_{s,lost}$	Reinforcing bar cross-sectional area, lost cross-sectional area
E_s	Young's modulus of reinforcing steel
EI, EI^I, EI^{II}, EI^y	Bending stiffness of wall cross-section (in general, uncracked, cracked, at yielding of reinforcement)
I_x	Second moment of inertia of reinforcing bar cross-section
K_0, K_{ah}, $\overline{K}$	Earth pressure coefficients (at rest $K_0 = 1 - \sin\varphi$, Coulomb's horizontal earth pressure coefficient, mean coefficient $\overline{K} = (K_0 + K_{ah})/2$)
M, M_{eff}, M_{exp}	Bending moment (in general, of simulated wall, of specimen)
M_j, $M_{j,u}$	Bending moment at construction joint (in general, maximum)
M_{top}	Bending moment at specimen head
M_{cr}, M_y	Cracking moment and yield moment of specimen cross-section
M_s	Local bending moment in reinforcing bar near corrosion pit
N_s	Normal force in reinforcing bar
N_{top}	Normal force at specimen head
R_{mill}	Mill radius
V, V_{eff}, V_{exp}	Shear force (in general, in simulated wall, in specimen)
V_{top}	Shear force at specimen head
V_s	Shear force in reinforcing bar
a_s	Reinforcement cross-sectional area per unit length
b	Specimen width
f_{cc}, f_c, f_{ct}	Concrete compressive strength (cube and cylinder), concrete tensile strength
$f_{y,stat}$, $f_{y,dyn}$, f_{yd}	Steel yield stress (static, dynamic, design value)
$f_{u,stat}$, $f_{u,dyn}$	Steel tensile strength (static, dynamic)
h, h_{eff}	Wall height above footing (specimen, simulated wall or existing wall (parametric study))
m_{Ed}, m_{Rd}	Design bending moment and bending resistance of retaining wall
n_c, n_{tot}	Number of damaged reinforcing bars in specimen, total number of reinforcing bars in specimen (of equal diameter)
q, q_{eff}	Distributed load (earth pressure): value above footing, distribution along z-axis of simulated wall
q_s	Bearing pressure acting laterally on reinforcing bar
s	Bar spacing
t_{foot}, t_{inf}	Thickness of footing, of wall/specimen above footing
t_p	Penetration depth of mill
v, v_{eff}, v_{exp}	Displacement (in general, of simulated wall, of specimen)
v_{top}, $v_{top,u}$	Displacement of specimen head (in general, maximum)
w_{cr}	Crack width
w_{foot}	Width of footing
z	Coordinate axis or lever arm of internal forces
z_{cr}, $z_{cr,eff}$, $z_{cr,exp}$	Height where bending moment equals cracking moment (in general, simulated wall, specimen)
α_{cr}, α_y	Bending stiffness factors $\alpha_{cr} = EI^{II}/EI^I$, $\alpha_y = EI^y/EI^I$
γ_{soil}, γ_c	Specific weight: of soil, of concrete
γ_q	Partial safety factor for load
δ	Wall friction angle
ε_s, $\varepsilon_{s,pl}$	Steel strain (in general, plastic amount $\varepsilon_{s,pl} = \varepsilon_s - \sigma_s/E_s$)
$\rho = a_s/t_{inf}$	Reinforcement ratio at wall base
σ_s, $\sigma_{s,uc}$	Steel stress (in general, of undamaged bars)
τ_b	Bond shear stress
φ	Internal angle of friction of soil
ζ_i, ζ_m	Individual relative cross-section loss per reinforcing bar, mean relative cross-section loss per specimen
Ø	Reinforcing bar diameter

7 Modelling the load-deformation behaviour of lap splices with the Tension Chord Model

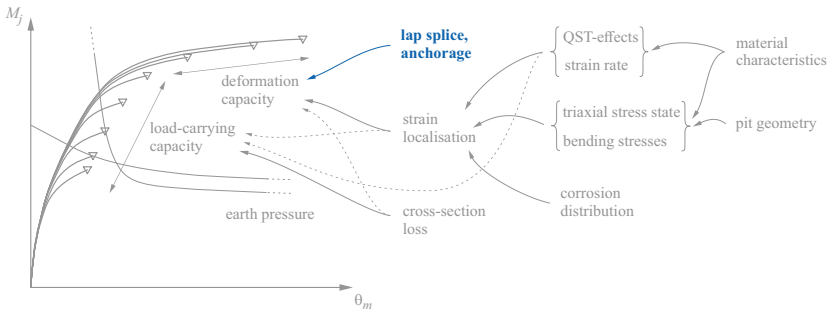

This chapter presents the findings of a theoretical study on the load-deformation behaviour of lap splices with an adapted version of the Tension Chord Model (TCM). It revealed that lap splices considerably decrease the deformation capacity of a reinforced concrete member at their location and that the deformation localises in the boundary cracks. The chapter corresponds to the published version of the following article:

> Haefliger, S., Kaufmann, W., Thoma, K. 'Modelling the load-deformation behaviour of lap splices with the Tension Chord Model,' *Engineering Structures*, vol. 252, p. 113606, 2022. doi: 10.1016/j.engstruct.2021.113606.

The lead author (Severin Haefliger) derived the theoretical fundamentals of the adapted TCM, conducted the parametric study, and validated the model against available experimental data, under the supervision of the second and the third author (Walter Kaufmann, Karel Thoma). The third author prepared the presented figures based on the drafts of the first author.

Abstract

Lap splices are part of virtually every structure made of reinforced concrete. As loads need to be transferred safely along these discontinuities, numerous studies focused on their strength. However, even though they are traditionally placed also in highly loaded regions of elements, which are potentially undergoing plastic deformations, little attention has been paid to their load-deformation behaviour and deformation capacity. This study presents a sound mechanical model based on the established Tension Chord Model to assess the load-deformation behaviour of lap splices. A thorough analysis of the load transfer mechanism reveals that the major part of the load is transferred at the beginning and the end of a lap splice. Therefore, the lap splice acts as a double-reinforced tensile element over a considerable length, which drastically reduces its deformation capacity to less than half of the minimum value expected for adjacent parts. This especially needs to be addressed in performance-based design methods, where the deformation demand is compared to the existing deformation capacity. The theoretical results are validated with a recently conducted experimental campaign, exhibiting excellent agreement between the model and the experimental data. Besides a comprehensive analysis of the influencing parameters, a simplified modelling approach for practical applications and design recommendations for new structures are presented in this publication.

7.1 Introduction

Lap splices are an indispensable element of reinforced concrete structures, as it is typically impossible to place the entire reinforcement as continuous bars. In the past, the primary objective was to reliably prevent a failure of the load transfer between the spliced bars. Consequently, research in this field has mainly focused on characterising the strength of lap splices and their safe design under various conditions (see, e. g. [44, 48, 68, 118]). However, deformation capacity and its distribution along the structure's elements is paramount for assessing existing structures, where load redistributions have to be considered, and the design of new structures using capacity design, such as, e. g. performance-based design in earthquake engineering, where the deformation demand is compared to the existing deformation capacity. As lap splices induce a discontinuity in the reinforcement layout, information on their load-deformation behaviour is of high importance to answer questions related to the deformation capacity of an element. However, this topic has only been treated scarcely in experimental and theoretical research over the last decades.

Almeida et al. [3] and Tarquini et al. [154] elaborated a comprehensive literature review on theoretical and experimental investigations on lap splices. They concluded that there are many studies regarding the strength of lap splices, but only a few studies investigated their inelastic behaviour and deformation capacity. Presumably, this knowledge gap led to modern code specifications, prohibiting lap splices in regions where plastic hinges are expected (e. g. above the supports of continuous bridges) [3]. However, efficient construction processes favour locating lap splices in highly loaded zones, potentially undergoing plastic deformations. Examples are cantilever retaining walls, where the reinforcement is commonly spliced just above the construction joint between footing and wall, or monolithically connected bridge piers, where lap splices can typically be found at the joints between foundation and pier, and between pier and bridge deck. These zones should provide sufficient ductility in both cases, as either the loading depends on the deformation (earth pressure for retaining walls) or as rotation capacity is needed in performance-based design (earthquake loading for bridges).

The knowledge gap regarding the load-deformation behaviour of lap splices was lately addressed by Tarquini et al., who analysed the problem experimentally [153, 154] with uniaxial cyclic tension and compression tests, as well as theoretically [152, 155] with Shell Element Simulations and using some aspects of the established Tension Chord Model [7, 114]. Their experiments aimed at investigating the influence of lap splice length, confining reinforcement and loading history on the deformation capacity of lap splices. They pointed out the importance of sufficient confinement of the longitudinal reinforcement, which besides the lap splice length, governed the behaviour. The load-deformation behaviour was numerically modelled using some aspects of the Tension Chord Model [155] but neglecting the tension stiffening effect. An empirical formulation was proposed to predict the ultimate deformation at failure, induced in most specimens by concrete splitting and a subsequent loss of bond [154].

In this paper, a mechanically sound approach is presented, which allows predicting the load-deformation behaviour of lap splices based on the concepts of the Tension Chord Model (TCM), including the tension stiffening effect. After revisiting the theory of the established TCM, the influence of a discontinuity in the reinforcement layout on the crack spacing is analysed. A set of equations based on equilibrium and kinematic conditions is derived to predict the deformation of a lap splice under a given tensile load. The model is validated using the experimental results of Tarquini et al. [153]. A comprehensive parameter variation reveals the influence of lap splice length, reinforcing bar diameter, reinforcement ratio, and concrete compressive strength. Based on the findings, a simplified modelling approach and design recommendations are deduced.

7.2 The established Tension Chord Model TCM

The characterisation of the force transfer between reinforcement and concrete, commonly referred to as bond, is highly challenging, which is reflected by the variety and scatter of proposed bond shear stress-

slip relationships (see, e. g. [33, 49, 56, 143]). The established Tension Chord Model (TCM) used in this paper circumvents the problem of accurately describing the relationship between bond shear stresses and slip by shifting the focus from the level of a differential element on the reinforcing bar to the structural level and its related parameters. This is possible by upscaling the reference length (for bond problems, this is approximately the bar diameter; for the TCM, this is the crack spacing, i. e. the distance between adjacent cracks, see Figure 7.1), and the fact, that the structurally relevant parameters, e. g. crack width and elongation, are obtained by integrating local strains over this reference length. Furthermore, as outlined below, the local bond shear stresses correspond to the derivative of the stresses in reinforcement and concrete, respectively. Hence, crack widths and elongations are related to the bond shear stresses by two integration steps. Mathematically, these integrations correspond to the calculation of the initial function mean values $\overline{f(x)}\big|_a^b = \int_a^b f(x)dx/(b-a)$. As only the integral $F = \int_a^b f(x)dx = \overline{f(x)}\big|_a^b(b-a)$ is of interest, knowing the initial function mean value $\overline{f(x)}\big|_a^b$ is sufficient, while the initial function's shape, i. e. moderate variations of strains and local bond shear stresses, are unimportant. This justifies the assumption of mean bond shear stresses for analysing the structural behaviour. While this simplification predicts the behaviour on a structural level very well, it clearly cannot be used for investigating the local bond behaviour (which is beyond the scope of this paper, as well as of the TCM).

With a stepped rigid-perfectly plastic bond stress-slip relationship, which relates the magnitude of bond shear stresses to the steel stresses (rather than to the slip), the TCM allows decoupling the kinematic relationships from the equilibrium of forces. The differential equation of bond can therefore be solved analytically. Hence, while reliably predicting the relevant output parameters on the structural level (element elongation, crack width, crack pattern), the calculation of deformations of a structural element in tension is greatly simplified and computationally much more efficient, making the model suitable for implementation in large-scale NLFE codes. First established by Marti et al. for tension chords [7, 114], the model was enhanced and comprehensively validated against experimental results by Kaufmann for membranes [22, 89] (known as Cracked Membrane Model CMM), by Kenel for bending elements [93], by Pfyl and Markic for fibre reinforced concrete [111, 126], by Burns for investigating the Service Limit State [29], and by Haefliger for corroded elements [72, 77]. The implementation of a constitutive relationship for reinforced concrete based on the TCM and CMM for nonlinear finite element analysis is presented by Thoma [156].

The original TCM describes a tension element of a composite material consisting of a single reinforcing bar and surrounding concrete, which is longitudinally divided into crack elements (CE) of length s_r, i. e. sections between two cracks (see Figure 7.1). Each CE combines the distinct load-deformation behaviour of reinforcing steel and concrete, coupled by bond, and therefore represents the load-deformation behaviour of the composed material, including the tension stiffening effect. The CE thus defines the basic module of the TCM, separated by two cracks, where the reinforcing bar alone transmits the applied load.

In a CE, bond stresses are defined as τ_{b0} for regions where the reinforcing bar is elastic, and τ_{b1} where the reinforcing bar yields, i. e. $\sigma_s(x) \geq f_{sy}$, with the following values proposed by [7, 114, 146]

$$\begin{aligned} \tau_{b0} &= 2f_{ct} \\ \tau_{b1} &= \tau_{b0}/2 = f_{ct} \end{aligned} \tag{7.1}$$

where f_{ct} denotes the concrete tensile strength. Note that for rigid bond (no slip), $0 \leq \tau_b \leq \tau_{b0}$ according to the rigid-perfectly plastic bond shear stress-slip relationship of the TCM. With the steel stress at the crack σ_{sr} – where the reinforcing bar transmits the external load F solely –, steel stresses $\sigma_s(x)$ in the CE evolve with the constant gradient (without calculating the corresponding local slip).

$$\begin{aligned} \sigma_{sr} &= F/A_s \\ \sigma_s(x+dx) - \sigma_s(x) &= 4\tau_b/\text{Ø} \end{aligned} \tag{7.2}$$

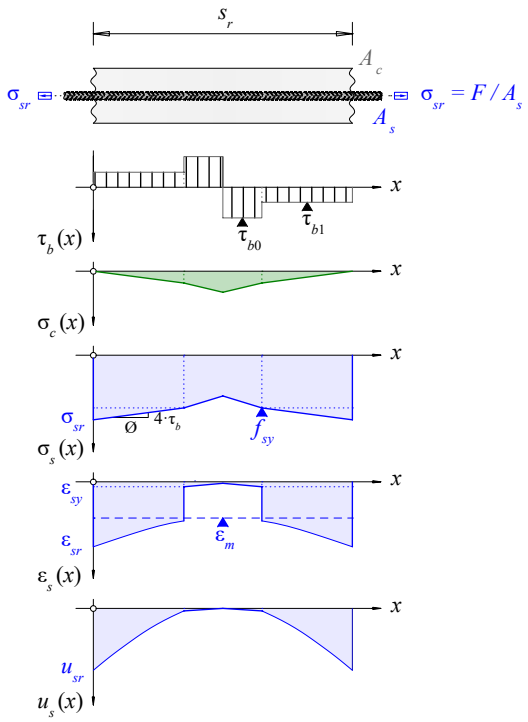

Fig. 7.1 – Crack element (CE) of length s_r and cross-sectional area A_c with reinforcing bar (cross-sectional area A_s) and external load F. Further indicated are the distribution of bond-stress $\tau_b(x)$, stress in concrete $\sigma_c(x)$, steel stresses $\sigma_s(x)$, steel strains $\varepsilon_s(x)$, and the elongation of the reinforcing bar $u_s(x)$ along the element. Index r denotes the value of the corresponding variable at the crack (e. g. σ_{sr} = steel stress at the crack), and ε_m denotes the mean strain of the entire CE.

with Ø = reinforcing bar diameter. Concrete stresses $\sigma_c(x)$ can be derived using the geometrical reinforcement ratio ρ

$$\sigma_c(x) = \frac{4\tau_{b0}\rho x}{\varnothing(1-\rho)} \qquad \rho = \rho_s = A_s/A_c \tag{7.3}$$

with A_s = cross-sectional area of reinforcing bar, A_c = cross-sectional area of tensile member (including A_s)[1]. Steel strains $\varepsilon_s(x) = f(\sigma_s(x))$ follow directly from the steel stress by using the stress-strain relationship of the bare reinforcement. Integrating the steel strains along the bar's axis yields the elongation of the reinforcing bar $u_s(x)$. By subtracting the concrete deformation $u_c(x)$, one gets the bond slip $\delta(x) = u_s(x) - u_c(x)$, from which the crack width w_r follows by integrating the bond slip over half the length of CEs at either side of the crack. Thereby, the concrete deformation is often neglected as it is one order of magnitude smaller than the elongation of the reinforcing bar. Hence, the contribution of a CE to the crack width is given by

$$w_r/2 = u_s(x = s_r/2) - u_c(x = s_r/2) \approx u_s(x = s_r/2) \tag{7.4}$$

corresponding to half the total crack width in case of equal CEs on either side of the crack. Dividing the total elongation by the original length of the CE, one gets the mean tensile strain

$$\varepsilon_m = \frac{w_r}{s_r} = \frac{2u_s(x = s_r/2)}{s_r} \tag{7.5}$$

[1]The published article contains an error in the equation for the concrete stresses $\sigma_c(x)$ (numerator and denominator are reversed). Equation (7.3) was corrected accordingly.

This strain represents the deformation of the CE and therefore allows deriving the deformation of a tension element, taking into account tension stiffening. With the decoupling of the kinematic relations from the equilibrium of forces, closed-form analytical expressions for the mean tensile strain as a function of the applied tensile load can be derived for common steel stress-strain relationships, see, e. g. [7] and [72].

Evaluating the TCM at the cracking load allows determining the crack spacing, i. e. the CE length. At the maximum theoretically possible crack spacing $s_{r,max}^{\mathrm{TCM}}$, the concrete stress in the middle of the CE just reaches the tensile strength, i. e. $\sigma_c(s_r/2) = f_{ct}$ in Equation (7.3), without forming an additional crack [114] (see Figure 7.1):

$$s_{r,max}^{\mathrm{TCM}} = \frac{f_{ct} \varnothing (1-\rho)}{2\tau_{b0}\rho} \tag{7.6}$$

Consequently, the minimum crack spacing is $s_{r,max}^{\mathrm{TCM}}/2$, representing the case where an additional crack forms in the middle of the CE. The actual crack distance can reach any value between these boundaries and cannot be theoretically determined. However, in experiments, the observed crack spacing often equals the distance between local discontinuities, e. g. stirrup spacing. Furthermore, statistical considerations suggest that the mean crack spacing adopts a value of approximately $0.67 s_{r,max}^{\mathrm{TCM}}$ [23, 79, 91, 117]. Hence, in the TCM, the mean crack spacing s_r is defined by

$$\begin{aligned} s_r &= \lambda \cdot s_{r,max}^{\mathrm{TCM}} \\ \lambda &\in [0.5, 1] \end{aligned} \tag{7.7}$$

Similar to the derivation of the crack spacing, the cracking load in terms of the stress at the crack is given by [114]

$$\sigma_{sr,cr}^{\mathrm{TCM}} = \frac{f_{ct}}{\rho}(1 + \rho(n-1)) \tag{7.8}$$

with $n = E_s/E_c$ representing the ratio of Young's moduli of steel and concrete. Because of the assumed constant concrete tensile strength f_{ct}, in load control (no drop of applied load at cracking) the crack pattern establishes at once and remains unchanged. The concrete stresses remain constant with increasing load, and only the steel stresses (and strains) increase proportionally.

7.3 TCM applied to lap splices - model description

To investigate the lap splice load-deformation behaviour, the basic principles of the TCM are applied to CEs containing two reinforcing bars. Figure 7.2 shows the first part of a lap splice consisting of a series of k CEs of length s_r^j, where Reinforcing Bar 1 introduces the load F into the lap splice. The load-free end of Reinforcing Bar 2 is located at a distance x_0 within the first CE. The two reinforcing bars share the force $F_1 + F_2 = F$ at the cracks, and bond stresses (τ_{b0} and τ_{b1}, respectively) lead to continuous unloading of the bars inside the CE, i. e. the steel stresses decrease towards the middle of the CE. In contrast to the original TCM, the location of the minimum steel stresses is not located at $x^j = s_r^j/2$ but can be anywhere inside the element, and is generally different for the two reinforcing bars. This leads to a persisting force increase or reduction of the corresponding reinforcing bar. Given the load F, the number of CEs k, and their length s_r^j, the resulting set of $2k$ unknowns for x_1^j and x_2^j, $j = 1...k$ for Reinforcing Bars 1 and 2 describes the stress state in the lap splice. Equilibrium of forces and compatibility of deformations at

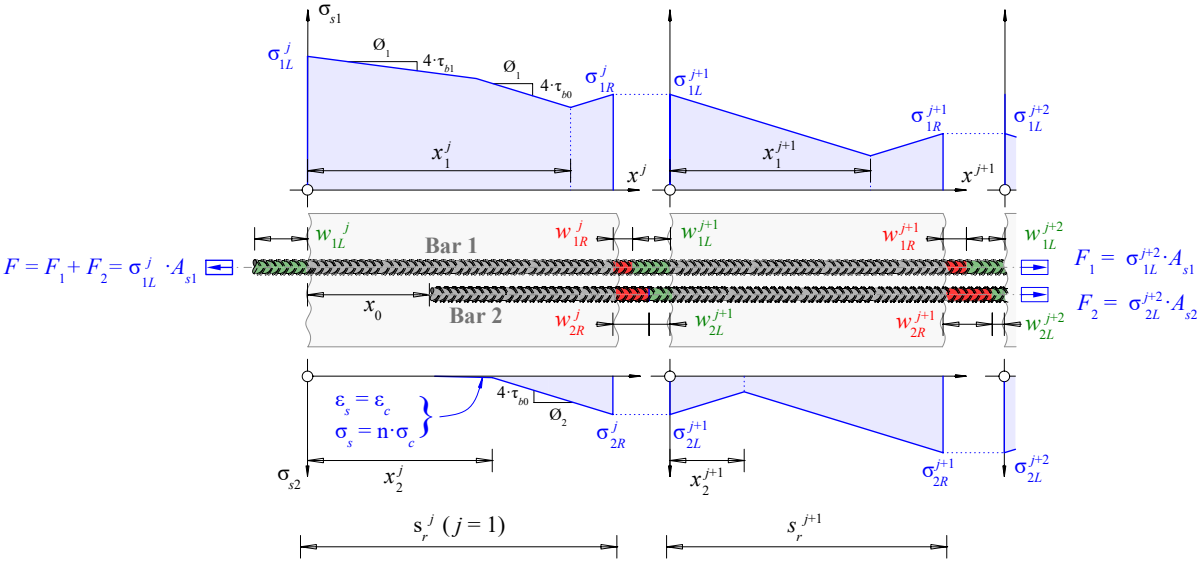

Fig. 7.2 – First part of a lap splice consisting of a series of k CEs of distinct length s_r^j. Bar 1 is spliced by Bar 2, whose end is located at a distance x_0 inside the first CE. Bar 1 introduces the total load F, which is then distributed among the two reinforcing bars. Indicated are the stress distribution of the two reinforcing bars, $\sigma_{s1}(x)$ for Bar 1 and $\sigma_{s2}(x)$ for Bar 2, and the contribution of the different parts of the reinforcement to the crack widths (in red, the contribution of CE j to a specific crack, and in green, the contribution of CE $j+1$, respectively).

each crack, neglecting concrete deformations, yield $2k-2$ equations (see Figure 7.2 for notation)

$$\begin{aligned} &A_{s1}\sigma_{1L}^j + A_{s2}\sigma_{2L}^j = A_{s1}\sigma_{1R}^j = A_{s2}\sigma_{2R}^j = F \\ &w_{1R}^j + w_{1L}^{j+1} = w_{2R}^j + w_{2L}^{j+1} \end{aligned} \tag{7.9}$$

$$\begin{aligned} w_{1L}^j &= \int_0^{x_1^j} \varepsilon_{s1}(x^j)dx^j \quad \text{and} \quad w_{1R}^j = \int_{x_1^j}^{s_r^j} \varepsilon_{s1}(x^j)dx^j \\ w_{2L}^j &= \int_0^{x_2^j} \varepsilon_{s2}(x^j)dx^j \quad \text{and} \quad w_{2R}^j = \int_{x_2^j}^{s_r^j} \varepsilon_{s2}(x^j)dx^j \end{aligned} \tag{7.10}$$

with $\sigma_{1R}^j = \sigma_{1L}^{j+1}$ and $\sigma_{2R}^j = \sigma_{2L}^{j+1}$, and $w_{2L}^{j=1} = w_{1R}^{j=k} = 0$. The boundary conditions at both ends of the lap splice deliver two additional equations

$$\begin{aligned} \sigma_{1L}^{j=1} &= F/A_{s1} & \sigma_{2L}^{j=1} &= 0 \\ \sigma_{1R}^{j=k} &= 0 & \sigma_{2R}^{j=k} &= F/A_{s2} \end{aligned} \tag{7.11}$$

The length s_r^j of every CE will generally be different. For equal reinforcing bar diameter and symmetric configurations of CEs with respect to the central vertical axis of the lap splice, it is sufficient to evaluate only one half of the entire lap splice, with the second boundary condition in Equation (7.11) changing to

$$\begin{aligned} \sigma_{1R}^{j=k/2} &= \sigma_{2R}^{j=k/2} && \text{if } k \text{ is even} \\ \sigma_{1R}^{j=(k+1)/2} &= \sigma_{2L}^{j=(k+1)/2} && \text{if } k \text{ is odd} \end{aligned} \tag{7.12}$$

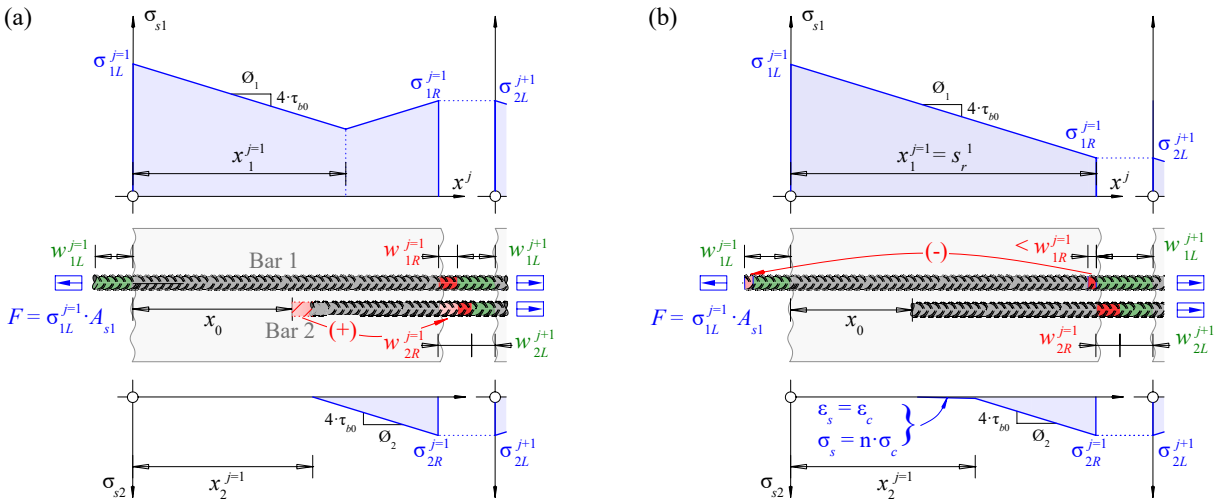

Fig. 7.3 – Slipping bond in the boundary element in case of a short embedment length of Reinforcing Bar 2 or at high load for Reinforcing Bar 1: (a) pull-out of Reinforcing Bar 2 and (b) pull-through of Reinforcing Bar 1.

The set of $2k$ equations can be solved for any external load F between cracking load and reinforcement rupture, i. e. $A_s \sigma_{sr,cr} \leq F \leq A_s f_{su}$ with f_{su} = reinforcement tensile strength. Due to the coupling of several CEs, the nonlinear system of equations can only be solved numerically. However, for the elastic range $F \leq A_s f_{sy}$, the convergence of the solving algorithm is much faster, as bond stresses are always $\tau_b = \tau_{b0}$ and the steel strains depend linearly on the corresponding stresses. This accelerates the integration to derive the deformations.

Depending on the bar diameter and the CE length, Bar 2 may experience slipping bond over the entire embedded length in the first CE, i. e. $x_2^{j=1} = x_0$, as illustrated in Figure 7.3(a). This happens if Bar 2 has a short embedment length in the first CE, and may as well occur at loads lower than the ultimate load $F_u < A_s f_{su}$. If the load is further increased, the unloaded end of Bar 2 experiences slip, and the compatibility condition of Equation (7.9) is thus no longer valid. Solutions for the system of equations at increasing loads can be found by abolishing this compatibility condition and instead setting $x_2^{j=1} = x_0$ for all further load steps. This implies that the steel stresses of Bar 2 are known and remain constant for all further load steps. Hence, Bar 2 is pulled out of the CE. The deformation $w_{2R}^{j=1}$ now consists of the elongation of Bar 2 due to the applied force and the end slip of Bar 2 inside the CE (indicated in Figure 7.3(a) in dark and light red, respectively). It can be determined from the compatibility condition $w_{2R}^{j} = w_{1R}^{j} + w_{1L}^{j+1} - w_{2L}^{j+1}$.

Similarly, Bar 1 may experience slipping bond over its entire embedded length in the first CE (with bond stresses acting in the same direction), or even in one of the subsequent CEs if they are short. In this case, the location of minimum stress in Bar 1 reaches the boundary of the CE, i. e. $x_1^{j} = s_r^{j}$, see Figure 7.3(b). Analogously to the case of a pull-out of Bar 2, the compatibility condition of Equation (7.9) no longer applies. Solutions for increasing load can be found by replacing this compatibility condition with $x_1^{j} = s_r^{j}$. This implies that the steel stress difference in Bar 1 between the cracks for all further load steps is given by $\sigma_{1L}^{j} - \sigma_{1R}^{j} = 4\tau_b s_r^{j} / \varnothing_1$ (note that the absolute stresses σ_{1L}^{j} and σ_{1R}^{j} can still increase), and that Bar 1 is pulled through the CE. The deformation w_{1R}^{j} can be determined from the compatibility condition $w_{1R}^{j} = w_{2R}^{j} + w_{2L}^{j+1} - w_{1L}^{j+1}$ and adopts a negative value indicating the dislocation of Bar 1; w_{1R}^{j} subsequently has to be added to the deformation w_{1L}^{j} at the other side of the CE. In combination with a drop in bond stress due to the yielding of Bar 1 (from τ_{b0} to τ_{b1}), the steel stress difference $\sigma_{1L}^{j} - \sigma_{1R}^{j}$ will decrease, which leads to an unloading of Bar 2 (by equilibrium, e. g. for the boundary CE $A_{s2}\sigma_{2R}^{j=1} = A_{s1}(\sigma_{1L}^{j=1} - \sigma_{1R}^{j=1})$). This is captured approximately by setting $w_{2R}^{j} = \text{const.}$ for all further load steps.

7.4 Length of crack elements and cracking load

The modelling approach outlined in Section 7.3 allows analysing members where two reinforcing bars of distinct diameters $\varnothing_1$ and $\varnothing_2$ overlap (reinforcement staggering). Lap splices represent a special case of reinforcement staggering, as the bars are of the same diameter $\varnothing_1 = \varnothing_2$. While this study focuses on this special case, the equations in this section are written in general form, using the diameter ratio $\eta = \varnothing_1/\varnothing_2$.

Generally, just as in the conventional TCM, the maximum CE length $s^j_{r,max}$, i. e. the maximum distance between two cracks, is defined as the length for which the maximum concrete stress just reaches the tensile strength f_{ct}, and the minimum steel stress of Bar 1 is thus $n \cdot f_{ct}$, where $n = E_s/E_c$ is the modular ratio (equal for both reinforcing bars, $E_{s1} = E_{s2} = E_s$):

$$\begin{aligned} &\max(\sigma_c(x)) = f_{ct} \\ &\min(\sigma^j_{s1}(x)) = n \cdot f_{ct} \end{aligned} \tag{7.13}$$

The second condition implies that concrete and reinforcing Bar 1 exhibit equal strains $\varepsilon_s = \varepsilon_c$ in this point at cracking. The cracking load is the corresponding external load to reach this stress state. The minimum CE length $s^j_{r,min}$ is the distance between a given crack and the location of maximum concrete stress, implying that another crack may form at this point.

To simplify the equations following in this section, the net cross-sectional area of concrete is defined as

$$A_{c,net} = A_c - A_{s1} - A_{s2} = \frac{A_c}{\eta^2}\left(\eta^2 - \rho(\eta^2+1)\right) \tag{7.14}$$

with $\rho = A_{s1}/A_c$.

7.4.1 Inner crack elements

To determine the minimum and maximum length of a CE laying inside the lap splice, the stress distribution for the two reinforcing bars and the surrounding concrete is assumed as shown in Figure 7.4. The length x^j_2 indicates the distance between the crack and the point where Bar 2 is in rigid bond and exhibits the same strain as the concrete, i. e. $\varepsilon_c = \varepsilon_{s2}$. According to Equation (7.13), the minimum CE length $s^{IE}_{r,min}$ extends from the crack to the point, where the concrete stress equals its tensile strength f_{ct}, and the steel stress in Bar 1 equals $\sigma_{s1} = n \cdot f_{ct}$. Formulating equilibrium at this section and deformation compatibility at the crack, one gets the minimum CE length and the steel stresses at cracking:

$$\begin{aligned} s^{IE}_{r,min} &= \frac{f_{ct}\varnothing_1}{4\tau_{b0}\rho}\frac{\eta^3\left(\eta^2+\rho(n-1-\eta^2)\right)\left(\eta^2-\rho(\eta^2+1)\right)\psi}{(\eta+1)\left(\eta^2+\rho(n-1-\eta^2)\right)+\eta(\psi-1)\left(\eta^2-\rho(\eta^2+1)\right)} \\ \psi &= \sqrt{\frac{\eta\left(\eta^2+\rho\left(n(\eta+1)-\eta^2-1\right)\right)}{\eta^2+\rho(n-1)(\eta^2+1)}} \end{aligned} \tag{7.15}$$

$$\begin{aligned} \sigma^{IE}_{1L,cr} &= \frac{f_{ct}}{\rho}\frac{\eta^3\left(\eta^2+\rho(n-1-\eta^2)\right)\left(\eta^2-\rho(\eta^2+1)\right)\psi}{(\eta+1)\left(\eta^2+\rho(n-1-\eta^2)\right)+\eta(\psi-1)\left(\eta^2-\rho(\eta^2+1)\right)} + n\rho \\ \sigma^{IE}_{2L,cr} &= \frac{f_{ct}}{\rho}\frac{\left(\eta^2+\rho\left(n(\eta+1)-\eta^2-1\right)\right)\left(\eta^2+\rho(n-1-\eta^2)\right)}{(\eta+1)\left(\eta^2+\rho(n-1-\eta^2)\right)+\eta(\psi-1)\left(\eta^2-\rho(\eta^2+1)\right)} \end{aligned} \tag{7.16}$$

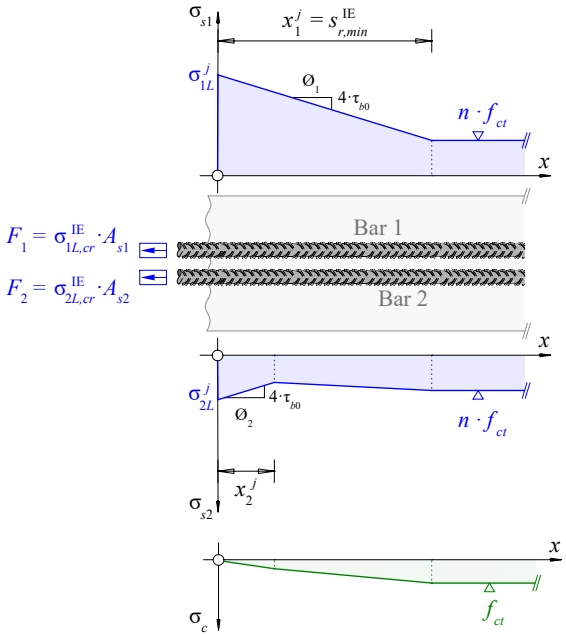

Fig. 7.4 – Stress distribution for both reinforcing bars $\sigma_{s1}(x)$ and $\sigma_{s2}(x)$, and for the surrounding concrete $\sigma_c(x)$ at cracking for a CE inside the lap splice.

Equations (7.15) and (7.16) were first derived by Alvarez [7] for the general case of mixed passive and prestressed reinforcement. The cracking load follows by simply multiplying the steel stresses given by Equation (7.16) with the respective cross-sectional areas of the reinforcing bars. Due to symmetry in the elastic loading range, the maximum CE length is

$$s_{r,max}^{IE} = 2s_{r,min}^{IE} \tag{7.17}$$

For $\eta = 1$, Equation (7.15) yields a CE length equal to the one from the original TCM with double the reinforcement ratio $\rho = 2\rho_s$

$$s_{r,min}^{IE}(\eta = 1) = s_{r,min}^{\mathrm{TCM}}(\rho = 2\rho_s) = \frac{f_{ct}\emptyset(1-2\rho)}{4\tau_{b0}2\rho} \tag{7.18}$$

and the cracking load of Equation (7.16) simplifies to

$$\sigma_{1L,cr}^{IE}(\eta = 1) = \sigma_{2L,cr}^{IE}(\eta = 1) = \frac{f_{ct}}{\rho}\frac{\left(1+2\rho(n-1)\right)}{2} \tag{7.19}$$

7.4.2 Boundary crack elements

To determine the minimum and maximum length of the boundary CE – the first CE inside which the reinforcing bars overlap –, two cases have to be distinguished: Case I, where the stress $\sigma_{s2} = n \cdot \sigma_c$ in Bar 2 is reached to the left of x_1^{I} = the location of the minimum stress $\sigma_{s1} = n \cdot f_{ct}$ in Bar 1 (Figure 7.5), i. e. $x_0 + x_{2a} < x_1^{\mathrm{I}}$, and Case II, where $x_0 + x_{2a} \geq x_1^{\mathrm{I}}$ (Figure 7.6).

Case I

Figures 7.5(a) and (b) illustrate the stress states of both reinforcing bars and the concrete stresses in the first part of the CE for Case I, directly after the crack to the left of the splice has occurred. The distance between the crack and the location of maximum concrete stress (and minimum steel stress in Bar 1) is

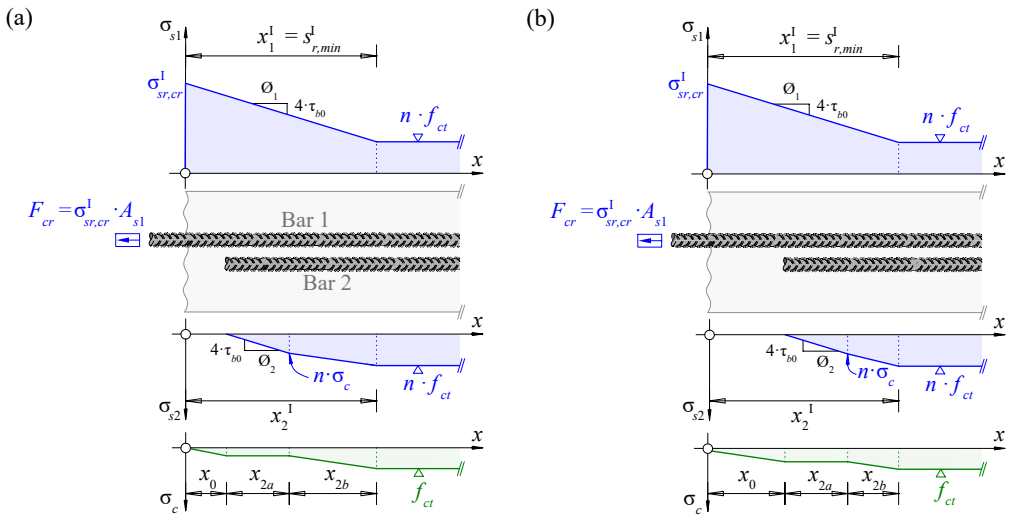

Fig. 7.5 – Stress distribution in Case I for both reinforcing bars $\sigma_{s1}(x)$ and $\sigma_{s2}(x)$, and for the surrounding concrete $\sigma_c(x)$ in a boundary element at cracking, with a crack occurring to the left of Bar 2, so that $x_0 + x_{2a} < x_1^{\mathrm{I}}$. (a) stress state for small $x_0 < x_{2a} + x_{2b}$; (b) stress state for increasing x_0 and $x_{2b} \to 0$.

defined by x_1^{I}. According to Equation (7.13), both reinforcing bars and the concrete are in rigid bond to the right of this location and exhibit the same strains $\varepsilon_c = \varepsilon_{s1} = \varepsilon_{s2}$, and hence, $\sigma_{s1} = \sigma_{s2} = n \cdot \sigma_c$. The stress in Bar 2 develops over the length $x_{2a} + x_{2b}$, separated into two sections x_{2a} and x_{2b}, with slipping and rigid bond, respectively. Note that bond slip in Section x_{2a} is caused by concrete displacements (relative to Bar 2) to the left, caused by the tensile concrete stresses induced by Bar 1, and that $0 \leq \tau_b \leq \tau_{b0}$ in Section x_{2b} (with rigid bond) due to the assumed rigid-perfectly plastic bond shear stress-slip relationship. With increasing distance x_0, the section x_{2b} decreases as shown in Figure 7.5(b) until at $x_{2b} \to 0$ the application boundary of Case I reached, i. e. $x_0 + x_{2a} = x_1^{\mathrm{I}}$.

Formulating equilibrium on the part delimited by the crack and the location of maximum concrete stress yields the minimum CE length $s_{r,min}^{\mathrm{I}}$ and the cracking load, as a function of the stress $\sigma_{sr,cr}^{\mathrm{I}}$ of Bar 1 at the crack:

$$\begin{aligned} \sigma_{sr,cr}^{\mathrm{I}} A_{s1} &= \left(\sigma_{sr,cr}^{\mathrm{I}} - \frac{4\tau_{b0} x_1^{\mathrm{I}}}{\varnothing_1}\right) A_{s1} + f_{ct}\left(A_{c,net} + n A_{s2}\right) \\ \Rightarrow s_{r,min}^{\mathrm{I}} &= x_1^{\mathrm{I}} = \left(1 - \rho + \frac{\rho(n-1)}{\eta^2}\right) \frac{f_{ct} \varnothing_1}{4\tau_{b0}\rho} \end{aligned} \tag{7.20}$$

$$\sigma_{sr,cr}^{\mathrm{I}} = \frac{f_{ct}}{\rho}\left(1 + \rho(n-1)\left(1 + \frac{1}{\eta^2}\right)\right) \tag{7.21}$$

The maximum boundary CE length is obtained if no crack forms between the CE of Figure 7.5 and the adjoining inner CE shown in Figure 7.4 (mirrored). The sum of the minimum lengths of these two elements (Equations (7.18) and (7.20)) equals the maximum length of the boundary CE:

$$s_{r,max}^{\mathrm{I}} = s_{r,min}^{\mathrm{I}} + s_{r,min}^{IE} \tag{7.22}$$

As observed from Equations (7.20) to (7.22), the distance x_0 does not influence the CE length. With Equation (7.20), the application limits for Case I can be written as

$$\begin{aligned} 0 &\leq x_0 < s_{r,min}^{\mathrm{I}} - x_{2a} \\ 0 &\leq x_0 < \left(\eta^2 - \rho\left(\eta^2 + 1 + n(1-\eta)\right)\right) \frac{f_{ct} \varnothing_1}{4\tau_{b0}\rho\eta^2} \end{aligned} \tag{7.23}$$

Tab. 7.1 – Equations for maximum and minimum CE length, $s_{r,min}$ and $s_{r,max}$, and cracking load $\sigma_{sr,cr}$ for a boundary element according to Equations (7.20) to (7.29) and $\eta = 1$.

	original TCM	Case I	Case II [1)]
application limits	-	$0 \le x_0 \le \frac{f_{ct}\varnothing}{4\tau_{b0}\rho}(1-2\rho)$	$\frac{f'_{ct}\varnothing}{4\tau_{b0}\rho}(1-2\rho) \le x_0 \le \frac{f'_{ct}\varnothing}{2\tau_{b0}\rho}(1-2\rho)$
$s_{r,min}$	$\frac{f_{ct}\varnothing}{4\tau_{b0}\rho}(1-\rho)$	$\frac{f_{ct}\varnothing}{4\tau_{b0}\rho}(1+\rho(n-2))$ $= \frac{f_{ct}\varnothing}{4\tau_{b0}\rho}(1-2\rho) + \frac{nf_{ct}\varnothing}{4\tau_{b0}}$	x_0, otherwise Case I applies (even if $f'_{ct} < f_{ct}$)
$s_{r,max}$	$2\frac{f_{ct}\varnothing}{4\tau_{b0}\rho}(1-\rho)$	$s^{\mathrm{I}}_{r,min} + s^{\mathrm{TCM}}_{r,min}(\rho = 2\rho_s)$ $= \frac{3}{2}\frac{f_{ct}\varnothing}{4\tau_{b0}\rho}(1-2\rho) + \frac{nf_{ct}\varnothing}{4\tau_{b0}}$	$s^{\mathrm{TCM}}_{r,min} + \frac{x_0}{2}$ $\frac{3}{2}\frac{f'_{ct}\varnothing}{4\tau_{b0}\rho}(1-2\rho)$ for $x_{0,min}$ $2\frac{f'_{ct}\varnothing}{4\tau_{b0}\rho}(1-2\rho)$ for $x_{0,max}$
$\sigma_{sr,cr}$	$\frac{f_{ct}}{\rho}\big(1+\rho(n-1)\big)$	$\frac{f_{ct}}{\rho}\big(1+2\rho(n-1)\big)$ $= \frac{f_{ct}}{\rho}\big(1+\rho(n-2)\big) + nf_{ct}$	$\frac{f_{ct}}{\rho}\big(1+\rho(n-1)\big)$

[1)] Case II only applies if the concrete tensile strength in the lap splice region f'_{ct} is lower than the concrete tensile strength in the surrounding tension element, i. e. $f'_{ct} \le 0.9...0.95 f_{ct}$ (see Section 7.4.2, Case I), or if the tensile force is higher in the lap splice (e. g. in a tension chord of a bending member, with the splice locating at the location of maximum bending moment). Otherwise, Case I governs.

For lap splices, the diameter ratio is $\eta = 1$ and Equations (7.20) to (7.23) can be simplified as shown in Table 7.1. The term $(1-2\rho)$ in the equations for Case I is almost equal to the term $(1-\rho)$ in the original TCM (less than 2% difference for typical reinforcement ratios ρ). It is caused by the slightly different net cross-sectional area of concrete ($A_{c,net} = A_c - 2A_s$ vs $A_{c,net} = A_c - A_s$). Compared to the original TCM, the resulting minimum length of the boundary CE in Case I is 3% to 13% longer (due to the additional term $nf_{ct}\varnothing/4\tau_{b0}$), and its maximum length is 19% to 24% shorter if evaluated for $\rho = 0.007...0.02$ and $n = 5.5...7.5$, respectively. Regarding the cracking load, the additional term $n \cdot f_{ct}$ for Case I (see Table 7.1) leads to approximately 5% to 10% higher values compared to the original TCM. This implies that cracks evolve first in the tension chord outside the lap splice and hence, the crack pattern around the lap splice (and the distance x_0) has already formed when the cracking load of the lap splice is reached. Note in this context, that for $\eta = 1$, the cracking load for the boundary CE equals the cracking load of the inner CEs, i. e. $F_{cr} = A_s\sigma^{\mathrm{I}}_{sr,cr}(\eta = 1) = F_1 + F_2 = 2A_s\sigma^{IE}_{1L,cr}(\eta = 1)$.

Case II

Figures 7.6(a) and (b) show the stress state of both reinforcing bars and the concrete stresses in the first part of a CE for Case II, directly after the crack at the left side has formed. For the limit case $x^{\mathrm{I}}_1 = x_0 + x_{2a}$, it is observed in Figure 7.6(a) that the maximum concrete stress occurs at a distance $x_0 = x^{\mathrm{II}}_1$ from the crack. The minimum CE length and the cracking load for Case II are therefore equal to the original TCM

$$s^{\mathrm{II}}_{r,min} = x^{\mathrm{II}}_1 = \frac{f_{ct}\varnothing_1}{4\tau_{b0}\rho}(1-\rho) \tag{7.24}$$

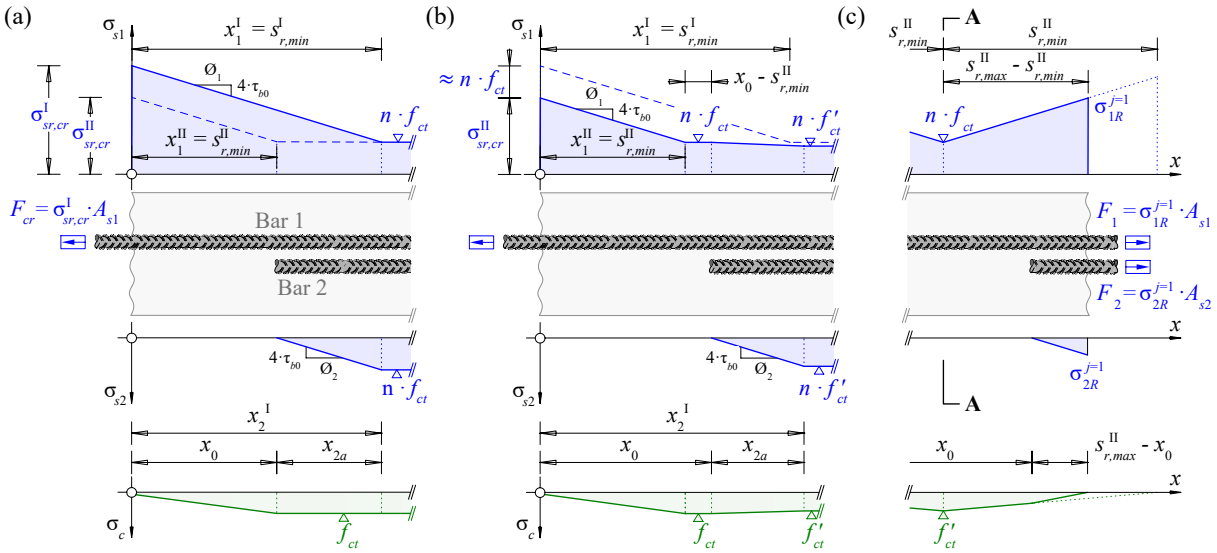

Fig. 7.6 – Stress distribution in Case II for both reinforcing bars $\sigma_{s1}(x)$ and $\sigma_{s2}(x)$, and for the surrounding concrete $\sigma_c(x)$ in a boundary element at cracking, with a crack occurring to the left of Bar 2, so that $x_0 + x_{2a} \geq x_1^{\mathrm{I}}$. (a) stress state for $x_1^{\mathrm{I}} = x_0 + x_{2a}$; (b) stress state for $x_1^{\mathrm{I}} < x_0 + x_{2a}$. (c) stress state in a lap splice at cracking for the particular case of a reduced concrete tensile strength in the lap splice region $f'_{ct} < f_{ct}$, with a crack occurring to the right of the unloaded end of Bar 2.

$$\sigma_{sr,cr}^{\mathrm{II}} = \frac{f_{ct}}{\rho}\left(1 + \rho(n-1)\right) \tag{7.25}$$

The location of maximum concrete stress and the minimum CE length $s_{r,min}^{\mathrm{II}}$ are unaffected by values $x_1^{\mathrm{I}} < x_0 + x_{2a}$ as shown in Figure 7.6(b). To the right of the unloaded end of Bar 2 in Figure 7.6(b), concrete stresses and the steel stress of Bar 1 have to decrease to fulfil the kinematic restriction of rigid bond $\varepsilon_c = \varepsilon_{s1} = \varepsilon_{s2}$. Formulating equilibrium, and using Equation (7.25), one gets

$$\begin{aligned} &\left(nA_{s1} + nA_{s2} + A_c\right)\sigma_c = A_{s1}\sigma_{sr,cr}^{\mathrm{II}} \\ &\Rightarrow \sigma_c = \alpha \cdot f_{ct} \\ &\alpha = \frac{\eta^2\left(1 + \rho(n-1)\right)}{\eta^2 + \rho(n-1)\left(\eta^2 + 1\right)} \end{aligned} \tag{7.26}$$

For a lap splice with reinforcing bars of equal diameter, i. e. $\eta = 1$, the factor α in Equation (7.26) is always $\alpha < 1$ (approximately $\alpha = 0.9...0.95$, for $\rho = 0.007...0.02$ and $n = 5.5...7.5$), and hence the concrete stress is $\sigma_c < f_{ct}$. Unless the tensile load varies along the element, this implies that with reaching the cracking load according to Equation (7.25), $\sigma_{sr,cr}^{\mathrm{II}} = \sigma_{sr,cr}^{\mathrm{TCM}}$, the lap splice region will remain uncracked (except for the theoretical case where the distance x_0 is exactly $x_0 = x_1^{\mathrm{I}} - x_{2a}$ and a crack may form inside the lap splice region, see Figure 7.6(a)). However, when reaching the cracking load of the lap splice $\sigma_{sr,cr}^{\mathrm{I}} > \sigma_{sr,cr}^{\mathrm{II}}$ (see Equation (7.21) and Table 7.1), a crack will form within the length $x_0 - s_{r,min}^{\mathrm{II}}$ in front of Bar 2 since the concrete tensile strength is exceeded (see Figure 7.6(b)). Because Equations (7.24) and (7.25), which are equal to the original TCM, apply for the part in front of Bar 2, the boundaries for the distance x_0 in Case II are

$$s_{r,min}^{\mathrm{II}} = s_{r,min}^{\mathrm{TCM}} = s_{r,min}^{\mathrm{I}} - x_{2a} \leq x_0 \leq s_{r,max}^{\mathrm{II}} = s_{r,max}^{\mathrm{TCM}} = 2s_{r,min}^{\mathrm{II}} \tag{7.27}$$

It follows (i) that always a crack will form within the length $s_{r,min}^{\mathrm{TCM}}$ in front of Bar 2, and hence, (ii) that the equations of Case I are valid without restrictions to describe the cracking load and the boundary element length.

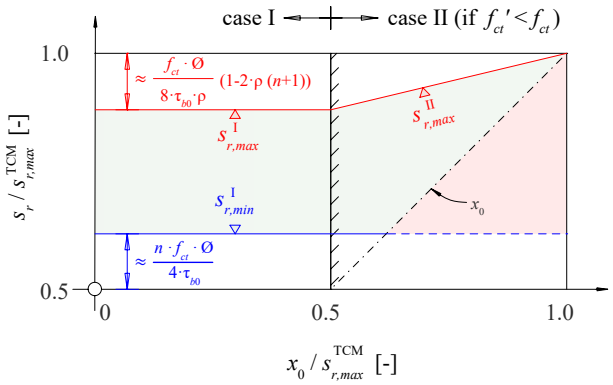

Fig. 7.7 – Potential CE lengths of a boundary element (normalised by the maximum element length of the original TCM $s_{r,max}^{TCM}$) as a function of the distance x_0. Valid CE lengths can only occur in the green-shaded area.

However, the cracking load of Case II $\sigma_{sr,cr}^{II}$ is only about 5% to 10% lower than $\sigma_{sr,cr}^{I}$, and the concrete tensile strength may vary considerably inside a structural element due to, e. g. the distribution of the aggregates or erratic compaction of concrete when vibrating. With the assumption that the concrete tensile strength in the lap splice region is lower and approximately $f_{ct}' = 0.9...0.95 f_{ct}$, the lap splice will crack at the same load $\sigma_{sr,cr}^{II} \approx \sigma_{sr,cr}^{TCM}$ as the other parts of the structural element. Therefore, a crack might form closely behind the end of Bar 2, as shown in Figure 7.6(c). Similarly, a crack may form at this location if the tensile force is higher in the lap splice, as is the case in a bending member with the splice located at the location of the maximum bending moment. Formulating equilibrium on the element shown in Figure 7.6(c) between Section A-A and the crack leads to the following equation for the maximum length of a boundary element in Case II

$$\begin{aligned} A_{s1} n f_{ct}' + A_{c,net} f_{ct}' &= A_{s1} \left(n f_{ct}' + \frac{4\tau_{b0}}{Ø_1} \left(s_{r,max}^{II} - s_{r,min}^{II}\left(f_{ct}'\right) \right) \right) + A_{s2} \frac{4\tau_{b0}}{Ø_2} \left(s_{r,max}^{II} - x_0 \right) \\ \Rightarrow s_{r,max}^{II} &= \frac{\eta}{\eta+1} \left(2 s_{r,min}^{II}\left(f_{ct}'\right) + \frac{x_0}{\eta} \right) = \frac{\eta}{\eta+1} \left(2 \frac{f_{ct}' Ø_1}{4\tau_{b0}\rho}(1-\rho) + \frac{x_0}{\eta} \right) \end{aligned} \tag{7.28}$$

Equation (7.28) indicates that the maximum CE length, in this case, depends on the distance x_0. For the limits of Equation (7.27) and $\eta = 1$, the maximum CE length is:

$$\begin{aligned} s_{r,max}^{II} \left(x_0 = s_{r,min}^{TCM} \right) &= 1.5 s_{r,min}^{TCM} \\ s_{r,max}^{II} \left(x_0 = s_{r,max}^{TCM} \right) &= 2 s_{r,min}^{TCM} = s_{r,max}^{TCM} \end{aligned} \tag{7.29}$$

The maximum CE length for $x_{0,max}$ coincides with the solution of the original TCM for the maximum crack spacing, which complies with the stress state shown as a dashed line in Figure 7.6(c).

Assuming that a crack forms at a distance $s_{r,min}^{II} \leq x_{cr} \leq x_0$, the separated element on the left in Figure 7.6(c) contains only one reinforcing bar, as the second bar only exists in the element to the right side of the considered crack. For the element to the right of the crack, the distance $x_0' = x_0 - x_{cr}$ is in the range $\left(x_{0,min} - s_{r,min}^{II}\right) = 0 \leq x_0' < \left(x_{0,max} - s_{r,min}^{II}\right) = s_{r,min}^{II} = s_{r,min}^{I} - x_{2a}$, see Equation (7.27). This equals the application limits for Case I (Equation (7.23)), which consequently also applies to this element. Therefore, Case II is only applicable if the length of the left CE is $s_r > x_0$, and the minimum CE length for Case II shall be rewritten as $s_{r,min}^{II} = x_0$.

Figure 7.7 represents all potential CE lengths of a boundary element (normalised by the maximum element length of the original TCM $s_{r,max}^{TCM}$) as a function of the normalised distance x_0. The element can take any length in the green shaded area, bounded by the two horizontal lines representing the minimum and maximum CE length, $s_{r,min}^{I}$ and $s_{r,max}^{I}$, and the vertical line at $x_0 / s_{r,max}^{TCM} = 0.5$. If the concrete tensile strength in the lap splice region is lower than in the adjacent tension chord, i. e. $f_{ct}' < f_{ct}$, CE lengths

Tab. 7.2 – Defined standard parameters to evaluate various influences on the lap splice response ($\eta = 1$).

f_c	[MPa]	30		$n = E_s/E_c$		[-]	6.6	
f_{ct}	[MPa]	2.9	(Eq. (7.32))	l_b		[Ø]	40	
E_c	[GPa]	31.1	(Eq. (7.32))	$s_{r,max}^{j=1}$	1. CE	[mm]	384	(Eq. (7.22))
τ_{b0}	[MPa]	5.6	(Eq. (7.1))	$s_{r,min}^{j=1}$	1. CE	[mm]	262	(Eq. (7.20))
τ_{b1}	[MPa]	2.9	(Eq. (7.1))	$s_{r,max}^{j}$	j. CE	[mm]	245	(Eq. (7.17))
Ø	[mm]	20		$s_{r,min}^{j}$	j. CE	[mm]	122.5	(Eq. (7.18))
ρ	[-]	0.01		$x_{0,max}^{\mathrm{I}}$	Case I	[mm]	122.5	(Eq. (7.23))

may also assume values in the green shaded area with $x_0/s_{r,max}^{\mathrm{TCM}} > 0.5$. For CE lengths shorter than the distance x_0, i. e. $s_r < x_0$, the corresponding point lays in the red shaded area. Such CE lengths cannot occur; instead, an element with a single reinforcing bar will be separated in front of the lap splice, and Case I applies for the boundary element with $x_0' < s_{r,min}^{\mathrm{TCM}}$.

In conclusion, the concept of s_r as shown in Equation (7.7) for the original TCM must be adapted to

$$\begin{aligned} s_r &= s_{r,min}^{\mathrm{I/II}} + (2\lambda - 1)\left(s_{r,max}^{\mathrm{I/II}} - s_{r,min}^{\mathrm{I/II}}\right) \\ \lambda &\in [0.5, 1] \end{aligned} \tag{7.30}$$

7.5 Parametric study

7.5.1 Modelling parameters

For the evaluations in Sections 7.5 and 7.6, material characteristics similar to those observed in the experiments of Tarquini et al. [153] are assumed. From the conducted tensile tests of the longitudinal reinforcement, a constitutive relationship according to [143] is adopted (see Figure 7.8)

$$\begin{aligned} &\text{for } 0 \le \varepsilon_s \le \varepsilon_{sy} = f_{sy}/E_s \\ &\qquad \sigma_s = E_s \varepsilon_s \\ &\text{for } \varepsilon_{sy} \le \varepsilon_s \le \varepsilon_{sh} \\ &\qquad \sigma_s = f_{sy} \\ &\text{for } \varepsilon_{sh} \le \varepsilon_s \le \varepsilon_{su} \\ &\qquad \sigma_s = f_{sy} + (f_{su} - f_{sy}) k_d \left(1 - \mathrm{e}^{(\varepsilon_{sh} - \varepsilon_s)/b}\right) \\ &\qquad b = \frac{\varepsilon_{sh} - \varepsilon_{su}}{\ln\left((k_d - 1)/k_d\right)} \end{aligned} \tag{7.31}$$

with $k_d = 1.06$ and steel characteristics given in Figure 7.8. A concrete compressive strength of $f_c = 30\,\mathrm{MPa}$ is assumed, and the concrete tensile strength f_{ct} and its Young's Modulus E_c are estimated from the concrete compressive strength, using the following equations

$$\begin{aligned} f_{ct} &= 0.3 f_c^{2/3} \qquad f_c \text{ and } f_{ct} \text{ in [MPa]} \\ E_c &= 10000 f_c^{1/3} \qquad f_c \text{ and } E_c \text{ in [MPa]} \end{aligned} \tag{7.32}$$

All assumed model parameters are summarised in Table 7.2.

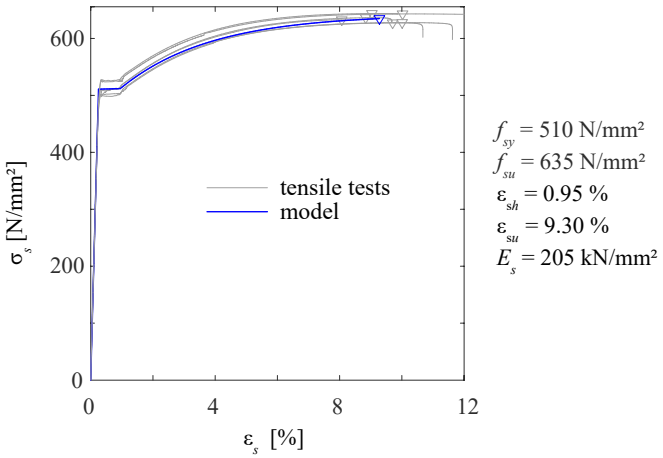

Fig. 7.8 – Results of steel tension tests (grey) reported in [153] and fitted model (blue) using the constitutive relationship of Equation (7.31)

7.5.2 Influence of CE length on load-deformation behaviour

To analyse the influences of different CE lengths on the stress distribution of the reinforcing bars, the described model is evaluated for a lap splice with overlapping length $l_b = 40Ø = 800\,\text{mm}$ using four distinct CE configurations: By assembling the minimum or maximum number of CEs, so that the total splice length is $l_{tot} = \min\left(\sum s_r^j\right) \geq l_b = 800\,\text{mm}$ or $l_{tot} = \max\left(\sum s_r^j\right) \leq l_b + 2x_{0,max}^{\text{I}} = 800 + 2 \cdot 122.5\,\text{mm}$, respectively, each with either short ($s_{r,min}^j, \forall j$) or long ($s_{r,max}^j, \forall j$) CEs.

Figure 7.9 shows the stress distribution for half of the total length in Reinforcing Bar 1 (blue) and 2 (red) for various load steps between cracking $F_{cr} = A_s \sigma_{sr,cr}$ and ultimate load $F_u = A_s f_{su}$. Apparent is the serrated stress distribution, with a local stress maximum at the crack and a local minimum inside the CE. Unlike the original TCM, the local minima of steel stresses are shifted from the CE centres towards the load-free end of each reinforcing bar, corresponding to the unloading of the bar in this direction. Towards the middle of the lap splice, the locations of the two minima are approaching each other, indicating that the load is balanced and carried equally by both bars.

Figure 7.9(a) shows the stress distribution for the lap splice consisting of three CEs with length $s_{r,max}^j$. The increasing external load leads to an increase of the activated embedded length of Bar 2 in the first CE, with the location of $\sigma_{s2}^{j=1} = n \cdot \sigma_c$ approaching the end of the bar at $x = 0$. The load of Bar 1 is transferred to Bar 2 mainly in the first CE, and the load difference decreases significantly already until the first crack. Figure 7.9(b) shows the stress distribution for a lap splice consisting of four CEs with length $s_{r,max}^j$, and consequently a distance x_0 much longer than in (a). The embedded length of Bar 2 in the first element is fully activated even for low external loads, and a considerable amount of the load is transferred from Bar 1 to Bar 2 only in the second element. As a consequence of the full activation over the embedded length and the necessity to fulfil deformation compatibility at the crack, Bar 2 is pulled out of the first CE (compare Section 7.3). Figure 7.9(c) shows the stress distribution for a lap splice consisting of five CE with length $s_{r,min}^j$. For higher external loads, Bar 1 yields over a considerable length, which leads to a decrease of bond stresses from τ_{b0} to $\tau_{b1} = \tau_{b0}/2$ and unloading of the embedded length of Bar 2 in the first CE by equilibrium. Furthermore, the reduction in bond stress causes the location of minimum stress for Bar 1 to shift to the right until it coincides with the crack location. Beyond this point, the load transfer in the first element stays constant, and the load is mainly transferred in the second CE (as in case (b)). For higher external loads, Bar 1 is pulled through the CE as deformation compatibility at the crack needs to be satisfied (compare Section 7.3). Figure 7.9(d) shows the stress distribution for the lap splice consisting of seven CE with length $s_{r,min}^j$, and a comparably long distance x_0. Here, the two phenomena described for cases (b) and (c) are combined: Because of the short embedded length of Bar 2 in the first element, the bar is pulled out. Consequently, there is only limited load transfer between

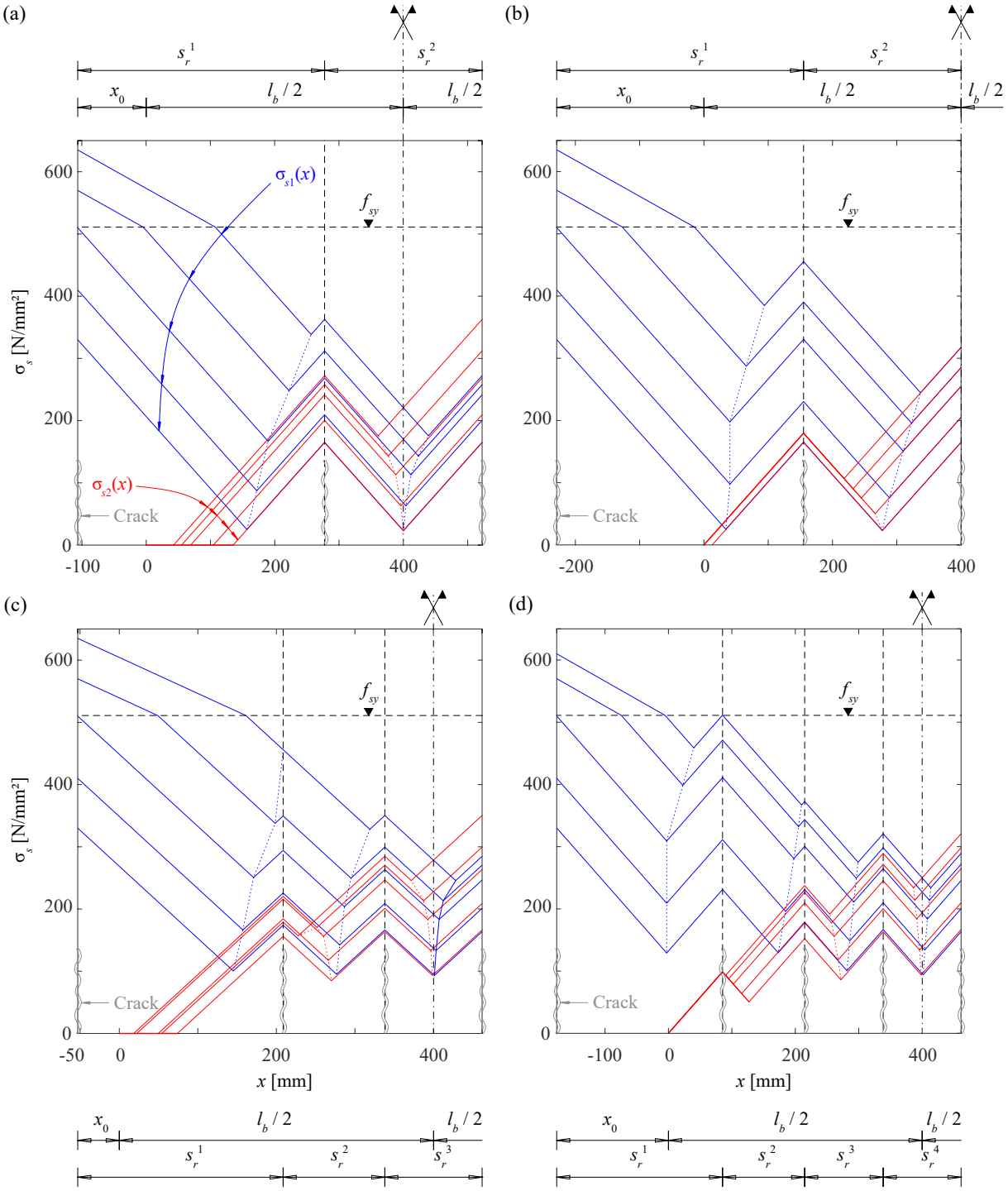

Fig. 7.9 – Influence of CE-length on load-deformation behaviour: Stresses in Reinforcing Bar 1 (blue) and 2 (red) over half of the lap splice for parameters according to Table 7.2 and various external loads between $A_s\sigma_{sr,cr}$ and $A_s f_{su}$. Indicated are the CEs (separated by the cracks = ordinate axes and vertical dashed lines) and the distance x_0 between the first crack and the unloaded end of Bar 2 (negative values on horizontal axis). A horizontal dashed line indicates the yield stress f_{sy}. (a) 3 CEs (min. number) with length $s^j_{r,max}$ ($\lambda = 1,\ \forall j$) (b) 4 CEs (max. number) with length $s^j_{r,max}$ ($\lambda = 1,\ \forall j$); (c) 5 CEs (min. number) with length $s^j_{r,min}$($\lambda = 0.5,\ \forall j$); (d) 7 CE (max. number) with length $s^j_{r,min}$($\lambda = 0.5,\ \forall j$).

the two reinforcing bars. As the second element is short and Bar 1 is still highly loaded, a pull-through of Bar 1 in the second element occurs. The load is mainly transferred in the second and third CE. As the implemented algorithm was not conceived to consider a pull-through of a bar in the second CE, the calculation stops shortly before reaching the ultimate load (in this case at $\sigma_{sr} = 610\,\text{MPa}$).

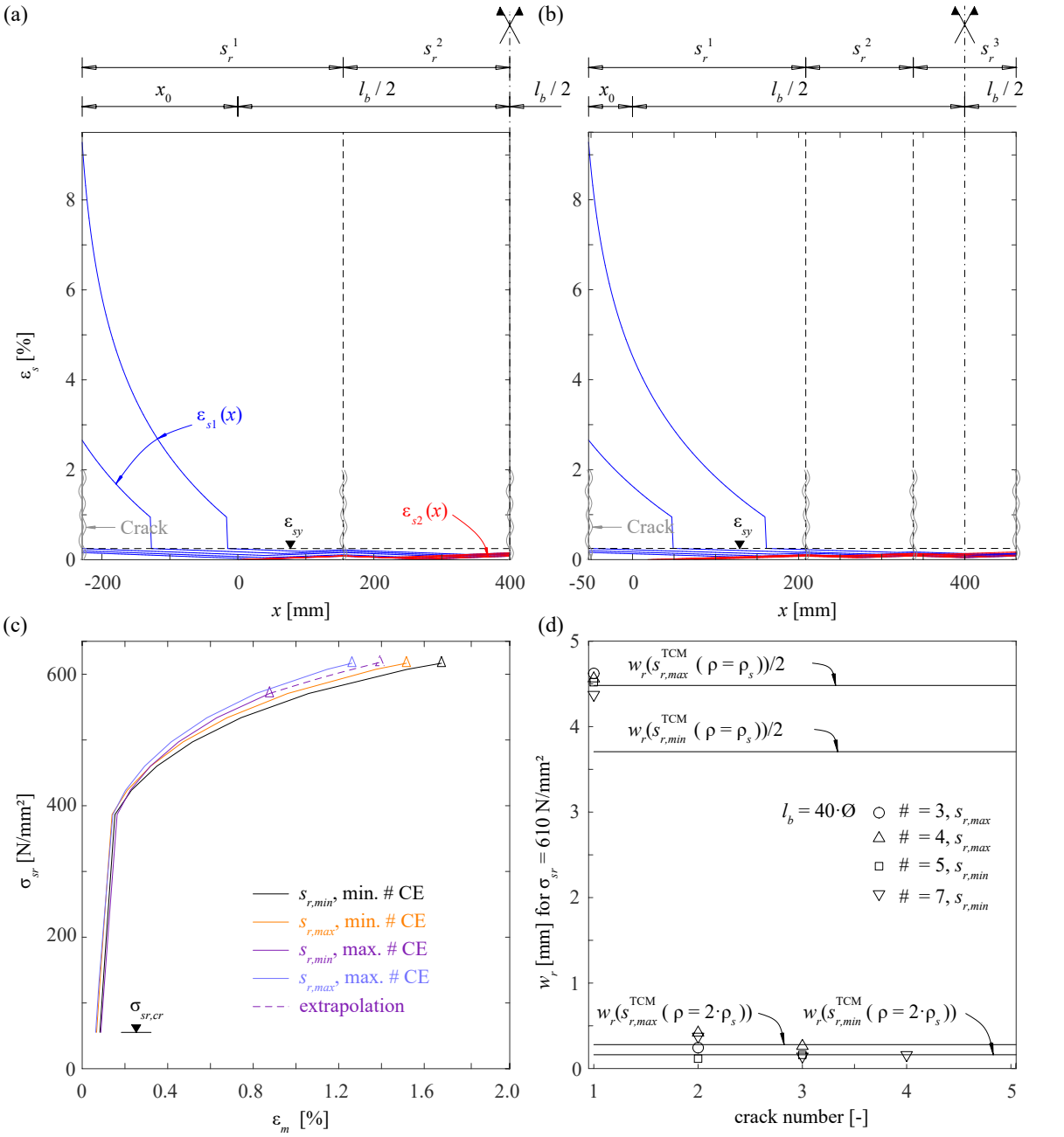

Fig. 7.10 – Influence of CE-length on load-deformation behaviour: (a, b) steel strains $\varepsilon_{s1}(x)$ and $\varepsilon_{s2}(x)$ of Bar 1 and 2 over half of the total lap splice length for the same CE-configuration and load steps as depicted in Figures 7.9(b) and (c). A horizontal dashed line indicates the strain at yield stress ε_{sy}; (c) stress at crack vs mean strain for the CE-configurations shown in Figure 7.9; (d) crack widths occurring along the lap splice for the CE-configurations shown in Figure 7.9. Note that for the first crack, only the contribution of the first CE to the crack width is shown (and the contribution of the adjacent single-reinforced CE would have to be added to receive the actual crack width). Horizontal lines indicate the minimum and maximum crack width expected by the original TCM for $\rho = \rho_s$ and $\rho = 2\rho_s$.

Figures 7.10(a) and (b) illustrate the steel strain distribution along half of the lap splice length for (a) the combination $\{$maximum number of CEs with length $s_{r,max}^j$, compare Figure 7.9(b)$\}$ and (b) the combination $\{$minimum number of CEs with length $s_{r,min}^j$, see Figure 7.9(c)$\}$, at the same load steps as in Figure 7.9. It can be observed that Bar 1 undergoes plastic deformations only in the first CE, and in case of Figure 7.10(a) even only inside the distance x_0. In all other parts of the lap splice, both reinforcing bars remain elastic. Figure 7.10(c) shows the steel stress at crack-mean strain diagrams for the four analysed lap splices of Figure 7.9; note that σ_{sr} (= steel stress at the crack crossed only by Bar 1) is proportional

to the applied load, i. e. $F = A_{s1}\sigma_{sr}$. It is visible that depending on the CE-combination (i. e. the crack pattern), the deformation capacity varies by $\Delta\varepsilon_m = 0.4\%$, with the combinations $\{$minimum number of CEs with length $s^j_{r,min}\}$ and $\{$maximum number of CEs with length $s^j_{r,max}\}$ setting a lower and upper bound, respectively.

Figure 7.10(d) shows the corresponding crack widths at $\sigma_{sr} = 610\,\text{MPa}$. Additionally, the minimum and maximum crack widths calculated with the original TCM for reinforcement ratios $\rho = \rho_s$ and $\rho = 2\rho_s$ are indicated. For the first crack, the indicated width represents the contribution of the first CE of the lap splice, and the contribution of the adjacent tension chord element would have to be added to receive the actual crack width. The contribution of the first CE to the crack width, i. e. the elongation of Bar 1 in the first element, approximately equals half the crack width of the original TCM, i. e. $w_r\big(s^{\text{TCM}}_{r,max}(\rho = \rho_s)\big)/2$ and $w_r\big(s^{\text{TCM}}_{r,min}(\rho = \rho_s)\big)/2$. The widths of Cracks 2 to 4 equal the crack widths expected by the original TCM for $\rho = 2\rho_s$ (except for some variation at the second crack). The similarity of the results per crack for all four CE-configuration reveals that neither the number of used CEs (and hence the variation in distance x_0) nor their length ($s^j_{r,min}$ or $s^j_{r,max}$) significantly influences the expected crack widths. Furthermore, the results indicate that the cracks at both ends of the lap splice generate approximately 90% of a lap splice's deformation capacity. The cracks inside the lap splice do not significantly contribute since their CEs behave similarly to a conventional tension chord with a double reinforcement ratio $\rho = 2\rho_s$.

7.5.3 Influence of lap splice length on load-deformation behaviour

Figure 7.11 shows the stress distributions at the ultimate load $\sigma_{sr} = f_{su}$ of the two reinforcing bars for seven lap splices with varying overlapping lengths of $l_b = 35...60\text{Ø}$ and the CE-configuration $\{s^j_{r,min}$, min. number of CEs$\}$. Below the graph, the CEs over half of the lap splice length with the two reinforcing bars and the varying distance x_0 is shown. The increase in overlapping length is accommodated by a higher number of CEs, and the length difference between the overlapping length and total lap splice length is compensated by the distance x_0, i. e. $l_{tot} = \sum s^j_r = l_b + 2x_0$. With the chosen CE configuration, the variation of x_0 for the different overlapping lengths is comparatively small, and the embedded length $s^{j=1}_r - x_0$ in the first CE is sufficient in all cases that no pull-out of Bar 2 occurs. The depicted stress distributions for the different overlapping lengths almost coincide, except for the short overlapping length $l_b = 35\text{Ø}$. This outlines the fact, that the load is transferred mainly in the first and the second CEs, i. e. in the discontinuity region of the lap splice. All remaining CEs for overlapping lengths longer than $l_b = 40\text{Ø}$ do not significantly contribute to the load transfer and behave like tension chord elements with double reinforcement ratio $\rho = 2\rho_s$.

Figure 7.12(a) shows the crack widths for the lap splices of Figure 7.11 at $\sigma_{sr} = 610\,\text{MPa}$, together with the minimum and maximum crack width calculated with the original TCM for the reinforcement ratios $\rho = \rho_s$ and $\rho = 2\rho_s$. Similar to Figure 7.10(d), the indicated width of the first crack corresponds to the contribution of the first CE of the lap splice, and the contribution of the adjacent single-reinforced tension chord element would have to be added to receive the actual crack width. As already observed for Figure 7.10(d), the contribution of the first CE to the crack width approximately equals half of the crack width expected by the TCM with $s^{\text{TCM}}_{r,max}(\rho = \rho_s)$, regardless of the actual overlapping length. The other crack widths are approximately equal to those corresponding to a tension chord with $s^{\text{TCM}}_{r,max}(\rho = 2\rho_s)$. This emphasis that plastic deformations localise at the beginning (and the end) of the lap splice, and demonstrates the discontinuous nature of lap splices regarding strain calculations: With increasing overlapping length, the total elongation for a specific external load stays approximately constant, i. e. $w_{tot} = \sum w^j_r \approx \text{const.}$, causing the mean strain over the lap splice $\varepsilon_m = \sum w^j_r / \sum s^j_r = w_{tot}/(l_b + 2x_0)$ to decrease. The stress at the crack vs mean strain of the seven lap splices is shown in Figure 7.12(b), indicating this pronounced decrease in deformation capacity with increasing overlapping length. For example, increasing the overlapping length from $l_b = 35\text{Ø}$ to $l_b = 60\text{Ø}$ results in a decrease of the deformation capacity by a factor of 1.6. Note in Figure 7.12(b) that the two curves for $l_b = 45\text{Ø}$ and $l_b = 50\text{Ø}$ are identical since their stress distribution and the total lap splice length are equal (see Figure 7.11).

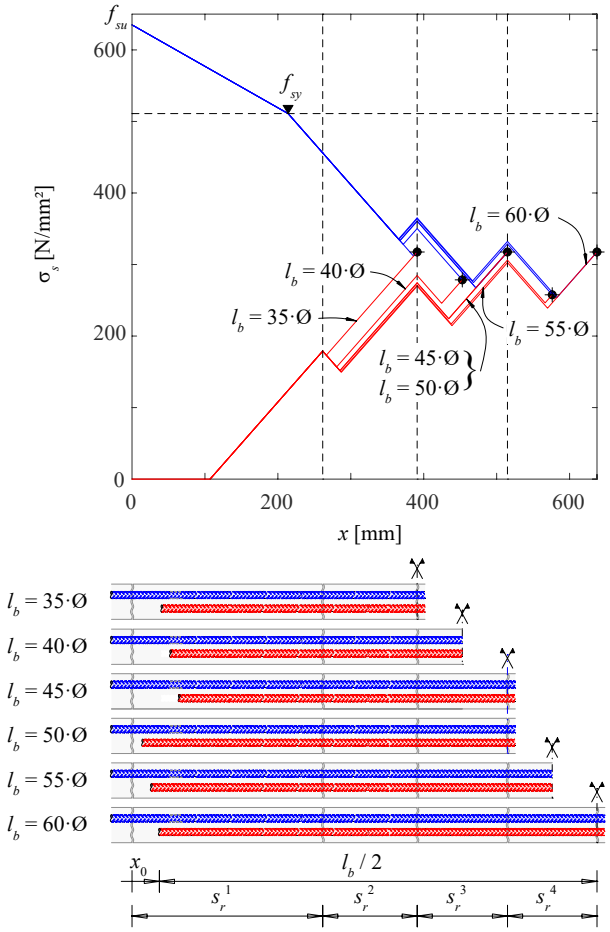

Fig. 7.11 – Influence of lap splice length on the load-deformation behaviour: Stresses for Reinforcing Bar 1 (blue) and 2 (red) over half of the lap splice for various lap splice lengths between $l_b = 35...60Ø$ at ultimate load $\sigma_{sr} = f_{su}$. A configuration with a minimum number of short CEs $s^j_{r,min}$ and parameters according to Table 7.2 were used. Below the graph, the CEs over half of the lap splice length with the two reinforcing bars and the distinct distance x_0 are shown.

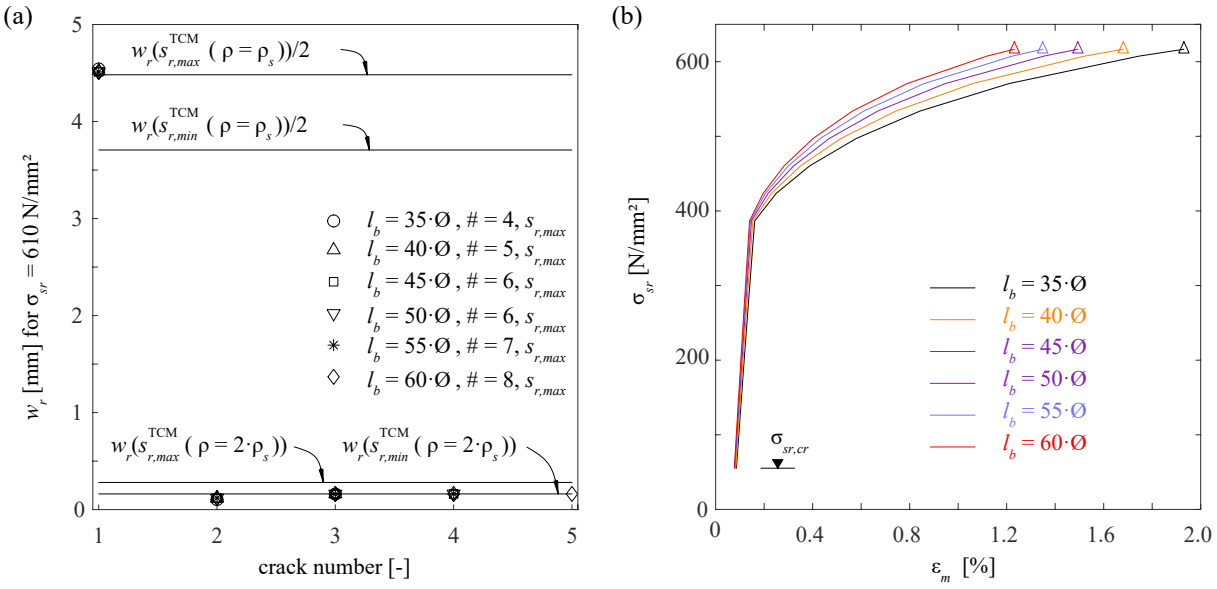

Fig. 7.12 – Influence of lap splice length on load-deformation behaviour: (a) crack widths occurring along the lap splices shown in Figure 7.11 with distinct overlapping length ($l_b = 35...60Ø$), along with the minimum and maximum crack width expected by the original TCM for $\rho = \rho_s$ and $\rho = 2\rho_s$; (b) stress at crack vs mean strain for the same lap splices.

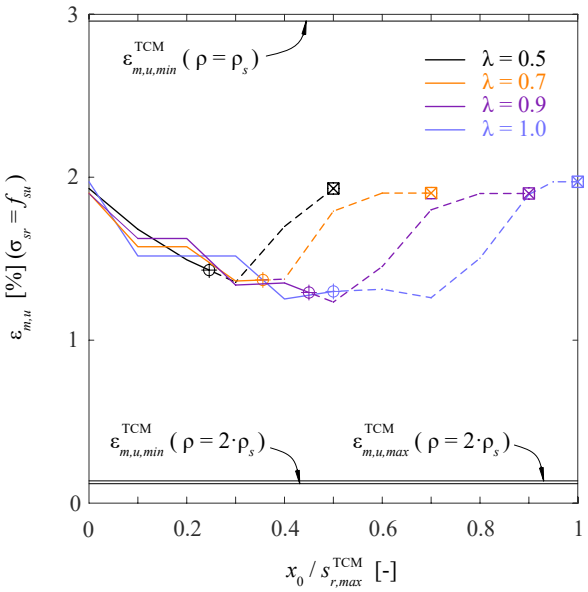

Fig. 7.13 – Influence of crack pattern in boundary element on deformation capacity $\varepsilon_{m,u}$: Lap splice with a varying distance x_0, overlapping length $l_b = 40\text{Ø}$ and CE length s_r^j according to Equation (7.30). Circles indicate the minimum deformation capacity at approximately $x_0 \approx 0.6 \cdot \lambda s^{TCM}_{r,min}$, and squares indicate the maximum distance $x^{II}_{0,max} = \lambda s^{TCM}_{r,max}$. The minimum and maximum deformation capacity according to the original TCM for $\rho = \rho_s$ and $\rho = 2\rho_s$ are shown with horizontal lines.

7.5.4 Influence of crack pattern in boundary element on deformation capacity

To investigate the influence of the distance x_0 on a lap splice's deformation capacity, a lap splice with overlapping length $l_b = 40\text{Ø}$ and parameters according to Table 7.2 and Figure 7.8 is analysed. The distance x_0 in the boundary element is varied in the range $0 \leq x_0 \leq s^{TCM}_{r,max}$. The CE lengths are chosen as s_r^j with $\lambda = [0.5,\ 0.7,\ 0.9,\ 1.0]$ according to Equation (7.30). The splice is modelled by choosing the number of CEs such that the difference between targeted and modelled total lap splice length is minimum, i. e. $\left| l_{tot} - \sum s_r^j \right| = \left| l_b + 2x_0 - \sum s_r^j \right| \rightarrow \min$.

Figure 7.13 shows the deformation capacity of the analysed lap splices for a given distance x_0 at maximum load $\sigma_{sr} = f_{su}$. The deformation capacity is highest at $x_0 = 0$ and decreases continuously for all CE lengths until $x_0 \approx 0.6 \cdot \lambda s^{TCM}_{r,max}$. The reason for this decrease in deformation capacity is an increase of the total lap splice length $l_{tot} = \sum s_r^j = l_b + 2x_0$, with the total elongation $w_{tot} = \sum w_r^j$ staying approximately constant (similar but less pronounced to an increase in overlapping length, compare Section 7.5.3, and Figure 7.12(b)). Note in this context that values $x_0 > 0.5 \cdot \lambda s^{TCM}_{r,max} = \lambda x^{I}_{0,max}$ (indicated with circles in Figure 7.13) correspond to Case II and can only be reached if the concrete tensile strength in the region of the lap splice is lower than in the other parts of the structural elements ($f'_{ct} < f_{ct}$, indicated as dashed lines, compare Section 7.4.2, Case II). For $0.6 \cdot \lambda s^{TCM}_{r,max} < x_0 < \lambda s^{TCM}_{r,max}$, the embedded length of Bar 2 is fully utilised and short, such that only a minor part of the force can be transferred from Bar 1 to Bar 2 (see Figure 7.9(d)). Consequently, Bar 1 is loaded above the yield point over the entire length of the first CE, generating large deformations in this part of the lap splice. Therefore, the total elongation and the deformation capacity again increase. For $x_0 = \lambda s^{TCM}_{r,max}$ (indicated with squares in Figure 7.13), the first CE contains only one reinforcing bar and represents a conventional tension chord element, which cannot be considered part of the lap splice. The lap splice itself behaves as for $x_0 = 0$ and exhibits maximum deformation capacity.

For the analysed lap splices, the deformation capacity decreases by approximately 35% for an increasing distance x_0 up to $0.6 \cdot \lambda s^{TCM}_{r,max}$. Hence, the location of the boundary crack, and consequently the crack pattern of the adjacent element, influences the deformation behaviour of a lap splice and requires considering the limiting cases $x^{I}_{0,min} = 0$ and $x^{I}_{0,max} = s^{TCM}_{r,min}$ when assessing a structure's deformation.

7.5.5 Influence of further lap splice parameters on deformation capacity

The influence of the bar diameter, the concrete compressive strength, the reinforcement ratio, and the overlapping length on the deformation capacity of a lap splice is analysed by a parameter variation. One parameter is varied in each analysis, whereas the others are held constant at their default values given in Table 7.2 (and marked bold in Table 7.3). The variation range of the varied parameters is given in Table 7.3. As described in Section 7.5.2, four CE-combinations are analysed for each varied parameter: maximum and minimum number of CEs in the range $l_b \leq \sum s_r^j \leq l_b + 2x_{0,max}^{\mathrm{I}}$, with either short ($s_{r,min}^j$) or long ($s_{r,max}^j$) CEs. The model is evaluated for a maximum stress $\sigma_{sr} = 610\,\mathrm{MPa}$, since a higher stress would cause a pull-through at inner CEs for some of the analysed configurations (e. g. lap splices with many short CEs). Figure 7.14(a) shows the influence of the bar diameter on the lap splice deformation capacity, along with the results calculated with the original TCM for one and two reinforcing bars (ρ_s and $2\rho_s$). The lines for the combinations $\left\{s_{r,max}^j\right.$, min. number of CE$\left.\right\}$ and $\left\{s_{r,min}^j\right.$, min. number of CE$\left.\right\}$, and the lines for the combinations $\left\{s_{r,max}^j\right.$, max. number of CE$\left.\right\}$ and $\left\{s_{r,min}^j\right.$, max. number of CE$\left.\right\}$ are virtually identical. In contrast to the original TCM, shorter CEs do not significantly increase a lap splice's deformation capacity. The deformation increase in the boundary elements is compensated by a larger number of CEs in the lap splice, which reduces the contribution of the boundary elements to the total deformation. On the other hand, as outlined in Section 7.5.4, a larger total lap splice length $l_{tot} = l_b + 2x_0$ reduces the deformation capacity due to the longer distance x_0. The effect appears to gain influence with increasing bar diameter.

Again in contrast to the original TCM, a lap splice's deformation capacity increases with increasing bar diameter (at an equal reinforcement ratio). The increasing diameter results in longer CEs, which leads to a composition with fewer CEs for the same overlapping length. As mainly the boundary elements contribute to the overall deformation capacity, their influence grows with a smaller number of CEs. Therefore, the deformation capacity increases discretely whenever the total number of CE is decreased (depicted jumps of the lines with increasing diameter in Figure 7.14(a)) and stays constant otherwise (e. g. in between diameter 22 mm and 30 mm).

Figure 7.14(b) shows the influence of the concrete compressive strength on a lap splice's deformation capacity. It decreases with increasing compressive strength, similar to the results obtained by the original TCM. As the concrete tensile strength and the bond strength increase due to their link to the compressive strength (compare Equation (7.32)), tension stiffening becomes more pronounced with increasing compressive strength, which leads to a decrease in deformation capacity.

Figure 7.14(c) shows the influence of an increasing reinforcement ratio, which leads to shorter CEs (compare Equation (7.6)). As described for Figure 7.14(a), the increase in deformation capacity due to the shorter CE is compensated by a larger number of CEs in the lap splice, which diminishes the contribution of the boundary elements to the total deformation. Therefore, the deformation capacity of a lap splice stays approximately constant with an increasing reinforcement ratio.

Figure 7.14(d) shows the influence of the overlapping length l_b. As pointed out in Section 7.5.3, a longer overlapping length reduces the deformation capacity of a lap splice, as the load is mainly transferred at both lap splice ends, and the inner elements behave similarly to conventional tension chord ele-

Tab. 7.3 – Varied parameters and applied variation range to analyse their influence on the deformation capacity of lap splices. Default values are marked in bold.

analysis	varied parameters		variation range
(a)	Ø	[mm]	12, 14, ... , **20**, ... , 26, 30
(b)	f_c	[MPa]	20, 25, **30**, ... , 50
(c)	ρ	[%]	0.7, 0.8, **1.0**, 1.2, ... , 2.0
(d)	l_b	[Ø]	30, 35, **40**, ... , 60

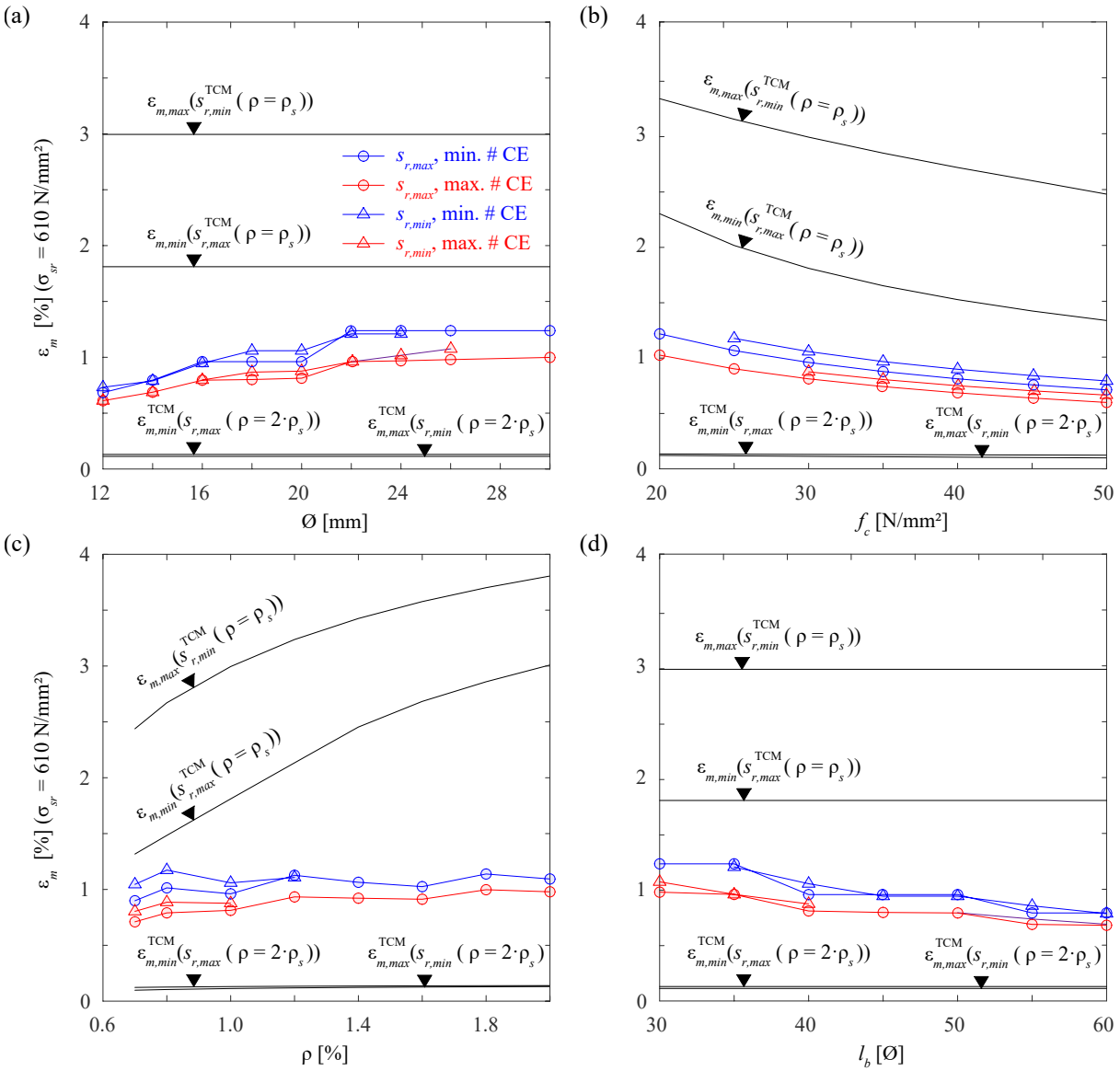

Fig. 7.14 – Influence of varying parameters on the mean deformation of lap splices with different CE-configurations and overlapping length $l_b = 40Ø$ at $\sigma_{sr} = 610\,\text{MPa}$. Variation of (a) reinforcing bar diameter; (b) concrete compressive strength; (c) reinforcement ratio; (d) lap splice length. Parameters chosen according to Table 7.2.

ments with double reinforcement ratio. For an increase of overlapping length from $l_b = 30Ø$ to $l_b = 60Ø$, the deformation capacity decreases by 30%…37%.

The parametric study indicates that lap splices exhibit a maximum deformation capacity of merely about 30% and 50% of the minimum deformation capacity of the adjacent elements, but are less sensitive to parameter variations than continuously reinforced tension chords. In all analysed cases, the deformation capacity is bounded by the two combinations $\{s^j_{r,min}$, min. number of CEs$\}$ and $\{s^j_{r,max}$, max. number of CEs$\}$. Hence, these two combinations can be used as lower and upper bound, respectively, to estimate a lap splice's deformation capacity.

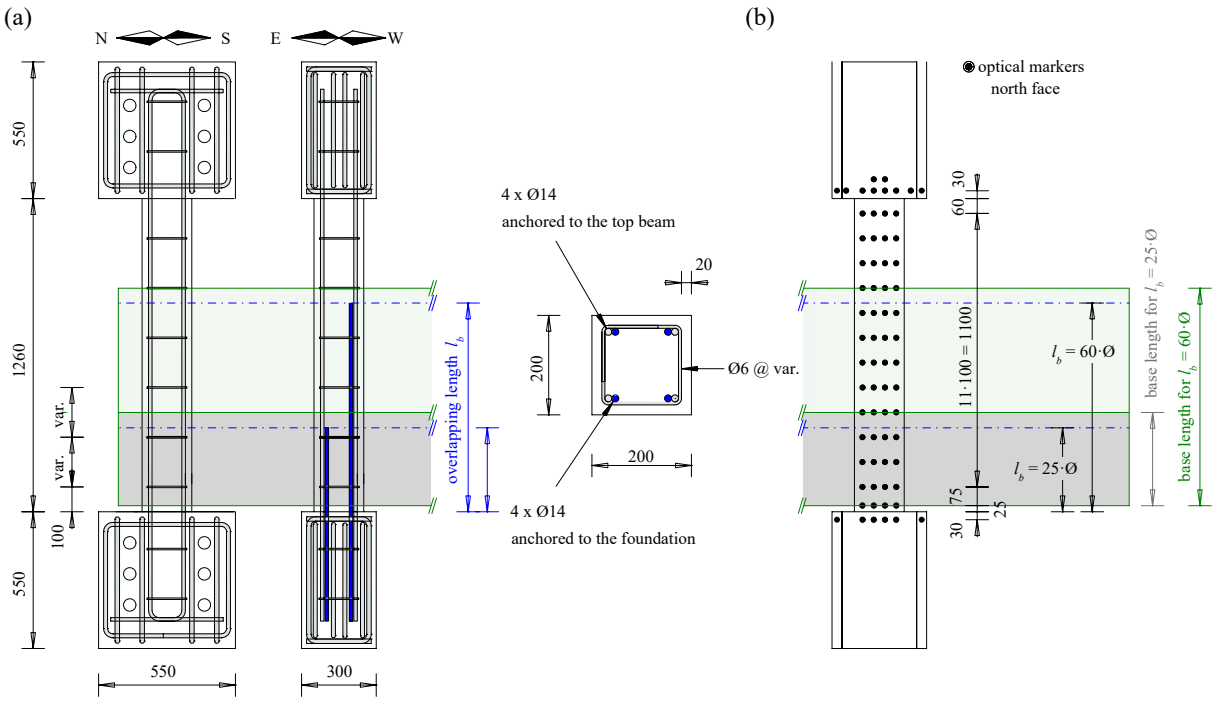

Fig. 7.15 – Experimental setup to investigate the behaviour of lap splices under cyclic loading [154]: (a) specimen geometry, reinforcing layout with indicated minimum and maximum lap splice lengths, and specimen cross-section; (b) optical marker positions for elongation measurement and examples of analysed sections (grey for $l_b = 25Ø$, green for $l_b = 60Ø$). The data of the optical marker just above the lap splice was used for elongation measurement. Figure modified from [154].

7.6 Experimental validation

7.6.1 Description of analysed experiments

Tarquini, Almeida and Beyer [153, 154] carried out 24 experiments on reinforced concrete members containing a lap splice and two reference tests with continuous reinforcement under uniaxial tension-compression cyclic loading. They published the excellently documented experimental data for free download on the Zenodo platform (https://doi.org/10.5281/zenodo.1205887). The most suited experiments were analysed herein to validate the above-proposed model.

Figure 7.15 shows the 1260 mm high specimens with a cross-section of 200x200 mm. Adjacent foundation blocks with dimensions 550x550x300 mm were used to anchor the reinforcement and to connect the specimens to the testing machine. The longitudinal reinforcement consisted of 4x Ø14 mm reinforcing bars of the same production batch with steel properties given in Figure 7.8. The bars were spliced above the bottom foundation, and four different overlapping lengths $l_b = [25,\ 40,\ 50,\ 60]Ø$ were tested. Some specimens contained transverse reinforcement, consisting of Ø6 mm closed stirrups, placed at variable spacing. The used concrete revealed a compressive strength similar to a C25/30. The specific properties of the analysed specimens are given in Table 7.4, along with the loading parameters. Further information on the specimens, the setup, and the instrumentation are published in [153, 154].

Additionally to the force measurement with a load cell, all specimens were instrumented by Linear Variable Differential Transducers (LVDTs) and a series of optical markers. In the following, the measurements with optical markers are used to evaluate the load-deformation behaviour; they are zeroed at the first tensile cycle. The analysed length, and hence the base length, is defined as the distance between the optical marker just above the joint between specimen and foundation block (to avoid any influences caused by the reinforcement anchorage), and the nearest optical marker above the respective overlapping length, see Figure 7.15.

Tab. 7.4 – Analysed experiments and corresponding concrete compressive strength f_c, stirrup spacing, overlapping length l_b, loading history, and failure mode, according to [153, 154].

experiment	f_c	stirrup spacing	l_b	loading history	failure mode
	[MPa]	[mm]	[Ø] and [mm]	[min., max. load, kN]	
P1	31.7	100	40Ø = 560	cyclic [-1074, +362]	splitting, loss of bond
P2	31.7	300	40Ø = 560	cyclic [-568, +323]	splitting, loss of bond
P3	31.7	200	40Ø = 560	cyclic [-682, +326]	splitting, loss of bond
P5	30.4	300	60Ø = 840	cyclic [-1018, +357]	splitting, loss of bond, and bar buckling
P6	31.7	200	40Ø = 560	monotonic [0, +321]	splitting, loss of bond
P8	31.7	200	40Ø = 560	monotonic [0, +340]	splitting, loss of bond
P10	31.7	100	60Ø = 840	cyclic [-1163, +311]	spalling, bar buckling, and concrete crushing
P11	33.2	200	25Ø = 350	cyclic [-281, +252]	splitting, loss of bond
P13	33.2	200	60Ø = 840	cyclic [-973, +363]	spalling, bar buckling, and concrete crushing
P14	31.7	no stirrups	60Ø = 840	cyclic [-835, +342]	splitting, loss of bond
P15	34.4	no stirrups	40Ø = 560	cyclic [-315, +322]	splitting, loss of bond
P18	34.4	200	50Ø = 700	cyclic [-1091, +355]	splitting, loss of bond
P19	33.5	120	40Ø = 560	monotonic [0, +333]	splitting, loss of bond

7.6.2 Calculation parameters

The concrete tensile strength f_{ct} and the concrete Young's Modulus E_c are estimated from the concrete compressive strength in Table 7.4, using Equation (7.32). The distance between the end of the second reinforcing bar and the closest crack is assumed as $x_0 = 0$. This assumption is justified by the observation that the lower lap splice boundary is located at the joint between tension chord and foundation block, which forms a geometrical discontinuity. Therefore, a crack was observed at this location in all analysed experiments. Similar to the concept in Section 7.5.4, the lap splices are modelled with the necessary number of CEs such that the difference between the experimental and modelled overlapping length $\left| l_b - \sum s_r^j \right|$ is a minimum. For the CEs, three different lengths are chosen: $s_{r,min}^j$ and $s_{r,max}^j$ as theoretical boundaries, and s_r^j with $\lambda = 0.67$ as best guess according to [79, 91]. With $\eta = 1$ and $\rho = \rho_s = 4 \cdot (14^2\pi)/200^2 = 1.5\%$, Equations (7.17), (7.18), (7.20), (7.22), and (7.30) yield the CE lengths summarised in Table 7.5. Since the spacing of the stirrups (100, 200, and 300 mm) was approximately equal or larger than the maximum crack distance $s_{r,max}^j$ in all experiments (except for the boundary element combined with 100 mm stirrup spacing), it did not influence the length of the CEs, as could otherwise be assumed, compare Section 7.3.

Tab. 7.5 – Length of CE according to Equations (7.17), (7.18), (7.20), (7.22), and (7.30) for Ø14, $\eta = 1$, $\rho = 0.015$, and $f_{ct} = 3$ MPa according to (7.32).

	$s_r^{j=1}$	$s_r^j \quad j \geq 2$
	[mm]	[mm]
$\lambda = 0.5$	121	55
$\lambda = 0.67$	140	74
$\lambda = 1.0$	176	110

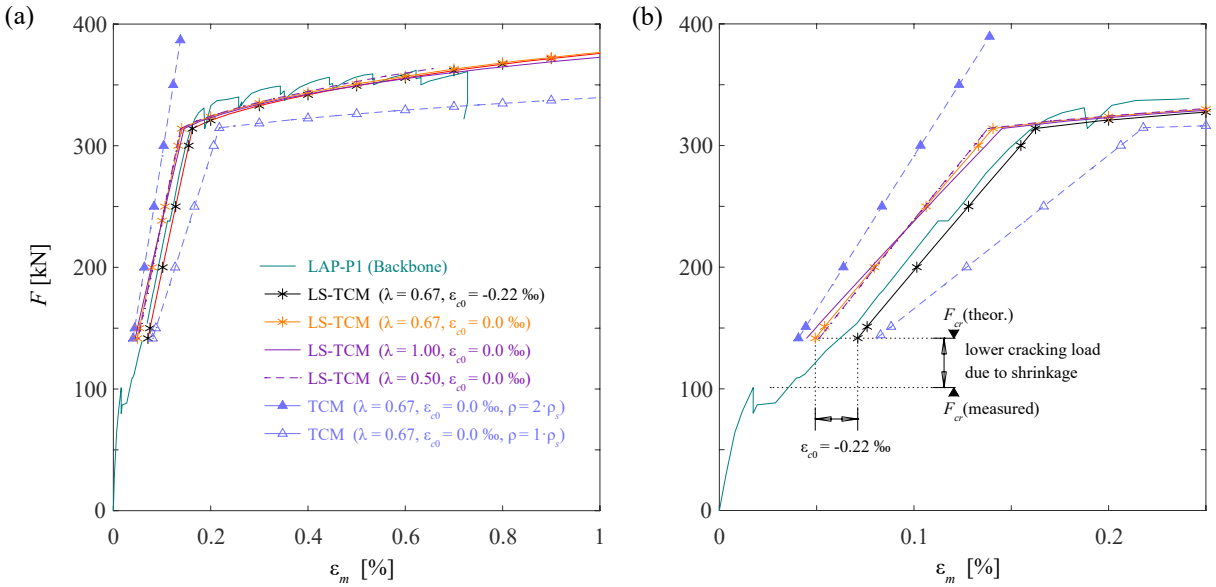

Fig. 7.16 – Experimental results of specimen P1 (load cycles only indicated with spikes), together with model calculations with different CE lengths ($\lambda = [0.5, 0.67, \text{and } 1.0]$) with and without accounting for shrinkage (ε_{c0}), and theoretical boundaries set by the original TCM. (a) full experimental curve range, (b) zoom to the elastic part; indicated are further the theoretical and experimentally observed cracking load.

For the model, the base length, the total elongation, and the corresponding mean strain are defined as

$$\begin{aligned} l_{\text{base}} &= \sum s_r^j + s_r^{\text{TCM}}/2 \\ \Delta &= \sum \left(w_{1L}^j + w_{1R}^j \right) - w_{1L}^{j=1} + \varepsilon_m^{\text{TCM}} \cdot s_r^{\text{TCM}}/2 \\ \varepsilon_m &= \Delta / l_{base} \end{aligned} \tag{7.33}$$

As shown in Figure 7.15, the first considered optical marker is just above the bottom crack separating the specimen and the foundation block. Therefore, the contribution $w_{1L}^{j=1}$ of the lap splice to the opening of this bottom crack is subtracted from the overall elongation Δ in Equation (7.33). On the other hand, to capture the influence on the deformation induced by the CE just above the lap splice (as the analysed region reaches to the optical marker above the lap splice, see Figure 7.15), half a conventional tension chord element with length $s_r = \lambda s_{r,max}^{\text{TCM}}$ is considered for the elongation Δ in Equation (7.33).

7.6.3 Results and Discussion

Figure 7.16(a) illustrates the result of Experiment P1 (green) together with the model predictions. Figure 7.16(b) shows a zoom of the elastic range. The load F is indicated as the total applied load, and the deformation is given as mean strain ε_m according to Equation (7.33). For the sake of better readability, the applied load cycles (compressive and tensile reloading) are omitted, and starting and endpoint are only indicated (spikes in the green curve). The two dashed blue lines illustrate the results obtained with the original TCM (single reinforcing bar) with the reinforcement ratio $\rho = \rho_s$ and $\rho = 2\rho_s$, representing the theoretical boundaries for all theoretical (and experimental) curves. The model results corresponding to $\lambda = 0.5$ and 1.0 are shown as magenta curves (dashed and solid); the red curve corresponds to $\lambda = 0.67$. The difference between these three curves is negligible in the elastic range but increases in the plastic range due to the much smaller slope of the curve. The black line is identical to the red line ($\lambda = 0.67$) but shifted by the shrinkage strain ε_{c0} of the reinforced element, which was estimated based on the difference between the theoretical and the experimentally observed cracking load, $F_{cr,\,theor}$ and

$F_{cr,\,exp}$ (see Figure 7.16(b)), and common mechanical concepts as

$$\begin{aligned}
\varepsilon_{c0} &= \frac{(F_{cr,\,exp} - F_{cr,\,theor})}{(EA)_{uncracked}} \frac{(1-\rho)}{n\rho} \\
F_{cr,\,theor} &= n \cdot f_{ct} \frac{(EA)_{uncracked}}{E_s} \\
(EA)_{uncracked} &= E_c A_c (1 + \rho(n-1))
\end{aligned} \tag{7.34}$$

The model accounting for shrinkage matches the experimental data in the elastic range excellently; the predicted stiffness (slope of the curve) is almost identical. The yield load is slightly underestimated, but nevertheless, the plastic range of the experiment is very well predicted. According to [153], the specimen failed in the experiment by splitting of the concrete and a subsequent loss of bond. Therefore, the ultimate deformation observed in the experiment is much lower than what could have been expected for a specimen failing by rupture of the reinforcement without loss of bond.

Figure 7.17 shows the predicted response for $\lambda = 0.67$, with and without a shift accounting for shrinkage, along with the results for all analysed experiments. Similar to Experiment P1, the specimens failed by splitting and bond loss (except for P10 and P13, which failed in compression by spalling, buckling of the reinforcing bars, and concrete crushing, compare Table 7.4). Hence, only the elastic branch and the beginning of the plastic load range are analysed. The model is in excellent agreement with the experimental data regarding elastic stiffness and the beginning of the plastic range. In the elastic range of the experimental curves, horizontal shifts are visible for all experiments with cyclic loading, which indicate starting points and endpoints of the load cycles. Obviously, these two points do not match, which indicates an impairment of bond induced by the cyclic loading (an issue also reported by, e. g. [94]). Accordingly, the experimental curve is shifted with respect to the model prediction. Nevertheless, the slope of the model fits the slope of the experimental curve very accurately in between these horizontal shifts, with the two lines being in parallel for most of the analysed experiments. Moreover, contrary to experiment P1, the yield point is predicted accurately for most experiments.

The model is designed for monotonic tensile loading, assuming steady bond conditions, and adopts failure by reaching the ultimate tensile load. Hence, it is not able (and does not aim) to account for the failure modes observed in the experiments of [153, 154]. Validation of the predicted deformation capacity was not possible, as the specimen design (partly confined longitudinal reinforcement) and loading (continuous bond degradation due to load cycles, compare [94]) lead to premature failure by splitting and bond loss. Hence, the model predictions on the deformation capacity at ultimate load (with a rupture of the longitudinal reinforcement) need to be validated in further experiments.

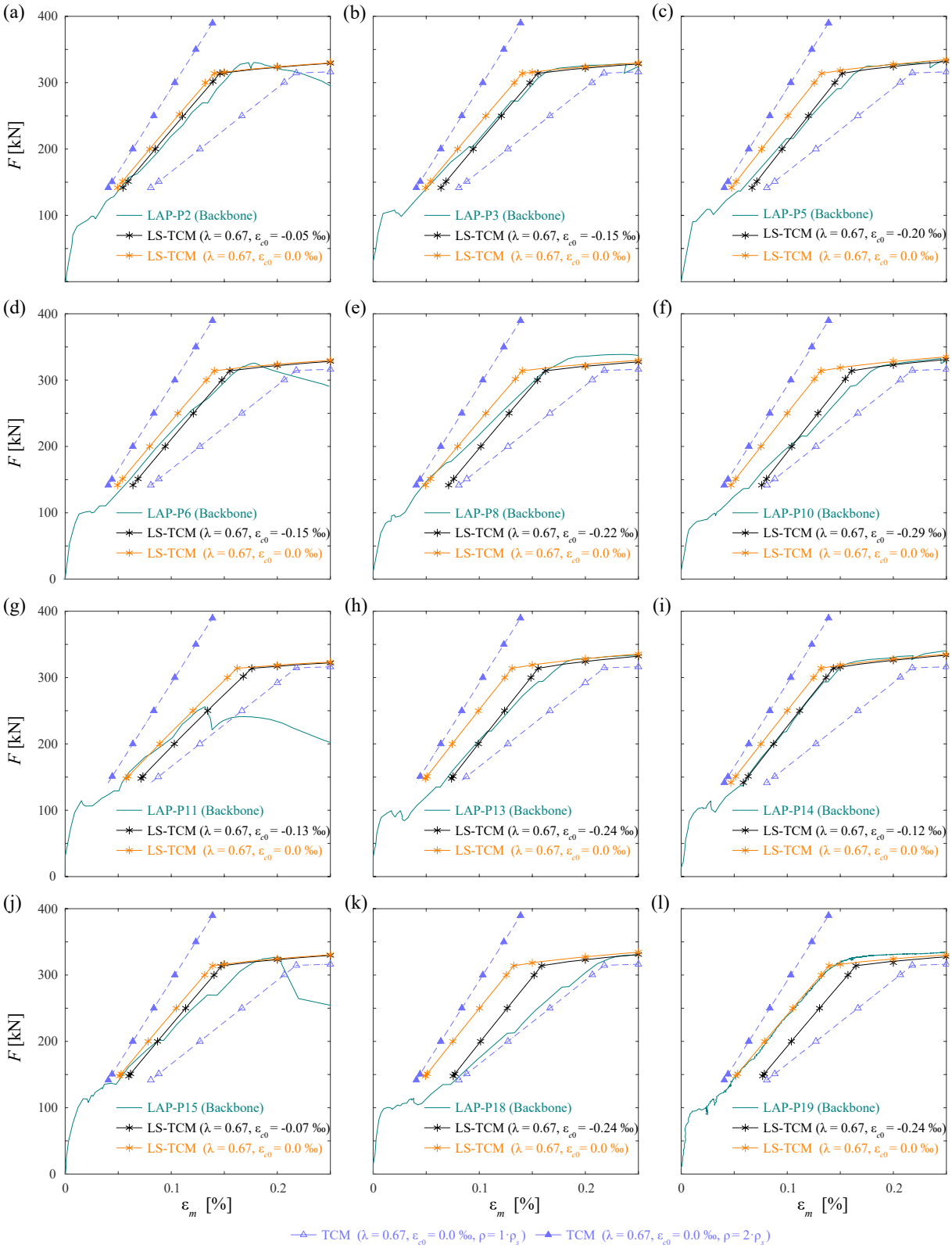

Fig. 7.17 – Experimental results of specimens P2-P19 (load cycles indicated as horizontal shifts in the experimental curves), together with the model calculation for $\lambda = 0.67$ with and without accounting for shrinkage (ε_{c0}), and theoretical boundaries set by the original TCM. Only the elastic part of the experiments is shown.

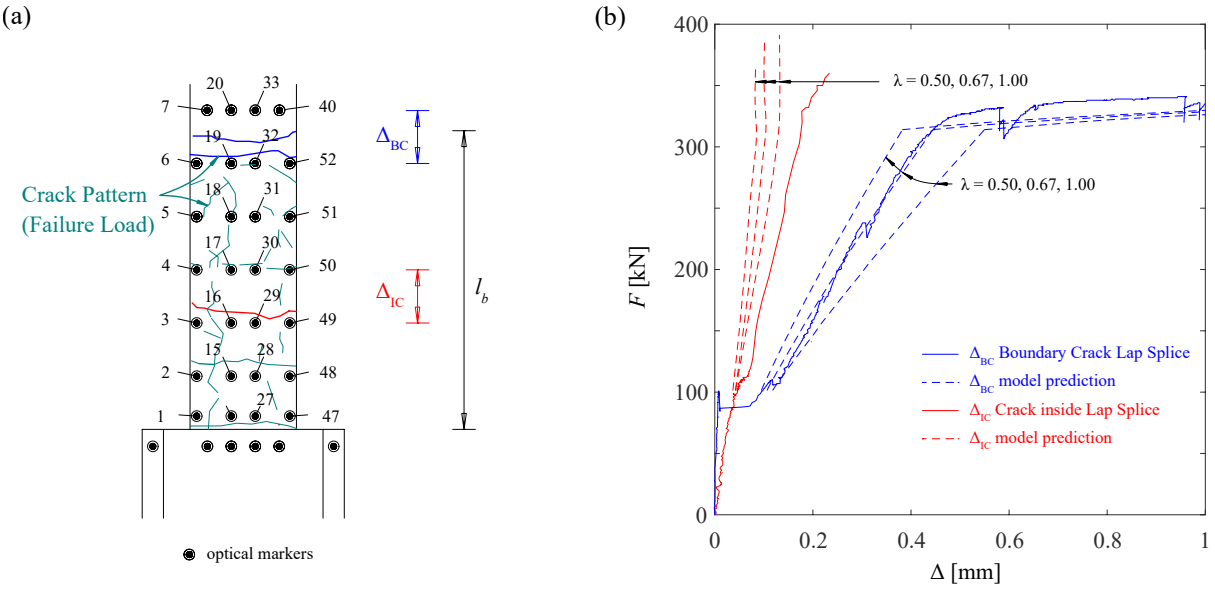

Fig. 7.18 – Experimental results and model predictions of crack widths of Specimen P1: (a) crack pattern for lower part of the specimen with cracks at boundary CE (blue) and inner CE (red). Further indicated are the overlapping length l_b and the base length to evaluate the crack width of the boundary CE Δ_{BC} and the inner CE Δ_{IC}; (b) load-crack width curve of boundary CE and inner CE (blue and red solid lines, respectively), along with model predictions (dashed lines).

Figure 7.18(a) shows the crack pattern at failure load in the lower part of Specimen P1 and the attached optical markers, along with the overlapping length and the base length to evaluate the deformation of a boundary CE Δ_{BC} and an inner CE Δ_{IC}, respectively. Figure 7.18(b) shows the elongation of the boundary CE and the inner CE (blue and red solid lines), together with model predictions (dashed lines). The elongation of the inner CE directly equals the crack width at this location. At the boundary CE, two cracks occurred, and the elongation equals the sum of their widths. Nevertheless, the spacing of these two cracks is very small (less than 40 mm), so that their behaviour can be treated in good approximation as of one single crack.

Figure 7.18(b) reveals that over the entire load path, the opening of the boundary crack is much larger than the opening of the inner crack. This leads to a significantly larger contribution of the boundary crack to the total lap splice elongation, confirming the theoretical observations described in Section 7.5.2. Furthermore, the crack widths predicted with the proposed model match the observed data exceptionally well, especially for the boundary crack and $\lambda = 0.67$. The crack width of the inner CE is slightly underestimated, with an absolute deviation of approximately 0.05 mm. However, considering the challenges when measuring such small elongations, this result is satisfying all the same.

7.7 Simplified approach to estimate the load-deformation behaviour of lap splices

The calculation of the load-deformation behaviour of a lap splice with the model described in Section 7.3 is elaborate, and the time expenses can hardly be justified for daily problems in engineering practice. Section 7.5.5 reveals that as a rule of thumb, a lap splice's deformation capacity can be assumed to be approximately half the deformation capacity of a conventional tension chord element with CE length $s_{r,max}^{TCM}$ ($\lambda = 1$), except for reinforcement ratios greater than $\rho > 0.015$. Here, or if the entire load-deformation behaviour is needed, the following simplified approach is proposed. Considering the findings of Sections 7.5.2 and 7.5.4 about the load-deformation behaviour depending on the established crack pattern, the chosen approach defines an upper and a lower bound for the deformation.

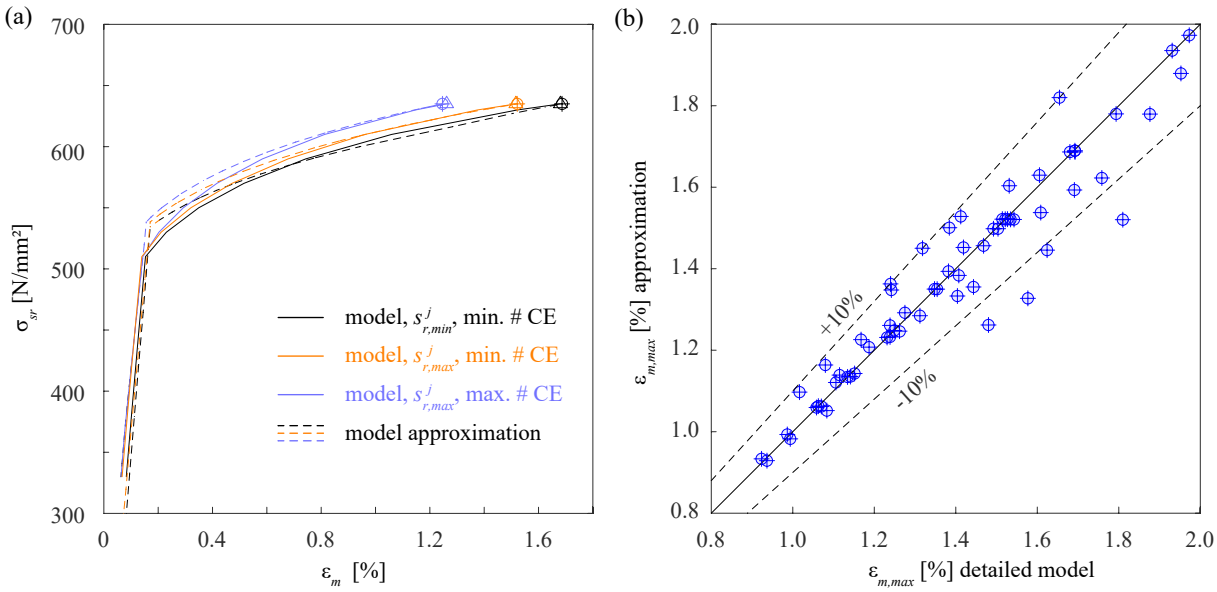

Fig. 7.19 – Simplified approach to estimate load-deformation behaviour: (a) comparison of original model curves (solid lines) and approximation (dashed lines) of a lap splice's stress-mean strain behaviour for three of the analysed CE-configuration of Section 7.5.2; (b) comparison of the lap splice's deformation capacity from the parameter study in Section 7.5.5 and the corresponding results of the approximation. Dashed lines indicate a deviation of +/-10% of the approximation from the original model.

1. Calculate the maximum and minimum length of the boundary elements $s^{BE}_{r,min}$ and $s^{BE}_{r,max}$ according to Equations (7.20) and (7.22) or Table 7.1 (Case I). Assume all inner elements to have the length of a conventional tension chord element with double reinforcement ratio according to Equations (7.17) and (7.18), i. e. $s^{IE}_{r,min} = s^{\mathrm{TCM}}_{r,min}(\rho = 2\rho_s)$ and $s^{IE}_{r,max} = 2s^{IE}_{r,min}$.

2. Use the overlapping length l_b of the lap splice and the CE with minimum length ($s^{BE}_{r,min}$ and $s^{IE}_{r,min}$) to determine the appropriate number of CEs (2 boundary elements and $(k_{min}-2)$ inner elements) for the upper bound. Use the total length $l_{tot} = l_b + 2x^{\mathrm{I}}_{0,max} \approx l_b + 2s^{IE}_{r,max}$ of the lap splice and the CE with maximum length ($s^{BE}_{r,max}$ and $s^{IE}_{r,max}$) to determine the appropriate number of CEs (2 boundary elements and $(k_{max}-2)$ inner elements) for the lower bound.

3. For the boundary elements, use the equations of the conventional TCM (see [7, 72]) to calculate the stress-mean strain relationship with a reinforcement ratio $\rho^{BE} = 1.046 \cdot \rho$ for the upper bound and $\rho^{BE} = 1.054 \cdot \rho$ for the lower bound, respectively (meaning that the stress at the crack σ_{sr} causes a mean strain $\varepsilon_m\left(\sigma_{sr}/\rho^{BE}\right)$). The adapted reinforcement ratio accounts for the contribution of the second reinforcing bar in the boundary element.

4. For the inner elements, use the equations of the conventional TCM (see [7, 72]) to calculate the stress-mean strain relationship with double reinforcement ratio $\rho^{IE} = 2\rho$ (meaning that the stress at the crack σ_{sr} causes a mean strain $\varepsilon_m\left(\sigma_{sr}/2\right)$).

5. The lower and upper bound of the mean strain over the entire lap splice can then be approximated as

$$\varepsilon^{\text{lower bound}}_{m,\,lap,\,approx} = \left(2s^{BE}_{r,max}\varepsilon_m\left(\rho^{BE}\right) + (k_{max}-2)\cdot s^{IE}_{r,max}\varepsilon_m\left(\rho^{IE}\right)\right) \Big/ \left(2s^{BE}_{r,max} + (k_{max}-2)\cdot s^{IE}_{r,max}\right)$$
$$\varepsilon^{\text{upper bound}}_{m,\,lap,\,approx} = \left(2s^{BE}_{r,min}\varepsilon_m\left(\rho^{BE}\right) + (k_{min}-2)\cdot s^{IE}_{r,min}\varepsilon_m\left(\rho^{IE}\right)\right) \Big/ \left(2s^{BE}_{r,min} + (k_{min}-2)\cdot s^{IE}_{r,min}\right) \tag{7.35}$$

Figure 7.19(a) shows the stress-mean strain curves for three of the analysed CE-configurations for a lap splice with overlapping length $l_b = 40Ø$ and standard parameters (Table 7.2) of Section 7.5.2:

$\{s^j_{r,max}$, max. number of CE, magenta, lower bound$\}$, $\{s^j_{r,max}$, min. number of CE, red$\}$, and $\{s^j_{r,min}$, min. number of CE, black, upper bound$\}$. With dashed lines, the corresponding approximation is shown. The approximation curves reveal a stiffer behaviour near the yield point compared to the original model due to the higher reinforcement ratio ρ^{BE}. Hence, the approximation underestimates deformations in this part. For higher loads, the original model curves and the corresponding approximation are in perfect agreement.

A comparison between the deformation capacity predicted by the original model for the lap splice configuration analysed in the parametric study in Section 7.5.5 and the approximation is given in Figure 7.19(b). With few exceptions, the approximation results are in the range of +/-10% and closely distributed around the diagonal. The mean value of the deviation is $\bar{x}\left(\varepsilon^{approx}_{m,u} - \varepsilon^{original}_{m,u}\right) = -3.3 \cdot 10^{-5}$ (= –0.03 millistrain), the standard deviation is $s\left(\varepsilon^{approx}_{m,u} - \varepsilon^{original}_{m,u}\right) = 6.8 \cdot 10^{-4}$ (= 0.68 millistrain).

7.8 Design recommendations

As outlined in Section 7.5, lap splices reduce the deformation capacity of structural elements to roughly half of their non-spliced capacity. Hence, they should be (i) avoided in zones where plastic hinges are likely to occur, (ii) kept as short as possible, and (iii) taken into account whenever structures are assessed using performance-based methods (comparison of deformation demand and deformation capacity).

The first recommendation is consistent with modern seismic design requirements [124], and is probably the most effective approach to guarantee sufficient ductility for a structural element. As indicated in the proposed reinforcement layout of Detail A in Figure 7.20, the entire lap splice is shifted outside the potential plastic hinge region, which is often assumed to be at least 1.3…1.5-times the section height, i. e. $> 1.3h$...$1.5h$ [1, 18]. The same concept can be applied to other structural elements, such as, e. g. retaining walls. For elements with a high reinforcement ratio or undergoing high compressive forces, the assumption for the plastic hinge length of $1.3h$...$1.5h$ has to be critically assessed.

In bridges where the superstructure is longitudinally stabilised only by the piers, i. e. superstructure is free to move at the abutments, the piers are often connected monolithically to the superstructure. Thereby, as shown in Figure 7.20, the top longitudinal reinforcement of the bridge girder is commonly continued above the pier (so-called continuous reinforcement). On the other hand, the vertical pier reinforcement continues into the bridge girder, being bent and anchored in the longitudinal direction, enabling the compression strut required for moment transfer to emerge (see stress field in Figure 7.20, Detail B). Conventionally, this anchorage length is not considered for the resisting moment of the superstructure, and the continuous reinforcement is dimensioned to cover the design hogging moment of the girder by itself. In reality, however, due to the deformation compatibility of the entire nodal region, the tension chord force above the pier is shared between the continuous girder reinforcement and pier reinforcement continuing into the girder, causing the diagram of effective moment resistance to increase above the pier (red dashed line in Figure 7.20). Since the length needed to transfer the load from the continuous girder reinforcement to the spliced pier reinforcement is much shorter than commonly assumed (as outlined in Sections 7.5.2 and 7.5.3), the major part of the anchorage length of the pier reinforcement acts as reinforcement staggering, which drastically reduces the bridge girder's deformation capacity above the pier. The same applies to buildings where the main structure consists of an RC frame with monolithic connections between columns and slabs. It is therefore strongly recommended (a) to include the anchoring reinforcement in the calculation of the moment resistance and deformation capacity of the superstructure (e. g. when checking the ductility by the ratio of the depth of compression zone to the effective depth, i. e. x_c/d) and (b) to partly reduce the amount of continuous reinforcement to account for the additional moment resistance induced by the pier reinforcement (red solid line in Figure 7.20) at least in cases where a high rotation capacity is required.

The second recommendation aims at keeping the region with reduced ductility as short as possible and, additionally, to increase the lap splice's deformation capacity (see Figure 7.14(d) and Section 7.5.5).

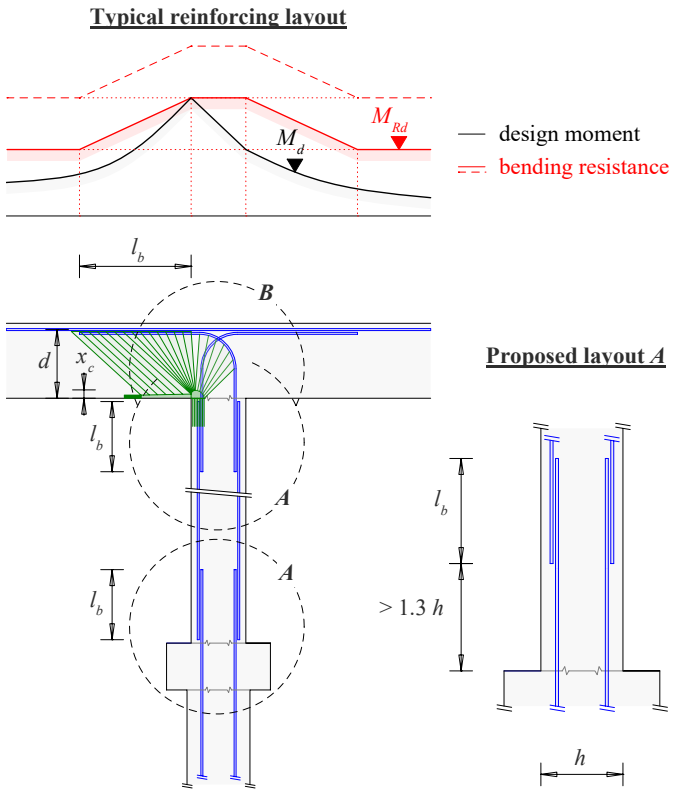

Fig. 7.20 – Design recommendations for lap splices: Detail A: Conventional and proposed reinforcement layout in highly loaded regions potentially undergoing plastic deformations. Detail B: Typical reinforcement layout above bridge piers which are monolithically connected to the bridge deck, along with the stress field and the moment distribution in this region. Shown are the moment resistance from conventional design, where the continuous reinforcement covers the design load alone (dashed line), and the moment resistance with the proposed reduction of the continuous reinforcement.

The minimum overlapping lengths given in various codes containing reasonable safety margins to avoid lap splice failure should be complied with but not exceeded, particularly if the lap splice is located in a zone potentially undergoing plastic deformations.

Finally, it is recommended to carefully assess the deformation capacity of elements containing a lap splice, especially if the corresponding region is highly loaded. If performance-based methods are used, deformation capacity should be approximated using the simplified method proposed in this paper.

7.9 Conclusions

Lap splices are an indispensable part of reinforced concrete structures. They have been, and still are often placed in regions where potential plastic deformations occur, e. g. in piers monolithically connected to the bridge deck, or directly above the construction joints of piers and retaining walls. Therefore, comprehensive knowledge of their load-deformation behaviour is essential to reliably assess such structural elements, especially if performance-based methods, comparing deformation demand and capacity, are applied.

This paper presents a mechanically consistent method to describe a lap splice's load-deformation behaviour based on the concepts of the established Tension Chord Model, together with predictions of the crack spacings and crack widths in the lap splice region. The deformation behaviour is studied in detail, and a parametric study is carried out to investigate different influences on the deformation capacity. A simplified modelling approach for practical use is developed, approximating the load-deformation behaviour of lap splices. Despite its straightforward formulation, the simplified approach exhibits high

accuracy compared with the original model and is therefore suitable for applications in engineering practice. Finally, three design recommendations for handling lap splices are presented.

The model is validated for the elastic and the first part of the plastic phase regarding load-deformation behaviour and crack width with experimental results published in [153, 154], revealing excellent agreement. As the specimens underwent cyclic loading and the lap splices were only partially confined, all of them failed by excessive splitting and a subsequent loss of bond. Hence, it was not possible to validate the deformation capacity predicted by the model. Therefore, the validation of the model for high plastic deformations in tension needs to be addressed in future research.

The study reveals the following general findings on the behaviour of lap splices:

- The crack spacing in lap splices is reduced to approximately half the crack spacing of the adjacent structural parts, except at the end of the second bar.
- The load transfer between the two reinforcing bars mainly occurs at both ends of the lap splice (in the first and the second crack element). The section in between these – which forms the largest part of a lap splice – behaves like a conventional structural element with a double reinforcement ratio. Here, the yield point is never exceeded and deformations are accordingly small. This load transfer mechanism is key for understanding the discontinuous behaviour of the lap splice region.
- Consequently, the crack elements at both ends of the lap splice exhibit most (typically > 90%) of the deformations. This leads to a wide crack at either end of the lap splice, whose crack widths exceed the crack widths observed outside the lap splice. In contrast, the crack widths in the central part of the lap splice remain much smaller compared to the element outside the lap splice region. Note that the large crack opening at the lap splice's ends may impair durability.
- The maximum deformation capacity of the entire lap splice is typically about half the minimum deformation capacity of the parts outside the splice. For high reinforcement ratios $\rho > 0.015$, the capacity even decreases to 1/3 (or even less). The effective deformation capacity depends strongly on the crack pattern but is less sensitive to parameter variations than a continuously reinforced tension chord.
- With the presented simplified approximation, an upper and lower bound of the expected deformation capacity of a lap splice can be derived. This is especially useful for practical applications to everyday engineering problems. Whenever assessing existing structures with lap splices located in zones potentially forming plastic hinges, their deformation capacity should be carefully analysed.
- For new structures, it is strongly recommended to place lap splices at least $1.3h$ (1.3 times the section height) away from highly loaded regions which potentially undergo plastic deformations. If this is not possible, account for the effect of lap splices (as additional reinforcement) on the behaviour. Furthermore, the overlapping length should be kept as short as possible.

Notation

A_c	Cross-sectional area of tension member (concrete and reinforcement)
A_s, A_{s1}, A_{s2}	Cross-sectional area of reinforcing bar (in general, of Bar 1, of Bar 2)
$A_{c,net}$	Cross-sectional area of concrete (without reinforcement)
E_c, E_s	Young's moduli of concrete and steel
F, F_1, F_2	External load, load of Bar 1, load of Bar 2
d	Effective reinforcement depth (section height minus concrete cover)
f_c	Concrete compressive strength
f_{ct}, f'_{ct}	Concrete tensile strength, with $f'_{ct} < f_{ct}$
f_{sy}, f_{su}	Steel yield stress and tensile strength
h	Section height
k	Total number of crack elements in lap splice
l_b, l_{tot}	Net overlapping length of reinforcing bars and total lap splice length with $l_{tot} = l_b + 2x_0 = \sum s_r^j$
$n = E_s/E_c$	Ratio of Young's moduli of steel and concrete
$s_{r,max}^{TCM}, s_{r,min}^{TCM}$	Maximum and minimum crack element length for original TCM
s_r, s_r^j	Crack element length (for element j)
$s_{r,max}^j, s_{r,min}^j$	Maximum and minimum length of crack element j of lap splice
$s_{r,max}^I, s_{r,min}^I, s_{r,max}^{II}, s_{r,min}^{II}$	Maximum and minimum length of boundary crack element for Case I and II
$u_c(x), u_s(x)$	Elongation of concrete section and reinforcing bar, respectively
w_r	Crack width
$w_{1L}^j, w_{1R}^j, w_{2L}^j, w_{2R}^j$	Contribution of Bar 1 and 2 to crack width of crack element j, left crack (L) and right crack (R)
x_0	Distance from end of Bar 2 (splicing bar) to left crack of boundary element
x_1^j, x_2^j	Location of minimum stress of Bar 1 and Bar 2 in crack element j
$x_1^I, x_2^I, x_1^{II}, x_2^{II}$	Distance from crack to location of maximum concrete stress in boundary crack element for Case I and II
x_{2a}, x_{2b}	Subdivision of length $x_2^I - x_0$: part with rigid bond, part with slipping bond
x_c	Depth of concrete compressive zone
Δ	Specimen deformation
$\varepsilon_c, \varepsilon_{c0}$	Concrete strain and shrinkage strain of reinforced concrete member
$\varepsilon_m, \varepsilon_{m,u}$	Mean strain of crack element (in general and at ultimate load = deformation capacity)
$\varepsilon_s, \varepsilon_{s1}, \varepsilon_{s2}$	Steel strain (in general, of Bar 1, of Bar 2)
$\varepsilon_{sy}, \varepsilon_{sh}, \varepsilon_{su}$	Steel strain at yielding, at onset of hardening and at ultimate load
$\lambda \in [0.5, 1]$	Factor for mean crack element length s_r
$\eta = \varnothing_1/\varnothing_2$	Ratio of reinforcing bar diameters in lap splice
$\rho = A_{s1}/A_c$	Reinforcement ratio for lap splice, defined using A_s of Bar 1 (Bar 2 considered via η)
$\rho_s = A_s/A_c$	Reinforcement ratio defined for TCM with single reinforcing bar
σ_c	Concrete stress
$\sigma_s, \sigma_{s1}, \sigma_{s2}$	Steel stress (in general, of Bar 1, and of Bar 2)
$\sigma_{1L}^j, \sigma_{1R}^j, \sigma_{2L}^j, \sigma_{2R}^j$	Steel stress in crack element j of Bar 1 and Bar 2, at left crack (L) and right crack (R)
$\sigma_{sr}, \sigma_{sr,cr}, \sigma_{sr,cr}^{TCM}$	Steel stress at crack (in general, at cracking load)
$\sigma_{sr,cr}^I, \sigma_{sr,cr}^{II}$	Steel stress at crack for boundary element in Case I and II at cracking load
τ_{b0}, τ_{b1}	Bond stress if reinforcing bar is elastic (0) and plastic (1), respectively
$\varnothing, \varnothing_1, \varnothing_2$	Reinforcing bar diameter (in general, of Bar 1, of Bar 2)

8 Modelling the load-deformation behaviour of retaining walls affected by local corrosion

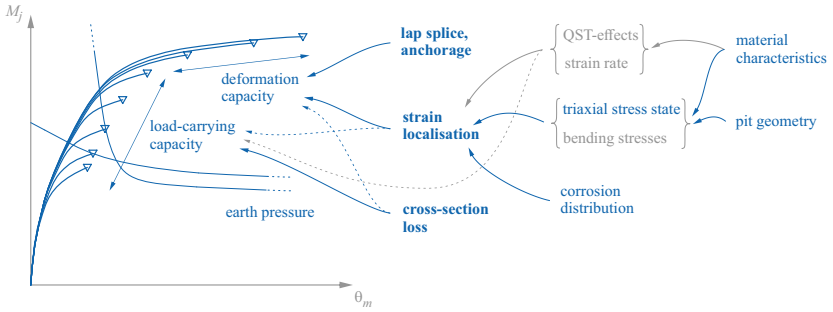

This chapter presents the findings of a modelling approach to predict the load-deformation behaviour of bending elements containing locally corroded reinforcing bars by combining the models presented in the previous chapters. Various further aspects influencing the behaviour are discussed, such as the effect of loading-unloading-sequences and the pullout behaviour of bent reinforcement. The model is validated against the results obtained in the experimental campaign on cantilever retaining wall segments, and conclusions regarding an observed softening effect are drawn. This chapter and the corresponding findings are not published nor submitted to a scientific journal. Severin Haefliger developed the presented modelling approaches and evaluated the resulting model predictions under the supervision of Walter Kaufmann.

8.1 Introduction

This chapter presents a modelling approach to predict the load-deformation behaviour of retaining walls containing locally corroded reinforcement. The chapter focuses on the effects of local corrosion damage observed in a pilot study conducted by the Swiss Federal Roads Office FEDRO [52] for existing cantilever retaining walls, which affects the main tensile reinforcement in the construction joint between the footing and the wall. Nevertheless, the model is generic and can be adapted to other corrosion situations and other types of structures.

The proposed model (see Figure 8.1) builds on existing moment-rotation relationships for flexural crack elements based on the Tension Chord Model (TCM), as developed by Burns [29], Kenel [93], and Pfyl [126]. These relationships are complemented with the findings regarding the load-deformation behaviour of corroded reinforcing bars, presented in the previous chapters, by means of the Corroded Tension Chord Model (CTCM) [72]. The model further accounts for the load-deformation behaviour of lap splices [75] – as commonly present directly above the construction joint in retaining walls – and includes a pull-out model for the anchorage of the reinforcement in the footing.

Thanks to its sound mechanical basis, the CTCM can readily be adapted to account for additional effects, such as the specific load-deformation behaviour of the reinforcing bar at a corrosion pit or a varying microstructure over the bar cross-section, as encountered in modern quenched and self-tempered (Tempcore®) reinforcing bars [71]. The latter effect is neglected here since most retaining walls affected by corrosion were built in the 1960s and 1970s, when only reinforcing bars with homogeneous

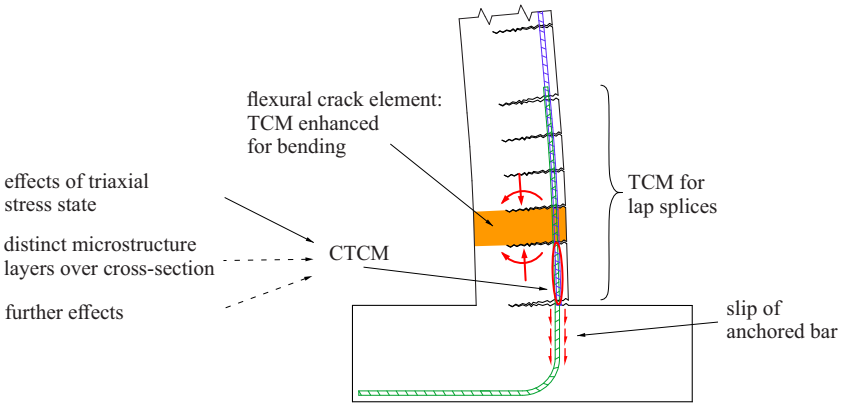

Fig. 8.1 – Combination of different models based on the TCM to assess the load-deformation behaviour of retaining walls affected by local corrosion of the reinforcement. The CTCM can be supplemented by other models describing specific effects regarding the load-deformation behaviour of the reinforcing bar at the corrosion pit. Figure adapted from [70].

microstructure were used (the Tempcore-process has found wide application only since the 1990s [137]). However, the CTCM is supplemented in the following to account for the effects of the triaxial stress state (TSS) at the corrosion pit and in its direct vicinity [76].

As mentioned in Section 1.3, the following aspects are not discussed in this chapter:

- The shear strength of retaining walls is deemed to be sufficient and thus not further investigated. The effect of shear forces on the tension chord force (tension shift) is, however, accounted for in a simplified manner.
- No load redistribution in longitudinal direction, i. e. between corroded and uncorroded segments of a retaining wall, is considered.
- The local load transfer between corroded and uncorroded reinforcing bars is not analysed in depth. As shown in the experimental campaign on retaining wall segments (Section 6.4.3), this transfer is possible by activating either the longitudinal reinforcement or the concrete tensile strength (no vertical cracks occurred in the experiments).

After briefly summarising existing moment-rotation models for flexural crack elements and their enhancement with the CTCM, the general application of the modelling concept to retaining walls and related aspects are introduced. The model is validated with the experiments on corroded retaining wall segments [74], and its accuracy is comprehensively discussed.

8.2 Modelling the moment-mean curvature relationship of flexural crack elements

Several approaches have been developed to predict the moment-mean curvature relationship of flexural crack elements (i. e. the moment-rotation relationship averaged over a flexural crack element) based on the TCM, i. e. consistently accounting for tension stiffening. As summarised by Galkovski et al. [64], the approaches can be divided into (i) models reducing the deformations obtained from a conventional cross-sectional analysis by considering tension stiffening a posteriori, and (ii) models which directly account for tension stiffening and related effects, such as a variable lever arm of internal forces, when formulating equilibrium. The first model type is referred to as tension chord-based model (TCB), and the second type as equilibrium-based models accounting for deformation compatibility (DC), as proposed by [64].

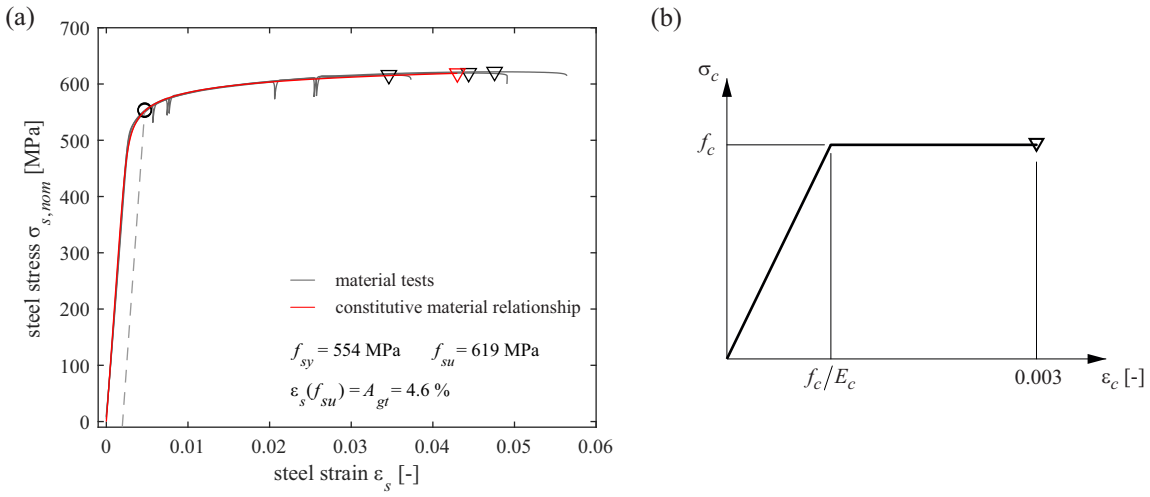

Fig. 8.2 – Constitutive relationships of (a) bare reinforcing steel and (b) concrete. Triangles indicate the peak load and the corresponding stress, and a circle indicates the yield stress (R_{p02}).

8.2.1 Constitutive material relationships

The stress-strain relationship of the bare reinforcing steel is modelled using Equation (5.5) of Section 5.3.2, with the coefficients $c_3 = 5.2 \cdot 10^{-7}$ and $c_4 = 0.18$, and steel characteristics as indicated in Figure 8.2(a) (equal to Figure 6.6). Figure 8.2(a) shows the results of the material tests (grey) and the constitutive relationship (red).

The concrete compression zone is modelled using a linear elastic-perfectly plastic stress-strain relationship as shown in Figure 8.2(b), a simplification often used in design (see, e. g. [145]). The concrete cylinder compressive strength f_c (different for every specimen and also different for wall and corresponding footing) and the elastic modulus E_c ($E_c \approx k_E \sqrt[3]{f_c}$ [MPa], $k_E = 10000$ [145]) result from the concrete material tests summarised in Table 6.3.

Bond is modelled according to the TCM [7] (see Section 2.3.1) using the concrete tensile strength f_{ct} summarised in Table 6.3.

The results obtained in Chapters 2 and 5 indicate that the stress-strain behaviour of the steel is decisive to accurately capture the load-deformation behaviour of a corroding structure. Hence, an elaborate constitutive relationship, closely matching that of the reinforcing bars, is used (Figure 8.2(a)). On the other hand, the shape of the stress-strain relationship of the concrete has a minor effect on the deformation capacity of bending elements due to the small depth of the compression zone, and rather influences the post-peak softening behaviour of the element. Since the latter is not analysed in this thesis, the simple bilinear relationship shown in Figure 8.2(b) is adopted.

8.2.2 Tension chord-based model TCB

Based on the TCM [7, 114], Burns [29] presented an approach to account for tension stiffening following a conventional cross-sectional analysis for elements in pure bending and linear elastic-cracked material behaviour. Formulating equilibrium at a crack for a rectangular cross-section, assuming plane sections to remain plane (hypothesis of Navier-Bernoulli), and neglecting the compression reinforcement, one gets:

$$\begin{aligned} N = 0 &= \sigma_s A_s - \frac{\sigma_c x_c b}{2} \\ M &= \sigma_c \frac{x_c^2 b}{3} + \sigma_s A_s (d - x_c) = \sigma_s A_s \left(d - \frac{x_c}{3} \right) \end{aligned} \tag{8.1}$$

with N, M = normal force and bending moment, σ_s, σ_c = steel and concrete stresses at the crack, b = section width, A_s = reinforcement cross-sectional area, d = effective static depth, and x_c = compression zone depth. With the curvature

$$\chi = \frac{\varepsilon_s}{d - x_c} = \frac{M}{EI} \tag{8.2}$$

where $\varepsilon_s = \sigma_s / E_s$, E_s = elastic modulus of steel, the bending stiffness EI^{II} of the fully cracked elastic cross-section follows as

$$EI^{II} = \frac{M(d - x_c)}{\varepsilon_s} = E_s A_s (d - x_c)\left(d - \frac{x_c}{3}\right) \tag{8.3}$$

Due to tension stiffening, the steel stresses and strains are highest at the crack and decrease towards the middle of a flexural crack element. Assuming a rigid-perfectly plastic bond shear stress-slip relationship following the TCM with a bond strength $\tau_{b0} = 2 f_{ct}$ for $\sigma_s(x) \leq f_{sy}$ (f_{ct} = concrete tensile strength, f_{sy} = steel yield stress), steel stresses and strains decrease linearly towards the middle of the crack element, similarly as in a tension chord introduced in Sections 2.3.1 and 7.2. Hence, a mean strain difference $\Delta\varepsilon_{sm}$ can be defined as the difference between the steel strain at the crack and the average strain along the tension chord. Using the notation of the TCM and Equation (2.A1) or (2.A2), the mean strain difference for linear elastic behaviour is

$$\Delta\varepsilon_{sm} = \varepsilon_s - \varepsilon_{sm} = \frac{\sigma_{sr}}{E_s} - \left(\frac{\sigma_{sr}}{E_s} - \frac{\tau_{b0} s_r}{E_s \varnothing}\right) = \frac{\tau_{b0} \lambda s_{r,max}}{E_s \varnothing} = \frac{\lambda f_{ct}(1 - \rho)}{2 E_s \rho} \tag{8.4}$$

with σ_{sr} = steel stress at crack, $s_r = \lambda \cdot s_{r,max}$ = crack element length (crack spacing), $\lambda \in [0.5, 1]$, $\varnothing$ = reinforcing bar diameter, $\rho = A_s / A_c$ = reinforcement ratio, and A_c = effective area of cross-section.

The mean strain difference is constant for a fully established crack pattern and independent of the external load, as seen from Equation (8.4). However, unlike for a tension chord, the effective reinforcement ratio ρ is not clearly defined for a flexural element and is still a focus of ongoing research [64]. A mechanically consistent approach consists in postulating that at crack formation (i. e. for the cracking moment), the steel stress at the crack in the flexural element is equal to the steel stress at the crack of a tension chord element with the effective reinforcement ratio ρ [29]; a recent study investigating the tension zone of reinforced concrete beams in four-point bending tests instrumented with fibre optic strain sensing showed that this assumption correlates well with experimental results [64]. Using this approach, Equations (8.2) and (7.8) yield

$$\begin{aligned} \sigma_{sr,cr} &= \frac{M_{cr} E_s (d - x_c)}{EI^{II}} \stackrel{!}{=} \frac{f_{ct}}{\rho}(1 + \rho(n-1)) \\ \rightarrow \rho &= \left(\frac{M_{cr} E_s (d - x_c)}{f_{ct} EI^{II}} - n + 1\right)^{-1} = \left(\frac{M_{cr}}{A_s f_{ct} (d - x_c/3)} - n + 1\right)^{-1} \\ &\approx \left(\frac{bh^2}{6 A_s (d - x_c/3)} - n + 1\right)^{-1} \end{aligned} \tag{8.5}$$

with M_{cr} = cracking moment, $\sigma_{sr,cr}$ = steel stress at crack for $M = M_{cr}$, $n = E_s / E_c$ = ratio of elastic moduli, E_c = elastic modulus of concrete, and h = section height. As seen from Equation (8.5), the equivalent reinforcement ratio is significantly higher than the geometrical reinforcement ratio $A_s/(bd)$. Using the mean strain difference $\Delta\varepsilon_{sm}$ of the tension chord, the mean curvature difference follows from the assumption of plane sections remaining plane as

$$\Delta\chi_m = \frac{\Delta\varepsilon_{sm}}{d - x_c} = \frac{\lambda f_{ct}(1 - \rho)}{2\rho E_s (d - x_c)} = \frac{\lambda}{2}\left(\frac{M_{cr}}{EI^{II}} - \frac{n f_{ct}}{E_s (d - x_c)}\right) \tag{8.6}$$

Subtracting the curvature difference from the curvature resulting from a conventional cross-sectional analysis (neglecting tension stiffening) yields the moment-mean curvature relationship accounting for tension stiffening.

Whereas Burns [29] analysed the elastic load-deformation behaviour of flexural elements to investigate questions related to serviceability, the approach can be enhanced for nonlinear material behaviour. The length of flexural crack elements $\lambda \cdot s_{r,max}$ follows from inserting the reinforcement ratio ρ determined by Equation (8.5) in the corresponding equation of the TCM (Equation (7.7) in Section 7.2). The assumption that a stabilised crack pattern does not change with increasing external load, i. e. the crack element length is constant, allows determining the mean steel strains ε_{sm} of a corresponding tension chord for arbitrary external loads using the TCM (Equations (2.A1) and (2.A2)). Inserting this mean steel strain in Equations (8.4) and (8.6) and combining the resulting mean curvature difference with a nonlinear cross-sectional analysis yields the mean curvature of a flexural crack element for elastic and plastic material behaviour.

8.2.3 Equilibrium-based models accounting for deformation compatibility

Equilibrium-based models accounting for the deformation compatibility of a flexural crack element have been established for conventionally reinforced concrete by Kenel [93] and for steel fibre reinforced concrete (including conventional reinforcement) by Pfyl [126]. The latter approach, which is very similar to Kenel's model and yields essentially the same results if the steel fibres are omitted (see comment at the end of this section), is presented below and used subsequently.

Consider a symmetrical crack element with the dimensions illustrated in Figure 8.3 (s_r = flexural crack spacing = element length), assuming rigid bond in the compression zone (i. e. steel and concrete strains coincide along the entire element). In the tension zone, however, the steel and concrete strains generally differ substantially, causing slip (i. e. relative displacements between steel and concrete, vanishing in Section I due to symmetry).

A cross-sectional analysis is first conducted for Section I at the centre between two cracks, assuming a linear distribution of the axial strains over the depth of the cross-section and accounting for the combined action of reinforcement and concrete in the compression and tension zone. Assuming a linear elastic behaviour of the concrete in Section I (but an arbitrary stress-strain relationship for the reinforcement), one gets by equilibrium:

$$\begin{aligned} N &= A_s\sigma_s^I\left(\varepsilon_s^I\right) && +E_c\varepsilon_{c,inf}^I b\frac{h-x_c^I}{2} && -E_c\varepsilon_{c,sup}^I b\frac{x_c^I}{2} && -E_sA_s'\varepsilon_s'^I \\ M &= \underbrace{A_s\sigma_s^I\left(\varepsilon_s^I\right)\left(d-x_c^I\right)}_{\text{tensile reinforcement}} && \underbrace{+E_c\varepsilon_{c,inf}^I b\frac{\left(h-x_c^I\right)^2}{3}}_{\text{concrete in tension}} && \underbrace{-E_c\varepsilon_{c,sup}^I b\frac{\left(x_c^I\right)^2}{3}}_{\text{concrete in compression}} && \underbrace{-E_sA_s'\varepsilon_s'^I\left(x_c^I+d-h\right)}_{\text{compressive reinforcement}} -N\left(\frac{h}{2}-x_c^I\right) \end{aligned} \tag{8.7}$$

with A_s' = cross-sectional area of reinforcement in compression zone. The concrete strains at the lower and upper edges of the cross-section, $\varepsilon_{c,inf}$ and $\varepsilon_{c,sup}$, and the steel strains in the compression zone, ε_s', are related by the conditions $\varepsilon_{c,inf} = (d-x_c^I)\varepsilon_{c,sup}/x_c^I$ and $\varepsilon_s' = (x_c^I-h+d)\varepsilon_{c,sup}/x_c^I$ (assuming equal concrete cover at top and bottom).

Following the concept of the TCM, the bond stresses acting along the reinforcing bar in the tensile zone merely depend on the steel stress, i. e. $\tau_{b0} = 2f_{ct}$ where $\sigma_s(x) \le f_{sy}$ and $\tau_{b1} = f_{ct}$ where $\sigma_s(x) > f_{sy}$.

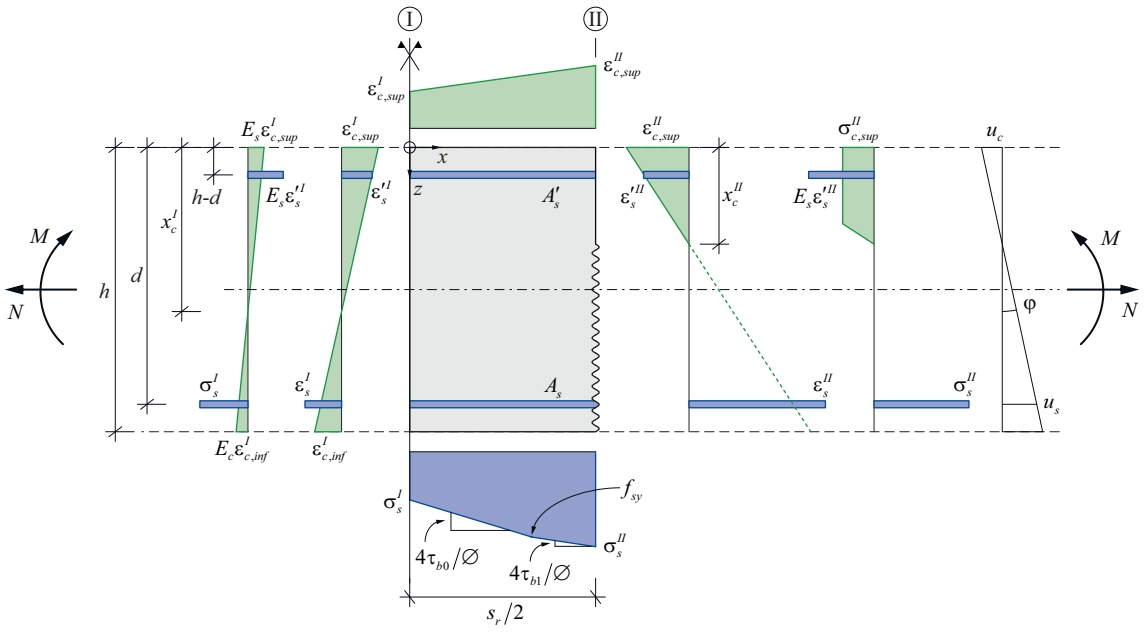

Fig. 8.3 – Half of a flexural crack element according to [93, 126] (symmetrical with respect to Section I) with the strain and stress distributions and the corresponding rotation at the centre between two cracks (Section I) and at the crack (Section II). Steel stresses along the reinforcing bar according to the TCM are shown at the bottom, and the concrete strain distribution is illustrated at the top.

Hence, starting from the steel stress σ_s^I in Section I, the steel stress in Section II follows as:

$$\begin{aligned}
\sigma_s^{II} &= \sigma_s^I + \frac{4\tau_{b0}}{\varnothing}\frac{s_r}{2} && \leq f_{sy} \quad \text{for } \sigma_s^I < f_{sy} \\
\sigma_s^{II} &= f_{sy} - \left(f_{sy} - \sigma_s^I\right)\frac{\tau_{b1}}{\tau_{b0}} + \frac{4\tau_{b1}}{\varnothing}\frac{s_r}{2} && > f_{sy} \quad \text{for } \sigma_s^I < f_{sy}. \\
\sigma_s^{II} &= \sigma_s^I + \frac{4\tau_{b1}}{\varnothing}\frac{s_r}{2} && > f_{sy} \quad \text{for } \sigma_s^I \geq f_{sy}
\end{aligned} \tag{8.8}$$

Using the steel stress determined by Equation (8.8), a cross-sectional analysis is now conducted in Section II, assuming a linear distribution of the axial strains over the depth of the compression zone. For arbitrary stress-strain relationships of steel and concrete, equilibrium yields:

$$\begin{aligned}
N &= A_s\sigma_s^{II} && - \int_0^{x_c^{II}} \sigma_c\left(\varepsilon_{c,sup}^{II}\right) b\,dz && - A'_s\sigma'^{\,II}_s\left(\varepsilon'^{\,II}_s\right) \\
M &= \underbrace{A_s\sigma_s^{II}\left(d - x_c^{II}\right)}_{\text{tensile reinforcement}} && \underbrace{- \int_0^{x_c^{II}} \sigma_c\left(\varepsilon_{c,sup}^{II}\right) z\,b\,dz}_{\text{concrete in compression}} && \underbrace{- A'_s\sigma'^{\,II}_s\left(\varepsilon'^{\,II}_s\right)\left(x_c^{II} - h + d\right)}_{\text{compressive reinforcement}} - N\left(\frac{h}{2} - x_c^{II}\right)
\end{aligned} \tag{8.9}$$

with the identical applied loads M and N as in Equation (8.7). For linear elastic material behaviour, the terms for the concrete contribution simplify to $\int_0^{x_c^{II}} \sigma_s\left(\varepsilon_{c,sup}^{II}\right) b\,dz = E_c\varepsilon_{c,sup}^{II} b\frac{x_c^{II}}{2}$ and $\int_0^{x_c^{II}} \sigma_s\left(\varepsilon_{c,sup}^{II}\right) b\,z\,dz = E_c\varepsilon_{c,sup}^{II} b\frac{\left(x_c^{II}\right)^2}{3}$.

As mentioned above, the steel strains in the tension zone do not need to be compatible with the concrete strain plane, as assumed in conventional cross-sectional analyses. Instead, compatibility is established by the condition that axial deformations vary linearly over the depth of the cross-section.

They vanish at the depth of the neutral axis in Section II, i. e.

$$\varphi = \frac{u_s}{d - x_c^{II}} = \frac{u_c}{x_c^{II}} \tag{8.10}$$

where φ = relative rotation of cross-section II. The reinforcing bar elongation u_s equals the integral of the steel strains (obtained from the steel stresses and a suitable constitutive relationship) over half the element length. The concrete strains are assumed to vary linearly along the element, and the shortening u_c follows by integration along the element half:

$$\begin{aligned} u_s &= \int_0^{s_r/2} \varepsilon_s(x)dx \\ u_c &= \int_0^{s_r/2} \varepsilon_{c,sup}(x)dx = \frac{\left(\varepsilon_c^I + \varepsilon_c^{II}\right)_{sup}}{2} \frac{s_r}{2} \end{aligned} \tag{8.11}$$

The six independent Equations (8.7) to (8.11) yield a unique solution for the six unknowns $\left\{\varepsilon_s^I,\ \varepsilon_{c,inf}^I,\ x_c^I,\ \varepsilon_s^{II},\ \varepsilon_{c,sup}^{II},\ x_c^{II}\right\}$ for any set of applied loads N and M. However, the validity of the made assumptions and the compliance with the boundary conditions, e. g. the material properties, need to be verified. In particular, the concrete stress $\sigma_{c,inf}^I$ in Section I should not excessively exceed the concrete tensile strength; the chosen crack element length might be inappropriate otherwise.

The theoretical upper bound of the crack element length $s_{r,max}$ is determined by treating it as unknown in Equations (8.7) to (8.11), and setting the concrete tensile strain in Section I equal to the strain at cracking, $\varepsilon_{c,inf}^I = f_{ct}/E_c$. As in the TCM, the lower bound of the crack element length is $s_{r,max}/2$ since an additional crack may form at the centre of two cracks with a spacing $s_{r,max}$.

The models of Kenel [93] and Pfyl [126] merely differ in the assumptions made regarding Section I. Whereas Pfyl considers concrete stresses over the entire cross-section (in the tension and compression zone) independent of the applied bending moment, Kenel neglects the concrete contribution in the tensile zone for $M > M_{cr}$ and, in such cases, superimposes the strain planes obtained for M_{cr} and $M - M_{cr}$ (with and without concrete contribution in the tensile zone, respectively). Interestingly, despite the very different concrete compressive stresses in Section I resulting for increased loads, the moment-mean curvature relationships predicted by both models almost coincide, with Pfyl's model being slightly softer.

8.2.4 Enhancement of equilibrium-based model with the CTCM

In the following, the concept of the CTCM is implemented in the equilibrium-based model of Pfyl introduced in Section 8.2.3, i. e. the tension chord (Equation (8.8)) is complemented by a corrosion pit, as illustrated in Figure 8.4: the cross-section of the reinforcing bar in tension is reduced to $(1-\zeta)A_s$ over a length $\beta \cdot s_r$ adjacent to one of the cracks bounding the flexural crack element (see Section 2.2.2 and Equation (2.1)). A loss of bond simulating the effect of a honeycomb is considered over an additional length $\delta \cdot s_r$, thereby reducing the length of the conventional flexural crack element to $(1-\beta-\delta)s_r$.

Over the length $(\beta+\delta)s_r$, the tensile force in the reinforcement is constant due to the loss of bond; hence, the concrete compressive stresses and the location of the neutral axis are constant over this length, and Equations (8.7) to (8.9) remain valid except for the shorter element length. As in the CTCM, steel stresses increase at the corrosion pit due to the reduced cross-sectional area. The deformations in Equation (8.11) at the crack (Section III) change to

$$\begin{aligned} u_s &= u_{s,uc} + u_{s,c} = \int_0^{(1-\beta-\delta)s_r/2} \varepsilon_s(x)dx + \beta s_r \varepsilon_s\left(\frac{\sigma_s^{II}}{1-\zeta}\right) + \delta s_r \varepsilon_s\left(\sigma_s^{II}\right) \\ u_c &= u_{c,uc} + u_{c,c} = \frac{\left(\varepsilon_c^I + \varepsilon_c^{II}\right)_{sup}}{2} \frac{(1-\beta-\delta)s_r}{2} + \varepsilon_{c,sup}^{II}(\beta+\delta)s_r \end{aligned} \tag{8.12}$$

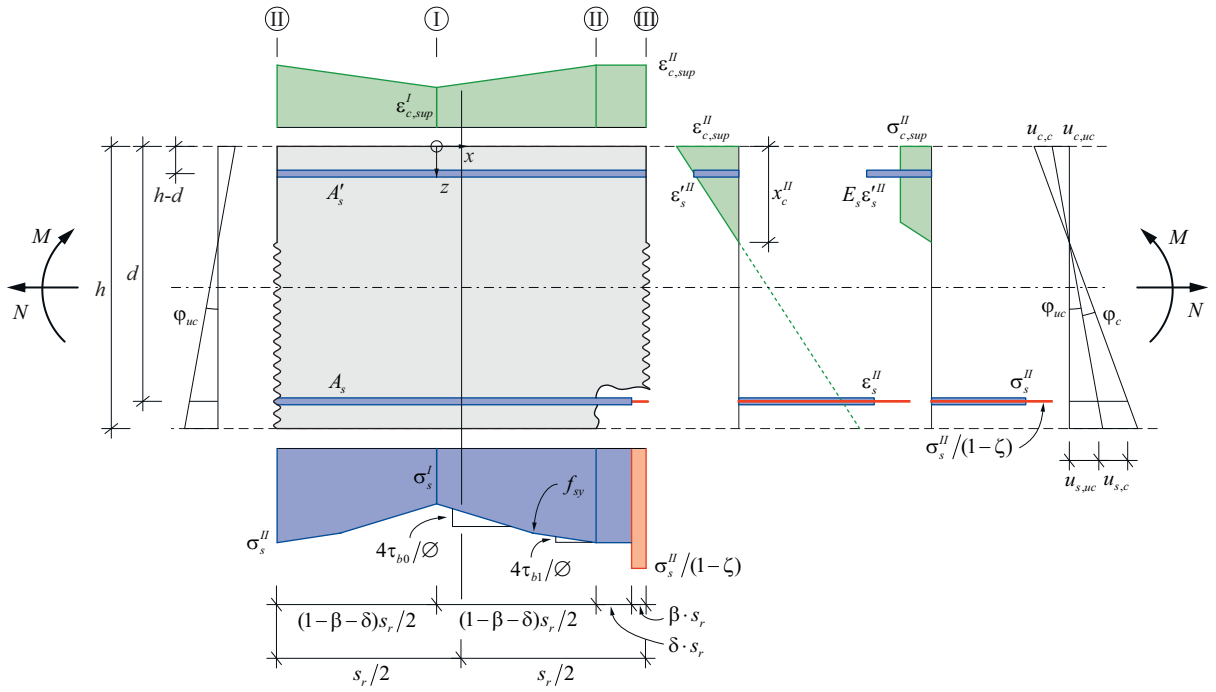

Fig. 8.4 – Entire flexural crack element with bond-free length $(\beta+\delta)\cdot s_r$ near the right crack, where the reinforcing bar exhibits a relative cross-section loss ζ over a length $\beta\cdot s_r$. Strain and stress distributions in Section III are shown along with the element rotation. The steel stress distribution along the reinforcing bar according to the CTCM is shown at the bottom and the concrete strain distribution at the top.

with $u_{s,uc}$, $u_{s,c}$ = elongation of the bar over its uncorroded and corroded (and bond-free) length, and $u_{s,uc}$, $u_{s,c}$ = shortening of concrete between Sections I-II and II-III, respectively. The deformation compatibility condition of Equation (8.10) is modified to

$$\varphi = \varphi_{uc} + \varphi_c = \frac{u_{s,uc} + u_{s,c}}{d - x_c^{II}} = \frac{u_{c,uc} + u_{c,c}}{x_c^{II}} \tag{8.13}$$

and the mean curvature over the entire flexural crack element changes to

$$\chi = \frac{\varphi_c + 2\varphi_{uc}}{s_r} \tag{8.14}$$

8.3 Modelling the load-deformation behaviour of corroded cantilever retaining walls

To predict the load-deformation behaviour of cantilever retaining walls with corroded main tensile reinforcement, the models for the moment-mean curvature relationships of corroded and uncorroded flexural crack elements presented in Sections 8.2.3 and 8.2.4 are combined with previously developed approaches capturing the effects of lap splices (Chapter 7) and the loading history (loading-unloading behaviour) [7, 94]. Furthermore, this section outlines how the effects of a triaxial stress state at the corrosion pit (Chapter 5) and the influence of longitudinal splitting cracks on the bond behaviour of flexural elements [2, 64] can be considered.

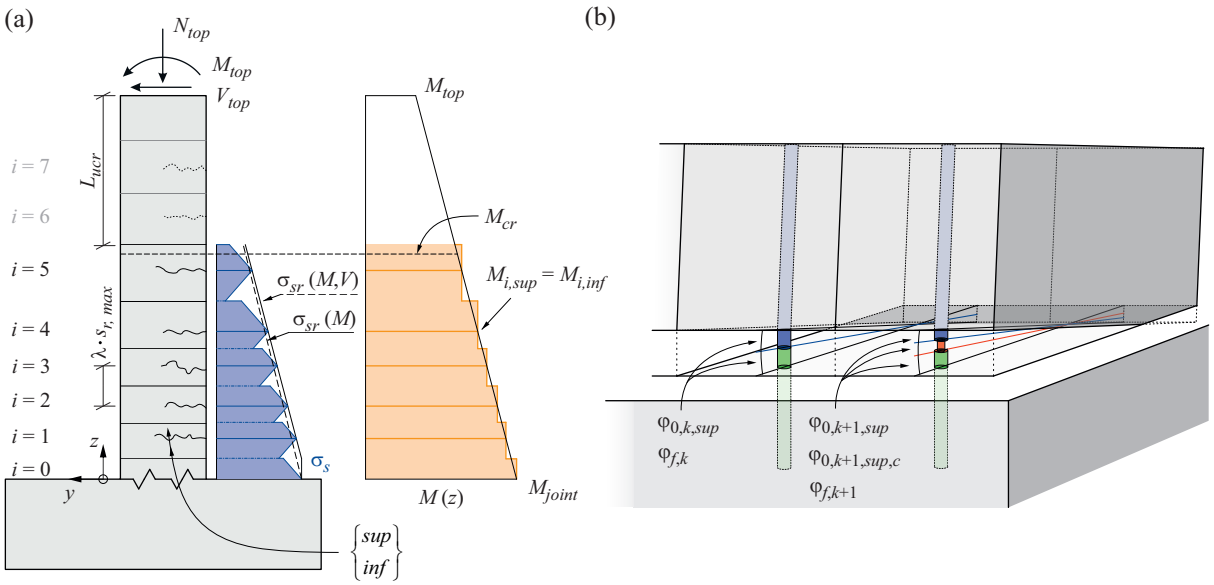

Fig. 8.5 – Dividing a retaining wall into several half crack elements: (a) definition of variables and loading of the wall as in the experiments (Chapter 6); (b) rotation compatibility of parallel flexural crack elements at construction joint.

8.3.1 General modelling concept

For the analysis, the retaining wall is discretised into flexural crack elements, whose load-deformation behaviour is subsequently predicted. It is assumed that crack elements in parallel (corresponding to the individual reinforcing bars with different corrosion damage) exhibit equal deformations. This assumption bases on the high in-plane stiffness of the uncracked concrete between adjoining cracks, and leads to force redistributions between elements of different stiffness. Finally, the deformations of the crack elements are summed up over the wall height to obtain the global deformation of the retaining wall.

Discretisation of the wall and assigning the loads

A retaining wall of a given height H, width B, and bar spacing s is divided into $k_{tot} = B/s$ wall strips of width $b = s$, i. e. one strip per reinforcing bar. For simplicity, only retaining walls with constant geometrical properties along their length, i. e. constant cross-section, reinforcing bar diameter and spacing, are considered in the following. All cracks are assumed to run horizontally along the entire wall width, dividing the wall height into layers of flexural crack elements. The mean crack spacing $s_r = \lambda \cdot s_{r,max}$ defines the height of the crack element layers, where $\lambda \in [0.5, 1]$ for every layer and $s_{r,max}$ = maximum crack element length resulting from the model described in Section 8.2.3. Each crack element is further divided into two half crack elements whose deformations are determined independently. For a simpler notation, the half crack elements above and below a crack are combined to one element and assigned the same index i, rather than considering a crack element bounded by two cracks. The subscript *inf* denotes the half crack element below the crack, and the subscript *sup* the one above, see Figure 8.5(a).

Retaining walls are generally subjected to a combination of vertical normal force and variable out-of-plane shear forces. Thus, the bending moment varies along the wall height, in contrast to the equilibrium-based models described in Section 8.2.3, which assume constant bending moments, i. e. $dM/dz = 0$. To use these models, the bending moment profile is approximated by a stepped distribution, where the bending moment M_i at the location of a crack corresponds to the exact value. It is kept constant over the adjacent half crack elements above and below the crack, resulting in a discontinuity at the centre between two cracks, see Figure 8.5(a).

Half crack elements subjected to a bending moment exceeding the cracking moment, i. e. $M_i > M_{cr}$, are modelled according to Section 8.2.3, resulting in a serrated steel stress distribution as shown in blue in Figure 8.5(a). The deformation of the sections in the uncracked region (potential cracks forming at a higher load are indicated with dotted lines in Figure 8.5(a)) is modelled using the uncracked elastic bending stiffness. The construction joint ($i = 0$) is assumed to be a cold joint with zero tensile strength, and thus to be cracked from the beginning. The influence of the shear force V is considered in the cross-sectional analysis of the cracked layers in Equations (8.7) and (8.9) by adding a tensile normal force $V \cdot \cot(\theta_r)$ to the tension and compression chord forces caused by bending. This corresponds to accounting for the tension shift in members without shear reinforcement as proposed in [87] (i. e. assuming cracks inclined at an angle θ_r to the z-axis transferring pure shear stresses in their direction). With the experimentally observed crack inclination of $\theta_r = 78°$ with respect to the vertical, this results in slightly higher tensile stresses for crack elements $i \geq 1$, denoted with $\sigma_{sr}(M,V)$ in Figure 8.5(a).

Moment-rotation behaviour of a cracked layer

The rotation $\varphi_{i,inf/sup}$ of the half crack elements is calculated for the corresponding bending moment $M_{i,k}$ using Equations (8.7) to (8.13). If the reinforcement is uncorroded, it is sufficient to calculate the rotation for one of the parallel crack elements along the wall width, with $M_{i,k} = M_i/k_{tot}$. For layers consisting of corroded and uncorroded reinforcing bars, however, different bending moments $M_{i,k}$ result for each parallel crack element due to the varying stiffness. The bending moments can be determined by requiring compatibility at the cracks, i. e. all parallel crack elements need to exhibit equal rotation:

$$\begin{aligned} &\varphi_{i,k} = \varphi_i \\ &\sum_{k=1}^{k_{tot}} M_{i,k} = M_i \end{aligned} \tag{8.15}$$

with the rotation of each parallel crack element corresponding to the sum of the rotations of the half crack elements above and below the crack, i. e. $\varphi_{i,k} = \varphi_{i,k,inf} + \varphi_{i,k,sup}$, see Figures 8.5(a) and (b). At the construction joint, the rotation is

$$\begin{aligned} &\varphi_{0,k} = \varphi_{0,k,sup} + \varphi_{f,k} \\ &\varphi_{f,k} = \frac{u_{s,f,k}}{d - x^{II}_{0,k,sup}} \end{aligned} \tag{8.16}$$

with $x^{II}_{0,k,sup}$ = compression zone depth of the half crack element above the construction joint. The rotation $\varphi_{f,k}$ in Equation (8.16) is caused by the pull-out of the reinforcement anchored in the footing, causing a deformation $u_{s,f,k}$, whose value is discussed in Section 8.4.

The compatibility condition in Equation (8.15) is similar to the one introduced in the CTCM for several corroded and uncorroded tension chords acting in parallel (Equation (2.23) in Section 2.3.3). It assumes that the in-plane stiffness of the parallel crack elements is sufficient to compensate for their differing moment-rotation behaviour, and that resulting load differences are balanced within one crack element layer, i. e. the half crack elements above and below the crack. This assumption was validated using fibre optic strain measurements in the experimental campaign on corroded retaining wall segments, where the load difference was found to be balanced within a length of less than two crack elements (see Section 6.4.3).

Load-deformation behaviour of the entire retaining wall

The moment-rotation relationships of the single half crack elements directly result from the calculations outlined in the previous section. Summing the rotation of the half crack elements below and above a

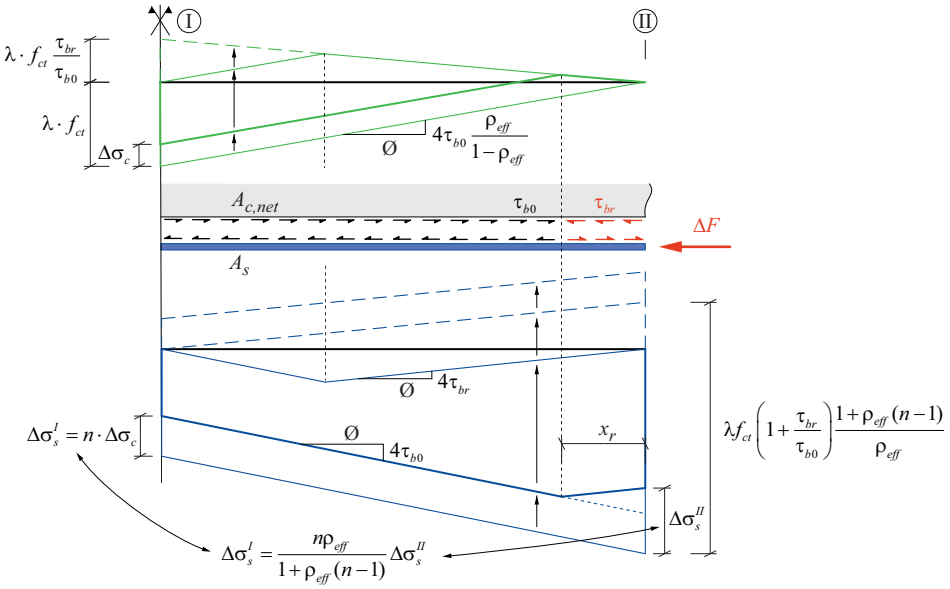

Fig. 8.6 – Unloading of a half crack element (Section I: centre between two cracks, Section II: at the crack) according to the TCM [7, 94]: Stress profiles of reinforcing bar (blue) and concrete (green) for a force decrease ΔF. $\tau_{br} < \tau_{b0}$ indicates the reversed bond stress for a slip reversal.

crack i and multiplying with the adjacent crack element length yields the wall displacement at crack $i+1$, and the wall head, respectively

$$v(z) = (\varphi_f + \varphi_{0,sup})\, s_{r,1} + \sum_{i \geq 1} (\varphi_{i,inf} + \varphi_{i,sup})\, s_{r,i+1} \tag{8.17}$$

with the length of the last crack element $s_{r,i} = L_{uncracked}$ (see Figure 8.5(a)) and φ_f according to Equation (8.16). Note that the elastic contribution of the uncracked wall section to the total wall rotation is neglected in Equation (8.17) as it is magnitudes smaller compared to the rotations resulting from the cracked part and the opening of the construction joint; the rigid-body rotation of the uncracked part is, however, accounted for.

8.3.2 Further effects on the moment-rotation behaviour

Load reversal

For an increasing cross-section loss at constant (or decreasing) load, the bending moment $M_{i,k}$ of the corroded crack elements decreases due to the reduced tensile stiffness of the reinforcing bar (see the behaviour of parallel Tension Chords in Section 2.3.3 and the experimental results in Section 6.4.3). The unloading of a reinforcing bar in concrete is accompanied by a progressive slip reversal and a reversal of the bond stress direction. Alvarez [7] presented a first concept to capture the unloading behaviour based on the TCM, which was revisited and experimentally validated by Koppitz et al. [94]. The concept assumes that a reversed slip immediately leads to reversed bond stresses, which propagate from the crack towards the crack element centre with decreasing load, see Figure 8.6. Experiments on reinforced concrete beams tested in four-point bending and instrumented with fibre optic strain sensing indicated that bond is degraded even for the first unloading-reloading cycle, and the reversed bond stresses τ_{br} are thus lower than the initial bond stresses τ_{b0} [94]. Based on the experimental results, a value $\tau_{br} = \tau_{b1}$ was suggested for regions undergoing slip reversal. For a full unloading-reloading cycle, the reduced bond stress leads to an asymmetric stress state in the crack element (Figure 8.6) and, therefore, to a hysteresis in the load-deformation curve.

The concept proposed in [94] is adopted for bending elements by replacing Equation (8.8) as outlined below. To this end, for the sake of conciseness, the effective reinforcement ratio ρ_{eff} of a bending element is introduced; this ratio is based on the fictitious net concrete area $A_{c,net}$ activated in tension at the crack element centre (Section I), assuming that constant tensile stresses λf_{ct} act over $A_{c,net}$ at crack formation. Since the tensile force $F_{c,cr} = \lambda f_{ct} A_{c,net}$ is transferred to the concrete by the bond shear stresses acting over half the crack spacing s_r, one gets:

$$\begin{aligned} F_{c,cr} &= \frac{4\tau_{b0}}{\O}\frac{s_r}{2}A_s \\ A_{c,net} &= \frac{F_{c,cr}}{\lambda f_{ct}} = \frac{2\tau_{b0}}{\lambda f_{ct}}\frac{s_r}{\O}A_s \\ \rho_{eff} &= \frac{A_s}{A_s + A_{c,net}} = \frac{\lambda f_{ct}\O}{2\tau_{b0}s_r + \lambda f_{ct}\O} \end{aligned} \tag{8.18}$$

Note that ρ_{eff} is defined as usual, based on the gross concrete area $A_c = A_{c,net} + A_s$, rather than the net concrete area. For a stress decrease $\Delta\sigma_s^{II}$ at the crack, slip reversal occurs over the length x_r, and the following equations are found by formulating equilibrium on the free body between Section I and II (see [94]):

$$\begin{aligned} & A_s\Delta\sigma_s^I + A_{c,net}\Delta\sigma_c^I = A_s\Delta\sigma_s^{II} \\ & \Delta\sigma_s^I = n\cdot\Delta\sigma_c^I && \text{for } \left|\Delta\sigma_c^I\right| \le \lambda f_{ct}\left(1+\frac{\tau_{br}}{\tau_{b0}}\right) \\ & \rightarrow \Delta\sigma_s^I = \frac{n\rho_{eff}}{1+\rho_{eff}(n-1)}\Delta\sigma_s^{II} && \text{for } \left|\Delta\sigma_s^{II}\right| \le \lambda f_{ct}\left(1+\frac{\tau_{br}}{\tau_{b0}}\right)\frac{1+\rho_{eff}(n-1)}{\rho_{eff}} \end{aligned} \tag{8.19}$$

For a steel stress decrease $\left|\Delta\sigma_s^{II}\right|$ exceeding the indicated application limit of Equation (8.19), the concrete stress in Section I remains constant at $\sigma_c = -\lambda f_{ct}\tau_{br}/\tau_{b0}$ (Figure 8.6) and the steel stress in the same section is $\sigma_s^I = \sigma_s^{II} + 2\tau_{br}s_r/\O$.

Lap splice

As outlined in Chapter 7, the load transfer between two reinforcing bars in a lap splice mainly occurs at its ends. The first and last crack element was found to behave approximately like a conventional crack element with a reinforcement ratio $\rho = \rho_s$, whereas all other crack elements behave like crack elements with double reinforcement ratio $\rho = 2\rho_s$ (regarding element length and load-deformation behaviour). These findings are adopted for modelling the lap splice in a retaining wall by assigning the double steel cross-sectional area $2A_s$ to the crack elements over the lap splice length, except for the first and the last crack element (i. e. the first and last two half crack elements).

In a lap splice, the load is transferred from one bar to the other by an asymmetric distribution of bond stresses and a shift of the location of minimum steel stress towards one of the cracks (see Figure 7.2). For high external loads and short crack elements, the reinforcing bar may even be pulled through the first crack element(s), see Figure 7.3(b). In this case, the location of minimum steel stress coincides with the crack location. Figures 7.9(b) and (c) show that a pull-through can occur for the first or even the first two crack elements.

Similarly, flexural crack elements subjected to a bending moment gradient $|dM(z)/dz| > 0$ exhibit an asymmetric bond stress distribution, as already discussed by Sigrist [146], causing a shift of the location of minimum steel stress to the less loaded side. The magnitude of the shift depends on the local bending moment gradient, which is typically substantial at the base of a retaining wall due to the triangular earth pressure distribution.

If a lap splice is placed in this zone of high bending moment gradient, the shifts of the minimum steel stress location caused by (i) the bending moment gradient and (ii) the lap splice boundary are superimposed, which leads to a considerable deformation increase on the side of the footing already for moderate loads. For high loads, a pull-trough of the reinforcing bar is likely to occur since the element length is short due to the high reinforcement ratio of the lap splice. To approximately capture the influence of the asymmetric steel stress distributions in the crack elements at the wall bottom on the global wall deformations, Equation (8.16) is modified, and the following rotations are used in Equation (8.17):

$$\begin{aligned} \varphi_0 &= \varphi_f + \varphi_{0,sup} + \varphi_{1,inf} \\ \varphi_1 &= \varphi_{1,sup} + \varphi_{2,inf} \\ \varphi_2 &= \varphi_{2,sup} \end{aligned} \tag{8.20}$$

with φ_i = rotation in crack i. With this modification, the rotations determined for the affected cracks (without considering the asymmetric steel stress behaviour) are partly assigned to the crack below, resulting in higher wall deflections. This approximation allows to use the model outlined in Section 8.2.3 and the discretisation proposed in Section 8.3.1 without underestimating the global wall deformations.

Bond stresses in case of splitting cracks

The occurrence of splitting cracks leads to significantly lower bond stresses, as shown by several studies (for an overview, see [33, 56, 57]). For a mean concrete compressive strength of 42 MPa (average strength of walls in experiments described in Chapter 6, see Table 6.3), the Model Code 2010 [57] proposes to reduce the maximum and residual bond strength in case of splitting cracks to 49%...56% of the reference values (for pull-out conditions, no splitting cracks). Recent studies on reinforced concrete beams and slab strips tested in four-point bending and instrumented with fibre optic strain sensing reported a very similar reduction [2, 64]; the measured bond strength was reduced by approximately 50% compared to literature values in the case of splitting cracks.

In the experiments on retaining wall segments (Chapter 6), splitting cracks occurred at load stages close to failure (i) at the outermost reinforcing bars (Bars 1 and 10) over the length of the lap splice and (ii) for many of the bars in the bottom crack element adjacent to the footing (see Figure 6.11(a)). For some of the experiments, additional splitting cracks were observed post-peak in the last crack element of the lap splice (0.9 m above the footing). The splitting cracks at the outermost reinforcing bars can be explained by the reduced lateral geometrical confinement, compared to the interior bars. The splitting cracks close to the footing at high loads are potentially caused by the situation of a yielding reinforcing bar, presumably pulled through the crack element (see previous section), next to the passive end of the splicing bar exhibiting almost no deformations. If these explanations apply, the phenomenon would have to be expected generally for lap splice ends undergoing high loads in combination with high load gradients. However, further studies are required to substantiate this hypothesis. Regardless of this remark, the experimentally observed splitting cracks are accounted for in the model by reducing the bond stress in the bottom crack element after yielding onset to 50% of the original value, i. e. $\tau_{b1} = f_{ct}/2$ (instead of $\tau_{b1} = f_{ct}$).

8.3.3 Stress-strain behaviour of corrosion pit

Triaxial stress state (TSS)

Since the influence of a triaxial stress state (TSS) on the stress-strain relationship of corroded reinforcing bars was investigated in Chapter 5 for axisymmetric damage, the results cannot directly be applied to the reinforcing bars in the experimental campaign exhibiting unilateral damage. Nevertheless, its potential

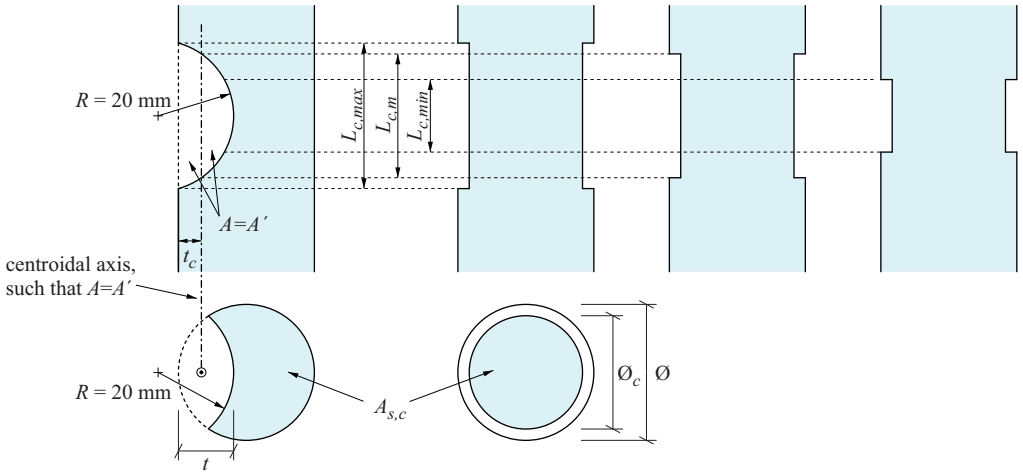

Fig. 8.7 – Approximating unilateral corrosion damage with an axisymmetric cross-section reduction of equal cross-sectional area $A_{s,c}$. Definition of maximum, mean, and minimum damage length L_c.

Tab. 8.1 – Maximum, mean, and minimum damage lengths L_c depending on the cross-section loss, defined according to Figure 8.7.

cross-section loss ζ [-]	maximum pit depth t [mm]	position of centroidal axis t_c [mm]	$L_{c,max}$ [mm]	$L_{c,m}$ [mm]	$L_{c,min}$ [mm]
0.10	3.4	1.4	15.0	12.0	7.5
0.15	4.5	1.9	16.7	13.6	8.4
0.20	5.5	2.3	17.9	14.8	9.0
0.30	7.3	3.0	19.2	16.4	9.6

influence can be investigated by approximating the geometry of a unilateral, spherical corrosion pit with an axisymmetric damage geometry of equal cross-section loss and three different damage lengths $\beta \cdot s_r = L_c$, see Figure 8.7. The maximum damage length $L_{c,max}$ equals the length over which the cross-section is reduced, and the minimum length is chosen to $L_{c,min} = L_{c,max}/2$. The mean length $L_{c,m}$ is defined by the intersection of the centroidal axis of the maximum pit cross-section with the pit boundary (see Figure 8.7). The resulting lengths L_c are summarised in Table 8.1 for a varying cross-section loss; note that the values are independent of the bar diameter.

A pertinent constitutive relationship is assigned to the corroded reinforcing bar over the length $\beta \cdot s_r = L_c$, based on (i) the original steel stress-strain curve, (ii) the damage geometry defined above, and (iii) the simplified model proposed in Section 5.7.3. The additional deformation resulting from the softer behaviour of the bar section over a distance 1Ø above and below the corrosion pit is assigned to the deformation of the pit for maximum model versatility (e. g. in case $\delta = 0$ in Equation (8.12)). Hence, the mean strain over the corrosion pit is

$$\overline{\varepsilon_\beta} = \frac{\overline{\varepsilon_{s,c}}\beta s_r + 2\left(\overline{\varepsilon_{s,uc}} - \varepsilon_{s,uc}\right)Ø}{\beta s_r} \tag{8.21}$$

with $\overline{\varepsilon_{s,c}}$, $\overline{\varepsilon_{s,uc}}$ and $\varepsilon_{s,uc}$ according to Equation (5.25). The steel strains $\varepsilon_{s,uc}$ need to be subtracted in Equation (8.21) since only the *additional* deformation of the parts above and below the pit is assigned to the pit deformation.

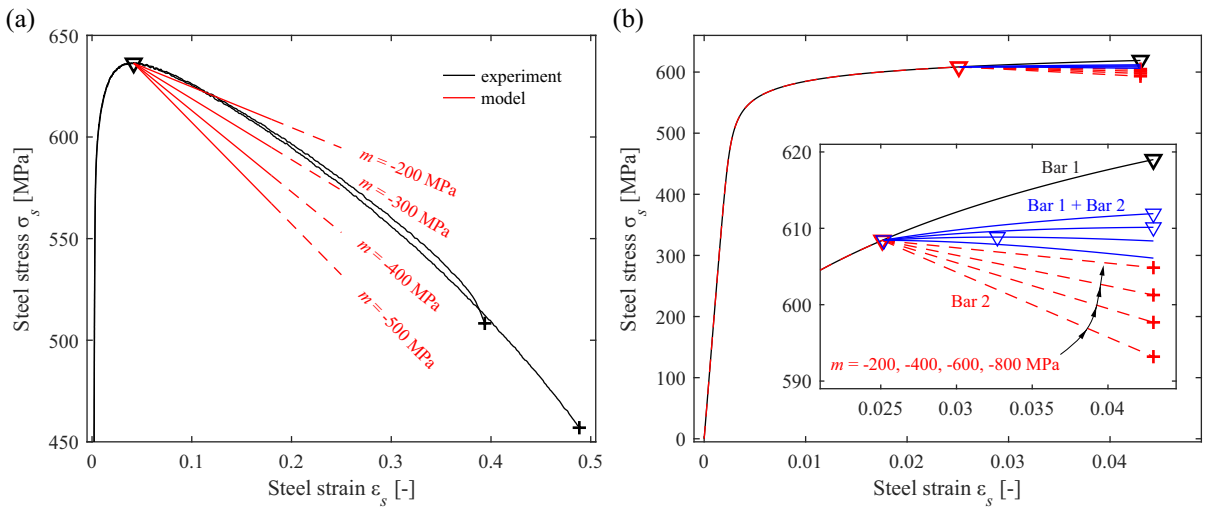

Fig. 8.8 – Post-peak softening of reinforcing bars with reduced cross-section: (a) stress-strain curve of tensile test on two reinforcing bars with initial diameter Ø = 20 mm and reduced diameter $Ø_c$ = 19 mm (black) and model predictions (red); (b) example to visualise the influence of post-peak softening. Stress-strain curve of Bar 1 (black) and Bar 2 (red), and of a system where both bars are connected in parallel (blue). Peak load is indicated with a triangle and actual rupture with a cross.

Post-peak softening behaviour

In a conventional material tensile test, the reinforcing bar undergoes necking after having reached the peak stress. Between the onset of necking and the eventual failure of the bar, the engineering stresses decrease with increasing deformation, similar to the softening behaviour of quasi-brittle materials. However, the term "post-peak softening" used in this context may not be entirely correct since the material in the necking zone still undergoes strain hardening, which is evident if stresses are referred to the actual cross-sectional area (true stresses), rather than to the nominal or original one (engineering stresses). The measured strains in the post-peak range depend on the reference length since only the necking region of 1..2Ø length is further deformed, whereas all other parts of the reinforcing bar are unloaded. For most application cases, this part of the stress-strain diagram is neglected since the load does not further increase. However, the post-peak softening behaviour after necking onset might influence the global behaviour of a corroding structure.

Figure 8.8(a) shows the steel stress-strain curves (black) of two reinforcing bars of diameter Ø = 20 mm, which exhibit a cross-section loss of approximately 10% ($Ø_c$ = 19 mm) over a length L_c = 15 mm and 19 mm, respectively. The measurements originate from the experimental campaign investigating the TSS (Chapter 5). Stresses refer to the reduced cross-sectional area, and strains were measured over the length of the damage zone, where necking occurred post-peak. The peak stress is denoted with a triangle and occurred at $A_{gt} = 0.042$, whereas the actual rupture occurred at $\varepsilon_{su} = 0.4...0.5$ (indicated with a cross). Hence, the additional post-peak elongation is $L_c \cdot (\varepsilon_{su} - A_{gt})$ = 5.4...8.7 mm (neglecting the elastic shortening of the unloaded uncorroded parts). The gradient of the post-peak softening varies in the range $m = d\sigma/d\varepsilon$ = -200...-500 MPa (red lines; the transition m = 0...-200 MPa over a short strain range after the peak stress is neglected here).

Tension chord elements containing corroded and uncorroded reinforcing bars connected in parallel need to exhibit the same deformation to fulfil compatibility (see Sections 2.3.3 and 8.3.1). Hence, if failure is associated with one or more corroded bars reaching their tensile strength, the elongation of all elements at peak load is typically strongly reduced due to strain localisation in the corroded bars. However, if failure is defined as the point when the corroded bars actually rupture and post-peak softening is considered, (i) a more pronounced load transfer from the corroded to the uncorroded bars is initiated, and (ii) the failure load is increased since the uncorroded bars are not yet fully utilised at the given strain. Therefore, the deformation capacity increases.

This behaviour is illustrated in a grossly simplified manner in Figure 8.8(b), using two reinforcing bars of equal length connected in parallel. Bar 1 exhibits a stress-strain characteristic corresponding to the black curve; Bar 2 exhibits characteristics as shown with red dashed curves. The behaviour of the coupled system is shown in blue, with peak loads indicated by triangles. It is observed that the load-carrying and deformation capacity of the coupled system is increased compared to the peak load and corresponding strain of Bar 2 (red triangle), depending on the gradient m of the softening branch.

Evidently, the actual behaviour is much more complicated since it further depends on the effective load distribution among the bars, and hence, on the number of corroded and uncorroded bars, the actual cross-section losses of the corroded bars, and the length of the uncorroded parts being unloaded post-peak and undergoing elastic shortening.

For the model validation with the experiments on corroded retaining wall segments, post-peak softening is tentatively considered to explore the potential influence of a softening element. It is accounted for in combination with the effect of a TSS (mean damage length), i. e. after having reached the increased tensile strength. A minimum softening gradient m is chosen (i. e. $\max(|m|)$) for which model convergence was reached. In any case, the rupture strain is assumed to $\varepsilon_{su} = 0.18$, and post-peak softening is assumed to occur over the length of the corrosion pit.

8.4 Load-deformation behaviour of reinforcement anchored in the footing

The anchorage of straight reinforcing bars is a fundamental topic in structural concrete research and has been investigated in many theoretical and experimental studies. Pull-out tests with long embedment lengths and similar experiments on structural elements were used to develop and validate bond models (e. g. [50, 97, 107, 143]). Other researchers successfully used bond models developed from pull-out tests with short embedment lengths to investigate the load-deformation behaviour of reinforcing bar anchorages [6, 123, 141].

However, only a few experimental campaigns have been dedicated to the behaviour of anchorages of bent reinforcing bars, such as the L-shaped bars commonly used at the base of retaining walls. Brantschen et al. [28] studied the bond shear stress-slip behaviour of hooked and U-shaped reinforcing bars using fibre optic strain measurements. Marques and Jirsa [112] and Soroushian et al. [148] investigated the pull-out behaviour of reinforcing bars with a 90°-end-hook in experimental campaigns, measuring the force-slip behaviour along the bar length [112], and presented a corresponding bond shear stress-slip model [148]. They reported zero slip at the free bar end (i. e. full anchorage of the bar at this point) until sudden failure of the specimen occurred by excessive spalling.

Since the bar geometry investigated in [28] does not apply to reinforcement with a large bending radius, as typically placed in the footings of retaining walls, and the model proposed by [148] was developed for rather short embedment lengths, the topic is revisited in the following section.

8.4.1 Results of experiments on retaining wall segments

In the specimens of the experimental campaign on retaining wall segments, the main reinforcement anchored in the footing below the construction joint runs vertically for 217 mm, is bent by 90° with a code-compliant mandrel diameter $d_1 = 15Ø = 270$ mm, and finally continues horizontally over a length of 677 mm to the opposite footing edge, see Figure 8.9(a). Figure 8.9(b) shows the steel stresses back-calculated from the fibre optic strain data (blue) of one representative L-reinforcing bar of Specimen CD-0 for specific bending moments at the construction joint. Figure 8.9(c) shows the corresponding slip of the same bar, obtained by integrating the measured strains. As mentioned in Section 6.3.5, the optical glass fibre was glued on the inside of the bend (see Figure 8.9(a)). The beginning and end of the bend are indicated with solid black lines, and dashed black lines indicate angular sections of 22.5°. A black dotted line indicates the point on the bar which lies directly below the wall edge.

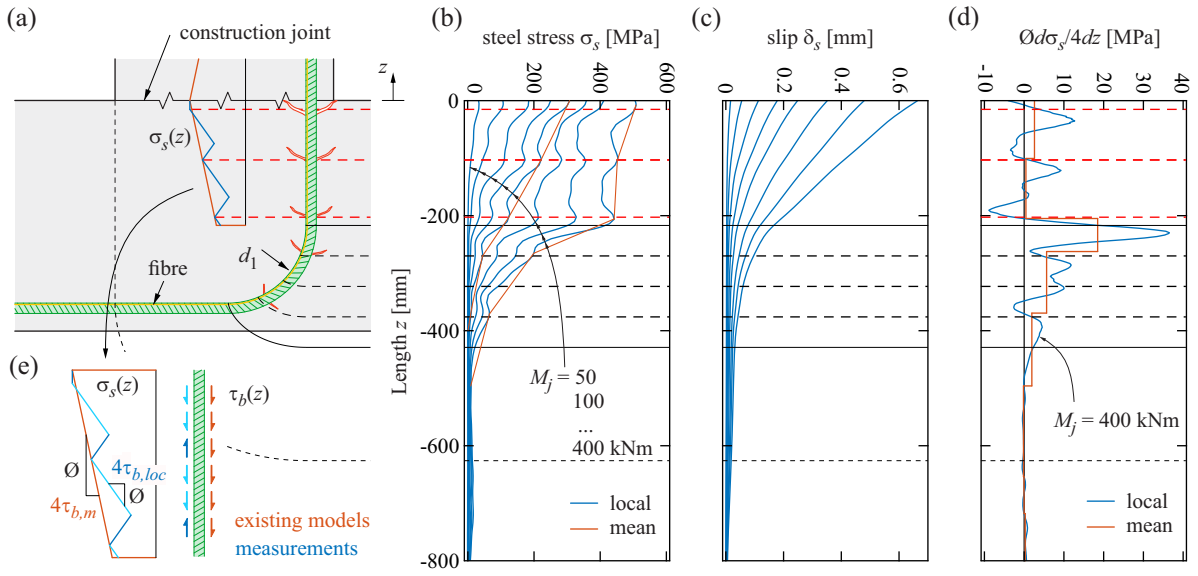

Fig. 8.9 – Pull-out behaviour of reinforcement anchored in the footing: (a) bent reinforcing bar below construction joint with presumed internal crack locations (red) and schematic steel stress distribution along the bar. (b) Steel stresses back-calculated from measured steel strains (blue) for specific bending moments in a reinforcing bar of CD-0, including mean steel stress decrease (orange). (c) Slip along reinforcing bar (= integrated steel strains) for same bending moments. (d) Scaled derivative of steel stresses (blue) and mean values between presumed cracks (orange) for M_j = 400 kNm. (e) Detail of steel stress distribution along the bar in straight part according to existing models (orange) and measurements (blue), and corresponding direction of bond stresses.

Generally, stresses are highest at the loaded end and decrease towards the bend, as seen in Figure 8.9(b). For bending moments $M_j \leq 100$ kNm (approximately $\sigma_s(z=0) = 100$ MPa at the construction joint), the vertical straight part of the bar is sufficient to anchor the load. For higher loads, the point of zero stress shifts into the bend, but not beyond its end. Steel stresses decrease much stronger in the bent part than in the straight part of the bar, reaching a maximum gradient in the first quarter of the bend. This strong decrease is caused by high bond forces acting on the inside of the bend, rather than by common bond shear stresses uniformly distributed around the bar perimeter. These high bond forces are enabled by the strong compressive forces between the bar and the surrounding concrete caused by the deviation of the bar in tension. This phenomenon was already described by [6, 148] and recently confirmed with modern measurement techniques by [28, 119].

Figure 8.9(b) reveals that the steel stresses undulate along the bar length, rather than decreasing monotonically; the red dashed lines indicate the location of the observed local peaks. The undulations first occur for stresses $\sigma_s(z=0) > 200$ MPa, intensify for higher loads and are most pronounced in the straight part. The gradient of the mean stresses between these peaks, indicated by the orange lines connecting the peaks, decreases with increasing load (compare the two orange lines for $\sigma_s(z=0) > 300$ MPa and $\sigma_s(z=0) > 500$ MPa). This contradicts existing bond and anchorage models (e. g. [49, 141]), which predict increasing bond stresses (i. e. increasing steel stress gradients) for the range of the observed slip $\delta_s < 1$ mm (Figure 8.9(c)). Two similar peaks, though less pronounced, are observed in the first and the last quarter of the bent part.

Figure 8.9(d) shows the scaled derivative of the steel stresses at a bending moment of M_j = 400 kNm, i. e.

$$\begin{aligned} T(z) &= \frac{Ø}{4}\frac{d\sigma_s}{dz} \\ &= \tau_b(z) \qquad \text{for } z < -217 \text{ mm} \end{aligned} \tag{8.22}$$

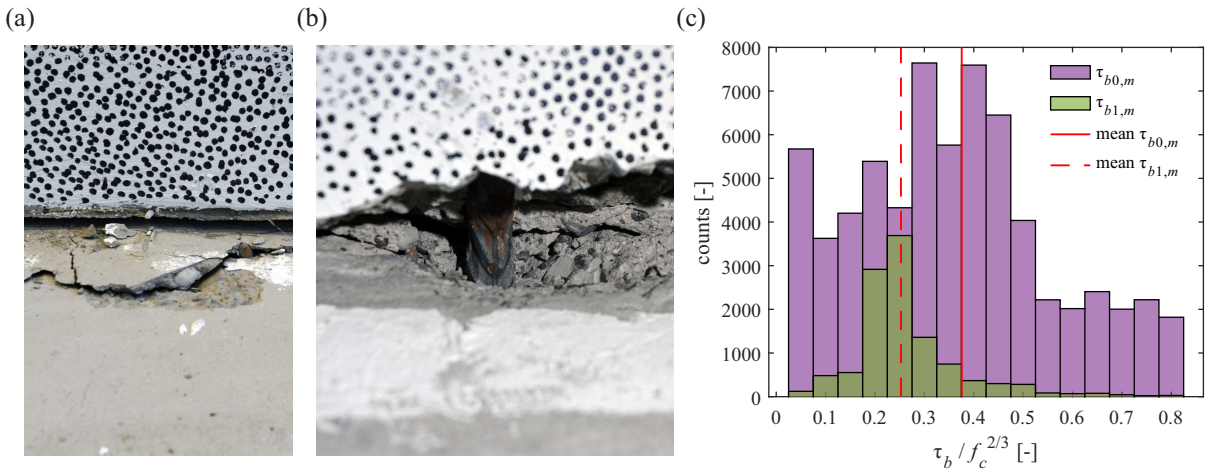

Fig. 8.10 – Evaluating the pull-out behaviour of the reinforcement anchored in the footing after the test. (a) Cone breakout at the construction joint. (b) Reinforcing bar after removing the breakout cone. (c) Normalised mean bond stresses observed in the elastic (τ_{b0}) and plastic (τ_{b1}) strain range of the reinforcement.

which corresponds to the local nominal bond shear stresses in the straight part of the bar $z <$ -217 mm (in the bent part, the nominal bond stresses are meaningless due to the different load transfer mechanism). The resulting nominal bond stresses are in a typical range of $|\tau_{b,loc}| \leq 10$ MPa but partly exhibit a negative sign, i. e. acting in the opposite direction. Hence, the mean bond stress (orange line) between two peaks is much smaller than the maximum local bond stress.

Based on these observations, the stress peaks presumably result from internal cracks and splitting cones (as schematically shown in Figure 8.9(a)). Similar as reported in [40], such cones were found at the surface of the specimen footings after the tests. Examples are shown in Figure 8.10(a) before removing the cone, and Figure 8.10(b) after cone removal. Consequently, it is assumed that the elements between the cracks in the straight part of the bar act as conventional crack elements subjected to a varying normal force, i. e. with their location of minimum stress shifted backwards from the element centre. Similar to lap splices and flexural crack elements (see Section 8.3.2), this shift allows for an overall stress decrease in a crack element. Although no loss of the local bond strength is observed, these internal cracks reduce the mean bond strength.

The standard modelling approach for the anchorage of straight reinforcing bars, which forms the basis of existing design codes (e. g. [145]), is shown in Figure 8.9(e) with an orange line. It assumes that steel stresses σ_s decrease linearly due to the bond shear stresses, which counteract the applied load. In contrast, the findings described here imply a steel stress distribution as indicated by the blue line, with bond stresses of magnitudes similar to existing bond models but alternating bond stress directions. Nevertheless, the principle of the established anchorage models can be adopted by accounting for the influence of the internal cracks on the mean bond stresses. Therefore, the latter are further analysed in the following.

The mean bond stresses were determined using the fibre optic strain data of the 50 L-reinforcing bars of the CD series (Chapter 6) at different bending moments $50 \leq M_j \leq 400$ kNm. The mean bond stress and the slip are determined in the straight part of the bar, i. e. for $-217 \leq z \leq 0$ mm, as

(i) the mean values between the (presumed) internal cracks, i. e. the locations of pronounced stress peaks, if such peaks occurred (similar as shown in Figure 8.9(d))

(ii) the mean values between $z = 0$ and the location where $\sigma_s = 0$ or the end of the straight part, i. e. $\max\{z|\sigma_s(x) = 0, z = -217 \text{ mm}\}$, if no stress peaks were observed (yet).

Similar as in the original TCM, two mean bond stress values are defined: $\tau_{b0,m}$ where the reinforcing bar is elastic, i. e. the observed mean strain between two cracks is $\varepsilon_{s,m} \leq 0.0024$, and $\tau_{b1,m}$ where the reinforcing bar exhibits plastic mean strains, i. e. $\varepsilon_{s,m} > 0.0024$. The limit of $\varepsilon_{s,m} = 0.0024$ equals the

Tab. 8.2 – Experimental results (mean and standard deviation) of the normalised mean bond stress in the elastic and plastic range of the reinforcing bar and normalised mean bond stresses according to Sigrist [146], for comparison.

	experimental results		Sigrist
	mean	standard deviation	
$\tau_{b0,m}/f_c^{2/3}$ [-]	0.37	0.24	0.55...0.65
$\tau_{b1,m}/f_c^{2/3}$ [-]	0.25	0.09	0.28...0.33

observed steel proportionality limit (i. e. the strain, where the bare steel stress-strain curve leaves the elastic straight line; for $\varepsilon_s = 0.0024$, the stress is $\sigma_{sy} = 480\,\text{MPa}$).

Figure 8.10(c) shows the histograms of the experimentally observed mean bond stresses $\tau_{b0,m}$ and $\tau_{b1,m}$, normalised with $f_c^{2/3}$. Additionally, Table 8.2 summarises the mean and standard deviation of the normalised mean bond stresses, along with the values reported by Sigrist [146] in order to calibrate the TCM. The mean bond stresses in the elastic and inelastic range are approximately 38% and 23%, respectively, lower than the values reported by Sigrist. The standard deviation is rather high for $\tau_{b0,m}$, reflecting the broad variation in the range of $\tau_{b0,m}/f_c^{2/3} = 0.1...0.4$.

While the lower values observed in the footings could be explained by the formation of internal cracks as outlined above, it must be noted that Sigrist determined the bond stresses from pull-out tests conducted by Engström [50] and Shima [143] on reinforcing bars with long embedment lengths, where internal cracks may also have occurred. Hence, the lower mean bond stresses observed in the footings could also be due to different bond conditions (steel characteristics, rib areas, etc.).

8.4.2 Anchorage model

The anchorage of the bent reinforcing bars is modelled using a surrogate straight bar, which is fixed at its end (i. e. zero slip) and is embedded over a length

$$L_b = z_{straight} + \frac{d_1 + Ø}{2}\frac{\pi}{2} \tag{8.23}$$

with $z_{straight}$ = length of the straight part and d_1 = mandrel diameter. The second term equals the length of the bend. The length and boundary condition (fixed end) were selected based on the observation that the slip at this point was virtually zero in all tests, even for high loads. The surrogate straight bar is loaded at its active end, and steel stresses decrease due to the reduced mean bond stresses

$$\begin{aligned} \tau_{b0} &= \frac{0.37}{0.6} \cdot (2 f_{ct}) = 1.2 f_{ct} \\ \tau_{b1} &= \frac{0.2}{0.3} \cdot (f_{ct}) = 0.65 f_{ct} \end{aligned} \tag{8.24}$$

according to the observations and values discussed in Section 8.4.1 (Table 8.2). The bond stress for plastic strains is slightly reduced (reduction of half a standard deviation) to compensate for the complete loss of bond in the top part of the anchorage due to the cone outbreaks observed in the experiments (see Figures 8.10(a) and (b)). For high applied loads, the surrogate bar is not fully anchored by these bond stresses; the remaining force is assumed to be resisted by the fictitious bearing at the fixed end.

8.4.3 Concluding remarks

The model presented in Section 8.4.2 is a strong simplification of the real behaviour of the anchorage of a bent bar with a large bending radius. For high loads, where low bond stresses τ_{b1} are assumed over almost the entire fictitious embedment length, the steel stresses in the bent part are strongly overestimated. This is obvious when considering Figure 8.9(b) for $M_j = 400\,\text{kNm}$, where the observed steel stress decreases rapidly in the first quarter of the bent part, but the model predicts stresses in the extension of the orange line. In contrast, compared to the observed large opening of the construction joint (see Figure 6.11, Section 6.4.1), which is caused to a significant part by the pull-out of the anchored reinforcement, the anchorage model does not overestimate the deformations. This leads to the conclusion that the experimentally observed pull-out of the reinforcement in the experiments is not only caused by the slip between reinforcement and concrete but also by an upward-directed movement of the bend due to concrete crushing under the high contact pressure. Such deformations and concrete deterioration were described by [112] and recently by [28]. Accordingly, the measured strains have to be interpreted carefully since the deformations caused by concrete crushing along the bend are superimposed to the results. If such deformations indeed took place in the experiments, the proposed model – having been calibrated on the experimental results – accounts for them as part of the predicted bar elongation.

8.5 Assessment of corroded retaining wall segments

The model presented in Section 8.3, including the additional effects discussed in Section 8.4, is validated with the results of the experimental campaign described in Chapter 6. After some comments on the model implementation, the model predictions are compared to the experimental results of the tests with increasing load (Series CD) and the hybrid tests (Series EP).

8.5.1 Model implementation

The modelling approach is implemented in *Matlab* as a load-controlled model, i. e. calculating the deformation of the structural system for a given load. This calculation strategy works well for monotonically increasing load steps, but convergence can be lost if several crack elements are unloaded to different extents (e. g. if several corroding bars reach post-peak softening in different load steps (Specimen CD-9-var) or if all bars are unloaded in one load step due to a global load reduction, but to different extents since corrosion is simultaneously increasing (Specimen EP-HD)). Calculations affected by convergence loss are mentioned in the discussion section.

The modelled wall segments are loaded identically as in the experiments with a combination of shear force and bending moment at the wall head according to Figure 6.9(b) and a normal compressive force of -56 kN. The loading of the modelled hybrid tests follows the moment-deflection curves shown in Figure 6.10. The crack element lengths are chosen as observed in the experiments, determined from the DIC measurements (see Figure 6.11), and the recess at damaged bars was considered by setting the parameter $(\beta + \delta) \cdot s_r = 100\,\text{mm}$. The cracking moment is set to $M_{cr} = 120\,\text{kNm}$, corresponding to the mean value observed in the experiments. The reinforcement yield stress, where the bond stresses decrease from τ_{b0} to τ_{b1} in the TCM, is set to the proportionality limit at $\sigma_{sy} = 480\,\text{MPa}$, i. e. the point where the bare steel stress-strain curve leaves the elastic straight line (in contrast to the definition of $f_{sy} = R_{p02} = 554\,\text{MPa}$ at 0.2% remaining plastic strain).

8.5.2 Results and discussion of experiments with constant cross-section loss

Figure 8.11(a) plots the bending moment at the construction joint M_j vs the displacement of the wall head v_{top} at z = 1.7 m of **Specimen CD-0**, i. e. the reference test without cross-section loss. The experimental curve is shown in black, and the model result in red. The maximum bending moment and corresponding head displacement according to the experiments and the model calculations are summarised in Table 3. The model prediction and the experimental data are in very good agreement, confirming the ability of the modelling approach to capture the load-deformation behaviour for the case without reinforcement cross-section loss. Despite the uncertainty regarding the appropriate modelling of the force-slip behaviour of the anchorage in the footing (Section 8.4.3), the model prediction is very satisfying.

Figure 8.11(b) shows the experimental results and model predictions for **Specimen CD-3-10** (3 bars with 10% cross-section loss). The model is evaluated using different assumptions: without the effect of a TSS (w/o TSS, red), with the effect of the TSS (green), and considering the TSS and post-peak softening after the onset of necking at the corrosion pit (blue). The different damage lengths used in the models are indicated with a circle (= maximum length), a triangle (= mean length), and a square (= minimum length). The post-peak softening gradient m is indicated in the figure legend. The model prediction of Specimen CD-0 is shown in grey as a reference.

The experimentally observed deformation capacity is slightly reduced for Specimen CD-3-10 compared to CD-0, but the peak bending moment is slightly higher. The model neglecting a potential influence of the TSS (i. e. merely considering strain localisation) strongly underestimates the deformation capacity. The model considering the effects of a TSS predicts increasing deformations at peak load with decreasing damage length and closely matches the experimental result when assuming a minimum dam-

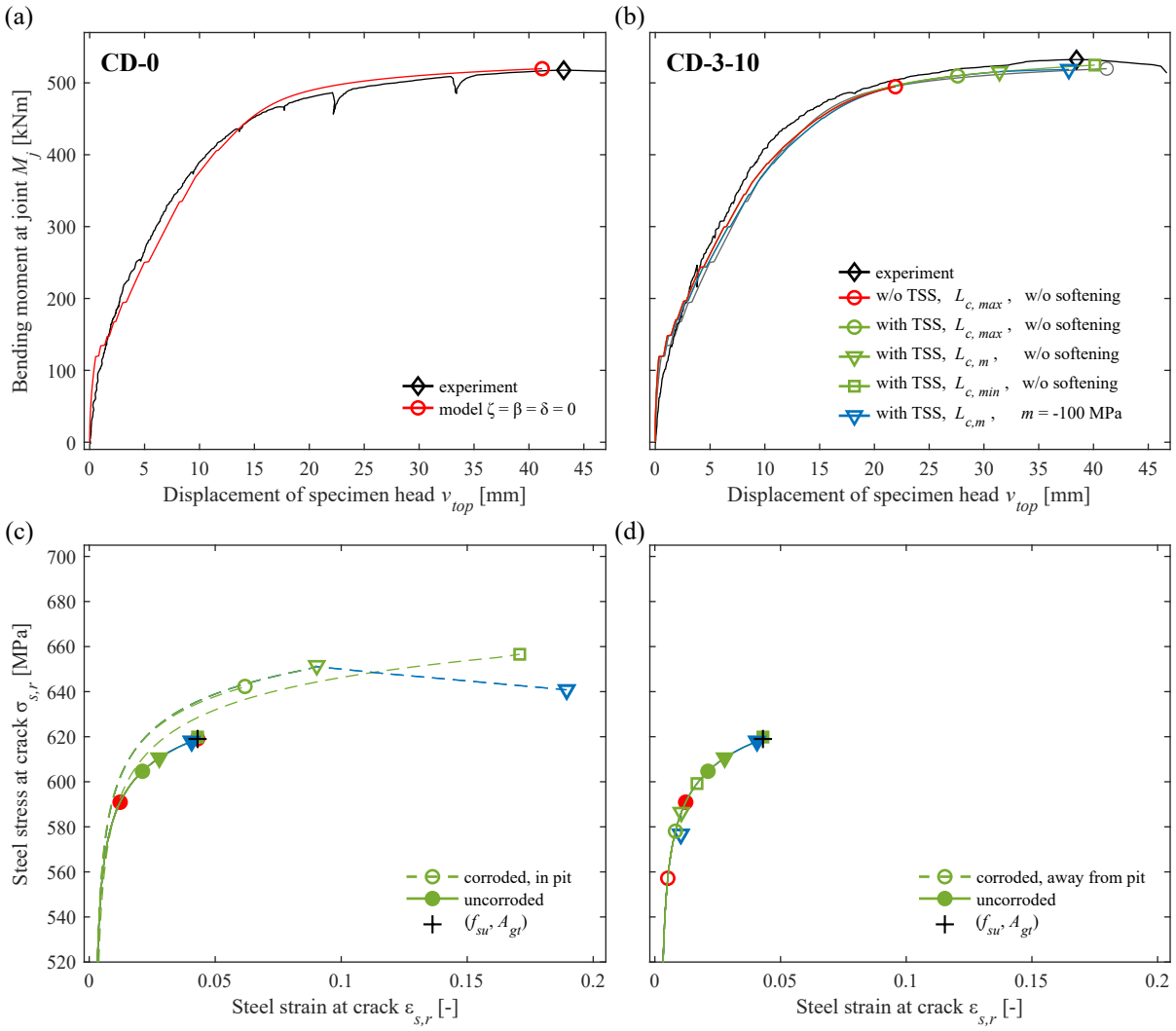

Fig. 8.11 – Experimental results and model predictions for Specimens CD-0 and CD-3-10. (a) Moment-displacement curve of CD-0 with experimental result (black) and model prediction (red). (b) Moment-displacement curve of CD-3-10 with experimental result (black) and different model predictions (coloured). (c) Stress-strain model curves of corroded (dashed lines) and uncorroded (solid lines) bars at the crack. For the corroded bars, the stresses and strains refer to the reduced cross-sectional area and the relative deformation over the pit length. (d) Same as (c), but stress and strain values of the corroded bars referred to the initial cross-sectional area and strains outside the pit. Marker shapes and colours in (c) and (d) correspond to same model assumptions as in (b).

age length. The model considering post-peak softening after necking onset also captures the behaviour accurately.

The finding that the model accounting for a TSS predicts larger deformations for a shorter damage length is counter-intuitive from the perspective of strain localisation but can be explained by the increasing apparent tensile strength with decreasing damage length (see Section 5.6.3). Figure 8.11(c) plots the steel stress vs the steel strain at the crack at different load stages for the corroded bars (dashed lines) and the uncorroded bars (solid lines); the marker types and colours correspond to those used in Figure 8.11(b). The stress in the corroded bars is referred to the reduced cross-sectional area, and the strains represent the relative deformations of the pit according to Equation (8.21). The solid lines essentially correspond to the material stress-strain relationship, as confirmed by the black cross indicating the tensile strength and corresponding strain of the bare undamaged steel. If no increase of the peak stress in the pit by the TSS is considered, the corroded reinforcing bars reach the peak stress (red empty circle behind the black cross), while the uncorroded bars just start to deform plastically (solid red circle). The increase

Tab. 8.3 – Experimental results and model predictions: maximum bending moment and corresponding head displacement.

Specimen	Experiment		Model									
			w/o TSS		with TSS						with TSS and p.-p. softening	
					$L_{c,max}$		$L_{c,m}$		$L_{c,min}$		$L_{c,m}$	
	M_{max} [kNm]	w_{max} [mm]	M_{max} [kNm]	w_{max} [mm]	M_{max} [kNm]	w_{max} [mm]	M_{max} [kNm]	w_{max} [mm]	M_{max} [kNm]	w_{max} [mm]	M_{max} [kNm]	w_{max} [mm]
CD-0	517.6	43.2	519.7	41.2								
CD-3-10	532.4	38.5	494.6	21.9	509.7	27.6	515.7	31.4	524.7	40.1	519.7	37.6
CD-9-30	449.9	25.6	438.5	15.2	443.5	15.6	440.5	15.1	451.6	16.1	468.6	23.0
CD-9-15	506.8	33.2	466.6	18.4	480.6	20.6	486.6	21.6	508.7	31.2	490.6	28.1
CD-9-var	480.8	30.6	444.5	14.7	450.5	15.1	448.5	14.7	453.6	14.9	477.6	21.2

of the tensile strength in the pit region caused by the TSS allows for a global force increase sufficient to induce considerable plastic deformations in the uncorroded reinforcing bars (solid green markers). The model prediction in Figure 8.11(b) is already considerably improved for the maximum damage length and meets the experimental result for the minimum damage length. Considering post-peak softening at the onset of necking has a similar effect: the decreasing steel stress at increasing steel strains in the corrosion pit leads to an increasing force transfer from the corroded to the uncorroded reinforcing bars. The applied load can be increased as long as the hardening of the uncorroded bars compensates the post-peak softening of the corroded bars (see Section 8.3.3).

While the steel stresses at the pit in Figure 8.11(c) may imply that the corroded bars are higher loaded than the uncorroded ones, it has to be noted that the stress of these bars in the part adjacent to the corrosion pit, with the initial cross-sectional area, is lower by a factor $(1-\zeta)$. This is illustrated in Figure 8.11(d), where the steel stresses and strains of the corroded bars refer to the initial cross-sectional area and to the relative deformations outside the pit (empty markers), respectively. The load carried by a corroded bar is thus lower than that carried by an uncorroded bar, and hence, the strains and the deformation of the half crack elements containing a corroded bar are lower outside the pit. For the model considering post-peak softening, the parts away from the pit are even unloaded, leading to a substantial load transfer towards the uncorroded bars. Nevertheless, the sum of deformations (rotations) exhibited by the pit and the corresponding crack element equals the deformation (rotation) of the crack elements containing an uncorroded bar (as required by the compatibility condition, see Equation (8.15)).

Figure 8.12 shows the experimental and model results for Specimens CD-9-30, CD-9-15, and CD-9-var with an equal mean cross-section loss of 9%, yet differently distributed among the reinforcing bars (3x 30%, 6x 15%, and {10%, 2x 15%, 20%, 30%}). Figures 8.12(a), (c), and (e) show the bending moment at the construction joint M_j vs the displacement of the wall head v_{top} at $z = 1.7$ m, and Figures 8.12(b), (d), and (f) the stresses and strains at the crack of the corroded and uncorroded bars. The stresses and strains of the corroded bars refer to the corrosion pit, i. e. the reduced cross-sectional area and the relative pit deformation according to Equation (8.21). The predictions used identical model assumptions as for Specimen CD-3-10 and are presented using the same colour and marker scheme. The model curve of CD-0 is again shown in grey as a reference.

For **Specimen CD-9-30** in Figure 8.12(a), the model predictions with and without the effects of the TSS do not differ significantly. The load-carrying capacity is reasonably captured but the corresponding deformation is strongly underestimated. In contrast, the model considering post-peak softening fits the experimental results better. This is explained by the stress-strain curves of the pit shown in Figure 8.12(b): the apparent tensile strength of the corroded bars is significantly increased with shorter damage length due to the TSS, but the corresponding strain at peak stress is only slightly higher than

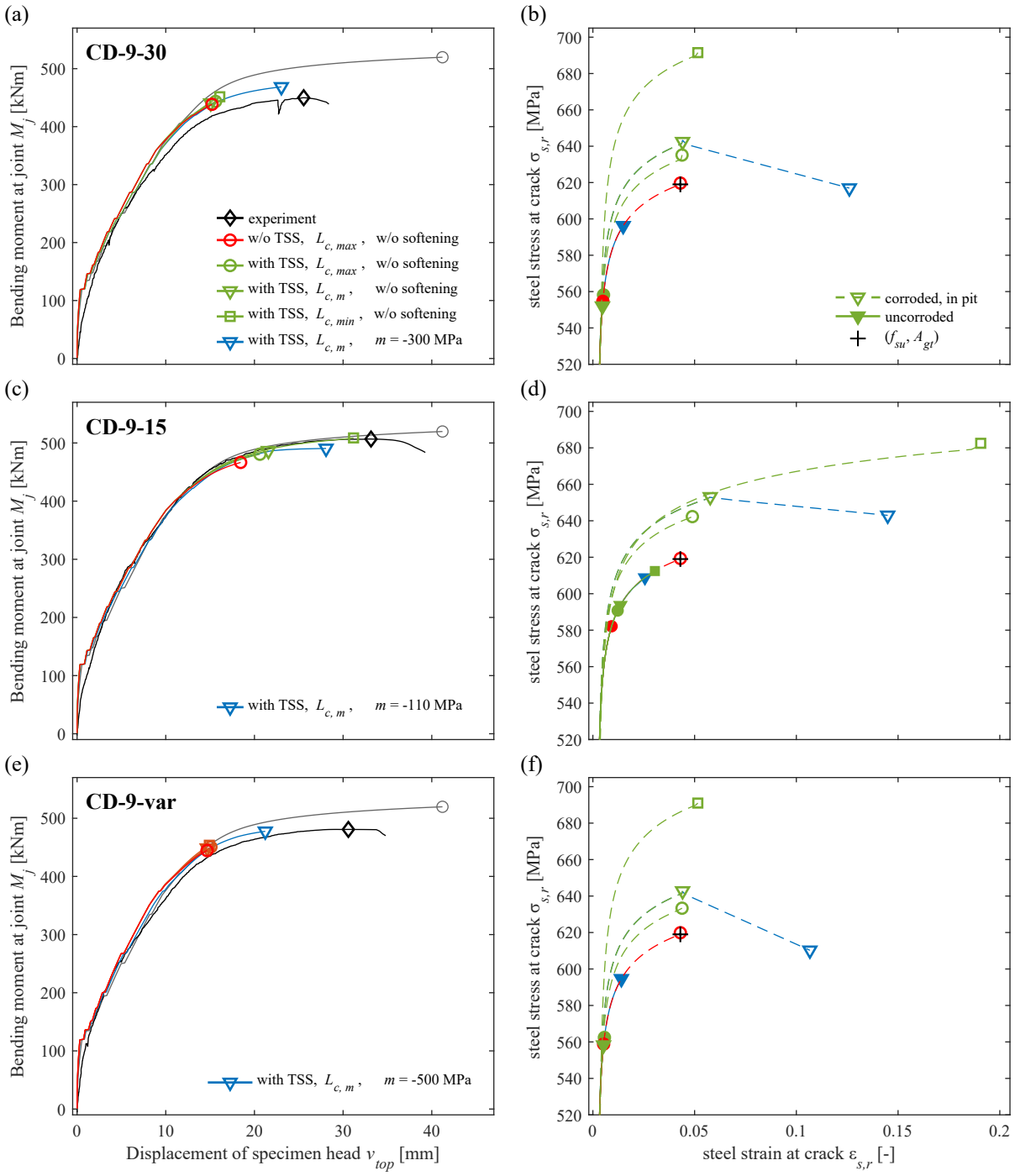

Fig. 8.12 – Experimental results and model predictions for Specimens (a,b) CD-9-30, (c,d) CD-9-15, and (e,f) CD-9-var. (a,c,e) Moment-displacement curves of experiments (black) and different model predictions (coloured). The model curve for Specimen CD-0 is shown as reference (grey). (b,d,f) Stress-strain model curves of corroded (dashed lines) and uncorroded (solid lines) bars at the crack. For the corroded bars, the stresses and strains refer to the reduced cross-sectional area and the relative deformation over the pit length.

A_{gt} since the maximum force carried by the section with reduced cross-sectional area is lower than the yield force of the adjacent parts of the bar. For the minimum damage length, the stress in the uncorroded parts is $\sigma_{s,uc} = (1-\zeta)\sigma_{s,c} = (1-0.3)\cdot 690$ MPa $= 483$ MPa; considering a stress increase by a factor $1/p_{\varepsilon,uc} = 1.15$ according to the TSS model to calculate the corresponding strains near the pit, one gets $\sigma_{s,uc}/p_{\varepsilon,uc} = 555$ MPa, which is equal to the yield stress. Hence, the increase in tensile strength due to the TSS is insufficient to compensate for the cross-section loss, and the behaviour is mainly governed by

strain localisation. On the other hand, post-peak softening in the pit region after necking onset leads to locally high deformations and, hence, to a load transfer from the corroded to the uncorroded bars. The increasing load of the uncorroded bars is associated with a global deformation increase.

The comparison of experimental results and model predictions, with the latter being consistently stiffer, implies that the model does not fully account for a softening effect being present at the pit and potentially in the parts in the direct pit vicinity. Apart from the post-peak softening included in the model, the softer behaviour could be due to a combination of TSS effects and local bending moments. Such bending moments were experimentally observed for unilateral pits, e. g. by [8], and confirmed in this study by the fibre optic strain measurements presented in Section 6.4.4. They are not captured by the current TSS modelling approach and could indeed lead to a softer axial behaviour due to superimposed bending stresses, as also hypothesised by [80].

The model predictions for **Specimen CD-9-15** in Figures 8.12(c) and (d) show similarities to the results of Specimens CD-3-10 and CD-9-30. The model considering a TSS with minimum damage length accurately captures the experimental result, as in this case the increase in tensile strength in the pit is sufficient to cause substantial yielding in the sections near the pit: $\sigma_{s,uc} = (1-\zeta)\sigma_{s,c} = (1-0.15)\cdot 683\,\text{MPa} = 580\,\text{MPa}$; considering the stress increase due to the TSS of $1/p_{\varepsilon,uc} = 1.08$, one gets $\sigma_{s,uc}/p_{\varepsilon,uc} = 626\,\text{MPa}$ for the strain calculation in the parts directly adjoining the pit, and hence, large plastic strains. However, similar to Specimen CD-9-30, the increased tensile strength of the models considering the TSS with mean or maximum damage does not cause significant plastic strains in the sections near the pit ($\sigma_{s,uc} \approx 544\,\text{MPa}$, $1/p_{\varepsilon,uc} \approx 1.05$). The deformations exhibited in the experiment are thus underestimated. The model with mean damage length but accounting for post-peak softening compensates partly for the underestimated deformations but underpredicts the peak load.

The model results for **Specimen CD-9-var** are shown in Figures 8.12(e) and (f). The stress-strain curves of the corroded bar in Figure 8.12(f) are illustrated for the bar with 30% cross-section loss. The overall result is similar to that of Specimen CD-9-30, with the bar affected by 30% cross-section loss dominating the behaviour. All models strongly underestimate the deformation capacity if no post-peak softening behaviour is considered. The best prediction is obtained with the model with post-peak softening, which, however, lost convergence before reaching the assumed rupture strain $\varepsilon_{su} = 0.18$. Possibly, a refined calculation ensuring convergence would lead to a better result, underlining the importance of considering post-peak softening and exploring potential further softening effects, such as bending due to unilateral corrosion.

8.5.3 Results and discussion of hybrid tests

Figure 8.13 compares the experimental results and model predictions of the tests with increasing cross-section loss (one at constant load, EP-CL, and two hybrid tests simulating the earth pressure decrease with increasing deformation, EP-LD and EP-HD, see Sections 6.3.7 and 6.4.2). Two approaches are used to model the deflection increase due to an increasing cross-section loss: the Intersection Approach (IA) and the Full Calculation Approach (FCA). The IA evaluates the retaining wall model at increasing load for varying cross-section losses, resulting in the red and blue load-deformation curves shown in Figure 8.13(a). As in the experiments, the cross-section of four reinforcing bars is reduced stepwise by 10%, and the model is evaluated considering the effects of the TSS, once with the maximum (red) and once with the minimum damage length (blue). For Specimen EP-CL, where the load was held constant during cross-section reduction at $M_j = 286\,\text{kNm}$ (solid black line), the intersection of the load-deformation curves with the horizontal moment line is determined (red and blue crosses), leading to a deflection increase with increasing corrosion. Similarly, the earth pressure models provided by [125] (dashed and dash-dotted black curves) are used for the Specimens EP-LD and EP-HD to find the intersection with the load-deformation curves.

The FCA evaluates the model for the entire load path as in the experiments, i. e. the simulated retaining wall is first loaded without cross-section loss to service load, and the cross-section of the corroding

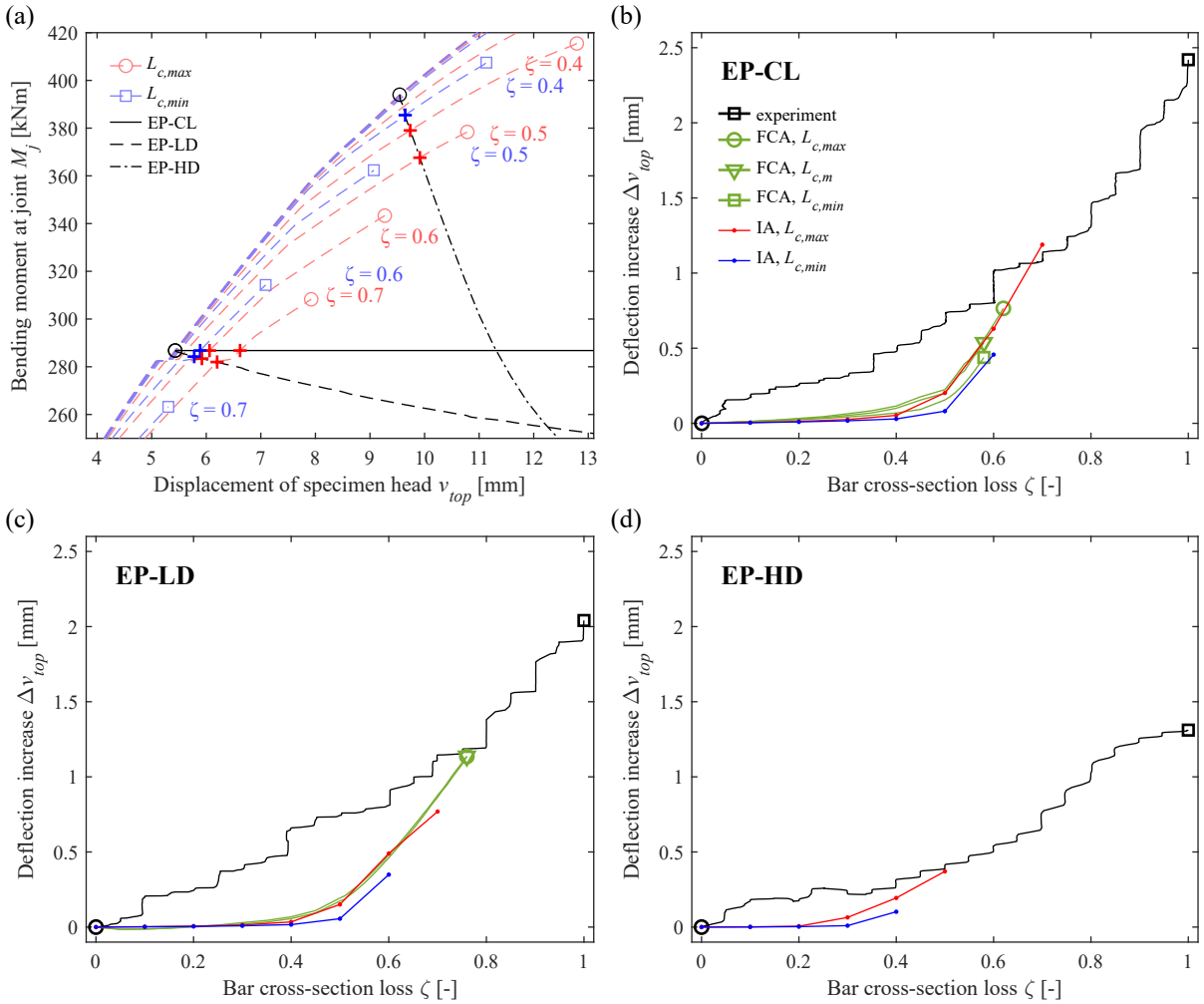

Fig. 8.13 – Experimental results and model predictions for the tests with increasing cross-section loss at constant or decreasing load (hybrid tests): (a) principle of Intersection Approach (IA), with load-deformation curves (coloured) and loading lines (black); (b-d) observed (black) and predicted (coloured) deflection increase at wall head.

bars is subsequently reduced stepwise at constant or decreasing load. The approach has the advantage that the unloading behaviour of the structure is simulated: Unloading-reloading a structure differs from a monotonic load increase – as in the IA – since the potentially reduced bond stresses and imposed deformations influence the global load-deformation behaviour (see Section 8.3.2). One of the drawbacks of the FCA is its challenges regarding model convergence since several parameters change simultaneously in a calculation step involving unloading effects.

The black lines in Figures 8.13(b) to (d) illustrate the experimentally observed deflection increase of the wall head (at $z = 1.7$ m) with increasing cross-section loss for the experiments of the EP series. Note that the cross-section loss ζ here refers to that of each of the four drilled bars, which is linked to the mean cross-section loss by a factor 4/10, i. e. $\zeta_m = 4/10 \cdot \zeta$. The coloured lines show the model predictions. The FCA was evaluated considering the effects of the TSS for the three different damage lengths, and its predictions are shown in green with the marker type indicating the damage length. For Specimen EP-HD, convergence was lost for all damage lengths beyond a cross-section loss of approximately 20%, and the FCA results are thus omitted in Figure 8.13(d). The same applies to EP-LD for the FCA with minimum damage length (Figure 8.13(c)). The predictions obtained from the IA with minimum and maximum damage length are shown in blue and red, respectively.

All model approaches underpredict the wall head displacements observed in the experiments up to a cross-section loss of $\zeta = 0.5$ for EP-CL and EP-LD, and $\zeta = 0.3$ for EP-HD, indicating that the models do not realistically account for the softening effect caused by the cross-section reductions in the elastic load range. However, it should be noted that the observed deformation increases are very small (0.3...0.7 mm for $\zeta = 0.5$ ($\zeta_m = 0.2$)); considering the dimensions of the specimens, these deflections (1/5700...1/2400 of the wall height) are an order of magnitude smaller than the accuracy of most models in structural concrete, given the uncertainties regarding materials, bond, geometry, etc. For higher cross-section losses, the deformation resulting from the two approaches increases and meets the experimental results for $\zeta = 0.6...0.7$ for EP-CL and EP-LD, and $\zeta = 0.4...0.5$ for EP-HD, respectively.

The IA and FCA give very similar results for all three specimens, indicating that accurately capturing the unloading behaviour is of minor importance for this kind of problem. The varying damage length has a noticeable effect, with higher accuracy of the model predictions with longer damage length in this case. Since the geometrical ratios are $L_c/(2Ø_c) \approx 0.7...1.2$ and $Ø_c/Ø \approx 0.5...0.6$ for large cross-section losses, the influence of the TSS strongly diminishes, and the apparent tensile strength does not increase ($p_\sigma \leq 1.01$, see Section 5.7). Therefore, the behaviour is governed by strain localisation, and longer damage lengths lead to larger deformations.

In Figures 8.13(b) to (d), the model curves do not reach $\zeta = 1.0$ since all approaches predict a failure of the damaged reinforcing bars for a cross-section loss of $\zeta = 0.6...0.7$, i. e. they underestimate the load transfer from the damaged to the undamaged reinforcing bars. This indicates that the model predicts an overly stiff force-elongation behaviour of the corroded bars for high cross-section losses. Since the bars were damaged unilaterally in the experiments causing a significant shift of the centroidal axis at the pit for high cross-section losses, it is hypothesised that local bending stresses softened the bars' response in the tests. As mentioned in Section 8.5.2, these effects are currently not captured by the models but might be relevant for a realistic failure estimate.

8.6 Conclusions

This chapter investigated a modelling approach combining various models based on the TCM to assess the load-deformation behaviour of cantilever retaining walls affected by local corrosion damage of the main tensile reinforcement at the construction joint between footing and wall.

The following conclusions can be drawn regarding the modelling approach in general:

- The models of Kenel [93] and Pfyl [126] only differ in the assumption regarding the concrete strain distribution at the centre between adjoining flexural cracks and yield very similar moment-mean curvature relationships. However, compared to the approach proposed by Burns [29], these models are computationally less efficient since they need several iteration loops to achieve convergence. In contrast, the approach of Burns is straightforward for implementation but has so far only been validated in the elastic load range. A possible model extension to plastic steel deformations is presented in Section 8.2.2 but needs further validation.
- All presented models for predicting the load-deformation behaviour of flexural crack elements assume constant bending moments along the crack element length and hence, symmetrical stress and deformation distributions. In the case of non-zero shear forces causing bending moment gradients, these distributions are no longer symmetrical, and the deformations are larger at one of the two cracks, as already shown by Sigrist [146]. The deformations may thus be substantially underestimated, especially at the location of structural elements amplifying the unequal deformation distribution (e. g. at the end of lap splices). An approach accounting for the influence of unequal stress distributions on the global deformation behaviour was presented in Section 8.3.2. The corresponding model predictions match the experimental results accurately, but further validation is needed regarding the general applicability of the approach.

- The anchorage of reinforcing bars with a 90°-bend of large mandrel diameter is very common in structural concrete. However, only a few experimental studies have been conducted on their pull-out behaviour. The experimental results of the campaign on retaining wall segments indicate that a considerable part of the displacement at the active bar end may result from concrete crushing in the bend, leading to a translation of the bar in addition to the slip between steel and concrete. Moreover, the bond strength above the bend appears to be reduced due to internal cracking. Since the experimental campaign was not designed to thoroughly investigate these phenomena and the results are thus merely indicative, it may be worth analysing the behaviour of this anchorage type in a separate experimental study using modern measurement techniques.
- Despite the model uncertainties described in the two previous points, the proposed modelling approach accurately captured the experimental result of the reference specimen, proving its suitability for conventional, non-damaged reinforced concrete structures.
- It is recommended to implement a future version of the modelling approach in a deformation-controlled way, i. e. to calculate the bending moments for a given deformation (rotation) of the crack element. Convergence problems, occurring especially when post-peak softening is considered, can thus be avoided.

The following conclusions can be drawn regarding the load-deformation behaviour of corroded reinforced concrete structures based on the comparison of the experimental results with the predictions of the different modelling approaches:

- The CTCM alone, considering merely the effect of strain localisation, considerably underestimates the deformation capacity observed in the experiments.
- Combining the CTCM with a simplified approach to capture the effects of a triaxial stress state occurring at concentric corrosion pits (Chapter 5) improves the prediction accuracy. The unilateral damage was approximated with a concentric damage of half the effective pit length. This approach accurately captured the load-deformation behaviour of specimens containing reinforcing bars with a maximum cross-section loss of 15%.
- However, the same approach underpredicts the deformation capacity of specimens containing reinforcing bars with more severe cross-section losses, unless an additional softening effect at the corrosion pit is considered. Apart from post-peak softening after the onset of necking considered in this study, softening may be caused by superimposed local bending moments at the pit, as outlined in the following point.
- The bent stress trajectories occurring at local corrosion pits strongly influence the bar load-deformation behaviour, as it was analysed in Chapter 5 for concentric damage. The behaviour for unilateral damage might be different since additional bending stresses – occurring due to a shift of the centroidal axis – potentially lead to a softer force-elongation behaviour of the bar at the pit. Since the corroded and uncorroded reinforcing bars are positioned in parallel, this softening causes a load transfer from the corroded to the uncorroded, not fully utilised bars (as in a system of soft and stiff springs in parallel), and thus increases the load-carrying and deformation capacity of the structure. This positive effect of the local stress state at the pit is not captured by established strain localisation models. It depends on the pit morphology and its influence on the load-deformation behaviour, which is only rudimentarily understood today. However, the assessment of the experimental campaign highlighted the importance of further investigating this relevant effect.
- The two approaches proposed in Section 8.5.3 to predict the deflection increase of retaining walls with increasing corrosion damage lead to similar results. It is thus recommended to use the more straightforward approach of seeking the intersection between the load-deformation curves of the structure (varying with the corrosion damage) and the load path. However, due to the issues outlined in the previous points and since the deformation increase caused by the increasing corrosion damage is very small, an accurate prediction for severe cross-section losses is challenging.

- The proposed modelling approach is suited to assess corroding retaining walls and leads to accurate results for bar cross-section losses lower than 15%. For more severe cross-section losses, the model predictions are conservative, and the actual load-deformation behaviour is more benign.

Notation

$A_{gt} = \varepsilon_s(f_{su})$	Steel strain at steel tensile strength
A_s, A'_s, $A_{s,c}$	Reinforcing bar cross-sectional area (in tension and compression zone, corroded section)
A_c, $A_{c,net}$	Concrete cross-sectional area (gross and net, with $A_{c,net} = A_c - A_s$)
B	Width of wall (in longitudinal direction)
E_s, E_c	Young's modulus of reinforcing steel and concrete
EI, EI^I, EI^{II}	Bending stiffness of wall cross-section (in general, uncracked, cracked)
$F_{c,cr}$	Force taken by concrete in crack element at the moment of cracking
H	Wall height
L_b	Anchorage length of bars in footing
L_c, $L_{c,max}$, $L_{c,m}$, $L_{c,min}$	Damage length (in general, maximum, mean, minimum), $L_c = \beta \cdot s_r$
M, M_{cr}	Applied bending moment (in general, at cracking)
$M_{i,k}$	Bending moment at crack i for vertical wall strip k
M_j	Bending moment at construction joint
M_{top}	Bending moment at specimen head
N, N_{top}	Normal force (in general, at specimen head)
R_{p02}	Steel stress at 0.2% plastic strain
V_{top}	Shear force at specimen head
b	Cross-section width
d	Effective static depth
d_1	Mandrel diameter
f_c, f_{ct}	Concrete cylinder compressive strength, concrete tensile strength
f_{sy}, f_{su}	Steel yield stress and tensile strength, with $f_{sy} = R_{p02}$
h	Cross-section height
m	Post-peak softening gradient
n	Ratio of elastic moduli, $n = E_s/E_c$
s	Bar spacing
s_r, $s_{r,max}$	Crack element length (in general, maximum), $s_r = \lambda \cdot s_{r,max}$,
t, t_c	Maximum pit penetration depth, position of bar's centroidal axis
u_s, u_c	Elongation of reinforcing bar and concrete compression (integrated strains over half the crack element length)
v, v_{top}	Displacement of retaining wall (in general, at wall head)
x_c	Compression zone depth
z	Vertical coordinate axis
$\beta \cdot s_r$	Length of corrosion pit
$\delta \cdot s_r$	Unbonded length
δ_s	Slip between reinforcing bar and concrete
ε_s, ε'_s	Steel strain (in tension zone, in compression zone)
ε_{su}	Rupture strain of bar (after post-peak softening)
$\varepsilon_{s,m}$	Mean strain of tension chord element / crack element
ε_c, $\varepsilon_{c,inf}$, $\varepsilon_{c,sup}$	Concrete strain (in general, at lower and upper edge of cross-section)
$\rho = A_s/A_c$	Reinforcement ratio
σ_c	Concrete stress
σ_s, $\sigma_{s,c}$, $\sigma_{s,uc}$	Steel stress (in general, referring to reduced and initial cross-sectional area)
σ_{sy}	Steel proportionality limit ($\sigma_s = E_s\varepsilon_s$ for $\sigma_s \leq \sigma_{sy}$)
τ_b, τ_{b0}, τ_{b1}, τ_{br}	Bond shear stress (in general, if $\sigma_s(x) \leq f_{sy}$, if $\sigma_s(x) > f_{sy}$, at unloading)
φ	Element rotation at crack (integrated curvature over half the crack element length)
$\varphi_{i,k,inf/sup}$	Rotation of half crack element at crack i for vertical wall strip k; subscript "inf" = below corresponding crack, "sup" = above corresponding crack
φ_f	Rotation of footing layer
ζ, ζ_m	Relative cross-section loss (of single reinforcing bar and mean loss of a structure)
χ	Curvature
$Ø$, $Ø_c$	Reinforcing bar diameter (initial, reduced due to corrosion)

9 Conclusions and outlook on future research

This chapter highlights the main findings of the thesis, draws final conclusions, and gives an outlook on future research.

9.1 Main findings

On the **level of the reinforcing bar**, local corrosion significantly influences the load-deformation behaviour of the region around the corrosion pit. *Strain localisation* resulting from the short damage length impairs the deformation capacity of the reinforcing bar, and the cross-section loss reduces its load-carrying capacity. However, depending on the pit geometry, a *triaxial stress state* may alter the apparent tensile strength and the corresponding strain. For an axisymmetrically damaged bar, the tensile strength (referred to the residual cross-sectional area) in the damaged section increases with decreasing pit length for low and moderate cross-section losses (depending on the ratio of pit length to residual diameter). The increased tensile strength at the pit leads to a stress and deformation increase in the uncorroded parts. Moreover, the undamaged parts close to the pit exhibit larger deformations due to a softer stress-strain behaviour, generating additional deformations. The sum of these effects attenuates strain localisation, and the deformation capacity is thus less impaired. However, the behaviour depends on the type of reinforcing steel since the steel stress-strain behaviour, particularly the ratio of tensile strength to yield stress and the gradient of the hardening branch, governs the intensity of the occurring strain localisation and triaxial stress state. Furthermore, the triaxial stress state influences the apparent uniaxial yield stress and potentially the movement of dislocations, which explains the altered shape of the stress-strain curve observed in the experimental results of many publications. Although clearly noticable, it seems that the altered yield behaviour has not been addressed in previous studies so far. Finally, it can be concluded that due to the effects related to strain localisation and the pit geometry, it is inappropriate to describe the corrosion damage by merely indicating the steel mass loss in the case of local corrosion.

For *quenched and self-tempered reinforcing steel*, corrosion leads to a change in the relative portion of the different microstructure layers to the remaining cross-sectional area and, hence, to an altered stress-strain behaviour. The deformation capacity increases moderately for axisymmetric damage while the yield stress and tensile strength decrease. In contrast, the properties of the residual bar remain approximately constant for unilateral damage.

The *strain rate* applied to a reinforcing bar influences its yield stress and tensile strength. The corroded sections of a bar tend to exhibit an increased yield stress and tensile strength in a tensile test since the strain rate in these sections is usually higher than the one applied in a reference material test (on an uncorroded bar) due to the lower tensile stiffness. However, this influence is less pronounced than the varying microstructure and pit geometry. A simplified model was formulated for all three effects (triaxial stress state, varying microstructure, and strain rate), successfully capturing their influence on the load-deformation behaviour of reinforcing bars.

On the **level of a structural concrete member**, local corrosion may pronouncedly impair its load-carrying and deformation capacity due to strain localisation occurring at the corrosion pits. For the case where the corrosion damage is limited to a single section of an RC member (e. g. above the construction joint of a cantilever retaining wall), the reduction in load-carrying and deformation capacity depends on the *total loss* of steel cross-sectional area and its *distribution among the reinforcing bars*. The capacity reduction is less pronounced if many bars exhibit a slight cross-section loss or very few bars a severe

cross-section loss, compared to the case where some bars exhibit a moderate cross-section loss. This finding is explained by the varying degree of strain localisation and implies that the mean cross-section loss is an insufficient indication to predict the load-deformation behaviour of corroded RC members.

For most **existing cantilever retaining walls** affected by local corrosion, the *rotation increase* due to an increasing cross-section loss is very limited in case of earth pressure loading (0.8...1.2 mm/m for 40% mean cross-section loss). In both hybrid tests, the plastic range of the load-deformation curve was not reached and the uncorroded bars merely exhibited elastic strains when the damaged bars had been drilled through, although the exhibited deformation was too small for the earth pressure to reach the active pressure. It was found that for a loose backfill, the effectively acting moment caused by the earth pressure is much lower than the yield moment due to the structural safety provided in design ($\gamma_d = 1.88$ based on the concept of SIA 162 [144] for walls built before 1989), which causes the retaining wall to exhibit merely elastic deformations up to a mean cross-section loss of approximately 60...70%. In the case of a compacted backfill, the initial earth pressure is higher, but decreases rapidly with additional wall deformation. In the hybrid tests, the additional deformation due to an increasing cross-section loss was even smaller than in the case of a loose backfill.

The *lap splice* above the construction joint – as typically found in retaining walls – combined with the reinforcement anchorage in the footing leads to a large opening of the joint, which is unfavourable regarding durability. Additionally, the double reinforcement ratio significantly stiffens the lap splice region, lowering its rotation capacity by at least 50%. Consequently, approximately 85% of the wall deformation is caused by a rotation of the entire wall around the construction joint, and only 15% by a deflection of the part above the lap splice. The finding that lap splice regions exhibit a reduced deformation capacity is further relevant for all parts of RC structures potentially undergoing plastic deformations, such as bridge decks above monolitically connected piers, where the anchorage of the pier reinforcement in the deck reduces the maximum deck rotation.

The **Corroded Tension Chord Model** combines the effects of tension stiffening and strain localisation. Thanks to its sound mechanical basis, it can readily be extended by models accounting for further effects, such as the triaxial stress state at the corrosion pit. On the other hand, it retains the modelling approach of the established TCM, i. e. to reliably capture the mean deformations of a crack element without having to solve the differential equation of bond. This allows the model to be included in a computationally efficient manner in higher-level structural models (e. g. as a constitutive material law in a Finite Element (FE) model). The CTCM was successfully applied in combination with the simplified model for the triaxial stress state to assess the experimental campaign on locally corroded retaining wall segments, capturing the load-deformation behaviour fairly well.

The *intersection approach*, i. e. setting the CTCM predictions (enhanced with approaches to capture the local effects at the pits) for specific cross-section losses equal to the load path of the earth pressure (see black dots on load-deformation curves in Figure 9.1), is suited to assess the load-deformation behaviour and the structural safety of cantilever retaining walls mainly loaded by the earth pressure. However, since the additional deformations caused by the increasing cross-section loss are in the range of merely a few millimetres, an accurate prediction of the behaviour is challenging.

The investigations on the triaxial stress state at the corrosion pits and the assessment of the experimental campaign with the CTCM revealed that models solely considering strain localisation significantly underestimate the residual deformation capacity of corroding structures. Furthermore, the experimental results indicated an additional **softening effect**, which seems to gain influence with an increasing unilateral cross-section loss. This softening might result from superimposed bending stresses at the unilateral corrosion pits, leading to higher mean normal strains as soon as the bar begins to yield. In fact, the fibre optic strain measurements revealed local bending strains, increasing with the unilateral cross-section loss. The effect could partly also be explained by post-peak softening at the pit after necking onset, being stabilised by a sufficient tensile stiffness of the uncorroded reinforcing bars.

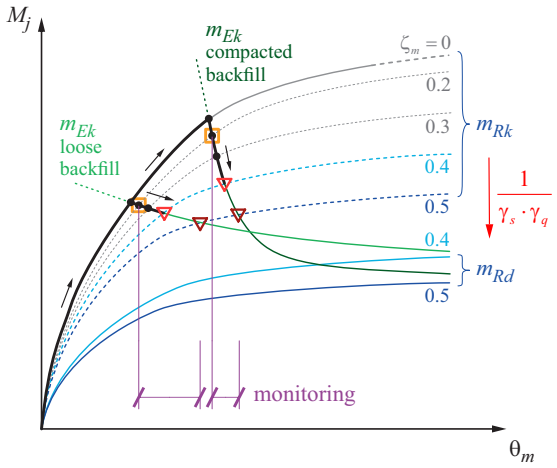

Fig. 9.1 – Schematic load-deformation behaviour of cantilever retaining wall segment for different cross-section losses on characteristic and design level (dashed and solid lines, respectively), along with earth pressure load paths (green) and the actual load-deformation behaviour in the hybrid tests for an increasing cross-section loss (black).

9.2 Conclusions

Based on the experimental curves observed in the hybrid tests, Figure 9.1 schematically illustrates the load paths (bending moment at construction joint vs mean rotation) of the earth pressure for a loose and a compacted backfill (green) along with the load-deformation curves of specimens exhibiting different corrosion damages (grey and blue). The latter curves represent the load-deformation behaviour if one accounts merely for the uncorroded bars, i. e. assuming a full cross-section loss of the corroded bars. As an example, the curve for $\zeta_m = 0.4$ considers 4 of 10 bars being fully corroded (cross-section loss $\zeta_i = 1$), while the remaining 6 bars are assumed to be uncorroded. Note that this scenario yields an upper bound of the deformation since, generally, the corroding reinforcing bars increase the stiffness until a cross-section loss $\zeta_i = 1$ is reached. The load paths followed in the two hybrid tests (with $\zeta_m = 0.4$) are shown in black; they ended at the light red triangle when the damaged bars were fully drilled through, thus lying on the dashed light blue curve with equal ζ_m.

Figure 9.1 highlights the challenges for **structural monitoring of corroding retaining walls**:

(i) Monitoring systems would need to be capable of measuring the small elastic deformations of the wall, in a range as observed during the drilling phase in the hybrid tests; significant plastic deformations due to an increasing cross-section loss are only expected to occur for a significant damage close to failure (e. g. for $\zeta_m \approx 0.6...0.7$ in Figure 9.1, curves not plotted). However, the *small deformations* due to an increasing cross-section loss *are superimposed by deformations caused by many other effects* (daily and seasonal temperature variations, temporary backwater pressure), which are typically much larger. This complicates detecting a weak long-term trend in the measured data caused by a progressing cross-section loss (even in the considered case shown in Figure 9.1, which rather underestimates the stiffness), and it may be highly demanding to indicate a reliable deformation limit.

(ii) The *initial cross-section loss* at the start of the structural monitoring, illustrated in Figure 9.1 with orange squares, is usually unknown. It is thus not possible to relate a measured deformation increase to an absolute cross-section loss. Due to the non-linear load path of the earth pressure and since the corrosion rate might not be constant, it even appears hardly feasible to reliably relate the measured deformation to a relative increase in cross-section loss. Moreover, the occurring corrosion damage per bar will hardly be equal, and the real behaviour thus much more complex than for the case illustrated in Figure 9.1.

(iii) In Figure 9.1, intersection points between the earth pressure load paths and the structure load-deformation curves, representing states of equilibrium, are found for mean cross-section losses $\zeta_m = 0.4$ and 0.5 (indicated with light and dark red triangles) if material and soil properties are considered on the characteristic level (dashed lines). However, if *partial safety factors* are considered (solid lines; for simplicity, $\gamma_s = 1.15$ and $\gamma_q = 1.35$ are both applied to the resistance, which can thus be compared to the characteristic earth pressure curves), an intersection point is found for $\zeta_m = 0.4$, but not for $\zeta_m = 0.5$. Hence, structural safety would only be sufficient for a cross-section loss $\zeta_m \leq 0.4$ (note that this could have been expected since the hybrid tests were dimensioned with a global safety factor in the range of $\gamma_d \approx 1.88$, as used in the design of typical Swiss cantilever retaining walls in the years between 1956 and 1989 [73]). This raises the question of whether a reduced safety margin can be accepted if the structure is monitored in return, which is, however, beyond the scope of this thesis.

Thanks to beneficial effects at the corrosion pit (triaxial stress state, additional softening effect), the deformation capacity of a structure is less severely impaired by local corrosion than assumed by established strain localisation models. Therefore, a plastic **redistribution of forces** for statically indeterminate systems (slabs, multi-span beams) from corroded to uncorroded regions might be possible if the uncorroded regions exhibit overcapacities. A corroding structure would thus not necessarily need to be retrofitted, and its service life could be extended under the conditions that (i) models for a reliable structural assessment – allowing to quantify the residual load-carrying and deformation capacity – exist, and (ii) the corrosion propagation can be reliably predicted or even stopped (e. g. by cathodic protection).

However, in practice, information on the necessary input parameters to reliably model the load-deformation behaviour of corroded structures is scarce. Often, the **construction documents** of older structures are incomplete or missing, and hence, little is known about the used steel type and the reinforcement layout. The methods for **structural health assessment**, e. g. half-cell potential mapping, resistivity measurements, and determining the chloride content and the carbonation depth, are suited to indicate if and where corrosion is likely to be present in a structure. However, no information can be derived from the results of these measurements on the pit geometry, the location of the pits regarding the different reinforcement layers, or the number of affected bars. As outlined in Section 1.2.1, these parameters are decisive to predict the load-deformation behaviour of a structural element, in particular, to account for the beneficial effects of a triaxial stress state.

For the simple case of corroding reinforcing bars being located in only one section of an RC member with constant mean cross-section loss ζ_m, the CTCM was evaluated for a varying number of corroding reinforcing bars n_c with an individual cross-section loss ζ_i, i. e. various combinations of $\{n_c, \zeta_i\}$. The analysis indicated that there exists a **critical combination** $\{n_c, \zeta_i\}_{crit}$ **for which the load-carrying and deformation capacity of the member is minimum** (see also [73]). For cantilever retaining walls, this critical combination could serve as a lower bound estimate for the case that only the mean cross-section loss is known but no information on the corrosion distribution is available. The conducted analysis assumed a simple load-bearing mechanism and only one corrosion pit of constant length per corroded bar. However, it might be possible to find similar critical pit combinations also for varying pit lengths and members with multi-dimensional load-bearing mechanisms.

9.3 Outlook on future research

On the **level of the reinforcing bars**, an approach was presented to capture the influence of a triaxial stress state at the corrosion pit on the local load-deformation behaviour of the reinforcing bar for axisymmetric damage. However, further research is needed to analyse the effects caused by different *pit geometries*, such as the observed additional softening effect potentially occurring due to unilateral damage. Possible parameters to be varied are the pit shape (narrow or wide, angular or circular), the pit geometry (depth and length), and the corresponding position of the centroidal axis with respect to the bar axis (i. e. unilateral or axisymmetric damage). It is proposed to compile a comprehensive set of pit geometries

with reasonable parameter boundaries and to conduct tensile tests on prepared bare reinforcing bars for a selected pit geometry subset. In a second step, Finite Element analyses could be conducted on the entire geometry set, and their results be validated with the results of the tensile tests. Possible correlations between the pit geometry and and the observed load-deformation behaviour of the bars could thus be identified. Particular attention should be paid to the stress-strain behaviour of the used reinforcing steel since it potentially influences the results, as outlined in Section 9.1.

On the **level of structural concrete elements**, this work applied the CTCM in combination with a first approach to consider the effects of the pit geometry on cantilever retaining walls, pointing out an additional softening effect not yet considered. Once this shortcoming is solved, *segmented retaining walls* could be analysed with the proposed algorithm for different geometrical, material, loading, and corrosion parameters – similar to a parametric study – to investigate whether a subset of walls can be identified that reacts sensitively to a certain corrosion scenario and, hence, needs to be assessed primarily.

The reduced deformation capacity of *lap splices* predicted by the proposed modelling approach has not been experimentally validated due to a lack of data in the ultimate load range. Furthermore, the load-deformation behaviour of a lap splice located in a zone with high gradients of normal force or bending moment might differ from that of a splice loaded by a constant normal force, as investigated in this study. Since a lap splice is positioned above the footing in most retaining walls and thus pronouncedly influences their overall deformation capacity, a validation of the model predictions and further investigations regarding the influence of the bending moment gradient would be essential.

The experimental results indicated that the *anchorage* of bent reinforcing bars with large radius differs significantly from that of straight bars regarding its load-deformation behaviour. Although the simplified anchorage model used in this study approximately captures the experimentally observed deformations, the underlying mechanical effects need to be investigated.

The simple load-bearing mechanism of longitudinally segmented retaining walls or beams in bending affected by corrosion can be accurately modelled using the proposed algorithm (CTCM for bending crack elements). However, a more sophisticated modelling strategy is needed for structural elements with a *multi-dimensional load-bearing mechanism* (e. g. slabs). The CTCM is located at the interface between a localised problem formulation for the corroding bar and understanding the corroded crack element as part of a continuum. It is thus suited to be included in an FE analyses tool as a constitutive material model, using similar approaches as presented by Thoma et al. [156], who included the TCM as a user-defined material in a Nonlinear Finite Element (NLFE) analysis software. Regarding the representative volume element, strategies need to be found to relate the local corrosion damage to a reference length (in the CTCM, this is the crack element length) while maintaining the approach of treating an FE element as a continuum. First promising steps in this direction were made in an explorative approach [67].

The influence of local corrosion on the load-carrying and deformation capacity of *slabs* has not yet been analysed, neither theoretically nor experimentally, although they represent a large part of the structural elements affected by chloride-induced pitting corrosion (e. g. bridge decks). The structural safety of such elements may be less impaired by local corrosion than expected due to the two-dimensional load-carrying mechanism and since the deformation capacity of corroded bars is less reduced than predicted by strain localisation models. Analysing selected pit patterns in a subarea of a modelled slab using the CTCM implemented in an NLFE analysis tool could help to understand the altered load-carrying behaviour. It is evident that the predicted behaviour needs experimental validation in a next step.

In practice, information on the extent of corrosion damage, the pit pattern, and the pit geometry is mostly missing. This issue might be tackled by analysing the influence of *statistically generated random pit patterns* on the load-carrying behaviour, similar to a Monte-Carlo simulation or using AI-based algorithms. In a later step, it may even be possible to combine such analyses of real structures with the results obtained from in-situ half-cell potential mapping.

As for slabs, little is known on the influence of local corrosion on *elements in shear* so far (e. g. shear walls and bridge girders). Combining the CTCM with the Cracked Membrane Model [89], which is already implemented in an NLFE analysis tool [156], could be a starting point to model and understand the corresponding implications.

References

[1] AASHTO, *AASHTO Guide Specifications for LRFD Seismic Bridge Design*, 2nd ed. Washington, DC: American Association of State Highway and Transportation Officials, 2011.

[2] Albertini, L., 'Influence of the relative rib area on the serviceability of reinforced concrete,' Master's Thesis, Institute of Structural Engineering, ETH Zurich, 2022.

[3] Almeida, J. P., Prodan, O., Tarquini, D. and Beyer, K., 'Influence of lap splices on the deformation capacity of rc walls. I: Database assembly, recent experimental data, and findings for model development,' *Journal of Structural Engineering*, vol. 143, no. 12, p. 04 017 156, 2017. DOI: 10.1061/(ASCE)ST.1943-541X.0001853.

[4] Almusallam, A. A., 'Effect of degree of corrosion on the properties of reinforcing steel bars,' *Construction and Building Materials*, no. 15, pp. 361–368, 2001.

[5] Almusallam, A. A., Al-Gahtani, A., Aziz, A. R., Dakhil, F. H. and Rasheeduzzafar, 'Effect of reinforcement corrosion on flexural behaviour of concrete slabs,' *Journal of materials in civil engineering*, vol. 8, no. 3, pp. 123–127, 1996.

[6] Alsiwat, J. M. and Saatcioglu, M., 'Reinforcement anchorage slip under monotonic loading,' *Journal of Structural Engineering*, vol. 118, no. 9, pp. 2421–2438, 1992. DOI: 10.1061/(ASCE)0733-9445(1992)118:9(2421).

[7] Alvarez, M., 'Einfluss des Verbundverhaltens auf das Verformungsvermögen von Stahlbeton,' Doctoral Dissertation no. 12719, Institute of Structural Engineering, ETH Zurich, 1998. DOI: 10.3929/ethz-a-001992959.

[8] Andisheh, K., Scott, A. and Palermo, A., 'Modeling the influence of pitting corrosion on the mechanical properties of steel reinforcement,' *Materials and Corrosion*, vol. 67, no. 11, pp. 1220–1234, 2016. DOI: 10.1002/maco.201508795.

[9] Andrade, F. X. C., Feucht, M., Haufe, A. and Neukamm, F., 'An incremental stress state dependent damage model for ductile failure prediction,' *International Journal of Fracture*, vol. 200, no. 1-2, pp. 127–150, 2016. DOI: 10.1007/s10704-016-0081-2.

[10] Apostolopoulos, C. A. and Papadakis, V. G., 'Consequences of steel corrosion on the ductility properties of reinforcement bar,' *Construction and Building Materials*, vol. 22, no. 12, pp. 2316–2324, 2008. DOI: 10.1016/j.conbuildmat.2007.10.006.

[11] Apostolopoulos, C., Drakakaki, A., Apostolopoulos, A., Matikas, T., Rudskoi, A. I. and Kodzhaspirov, G., 'Characteristic defects-corrosion damage and mechanical behavior of dual phase rebar,' *Materials Physics and Mechanics*, vol. 30, 2017.

[12] Apostolopoulos, C. A., Diamantogiannis, G. and Apostolopoulos, A. C., 'Assessment of the mechanical behavior in dual-phase steel B400C, B450C, and B500B in a marine environment,' *Journal of Materials in Civil Engineering*, vol. 28, no. 2, p. 04 015 097, 2016. DOI: 10.1061/(ASCE)MT.1943-5533.0001271.

[13] Apostolopoulos, C., 'Structural integrity problems in dual-phase high ductility steel bar,' *Journal of Applied Mechanical Engineering*, vol. 1, no. 5, p. 1 000 115, 2012. DOI: 10.4172/2168-9873.1000115.

[14] Apostolopoulos, C., Konstantopoulos, G. and Koulouris, K., 'Seismic resistance prediction of corroded S400 (BSt420) reinforcing bars,' *International Journal of Structural Integrity*, vol. 9, no. 1, pp. 119–138, 2018. DOI: 10.1108/IJSI-02-2017-0008.

[15] Apostolopoulos, C. A., Demis, S. and Papadakis, V. G., 'Chloride-induced corrosion of steel reinforcement – Mechanical performance and pit depth analysis,' *Construction and Building Materials*, vol. 38, pp. 139–146, 2013. DOI: 10.1016/j.conbuildmat.2012.07.087.

[16] Apostolopoulos, C. A., Koulouris, K. F. and Apostolopoulos, A. C., 'Correlation of surface cracks of concrete due to corrosion and bond strength (between steel bar and concrete),' *Advances in Civil Engineering*, vol. 2019, 2019. DOI: 10.1155/2019/3438743.

[17] Azad, A. K., Ahmad, S. and Azher, S. A., 'Residual strength of corrosion-damaged reinforced concrete beams,' *ACI Materials Journal*, vol. 104, no. 1, pp. 40–47, 2007. DOI: 10.14359/18493.

[18] Bachmann, H., 'Zur plastizitätstheoretischen Berechnung statisch unbestimmter Stahlbetonbalken,' Doctoral Dissertation no. 4069, Institute of Structural Engineering, ETH Zurich, 1967. DOI: 10.3929/ethz-a-000150808.

[19] Basaran, M., 'Stress state dependent damage modeling with a focus on the lode angle influence,' Doctoral Dissertation, Institute of General Mechanics, RTWH Aachen, 2011.

[20] Baumgartner, A., Fraundorfer, A., Dauberschmidt, C. and Kustermann, A., 'Veränderung der mechanischen Kenngrößen von Betonstabstählen durch chloridinduzierte Korrosion,' *Beton- und Stahlbetonbau*, vol. 114, no. 6, pp. 409–418, 2019. DOI: 10.1002/best.201900009.

[21] Bautista, A., Pomares, J., González, M. and Velasco, F., 'Influence of the microstructure of TMT reinforcing bars on their corrosion behavior in concrete with chlorides,' *Construction and Building Materials*, vol. 229, p. 116 899, 2019. DOI: 10.1016/j.conbuildmat.2019.116899.

[22] Beck, A., Gehri, N., Mata-Falcón, J. and Kaufmann, W., 'Cracked Membrane Model with fixed, interlocked cracks: Numerical implementation and validation,' *Journal of Structural Engineering*, vol. 146, no. 2, p. 04 019 193, 2020. DOI: 10.1061/(ASCE)ST.1943-541X.0002461.

[23] Beeby, A., 'The prediction of crack widths in hardened concrete,' *The Structural Engineer*, vol. 57A, no. 1, pp. 9–17, 1979.

[24] Berto, L., Simioni, P. and Saetta, A., 'Numerical modelling of bond behaviour in RC structures affected by reinforcement corrosion,' *Engineering Structures*, vol. 30, no. 5, pp. 1375–1385, 2008. DOI: 10.1016/j.engstruct.2007.08.003.

[25] Bertolini, L., Elsener, B., Pedeferri, P., Redaelli, E. and Polder, R. B., *Corrosion of Steel in Concrete - Prevention, Diagnosis, Repair*, 2nd ed. Weinheim: Wiley-VCH, 2013.

[26] Bilcik, J. and Holly, I., 'Effect of reinforcement corrosion on bond behaviour,' *Procedia Engineering*, vol. 65, pp. 248–253, 2013. DOI: 10.1016/j.proeng.2013.09.038.

[27] Bramfitt, B. L. and Arlan, O., *Metallographer's Guide – Practices and Procedures for Irons and Steels*, 1st ed. Materials Park OH: ASM International, 2002.

[28] Brantschen, F., Faria, D., Fernández Ruiz, M. and Muttoni, A., 'Bond behaviour of straight, hooked, U-shaped and headed bars in cracked concrete,' *Structural Concrete*, vol. 17, no. 5, pp. 799–810, 2016. DOI: 10.1002/suco.201500199.

[29] Burns, C., 'Serviceability analysis of reinforced concrete based in the tension chord model,' Doctoral Dissertation no. 19979, Institute of Structural Engineering, ETH Zurich, 2011. DOI: 10.3929/ETHZ-A-007179384.

[30] Cadoni, E., Dotta, M., Forni, D. and Tesio, N., 'High strain rate behaviour in tension of steel B500A reinforcing bar,' *Materials and Structures*, vol. 48, no. 6, pp. 1803–1813, 2015. DOI: 10.1617/s11527-014-0273-z.

[31] Cadoni, E., Dotta, M., Forni, D., Tesio, N. and Albertini, C., 'Mechanical behaviour of quenched and self-tempered reinforcing steel in tension under high strain rate,' *Materials & Design*, vol. 49, pp. 657–666, 2013. DOI: 10.1016/j.matdes.2013.02.008.

[32] Cadoni, E., Fontana, M., Forni, D. and Knobloch, M., 'High strain rates testing and constitutive modeling of B500B reinforcing steel at elevated temperatures,' *The European Physical Journal Special Topics*, vol. 227, pp. 179–199, 2018. DOI: 10.1140/epjst/e2018-00046-4.

[33] Cairns, J., 'Bond and anchorage of embedded steel reinforcement in *fib* Model Code 2010,' *Structural Concrete*, vol. 16, no. 1, pp. 45–55, 2015. DOI: 10.1002/suco.201400043.

[34] Cairns, J., Plizzari, G. A., Du, Y., Law, D. W. and Franzoni, C., 'Mechanical properties of corrosion-damaged reinforcement,' *ACI Materials Journal*, vol. 102, no. 4, pp. 256–264, 2005.

[35] Castel, A., François, R. and Arliguie, G., 'Mechanical behaviour of corroded reinforced concrete beams —Part 1: Experimental study of corroded beams,' *Materials and Structures*, vol. 33, no. 9, pp. 539–544, 2000.

[36] Castel, A., François, R. and Arliguie, G., 'Mechanical behaviour of corroded reinforced concrete beams —Part 2: Bond and notch effects,' *Materials and Structures*, vol. 33, no. 9, pp. 545–551, 2000.

[37] Castel, A., Khan, I., François, R. and Gilbert, R. I., 'Modeling steel concrete bond strength reduction due to corrosion,' *ACI Structural Journal*, vol. 113, no. 5, pp. 973–982, 2016. DOI: 10.14359/51688925.

[38] CEN, *Eurocode 2: Design of Concrete Structures - Part 1-1: General Rules and Rules for Buildings (EN 1992-1-1:2004)*. Brussels: European Committee for Standardisation (CEN), 2010.

[39] Chen, E., Berrocal, C. G., Fernandez, I., Löfgren, I. and Lundgren, K., 'Assessment of the mechanical behaviour of reinforcement bars with localised pitting corrosion by Digital Image Correlation,' *Engineering Structures*, vol. 219, p. 110 936, 2020. DOI: 10.1016/j.engstruct.2020.110936.

[40] Ciampi, V., Eligehausen, R., Bertero, V. V. and Popov, E. P., 'Analytical model for deformed bar bond under generalized excitations,' in *Advanced mechanics of reinforced concrete : IABSE colloquium*, Delft, The Netherlands, 1981. DOI: 10.18419/opus-7970.

[41] Coronelli, D. and Gambarova, P. G., 'Structural assessment of corroded reinforced concrete beams: Modeling guidelines,' *Journal of Structural Engineering*, vol. 130, no. 8, pp. 1214–1224, 2004.

[42] Correlated Solutions, *Vic-3D Software Manual*, version 8.4, Irmo, SC: Correlated Solutions Inc., 2019.

[43] Cottrell, A. H. and Bilby, B. A., 'Dislocation theory of yielding and strain ageing of iron,' *Proceedings of the Physical Society. Section A*, vol. 62, no. 1, pp. 49–62, 1949. DOI: 10.1088/0370-1298/62/1/308.

[44] Darwin, D., 'Tension development length and lap splice design for reinforced concrete members,' *Progress in Structural Engineering and Materials*, vol. 7, no. 4, pp. 210–225, 2005. DOI: 10.1002/pse.206.

[45] Delwiche, D. E. and Moon, D. W., 'Orientation of Lüders band fronts,' *Materials Science and Engineering*, vol. 7, pp. 203–207, 1971. DOI: 10.1016/0025-5416(71)90146-7.

[46] Du, Y. G., Clark, L. A. and Chan, A. H. C., 'Effect of corrosion on ductility of reinforcing bars,' *Magazine of Concrete Research*, vol. 57, no. 7, pp. 407–419, 2005. DOI: 10.1680/macr.2005.57.7.407.

[47] Dubs, R. and Haefliger, S., 'Verbundverhalten von Stahlbeton - Ausziehversuche zur Analyse von Verbundmodellen und Entwicklung eines Kegelausbruchmodells,' Master's Thesis, Institute of Structural Engineering, ETH Zurich, 2015.

[48] Einea, A., Yehia, S. and Tadros, M. K., 'Lap splices in confined concrete,' *ACI Structural Journal*, vol. 96, no. 6, pp. 947–955, 1999. DOI: 10.14359/769.

[49] Eligehausen, R., Popov, E. P. and Bertero, V. V., 'Local bond stress-slip relationships of deformed bars under generalized excitations: Experimental results and analytical model,' Earthquake Engineering Research Center, University of California, Berkeley, UCB/EERC-83/23, 1983. DOI: 10.18419/opus-8473.

[50] Engström, B., 'Ductility of tie connections in precast structures,' Doctoral Dissertation, Chalmers University of Technology, Göteborg, 1992.

[51] Fasl, J., Larosche, C. J. and Fraczek, J., 'Ductility behaviour of corroded bars in concrete slabs,' *Concrete International*, vol. 38, no. 4, pp. 55–61, 2016.

[52] FEDRO, 'Evaluation de l'état des murs de soutènement béton à semelle. Etude pilote. Rapport de synthèse des phases 1 et 2.,' Technical Report, UVEK, Swiss Federal Roads Office FEDRO, 2014.

[53] Fernandez, I., Bairán, J. M. and Marí, A. R., 'Corrosion effects on the mechanical properties of reinforcing steel bars. Fatigue and σ–ε behavior,' *Construction and Building Materials*, vol. 101, pp. 772–783, 2015. DOI: 10.1016/j.conbuildmat.2015.10.139.

[54] Fernandez, I., Bairán, J. M. and Marí, A. R., '3D FEM model development from 3D optical measurement technique applied to corroded steel bars,' *Construction and Building Materials*, vol. 124, pp. 519–532, 2016. DOI: 10.1016/j.conbuildmat.2016.07.133.

[55] Fernandez, I., Bairán, J. M. and Marí, A. R., 'Mechanical model to evaluate steel reinforcement corrosion effects on σ – ε and fatigue curves. Experimental calibration and validation,' *Engineering Structures*, vol. 118, pp. 320–333, 2016. DOI: 10.1016/j.engstruct.2016.03.055.

[56] *fib*, fib *Bulletin 10: Bond of Reinforcement in Concrete*. Lausanne: *fib* fédération internationale du béton, 2000.

[57] *fib*, fib *Model Code for Concrete Structures 2010*. Lausanne: *fib* fédération internationale du béton, 2013.

[58] Finozzi, I., Saetta, A. and Budelmann, H., 'Structural response of reinforcing bars affected by pitting corrosion: Experimental evaluation,' *Construction and Building Materials*, vol. 192, pp. 478–488, 2018. DOI: 10.1016/j.conbuildmat.2018.10.088.

[59] Flynn, P. D. and Roll, A. A., 'A re-examination of stresses in a tension bar with symmetrical U-shaped grooves,' *Experimental Mechanics*, vol. 6, no. 2, pp. 93–98, 1966. DOI: 10.1007/BF02326227.

[60] Foecke, T., Iadicola, M., Lin, A. and Banovic, S., 'A method for direct measurement of multiaxial stress-strain curves in sheet metal,' *Metallurgical and Materials Transactions A*, vol. 38A, pp. 306–313, 2007. DOI: 10.1007/s11661-006-9044-y.

[61] Forni, D., Chiaia, B. and Cadoni, E., 'Strain rate behaviour in tension of S355 steel: Base for progressive collapse analysis,' *Engineering Structures*, vol. 119, pp. 164–173, 2016. DOI: 10.1016/j.engstruct.2016.04.013.

[62] François, R., Khan, I. and Dang, V. H., 'Impact of corrosion on mechanical properties of steel embedded in 27-year-old corroded reinforced concrete beams,' *Materials and Structures*, vol. 46, no. 6, pp. 899–910, 2013. DOI: 10.1617/s11527-012-9941-z.

[63] Galkovski, T., Lemcherreq, Y., Mata-Falcón, J. and Kaufmann, W., 'Fundamental studies on the use of distributed fibre optical sensing on concrete and reinforcing bars,' *Sensors*, vol. 21, no. 22, p. 7643, 2021. DOI: 10.3390/s21227643.

[64] Galkovski, T., Mata-Falcón, J. and Kaufmann, W., 'Effective reinforcement ratio of RC beams: Validation of modelling assumptions with high-resolution strain data,' *Structural Concrete*, vol. 23, no. 3, pp. 1353–1369, 2022. DOI: 10.1002/suco.202100739.

[65] Gehri, N., Mata-Falcón, J. and Kaufmann, W., 'Automated crack detection and measurement based on digital image correlation,' *Construction and Building Materials*, vol. 256, p. 119 383, 2020. DOI: 10.1016/j.conbuildmat.2020.119383.

[66] Gehri, N., Mata-Falcón, J. and Kaufmann, W., 'Refined extraction of crack characteristics in Large-scale concrete experiments based on digital image correlation,' *Engineering Structures*, vol. 251, Part A, p. 113 486, 2022. DOI: 10.1016/j.engstruct.2021.113486.

[67] Gianinazzi, S., 'Influence of local corrosion on the load-bearing behaviour of bridge cantilevers,' Master's Thesis, Institute of Structural Engineering, ETH Zurich, Zurich, 2022.

[68] Gilbert, R. I. and Kilpatrick, A. E., 'The strength and ductility of lapped splices of reinforcing bars in tension,' *Australian Journal of Structural Engineering*, vol. 16, no. 1, pp. 35–46, 2015.

[69] Haefliger, S., Fomasi, S. and Kaufmann, W., 'Influence of quasi-static strain rate on the stress-strain characteristics of modern reinforcing bars,' *Construction and Building Materials*, vol. 287, p. 122 967, 2021. DOI: 10.1016/j.conbuildmat.2021.122967.

[70] Haefliger, S. and Kaufmann, W., 'Experiments on locally corroded retaining wall segments and their assessment with the Corroded Tension Chord Model,' in *Abstract Proceedings of the CAC-RCS DAYS 2021 – Capacity Assessment of Corroded Reinforced Concrete Structures*, online: *fib* fédération internationale du béton, 2021, pp. 117–121. DOI: 10.3929/ethz-b-000527046.

[71] Haefliger, S. and Kaufmann, W., 'Influence of cross section loss on the stress-strain characteristics of corroded quenched and self-tempered reinforcing bars,' *Construction and Building Materials*, vol. 282, p. 122 598, 2021. DOI: 10.1016/j.conbuildmat.2021.122598.

[72] Haefliger, S. and Kaufmann, W., 'Corroded Tension Chord Model: Load-deformation behavior of structures with locally corroded reinforcement,' *Structural Concrete*, vol. 23, no. 1, pp. 104–120, 2022. DOI: 10.1002/suco.202100165.

[73] Haefliger, S. and Kaufmann, W., 'Load-carrying and deformation capacity of cantilever retaining walls affected by local corrosion of the reinforcement,' Research Report AGB 2015/028, no. 716, UVEK, Swiss Federal Roads Office FEDRO, 2023.

[74] Haefliger, S. and Kaufmann, W., 'Load-deformation behavior of locally corroded retaining wall segments: Experimental results,' *Structural Concrete*, vol. 24, no. 1, pp. 288–317, 2023. DOI: 10.1002/suco.202200405.

[75] Haefliger, S., Kaufmann, W. and Thoma, K., 'Modelling the load-deformation behaviour of lap splices with the Tension Chord Model,' *Engineering Structures*, vol. 252, p. 113 606, 2022. DOI: 10.1016/j.engstruct.2021.113606.

[76] Haefliger, S., Thoma, K. and Kaufmann, W., 'Influence of a triaxial stress state on the load-deformation behaviour of corroded reinforcing bars,' *submitted to Construction and Building Materials*, 2022.

[77] Haefliger, S., Yilmaz, D., Angst, U. and Kaufmann, W., 'Corroded Tension Chord Model (CTCM) for concrete structures with locally corroded reinforcement,' in *Proceedings of the* fib *CAC-RCS DAYS 2020 - Capacity Assessment of Corroded Reinforced Concrete Structures*, online: *fib* fédération internationale du béton, 2020, pp. 171–178. DOI: 10.3929/ethz-b-000458172.

[78] Hancock, J. and Mackenzie, A., 'On the mechanisms of ductile failure in high-strength steels subjected to multi-axial stress-states,' *Journal of the Mechanics and Physics of Solids*, vol. 24, no. 2-3, pp. 147–160, 1976. DOI: 10.1016/0022-5096(76)90024-7.

[79] Heinzmann, D., 'Rissbreitenbeschränkung und Mindestbewehrung,' presented at the Aktuelle Fragen und Entwicklungen im Brückenbau (Zurich), 2016.

[80] Hingorani, R., Pérez, F., Sánchez, J., Fullea, J., Andrade, C. and Tanner, P., 'Loss of ductility and strength of reinforcing steel due to pitting corrosion,' presented at the VIII International Conference on Fracture Mechanics of Concrete and Concrete Structures FraMCoS-8, Toledo, 2013.

[81] Honeycombe, R., *The Plastic Deformation of Metals*, 2nd ed. London: Edward Arnold, 1984.

[82] Hortigón Fuentes, B., Gallardo Fuentes, J. M., Gümpel, P. and Strittmacher, J., 'Wirkung der Tempcore-Behandlung auf die Zugeigenschaften von Stabstahl,' *Stahl und Eisen*, vol. 138, no. 12, pp. 45–52, 2018.

[83] Imperatore, S. and Rinaldi, Z., 'Mechanical behaviour of corroded rebars and influence on the structural response of R/C elements,' in *Concrete Repair, Rehabilitation and Retrofitting II*, London: Taylor & Francis, 2009, pp. 489–495.

[84] Imperatore, S., 'Mechanical properties decay of corroded reinforcement in concrete – an overview,' *Corrosion and Materials Degradation*, vol. 3, no. 2, pp. 210–220, 2022. DOI: 10.3390/cmd3020012.

[85] Kashani, M. M., Crewe, A. J. and Alexander, N. A., 'Nonlinear stress–strain behaviour of corrosion-damaged reinforcing bars including inelastic buckling,' *Engineering Structures*, vol. 48, pp. 417–429, 2013. DOI: 10.1016/j.engstruct.2012.09.034.

[86] Kashani, M. M., Crewe, A. J. and Alexander, N. A., 'Use of a 3D optical measurement technique for stochastic corrosion pattern analysis of reinforcing bars subjected to accelerated corrosion,' *Corrosion Science*, vol. 73, pp. 208–221, 2013. DOI: 10.1016/j.corsci.2013.03.037.

[87] Kaufmann, W., 'Strength and deformations of structural concrete subjected to in-plane shear and normal forces,' Doctoral Dissertation no. 12711, Institute of Structural Engineering, ETH Zurich, 1998. DOI: 10.3929/ethz-a-001972931.

[88] Kaufmann, W., Beck, A., Karagiannis, D. and Werne, D., 'The Large Universal Shell Element Tester LUSET,' Technical Report, IBK Report no. 506, Institute of Structural Engineering, ETH Zurich, 2019. DOI: 10.3929/ethz-b-000379657.

[89] Kaufmann, W. and Marti, P., 'Structural Concrete: Cracked Membrane Model,' *Journal of Structural Engineering*, vol. 124, no. 12, pp. 1467–1475, 1998. DOI: 10.1061/(ASCE)0733-9445(1998)124:12(1467).

[90] Kaufmann, W., Mata-Falcón, J. and Amin, A., 'Compression field analysis of fiber-reinforced concrete based on Cracked Membrane Model,' *ACI Structural Journal*, vol. 116, no. 5, pp. 213–224, 2019. DOI: 10.14359/51716763.

[91] Kaufmann, W. *et al.*, *Compatible Stress Field Design of Structural Concrete: Principles and Validation*. Zurich; Brno: ETH Zurich, Institute of Structural Engineering (IBK); IDEA StatiCa s.r.o., 2020.

[92] Keleştemur, O., Kelestemur, M. H. and Yildiz, S., 'Improvement of mechanical properties of reinforcing steel used in the reinforced concrete structures,' *Journal of Iron and Steel Research International*, vol. 16, no. 3, pp. 55–63, 2009. DOI: 10.1016/S1006-706X(09)60044-3.

[93] Kenel Lüthold, A., 'Biegetragverhalten und Mindestbewehrung von Stahlbetonbauteilen,' Doctoral Dissertation no. 14874, Institute of Structural Engineering, ETH Zurich, 2002. DOI: 10.3929/ETHZ-A-004470989.

[94] Koppitz, R., Kenel, A. and Keller, T., 'Tension Chord Model modification for uniaxial unloading and reloading in elastic and plastic states,' *Journal of Structural Engineering*, vol. 140, no. 10, p. 04 014 077, 2014. DOI: 10.1061/(ASCE)ST.1943-541X.0000999.

[95] Krempl, E., 'An experimental study of room-temperature rate-sensitivity, creep and relaxation of AISI type 304 stainless steel,' *Journal of the Mechanics and Physics of Solids*, vol. 27, no. 5-6, pp. 363–375, 1979. DOI: 10.1016/0022-5096(79)90020-6.

[96] Kun, Q., Li-Ming, Y. and Shi-Sheng, H., 'Mechanism of strain rate effect based on dislocation theory,' *Chinese Physics Letters*, vol. 26, no. 3, p. 036 103, 2009. DOI: 10.1088/0256-307X/26/3/036103.

[97] Kwak, H.-G. and Na, C.-K., 'Anchorage slip effect in RC structures,' *Magazine of Concrete Research*, vol. 61, no. 5, pp. 331–343, 2009. DOI: 10.1680/macr.2008.00070.

[98] Lampert, P., Wegmüller, A. and Thürlimann, B., 'Einfluss der Dehngeschwindigkeit auf Festigkeitswerte von Armierungsstählen,' *Schweizerische Bauzeitung*, vol. 85, no. 14, pp. 248–254, 1967.

[99] Lang, H.-J., Huder, J., Amann, P. and Puzrin, A. M., *Bodenmechanik und Grundbau*, 9th ed. Berlin, Heidelberg: Springer, 2011. DOI: 10.1007/978-3-642-14687-9.

[100] Lemcherreq, Y., Galkovski, T., Mata-Falcón, J. and Kaufmann, W., 'Application of distributed fibre optical sensing in reinforced concrete elements subjected to monotonic and cyclic loading,' *Sensors*, vol. 22, no. 5, p. 2023, 2022. DOI: 10.3390/s22052023.

[101] Lemcherreq, Y., Haefliger, S. and Kaufmann, W., 'Discontinuous yielding in bare and embedded reinforcing bars: Implications on the determination of steel and bond shear stresses from strain measurements,' *Engineering Structures*, vol. 278, p. 115 235, 2023. DOI: 10.1016/j.engstruct.2022.115235.

[102] Li, D., Wei, R., Li, L., Guan, X. and Mi, X., 'Pitting corrosion of reinforcing steel bars in chloride contaminated concrete,' *Construction and Building Materials*, vol. 199, pp. 359–368, 2019. DOI: 10.1016/j.conbuildmat.2018.12.003.

[103] Lim, S., Akiyama, M. and Frangopol, D. M., 'Assessment of the structural performance of corrosion-affected RC members based on experimental study and probabilistic modeling,' *Engineering Structures*, vol. 127, pp. 189–205, 2016. DOI: 10.1016/j.engstruct.2016.08.040.

[104] Lin, H., Zhao, Y., Ožbolt, J. and Hans-Wolf, R., 'The bond behavior between concrete and corroded steel bar under repeated loading,' *Engineering Structures*, vol. 140, pp. 390–405, 2017. DOI: 10.1016/j.engstruct.2017.02.067.

[105] Lode, W., 'Versuche über den Einfluß der mittleren Hauptspannung auf das Fließen der Metalle Eisen, Kupfer und Nickel,' *Zeitschrift für Physik*, vol. 36, pp. 913–939, 1926. DOI: 10.1007/BF01400222.

[106] LUNA, *ODiSI 6000 Series – Optical Distributed Sensor Interrogators*. Roanoke, VA: Luna Innovations Inc., 2021.

[107] Malek, A., Scott, A., Pampanin, S. and Hoult, N. A., 'Postyield bond deterioration and damage assessment of RC beams using distributed fiber-optic strain sensing system,' *Journal of Structural Engineering*, vol. 145, no. 4, p. 04 019 007, 2019. DOI: 10.1061/(ASCE)ST.1943-541X.0002286.

[108] Malvar, L. J., 'Review of static and dynamic properties of steel reinforcing bars,' *ACI Materials Journal*, vol. 95, no. 5, pp. 609–616, 1998. DOI: 10.14359/403.

[109] Mancini, G. and Tondolo, F., 'Effect of bond degradation due to corrosion - a literature survey,' *Structural Concrete*, vol. 15, no. 3, pp. 408–418, 2014. DOI: 10.1002/suco.201300009.

[110] Mangat, P. S. and Elgarf, M. S., 'Flexural strength of concrete beams with corroding reinforcement,' *ACI Structural Journal*, vol. 96, no. 1, pp. 149–158, 1999. DOI: 10.14359/606.

[111] Markić, T., Amin, A., Kaufmann, W. and Pfyl, T., 'Strength and deformation capacity of tension and flexural RC members containing steel fibers,' *Journal of Structural Engineering*, vol. 146, no. 5, p. 04 020 069, 2020. DOI: 10.1061/(ASCE)ST.1943-541X.0002614.

[112] Marques, J. L. G. and Jirsa, J. O., 'A study of hooked bar anchorages in beam-column joints,' *ACI Journal Proceedings*, vol. 72, no. 5, pp. 198–209, 1975. DOI: 10.14359/11131.

[113] Marti, P., 'Size effect in Double-Punch Tests on concrete cylinders,' *Materials Journal*, vol. 86, no. 6, pp. 597–601, 1989. DOI: 10.14359/2261.

[114] Marti, P., Alvarez, M., Kaufmann, W. and Sigrist, V., 'Tension Chord Model for Structural Concrete,' *Structural Engineering International*, vol. 8, no. 4, pp. 287–298, 1998. DOI: 10.2749/101686698780488875.

[115] Maslehuddin, M., Allam, I. A., Al-Sulaimani, G. J., Al-Mana, A. and Abduljauwad, S. N., 'Effect of rusting of reinforcing steel on its mechanical properties and bond with concrete,' *ACI Materials Journal*, vol. 87, no. 5, pp. 496–502, 1990. DOI: 10.14359/1902.

[116] Mata-Falcón, J., Haefliger, S., Lee, M., Galkovski, T. and Gehri, N., 'Combined application of distributed fibre optical and digital image correlation measurements to structural concrete experiments,' *Engineering Structures*, vol. 225, p. 111 309, 2020. DOI: 10.1016/j.engstruct.2020.111309.

[117] Meier, H. H., 'Berücksichtigung des wirklichkeitsnahen Werkstoffverhaltens beim Standsicherheitsnachweis turmartiger Stahlbetonbauwerke,' Doctoral Dissertation, University of Stuttgart, 1983.

[118] Metelli, G., Cairns, J. and Plizzari, G., 'The influence of percentage of bars lapped on performance of splices,' *Materials and Structures*, vol. 48, no. 9, pp. 2983–2996, 2015. DOI: 10.1617/s11527-014-0371-y.

[119] Monney, F., Fernández Ruiz, M. and Muttoni, A., 'Design against splitting failures in reinforced concrete due to concentrated forces and minimum bend diameter of reinforcement,' *Engineering Structures*, vol. 245, p. 112 902, 2021. DOI: 10.1016/j.engstruct.2021.112902.

[120] Murugesan, M. and Jung, D., 'Johnson Cook material and failure model parameters estimation of AISI-1045 medium carbon steel for metal forming applications,' *Materials*, vol. 12, no. 4, p. 609, 2019. DOI: 10.3390/ma12040609.

[121] Noville, J. F. and Jean-François, N., 'TEMPCORE®, the most convenient process to produce low cost high strength rebars from 8 to 75 mm,' presented at the METEC & 2nd ESTAD European Steel Technology and Application Days, Düsseldorf, 2015.

[122] Palsson, R. and Mirza, M. S., 'Mechanical response of corroded steel reinforcement of abandoned concrete bridge,' *ACI structural journal*, vol. 99, no. 2, pp. 157–162, 2002. DOI: 10.14359/11538.

[123] Pan, W.-H., Tao, M.-X. and Nie, J.-G., 'Fiber beam–column element model considering reinforcement anchorage slip in the footing,' *Bulletin of Earthquake Engineering*, vol. 15, no. 3, pp. 991–1018, 2017. DOI: 10.1007/s10518-016-9987-3.

[124] Paulay, T. and Priestley, M. N., *Seismic Design of Reinforced Concrete and Masonry Buildings*. New York: John Wiley & Sons, 1992.

[125] Perozzi, D., 'Quantification of the earth pressure acting on corrosion-damaged cantilever retaining walls: An analysis of the soil-structure interaction,' Doctoral Dissertation no. 28837, Institute of Geotechnical Engineering, ETH Zurich, 2022. DOI: 10.3929/ethz-b-000591353.

[126] Pfyl, T., 'Tragverhalten von Stahlfaserbeton,' Doctoral Dissertation no. 15005, Institute of Structural Engineering, ETH Zurich, 2003. DOI: 10.3929/ETHZ-A-004502831.

[127] Pilkey, W. D. and Pilkey, D. F., *Peterson's Stress Concentration Factors*, 3rd ed. New Jersey: John Wiley & Sons, 2008.

[128] Qian, H., Yan, D., Chen, S., Chen, G., Tian, Y. and Chen, G., 'Effect of high temperature exposure and strain rate on mechanical properties of high-strength steel rebars,' *Journal of Materials in Civil Engineering*, vol. 31, no. 11, p. 04 019 261, 2019. DOI: 10.1061/(ASCE)MT.1943-5533.0002906.

[129] Ramberg, W. and Osgood, W. R., 'Description of stress–strain curves by three parameters,' Technical Note no. 902, National Advisory Committee for Aeronautics, Washington DC., 1943.

[130] Ray, A. *et al.*, 'Microstructure and properties of thermomechanically strengthened reinforcement bars: A comparative assessment of plain-carbon and low-alloy steel grades,' *Journal of Materials Engineering and Performance*, vol. 6, no. 3, pp. 335–343, 1997. DOI: 10.1007/s11665-997-0098-9.

[131] Rebhan, M. J., 'Korrosionsschäden bei Winkelstützmauern,' Doctoral Dissertation, Graz University of Technology, 2019.

[132] Reckling, K.-A., *Plastizitätstheorie und ihre Anwendung auf Festigkeitsprobleme*. Berlin, Heidelberg: Springer, 1967.

[133] Rehm, G. and Russwurm, D., 'Assessment of concrete reinforcing bars made by the Tempcore process,' *Betonwerk + Fertigteiltechnik*, vol. 6, pp. 300–307, 1977.

[134] Rocha, M., Brühwiler, E. and Nussbaumer, A., 'Geometrical and material characterization of quenched and self-tempered steel reinforcement bars,' *Journal of Materials in Civil Engineering*, vol. 28, no. 6, p. 04 016 012, 2016. DOI: 10.1061/(ASCE)MT.1943-5533.0001355.

[135] Rodriguez, J., Ortega, L. and Casal, J., 'Load carrying capacity of concrete structures with corroded reinforcement,' *Construction and Building Materials*, vol. 11, no. 4, pp. 239–248, 1997. DOI: 10.1016/S0950-0618(97)00043-3.

[136] Rösler, J., Harders, H. and Bäker, M., *Mechanisches Verhalten der Werkstoffe*, 3rd ed. Wiesbaden: Vieweg + Teubner, 2008.

[137] Russwurm, D., *Betonstähle für den Stahlbetonbau*. Wiesbaden, Berlin: Bauverlag, 1993.

[138] Ryser, M., Kölz, E., Steiger, A. and Schiegg, Y., 'Hazard-analysis of existing retaining walls,' Research Report AGB 2015/026, no. 707, UVEK, Swiss Federal Roads Office FEDRO, 2021.

[139] Santos, J. and Henriques, A. A., 'Strength and ductility of damaged Tempcore rebars,' *Procedia Engineering*, vol. 114, pp. 800–807, 2015. DOI: 10.1016/j.proeng.2015.08.029.

[140] Seelhofer, H., 'Ebener Spannungszustand im Betonbau: Grundlagen und Anwendungen,' Doctoral Dissertation no. 18486, Institute of Structural Engineering, ETH Zurich, 2009. DOI: 10.3929/ETHZ-A-005901914.

[141] Sezen, H. and Setzler, E. J., 'Reinforcement slip in reinforced concrete columns,' *ACI Structural Journal*, vol. 105, no. 3, pp. 280–289, 2008. DOI: 10.14359/19787.

[142] Shima, H., Chou, L.-L. and Okamura, H., 'Bond characteristics in post-yield range of deformed bars,' *Journal of the Japan Society of Civil Engineers*, vol. 1978, no. 378, pp. 213–220, 1987. DOI: 10.2208/jscej.1987.378_213.

[143] Shima, H., Chou, L.-L. and Okamura, H., 'Micro and macro models for bond in reinforced concrete,' *Journal of the Faculty of Engineering*, vol. XXXIX, no. 2, pp. 133–194, 1987.

[144] SIA, *Swisscode SIA 162: Für Die Berechnung und Ausführung der Beton- und Eisenbetonbauten*. Zurich: Swiss Society of Engineers and Architects (SIA), 1956.

[145] SIA, *Swisscode SIA 262: Concrete Structures*. Zurich: Swiss Society of Engineers and Architects (SIA), 2013.

[146] Sigrist, V., 'Zum Verformungsvermögen von Stahlbetonträgern,' Doctoral Dissertation no. 11169, Institute of Structural Engineering, ETH Zurich, 1995. DOI: 10.3929/ethz-a-001475252.

[147] Sorkine-Hornung, O. and Rabinovich, M., 'Least-squares rigid motion using SVD,' Technical Note, Department of Computer Science, ETH Zurich, 2017.

[148] Soroushian, P., Obaseki, K., Nagi, M. and Rojas, M. C., 'Pullout behavior of hooked bars in exterior beam-column connections,' *ACI Structural Journal*, vol. 85, no. 3, pp. 269–276, 1988. DOI: 10.14359/2623.

[149] Al-Sulaimani, G. J., Kaleemullah, M. and Basunbul, I. A., 'Influence of corrosion and cracking on bond behavior and strength of reinforced concrete members,' *ACI Structural Journal*, vol. 87, no. 2, pp. 220–231, 1990. DOI: 10.14359/2732.

[150] Takagishi, Y., Ichikawa, H., Tabuchi, H. and Moriwake, A., 'Experimental study on deterioration and repairing of a marine concrete structure,' *ACI Special Publication*, vol. 109, pp. 253–276, 1988. DOI: 10.14359/2761.

[151] Tang, F., Lin, Z., Chen, G. and Yi, W., 'Three-dimensional corrosion pit measurement and statistical mechanical degradation analysis of deformed steel bars subjected to accelerated corrosion,' *Construction and Building Materials*, vol. 70, pp. 104–117, 2014. DOI: 10.1016/j.conbuildmat.2014.08.001.

[152] Tarquini, D., Almeida, J. P. and Beyer, K., 'Influence of lap splices on the deformation capacity of RC walls. II: Shell element simulation and equivalent uniaxial model,' *Journal of Structural Engineering*, vol. 143, no. 12, p. 04 017 157, 2017. DOI: 10.1061/(ASCE)ST.1943-541X.0001859.

[153] Tarquini, D., Almeida, J. P. and Beyer, K., 'Uniaxial cyclic tests on reinforced concrete members with lap splices,' *Earthquake Spectra*, vol. 35, no. 2, pp. 1023–1043, 2019. DOI: 10.1193/041418EQS091DP.

[154] Tarquini, D., de Almeida, J. P. and Beyer, K., 'Experimental investigation on the deformation capacity of lap splices under cyclic loading,' *Bulletin of Earthquake Engineering*, vol. 17, no. 12, pp. 6645–6670, 2019. DOI: 10.1007/s10518-019-00692-3.

[155] Tarquini, D., de Almeida, J. P. and Beyer, K., 'Extended Tension Chord Model for boundary elements of RC walls accounting for anchorage slip and lap splices presence,' *International Journal of Concrete Structures and Materials*, vol. 14, no. 2, 2020. DOI: 10.1186/s40069-019-0381-9.

[156] Thoma, K., 'Finite element analysis of experimentally tested RC and PC beams using the Cracked Membrane Model,' *Engineering Structures*, vol. 167, pp. 592–607, 2018. DOI: 10.1016/j.engstruct.2018.04.010.

[157] Uomoto, T. and Misra, S., 'Behavior of concrete beams and columns in marine environment when corrosion of reinforcing bars takes place,' *ACI Special Publication*, vol. 109, pp. 127–146, 1988. DOI: 10.14359/2796.

[158] VDI, *Optische Messverfahren - Bildkorrelationsverfahren - Grundlagen und Begriffe*. Düsseldorf: Verein Deutscher Ingenieure, 2018.

[159] Voyiadjis, G. Z. and Abed, F. H., 'Microstructural based models for bcc and fcc metals with temperature and strain rate dependency,' *Mechanics of Materials*, vol. 37, no. 2-3, pp. 355–378, 2005. DOI: 10.1016/j.mechmat.2004.02.003.

[160] Wang, L., Liming, Y., Xinlong, D. and Xiquan, J., *Dynamics of Materials*. London: Academic Press, 2019.

[161] Wirion, C., 'Load-carrying and deformation capacity of concrete tension members and retaining walls with locally corroded reinforcement,' Master's Thesis, Institute of Structural Engineering, ETH Zurich, 2019.

[162] Yilmaz, D., Haefliger, S., Kaufmann, W. and Angst, U., 'New conceptual approach combining the probabilistic nature of localised rebar corrosion and the load-deformation behaviour,' in *Proceedings of the* fib *CACRCS DAYS 2020 - Capacity Assessment of Corroded Reinforced Concrete Structures*, online: *fib* fédération internationale du béton, 2020, pp. 449–456. DOI: 10.3929/ETHZ-B-000464554.

[163] Zeng, C., Zhu, J.-H., Xiong, C., Li, Y., Li, D. and Walraven, J., 'Analytical model for the prediction of the tensile behaviour of corroded steel bars,' *Construction and Building Materials*, vol. 258, p. 120 290, 2020. DOI: 10.1016/j.conbuildmat.2020.120290.

[164] Zeng, X., Wang, Z. and Huo, J., 'Tensile behavior of 400 MPa-grade anti-earthquake hot-rolled ribbed bar (HRB400E) over a wide strain rate range,' *Construction and Building Materials*, vol. 249, p. 118 729, 2020. DOI: 10.1016/j.conbuildmat.2020.118729.

[165] Zhang, J. and Jiang, Y., 'Lüders bands propagation of 1045 steel under multiaxial stress state,' *International Journal of Plasticity*, vol. 21, no. 3, pp. 651–670, 2005. DOI: 10.1016/j.ijplas.2004.05.001.

[166] Zhu, W., François, R., Poon, C. S. and Dai, J.-G., 'Influences of corrosion degree and corrosion morphology on the ductility of steel reinforcement,' *Construction and Building Materials*, vol. 148, pp. 297–306, 2017. DOI: 10.1016/j.conbuildmat.2017.05.079.